Science

AAAS

GENETIC CROSSING

Ancient DNA traces linguistic links that tie Anatolia to Europe   pp. 908, 922, 939, 940, & 982

2022 Welch Conference

NEW LOCATION | NEW EXPERIENCE | OCTOBER 24–25, 2022

This in-person and live-streamed conference will feature the theme, **"Molecules and Sculpted Light,"** an exploration of light at the molecular level, in addition to the keynote address by Dr. Peter Hotez and virtual poster sessions welcoming young scientists from around the globe.

The conference will be held in the Grand Ballroom of **The Post Oak Hotel at Uptown Houston,** conveniently located minutes from The Galleria, Memorial Park, and dozens of restaurants and retail offerings.

W. E. MOERNER
Conference Chair, Stanford University

Molecules and Sculpted Light

Light interacts with molecules in myriad ways producing the colors we see in the world around us, skin damage from sunshine, chemical transformations resulting in new molecules and more. The light produced by fluorescent molecules (like those found in day-glow socks) can be sculpted by optics which allows scientists to detect nanoscale properties of individual molecules such as the precise position of the molecule in three dimensions, how it is oriented with respect to other molecules, and the lifetime of its excited state. The conference explores the latest developments that exploit the use of sculpted light to develop novel technologies to explore the world at the molecular level.

PETER HOTEZ, M.D., PH.D.
Dean, National School of Tropical Medicine, Baylor College of Medicine

New in 2022, the conference will feature a keynote address by Dr. Peter Hotez of Texas Children's Hospital and Baylor College of Medicine.

COVID-19 Vaccines: Science vs Anti Science

The Texas Children's Hospital Center for Vaccine Development is leading the development of new vaccines for poverty-related neglected diseases and COVID-19. Since May 2021, an estimated 200,000 unvaccinated Americans have died because they refused COVID-19 vaccines. They were victims of growing anti science aggression, which has now become a dominant and lethal social force and disease determinant in the U.S.

CAROLYN R. BERTOZZI
Anne T. and Robert M. Bass Professor of Chemistry, Stanford University

The 2022 Welch Award in Chemistry Lecture

Therapeutic Opportunities in Glycoscience

Cell surface glycans constitute a rich biomolecular dataset that drives both normal and pathological processes. Their "readers" are glycan-binding receptors that can engage in cell-cell interactions and cell signaling. Our research focuses on mechanistic studies of glycan/receptor biology and applications of this knowledge to new therapeutic strategies. Our recent efforts center on pathogenic glycans in the tumor microenvironment and new therapeutic modalities based on the concept of targeted degradation.

Virtual Poster Sessions

The Welch Foundation wants to hear about your research! For the first time, the Welch Conference will feature a virtual poster session inviting young scientists to present their research, answer questions, and engage with audiences from all over the world.

For registration, live-stream information, and a complete program, visit our website at **welch1.org/conference/**

CONTENTS

26 AUGUST 2022 • VOLUME 377 • ISSUE 6609

914

Male ostracods light
up Caribbean waters.

PHOTO: KYLE MCBURNIE

CONTENTS

RESEARCH

918 & 1008

Zebra and wildebeest on the move in one of the largest remaining mammal migrations.

ON THE COVER

This image inspired by Bronze Age art depicts people of diverse cultures spreading their genes between West Asia and Southeast Europe. From left to right: Mycenaean, Minoan, Hittite, Armenian, and Urartian. A total of 1317 ancient genomes spanning 10,000 years were analyzed to reveal the manifold connections between these regions that are invisible in modern DNA. See pages 908, 922, 939, 940, and 982. *Image: Oliver Uberti Creative*

PHOTO: EVAN FRICKE

The FDA and scientific priorities

Earlier this year, when I was confirmed as the new commissioner of the US Food and Drug Administration (FDA), the world faced ongoing public health issues related to the pandemic and war in Ukraine, among other challenges. Most notably, the US is experiencing a flattening or decline in life expectancy compared with other high-income countries. As part of a wider effort to reverse this decline, relationships between FDA and the biomedical ecosystem should be reimagined to facilitate more effective translation of science into successful health interventions.

The biomedical community's response to COVID-19 has provided multiple tools—vaccines; antiviral medications and other therapeutics; diagnostic testing—that can help prevent infection and transmission and treat patients. FDA's flexibility and guidance regarding compressed time frames for research, development, testing, and regulatory approval were crucial in responding to this ever-changing public health threat. Equally important was the ability to streamline clinical trials to efficiently produce data that enabled a clear understanding of the risks and benefits for new or repurposed therapeutics. FDA will apply these lessons, where relevant, to other areas of biomedical product development. A reciprocal emphasis on reinventing research translation across biomedical sectors is needed to meet the moment.

Despite progress in treating cancer and rare diseases, declines in US life expectancy are driven by common, chronic diseases (CCDs), including cardiometabolic, lung, and kidney disease, along with mental health conditions. Use of tobacco products and increases in deaths due to opioid overdose are also driving negative national statistics. Existing approaches to develop and assess pharmacologic therapies, medical devices, and interventions for CCDs and addiction, including behavioral techniques, should be reexamined by the biomedical community. While the FDA revitalizes its approaches, the biomedical community should also review its priorities so that it can deliver more new therapies in these areas, particularly for those suffering most: racial and ethnic minorities, people with less education and wealth, and those living in rural areas. Consortia comprising patients, researchers, regulators, and the medical products industry are needed, as exemplified by substantial progress in therapies for cystic fibrosis, type 1 diabetes mellitus, and multiple myeloma. FDA will focus on translating new science into treatments and diagnostics, working closely with the National Institutes of Health and its grantees, the recently formed Advanced Research Projects Agency for Health, and patient advocacy groups.

Integrating research and clinical care with access to digital information presents enormous potential to benefit the research enterprise and health outcomes. However, societal norms for research participation and data sharing should be revamped, including attention to cyberattack vulnerability. It is hoped that modernizing FDA's digital infrastructure will prompt complementary efforts by the biomedical community to evolve a national digital infrastructure that enables swift, systematic gathering of patient data, collectively yielding detailed understanding of "real-world" benefits and risks of medical products. This network should also support faster, more comprehensive approaches to risk–benefit issues for food, where considerations of nutritional value, supply-chain data, presence of toxic substances, whole-genome pathogen sequencing, and impact of intentional gene modification can be integrated with health outcomes. In the face of global climate change, a safe, resilient, and effective food system is a priority. Involving consumers and patients directly in the process of FDA's technology development represents a major opportunity to harness social science and human behavioral research and engage with the public more meaningfully.

Misinformation has undermined the credibility of science and evidence-based processes that improve societal well-being. The FDA is working to restore public confidence by prioritizing clear, direct, and transparent communication as a priority. However, broader efforts spanning the biomedical ecosystem are needed to create an effective consortium that ensures access to truthful information about biomedical science and health.

Although FDA's primary mission is to safeguard the well-being of Americans, it operates in a global environment. FDA will continue to work with scientific, public health, and regulatory communities around the world to establish robust information systems for monitoring viral and biological environments, disease transmission, and the safety of medicines and food produced outside the US. COVID-19 has been a clarion call for public health agencies and biomedical scientists worldwide to collaborate as never before.

–Robert M. Califf

> "...relationships between FDA and the biomedical ecosystem should be reimagined..."
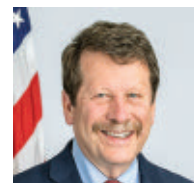
Robert M. Califf
is commissioner of the US Food and Drug Administration, Silver Spring, MD, USA. commissioner@fda.hhs.gov

NEWS

IN BRIEF

Edited by **Jeffrey Brainard**

Climate change has left the Iberian Peninsula at its driest in 1200 years. Drought shrank a reservoir to reveal a prehistoric monument in Spain this month.

ARCHAEOLOGY

Drought exposes 'Spanish Stonehenge' for study

Scientists are rushing to examine a 7000-year-old stone circle in central Spain that had been drowned by a reservoir for decades and was uncovered after the drought plaguing Europe lowered water levels. Nicknamed the "Spanish Stonehenge"—although 2000 years older than the U.K. stone circle—the Dolmen of Guadalperal (above) was described by archaeologists in the 1920s. The approximately 100 standing stones, up to 1.8 meters tall and arranged around an oval open space, were submerged in the Valdecañas reservoir after the construction of a dam on the Tagus River in 1963.

The water has receded a few times since, most recently in 2019, when archaeologists worked to create a digital record of the site. This time they hope to better understand engravings on the stones, which include a human figure and a squiggly line, and document any further damage to the monument's porous granite. The drought has uncovered other historic sites across Europe, such as a Roman fort in Spain, World War II–era German warships in the Danube River, and "hunger stones"—bearing dates engraved by people suffering from famines caused by past droughts—in the Danube, Elbe, and other rivers.

Fauci sets a date to step down

LEADERSHIP | Anthony Fauci, the physician and immunologist who has led the $6.3 billion U.S. National Institute of Allergy and Infectious Diseases (NIAID) for 38 years and has been an ardent, embattled voice for scientific evidence during the COVID-19 pandemic, will leave government service in December. Fauci, 81, is also resigning as chief of an NIAID immunology lab and as President Joe Biden's chief medical adviser. In a statement, he said he intends to continue to mentor future scientific leaders. He told *The Washington Post* that his plans also include writing a book and teaching. The tireless, blunt Brooklyn native has served under seven presidents and helmed NIAID from the early days of the HIV/AIDS epidemic in the 1980s through the 2001 anthrax attacks, the 2009 swine influenza pandemic, and outbreaks of West Nile, Ebola, and Zika viruses. As a member of former President Donald Trump's White House Coronavirus Task Force, Fauci became an icon in the United States and worldwide, working to counter Trump's public misstatements about the pandemic. Fauci also clashed with Republican lawmakers such as Senator Rand Paul (KY) over pandemic public health measures and their baseless assertions that the SARS-CoV-2 virus originated in a lab in Wuhan, China, that had received NIAID funding.

Gene therapy for a blood disease

BIOMEDICINE | The U.S. Food and Drug Administration last week approved a genetic treatment for the blood disorder beta-thalassemia, marking the third U.S. gene therapy for a rare disease. The disorder causes low hemoglobin and severe anemia, and the regular blood transfusions used to treat it can cause iron buildup that damages organs. The new treatment, Zynteglo, from manufacturer bluebird bio, relies on a virus to deliver a gene for hemoglobin into the patient's bone marrow cells, grown in culture; the cells are then infused back into the body. In clinical trials, 89% of treated patients no longer required transfusions. Zynteglo won European approval in 2019 but was removed from the market after countries balked over the high price; in the United States it will cost $2.8 million per one-time treatment, making it one of the most expensive drugs ever. Bluebird is testing a different product that uses the same method for sickle cell anemia, which is more common in the United States than thalassemia.

How rabbits invaded Australia

GENETICS | Most of Australia's rabbits, which have become a scourge of crops and native plants, descended from a single introduction by a farmer in 1859, a genetics study has found. Rabbits were repeatedly brought to Australia, including aboard the first fleet of British ships to reach Sydney, in 1788. But the fateful introduction came in 1859, when relatives in England of Thomas Austin, a wealthy settler, sent him bunnies that he used to establish a colony on his estate outside of Melbourne. These animals may have had a leg up in colonizing the continent: The DNA of their contemporary progeny includes a large amount from wild ancestors, which may have given Austin's brood an adaptive edge in Australia, says the study in this week's issue of the *Proceedings of the National Academy of Sciences*. The findings may aid efforts to find new ways to control the country's rabbit populations and perhaps eradicate them.

A cheaper way to save forests

CONSERVATION | To get the most for their money, forest conservationists should target areas where relatively small investments could protect lots of species, rather than pushing to preserve a specific percentage of the landscape, a study argues. The analysis, published by economists in the 17 August issue of *Nature*, comes as many advocates are urging nations to adopt a new goal of protecting 30% of their lands by 2030. That "30x30" goal risks wasting limited resources, the authors say. Instead, they offer a 50-year plan, based on a study of 458 forested regions, that calls for first saving relatively species-rich forests where conservation costs are low. They found that limiting deforestation in the plan's first year in just 18 regions—including in Turkey's Anatolian Peninsula and in Melanesia, for example—would produce the greatest benefit. Their plan would protect a total of 46 regions within a decade. It gives a lower priority to saving forests where costs would be high, such as near cities in Brazil.

Mum's the word on flawed papers

PUBLISHING | One-third of 330 top-ranked scientific journals do not publish outsiders' critiques of papers after they appear, even though most of these journals belong to a publishing organization, the Committee on Publication Ethics, that encourages members to publish critiques, a study found. Among the majority that do run critical letters, commentaries, or online comments, many impose deadlines and limit length. Together, these choices by both types of journals raise barriers to correcting flawed papers, the study's authors write this week in *Royal Society Open Science*. In the 207 journals that accepted comments, only about 2% of 2066 randomly selected papers mentioned the existence of a relevant, postpublication critique, the team found. Its study analyzed the 15 journals with the highest journal impact factors in each of 22 scientific disciplines. All 15 journals in clinical medicine published critiques; only two math journals did.

2019 Event Horizon Telescope image   2022 photon ring image

ASTRONOMY
Black hole's 'photon ring' unveiled

Like art restorers discovering a hidden image under an old master, astrophysicists have reprocessed data used to create the first image of a black hole and sifted out only the light from its "photon ring." The crisp, bright circle (above, right) shows photons held in a tight orbit near the edge of the event horizon, the point at which even light cannot escape the black hole's gravity. To reveal the ring, researchers reanalyzed the now-iconic image of the supermassive black hole in the nearby galaxy M87, released in 2019 by the Event Horizon Telescope. That image (above, left) shows a fuzzy, fiery band of light that combines photons escaping from the ring and emissions from matter swirling around the black hole. New algorithms were able to tease out just the photons that came from the ring. The researchers reported last week in *The Astrophysical Journal* that the ring's size, structure, and unvarying nature closely match theoretical predictions, confirming the ability of strong gravity to bend light into a tight curve.

IN DEPTH

Researchers sampled DNA from individuals including this man, buried about 8000 years ago in Turkey.

HUMAN EVOLUTION

Ancient DNA from the Near East probes a cradle of civilization

Studies seek clues to origins of farming, early languages

By **Andrew Curry**

Few places have shaped Eurasian history as much as the ancient Near East. Agriculture and some of the world's first civilizations were born there, and the region was home to ancient Greeks, Troy, and large swaths of the Roman Empire. "It's absolutely central, and a lot of us work on it for precisely that reason," says German Archaeological Institute archaeologist Svend Hansen. "It's always been a bridge of cultures and a key driver of innovation and change."

But one of the most powerful tools for unraveling the past, ancient DNA, has had little to say about this crucible of history and culture, in part because DNA degrades quickly in hot climates.

Now, in three papers in this issue, researchers present DNA from more than 700 individuals who lived and died in the region over more than 10,000 years. Taken together, the studies survey the history of the Near East through a genetic lens, exploring the ancestry of the people who first domesticated plants and animals, settled down into villages, spread the precursors of modern languages, and peopled Homer's epics.

The massive data set includes DNA from burials stretching from Croatia to modern-day Iran, in a region the authors call the Southern Arc. "The sample size is phenomenal, and fascinating," says Wolfgang Haak, a geneticist at the Max Planck Institute for Evolutionary Anthropology who was not part of the team. "The beauty of this is it's bringing it all together in a bigger narrative."

That narrative is no simple tale. The geneticists, led by David Reich and Iosif Lazaridis of Harvard University, worked with archaeologists and linguists, gathering thousands of skeletal samples and extracting and analyzing DNA, mostly from the dense petrous bone of the ear, over nearly 4 years. They applied better extraction methods and compared new samples with existing data, allowing them to identify even short bits of DNA.

Their genetic story starts with the early days of farming, a period known as the Neolithic. Farming began in Anatolia in what is present-day Turkey. But the DNA shows that the people who experimented with planting wheat and domesticating sheep and goats starting about 10,000 years ago weren't simply descendants of earlier hunter-gatherers living in the area. Dozens of newly sequenced genomes suggest Anatolia absorbed at least two separate migrations from about 10,000 to 6500 years ago. One came from today's Iraq and Syria and the other from the Eastern Mediterranean coast. In Anatolia they mixed with each other and with the descendants of earlier hunter-gatherers. By about 6500 years ago, the populations had coalesced into a distinct genetic signature.

Another genetic contribution came from the east about 6500 years ago, as hunter-gatherers from the Caucasus entered the region. Then about 5000 years ago, a fourth group—nomads from the steppes north of the Black Sea, known as the Yamnaya—arrived, adding to the genetic picture but not fundamentally redrawing it. "The people of the Southern Arc are mostly coming from Levantine, Anatolian, and Caucasus components," Lazaridis says. "The Yamnaya are like a layer of sauce, added after 3000 B.C.E."

This scenario supports existing evidence that agriculture arose in a network of people interacting and migrating in this region, others say. "This fits really well with archaeological data," says Barbara Horejs, scientific director of the Austrian Archaeological Institute, who was not part of the team.

But other scholars question the team's conclusion about the origins of a different cultural shift, the spread of Indo-European languages. Nearly every language spoken in Europe today stems from a common root, shared with Indian languages. Researchers have for years traced it to the Bronze Age Yamnaya, who rode both east and west from

the steppes. But the authors of the new papers argue the Black Sea steppe wasn't the birthplace of Indo-European, but rather a stop along a journey that began earlier and farther to the south, perhaps around modern-day Armenia.

Because of similarities between Indo-European and Anatolian languages such as ancient Hittite, linguists had guessed the Yamnaya had left both genes and language in Anatolia, as well as Europe. But the new analysis finds no Yamnaya ancestry among ancient Anatolians. The team suggests they and the Yamnaya instead share common ancestors in a hunter-gatherer population in the highlands east of Anatolia, including the Caucasus Mountains. That area, they argue, is the most likely place for people to have spoken an Anatolian-Indo-European root language, perhaps between 5000 and 7000 years ago. "That Caucasus component is a unifying type of ancestry we find in all places where ancient Indo-European languages are spoken," says Lazaridis, who is first author on all three papers.

However, Guus Kroonen, a linguist at Leiden University, says this contradicts linguistic data. The early people of the Caucasus would have been familiar with farming, he says, but the deepest layers of Indo-European have just one word for grain and no words for legumes or the plow. Those speakers "weren't very familiar with agriculture," he says. "The linguistic evidence and the genetic evidence don't seem to match."

Lazaridis says it's possible the root tongue "was originally a hunter-gatherer language," and so lacked terms for farming. The team agrees more evidence of "Proto-Indo-Anatolians" is needed, but says the Caucasus is a promising place to look.

Throughout, the papers address some critiques of previous ancient DNA work. Some archaeologists have complained that earlier research attributed almost everything—status, identity, power shifts—to pulses of migration recorded in DNA. But the new papers acknowledge, for example, that some migrations into Anatolia may not have been relevant or even perceptible to those living at the time. "That's a response to criticisms coming from the archaeological literature," says Hartwick College archaeologist emeritus David Anthony, who is not a co-author but has worked with the team. "It's really healthy."

In another example, Yamnaya were buried in elite tombs after they moved into the region north of Greece, suggesting a link between ancestry and social status.

But during the later Mycenaean period in Greece—the time Homer mythologized—the new data suggest Yamnaya descendants had little impact on Greek social structure.

Evidence comes in part from the spectacular Mycenaean burial of the Griffin Warrior, a man who died in 1450 B.C.E. near Pylos, Greece. He carried no traces of steppe ancestry, though dozens of both elite and humbler graves in Greece did. University of Cincinnati archaeologist Shari Stocker, who helped excavate the tomb in 2015 and collaborated on the new studies, says the lack of correlation between social status and steppe ancestry is no surprise—and a welcome dose of nuance from geneticists.

The papers also acknowledge the nuances of identity in later periods, for example in Imperial Rome. Previous genetic studies had shown that as the empire coalesced, the ancestry of people in and around the city of Rome shifted, with most having roots not in Europe, but farther east.

After obtaining dozens of additional Roman-era genomes from the region, the team zeroed in on the source of those newcomers: Anatolia. But the researchers agree that people with "Anatolian" DNA moving to the Italian peninsula likely saw themselves as citizens or slaves of Rome, rather than as part of a distinct "Anatolian" ethnic group. Contemporary chroniclers remarked on the new faces in Rome—and referred to many of them as "Greeks," perhaps because the eastern peoples had spoken Greek for centuries, Lazaridis says.

Some archaeologists still think the papers claim too much influence for ancestry. "DNA cannot tell us anything about how people shape their life worlds, what their social status was," says archaeologist Joseph Maran of Heidelberg University. He says terms like "Yamnaya ancestry" suggest the Yamnaya spread by moving directly from place to place, rather than through a complex mingling of their descendants with local populations over centuries or more. "Equating history with 'mobility' and 'migrations' is … old-fashioned."

And although the studies are a big step forward, in covering 10,000 years with 700 samples, they leave plenty of questions unanswered, with large stretches of time and space represented by a handful of samples.

All the same, several archaeologists including Horejs think this injection of DNA data will shape research going forward. "It's our task now, and obligation as archaeologists, to use this new data to rethink archaeological models," she says. ■

> ## "The beauty of this is it's bringing it all together in a bigger narrative."
> **Wolfgang Haak**,
> Max Planck Institute for Evolutionary Anthropology

Global drought experiment reveals the toll on plant growth

Artificial droughts sharply cut carbon storage

By **Elizabeth Pennisi**

Europe and many other parts of the world are currently grappling with extreme drought—and that could be bad news for efforts to curb climate change, concludes a new global study of how shrubs and grasses respond to parched conditions.

Grasslands and shrublands cover more than 40% of Earth's terra firma, and they remove hefty amounts of carbon dioxide from the air. But by deliberately blocking precipitation from falling at 100 research sites around the world, researchers found that a single year of drought can reduce the growth of vegetation by more than 80%, greatly diminishing its ability to absorb carbon dioxide. Overall, plant growth in the artificially drought-stricken grassy patches fell by 36%, far more than earlier estimates. But the study, presented last week at the annual meeting of the Ecological Society of America in Montreal, also found great variability: Vegetation at 20% of the sites continued to thrive despite the lack of water.

"I was surprised at how much drought impacts varied," says Drew Peltier, a physiological ecologist at Northern Arizona University who was not involved in study. "This suggests there is some resilience in these systems; the question is how much and for how long."

A decade ago, with droughts forecast to become more frequent and severe in a warming world, three ecologists—Melinda Smith of Colorado State University; Osvaldo Sala of Arizona State University, Tempe; and Richard Phillips from the University of Indiana, Bloomington—grew frustrated with their field's inability to come up with consistent results about how dry weather affects plant productivity, particularly in grasslands and shrublands. So, they and their colleagues hammered out a standardized procedure for creating artificial droughts in the field and put out a call for researchers willing to partic-

ipate in what they dubbed the International Drought Experiment (IDE).

"We expected to have about 20 sites," Smith recalls, but what's called Drought-Net has grown to 139. Some are in places, such as Iran and parts of South America, where scientists had conducted little drought research. Most are in shrub- and grasslands, where it's easier to erect structures to block precipitation.

Each team agreed to re-create the conditions of the worst drought documented in their region over the preceding century. Most blocked precipitation by mounting plastic roofing slats over 1-meter squares of ground; the slats were spaced according to how much rain, sleet, or snow needed to be diverted. On average, the roofed plots received less than half of their typical precipitation.

Each team tallied the kinds and numbers of plants in the covered areas, as well as in similar plots left open for comparison. After a year of treatment, the researchers surveyed the plants again and harvested, dried, and weighed all of the aboveground plant material in the roofed and open plots.

This year, drought scorched these soccer fields in London and stressed shrubs and grasses across the globe.

Last week, the researchers reported initial results from 100 shrubby and grassy sites. At some, such as plots of shortgrass prairie in Colorado, there was "catastrophic loss," reported Kate Wilkins, a grassland ecologist now at the Denver Zoo who worked with Smith. Plant productivity in the water-starved area declined by 88%. "What surprised me was just how dead it was," Wilkins said.

In contrast, in a temperate grassland in Germany the simulated drought "did not have any significant effect," says disturbance ecologist Anke Jentsch-Beierkuhnlein from the University of Bayreuth. In general, the climate at the German site was wetter and the drought less severe than on the prairie.

Overall, plants in wetter environments withstood this short-term drought better than those in drier climes, and shrub-

dominated plots fared better than those dominated by grasses, Wilkins reported. Shrubs tend to have more extensive roots that can reach moisture deep in the soil. The average decline seen in the grassy plots—36%—is "almost twice as much of a reduction as other studies have shown," notes Elsa Cleland, an ecologist at the University of California, San Diego. But she and others think the data are believable because the study used standard methods across a wide variety of sites.

Many researchers have continued to monitor their plots, with some planning to collect data for four or more years, in part to simulate prolonged droughts. The additional data could help climate modelers sharpen estimates of how much less carbon is absorbed by shrub- and grasslands in a drought, says Sarah Evans, an ecologist at Michigan State University's W.K. Kellogg Biological Station. IDE results could also help ecologists forecast which ecosystems are most at risk during dry spells, as well as broader ecological ripple effects. Less plant matter can mean less food for grazing animals such as rodents and for

their predators, Evans notes. "The health of many ecosystems and their biodiversity relies on plant production," she says.

Farmers, ranchers, and land managers might also benefit. Jentsch-Beierkuhnlein notes that during the current European drought, intensively managed grasslands with relatively few species, such as hayfields, have been hard hit. Planting more diverse assemblages might enable such grasslands to "keep delivering ecosystem services even under severe drought," she says.

That's an important insight, says Andrew Hector, an ecologist at the University of Oxford, given the extreme heat and drought of recent years. "The main message of these extreme conditions is that climate change … is happening already," he says. They "show just how relevant [the IDE] is." ∎

Researchers watch how Arctic storms chew up sea ice

Airborne campaign to study summer cyclones could reveal air-ice interactions

By **Eric Hand**

The storm began somewhere between Iceland and Greenland, as disturbances high and low in the atmosphere united into a full-fledged cyclone. One day later, the vast spiral of winds had grown nearly as big as Mongolia. It was on a beeline for Svalbard, the archipelago between Norway and the North Pole, and heading for the thin floes girding the Arctic's vulnerable pack of summer sea ice. And that made John Methven very, very happy.

Last week, Methven, an atmospheric dynamicist at the University of Reading, flew through the storm as part of an airborne campaign based out of Svalbard's Longyearbyen, the world's northernmost town. As his Twin Otter plane shuddered through tropical storm–force winds of 100 kilometers per hour, flying just 15 to 30 meters above the sea surface, Methven and the crew took measurements of the ice, water, and air before returning to a bumpy landing on Svalbard. It was the third, and strongest, cyclone that U.K., U.S., and French teams had captured in a monthlong effort.

"It's really exciting to get this sequence [of cyclones]," says Methven, leader of the U.K. component of the Thin Ice campaign, the first airborne project to study how these summertime storms affect sea ice. "People are going to be pretty pleased."

With data from the ice-skimming plane, a second aircraft flying through the tops of the storms, and dozens of weather balloons, the Thin Ice teams hope to learn how these common but poorly understood storms form, function, and chew up sea ice. They also plan to gauge how the properties of the sea ice—smooth, rough, or missing—feed back into the storms themselves. The data should help improve Arctic weather models and sharpen the picture of how summer cyclones may be accelerating the retreat of
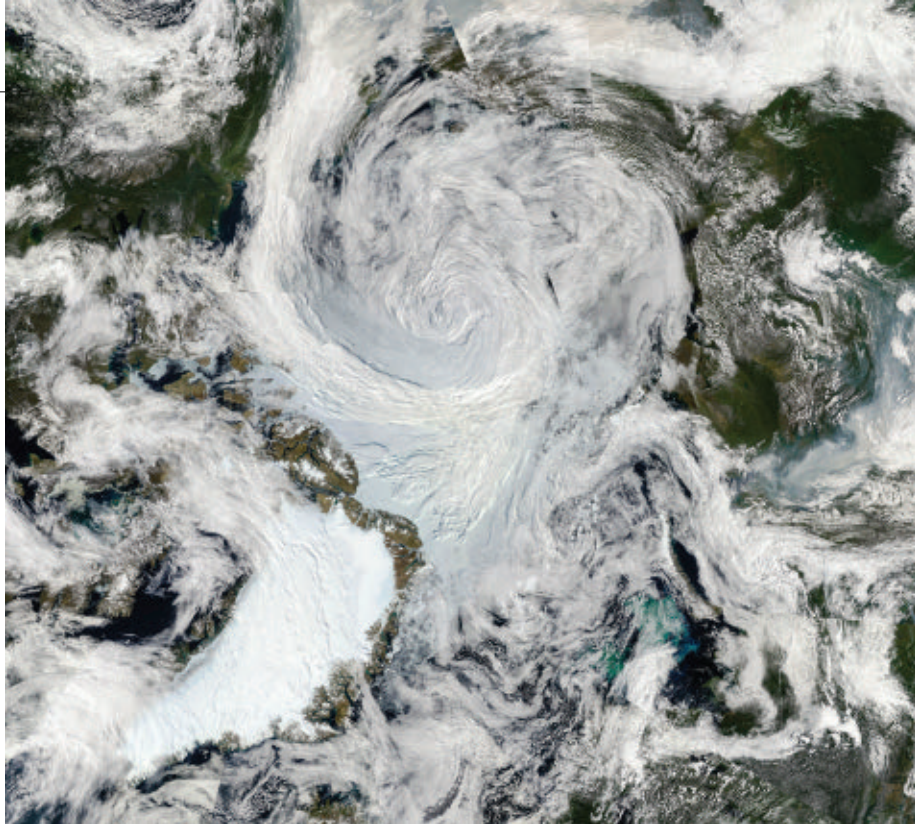
The Great Arctic Cyclone of 2012 spanned the Arctic Ocean and erased 500,000 square kilometers of ice.

Arctic sea ice, already on the run because of global warming.

The storms whip up waves that menace Arctic fishing vessels and send storm surges into coastal villages. "A lot of these communities are having to move," says Julienne Stroeve, a polar scientist at the University of Manitoba (U of M). "They're falling into the ocean." The cyclones also threaten the cargo and cruise ships rushing to take advantage of newly ice-free passages in the summer. Better models will "make it safer" to travel the region, says Alex Crawford, an Arctic climate scientist at U of M. "You'll have a better clue to stay in port or go on."

Summertime Arctic cyclones are very different beasts from tropical cyclones: not as powerful but sometimes larger. The aptly named Great Arctic Cyclone of 2012 stretched 5000 kilometers across, spanning the entire Arctic Ocean. With little topographic relief to disrupt them, the storms can wander around the Arctic Ocean for weeks on end. "There's nothing to get rid of them," Methven says.

Hurricanes are fueled by the energy in water vapor rising from a warm ocean, but Arctic cyclones get their spark from horizontal temperature differences. At high altitude, kinks in the polar vortex, a collar of winds 5 to 8 kilometers up that keeps warm midlatitude air separated from cold Arctic air, can start air spinning. Near the surface, temperature differences between the ocean and the ice front, or between land and the ocean, can do the same. When a low-level spin-up meets up with one at the top, they intensify into a cyclone. Other Arctic cyclones are imports—storms from lower latitudes that wind up in the "garbage bin" of the Arctic, Crawford says.

Unlike hurricanes, Arctic cyclones blow across an ocean partly covered by sea ice—with complex consequences for both winds and ice. Early in the summer, the storms' cloud cover can inhibit melting. But by August, as ice thins near the edge of the pack, cyclones can speed melting by pushing floes to warmer waters, breaking up ice into smaller floes that melt more easily, and creating waves that stir up warmer waters. Meanwhile, the rough surface of the ice can act as a brake on the winds. Yet the friction can also help a storm persist by keeping its core stable, Methven says.

Weather and climate models struggle to forecast both the storms and their interactions with sea ice. In early August, two leading models differed by a full day in when they predicted a major storm would arrive, says Jim Doyle, an atmospheric scientist at the Naval Research Laboratory and the leader of the U.S. component of Thin Ice. Methven says the U.K. Met Office's model creates storms that tend to melt summer ice too fast, whereas the model at the European Centre for Medium-Range Weather Forecasts leaves too much ice lingering.

The models perform poorly in part because data on Arctic conditions are relatively scant, with few weather stations. The models also struggle with the physics of Arctic clouds, which often contain a mix of frozen and liquid droplets. "Getting the balance between the liquid and ice phase is really, really hard," says Ian Renfrew, a meteorologist at the University of East Anglia. Thin Ice's high-flying aircraft will help tune models by gathering detailed cloud data from within the storm.

Modelers are also eager for surface-level data, especially along the rough, busted-up perimeter of the ice pack, a region called the marginal ice zone. In the past few years, Renfrew says, a few models have begun to include a parameter to account for the roughness of the marginal ice instead of treating it as uniformly smooth. That seems to improve the models' forecasts of cyclones and ice loss, but researchers don't know whether their parameter matches reality. By directly measuring the roughness of the ice and how its friction pushes back on storms, the ice-skimming flights should help models forecast the complex interplay of winds and ice.

The storms are a major driver of sea-ice retreat. The 2012 Great Arctic Cyclone destroyed 500,000 square kilometers of ice—an area the size of Spain, says Steven Cavallo, an atmospheric scientist at the University of Oklahoma, Norman. Cyclones routinely destroy a couple hundred thousand square kilometers of ice and could ultimately be responsible for up to 40% of annual ice losses, he says. "We think it's pretty significant. And it's growing."

Doyle doesn't see any sign that climate change is creating stronger or more frequent summertime storms, in recent decades at least. But he says warming makes the ice more vulnerable to the regular parade of cyclones. "The ice is thinning, and so the Arctic cyclones are having a much bigger impact."

Models suggest the Arctic will lose all its summer sea ice by 2050, if not sooner. How that will affect the summer storms is "the million-dollar question," says Elina Valkonen, an atmospheric scientist at Colorado State University. Competing forces are at work. The open, warmer ocean is expected to provide more moisture and fuel for storms, but it would also reduce the low-level spin-ups that spark them, by eliminating temperature gradients at what was once the ice front and between ocean and land.

In unpublished work, Valkonen and colleagues looked at scenarios for the year 2100 from a set of models tuned for an ice-free Arctic. They found no change in the predicted barometric pressure for the summer storms, which defines their strength. And although the number of storms rose slightly, that was only due to imported storms from lower latitudes, not cyclones generated in the Arctic. Still, it might not all be good news. Without rough ice to slow them, the storms tended to be longer lasting, with faster winds, Valkonen says. "When you're a fisherman in the Arctic, that's what you care about." ∎

Avian influenza devastated Caspian tern populations on Lake Michigan islands.

ANIMAL HEALTH

Deadly bird flu establishes a foothold in North America

H5N1 has continued to kill wild birds and poultry this summer. The fall migration could bring it back in force

By **Erik Stokstad**

When an outbreak of highly pathogenic H5N1 avian influenza spread across North America this spring, researchers hoped for a replay of what happened after a different avian flu variant arrived in the United States in December 2014. Although more than 50 million birds died or were destroyed in a matter of months, costing farmers more than $1.6 billion, the virus had essentially vanished by June 2015. Poultry outbreaks ended, wild birds stopped dying, and migratory waterfowl didn't bring the virus back when they returned from their summer breeding grounds in Canada.

But this time is different. H5N1 infections in both wild bird species and poultry have continued in parts of the United States and Canada over the summer, dashing hopes that warmer temperatures would halt the spread. And whereas the 2015 outbreak primarily affected Midwest poultry farms, H5N1 has spread to practically the entire continental United States and infected at least 99 wild bird species, a record. Whether migratory birds will cause additional introductions in the fall is "the million-dollar question," says Bryan Richards, emerging disease coordinator at the U.S. Geological Survey's National Wildlife Health Center.

Even if they don't, scientists worry the virus may continue to circulate year-round, posing a permanent threat to poultry farming and wild birds, including several endangered species. "Impacts on wild birds may persist for a very, very long time," Richards says. Europe may show what lies ahead: There H5N1 has already become a fixture in wild birds and has caused bigger and bigger outbreaks over the past 3 years, causing record damages to the poultry industry (*Science*, 13 May, p. 682).

H5N1 first emerged in poultry in China's Guangdong province in 1996 and since then has caused several major outbreaks around the world. It has evolved to infect waterfowl species without causing significant harm, allowing the birds to spread the virus far and wide. In the current outbreak, waterbirds are thought to have carried the virus to Canada from Europe and then down the eastern seaboard (*Science*, 29 April, p. 441). Bald eagles, owls, and other predators died after eating infected waterbirds. In February, H5N1 reached the Mississippi flyway, where snow geese and other species migrate to northern Canada. Along the way it infected poultry operations, forcing farmers to cull 40 million chickens and turkeys. Later in the spring, the virus slowly moved westward.

By now, H5N1 has been detected in more than 2000 wild birds in the United States, compared with just 99 during the 2015 outbreak; biologists suspect the virus is much more transmissible than its predecessors. "It has just exploded in the breadth of species that it's observed in," says Wendy Puryear, a wildlife virologist at Tufts University.

Infections began to fall in May, although some species continued to be afflicted. Black vultures, which pick up H5N1 when they scavenge carcasses, are still dying by the hundreds, says Rebecca Poulson, a wildlife disease researcher at the University of Georgia. "It's still hitting those scavengers pretty hard," she says. And in June, researchers in New England were surprised when a second wave of infections struck seabirds. "All of a sudden, it was like a switch had been flipped again," Puryear says.

Seabirds are particularly vulnerable because many nest in dense colonies. Northern gannet populations crashed in parts of eastern Canada, as they have in Europe. In Lake Michigan, Caspian terns—locally endangered—were very hard hit. H5N1 rarely infects mammals, but this wave has killed hundreds of harbor seals in Maine; Puryear and colleagues are trying to learn whether the virus can spread between seals or they all were infected by birds or their feces. The United States and the United Kingdom have each seen one human H5N1 case so far.

Now, all eyes are on the migratory birds, which fan out over a large area as they return to the United States from the north and could spread the virus widely. Researchers with the Canadian Wildlife Service (CNS) have collected samples from 1000 snow geese on their Arctic breeding grounds, but testing them for H5N1 could take another month or two, says CNS waterfowl biologist Jim Leafloor. U.S. federal and state biologists are already testing live and hunter-killed migratory ducks and geese.

Regardless of whether a new surge of infections arrives from the north, many researchers say the virus is already entrenched in some parts of the United States. If those areas overlap major poultry farming areas, the consequences could be serious. Farmers could face a constant risk of major losses, and Richards says they would need to maintain or tighten biosecurity measures—meticulously cleaning boots and equipment, for example.

Much remains to be learned. In wild birds, for example, just how H5N1 moves from one individual to another and between species is still a mystery, says Tufts wildlife virologist Kaitlin Sawatzki. "It's going to be a very complicated story," she says. "It's hard to predict, and we're nervous." ■

Many-eyed scope will make movies of the stars

Argus Array will combine hundreds of off-the-shelf telescopes to capture fleeting events

By **Daniel Clery**

Argus Panoptes, the all-seeing, many-eyed giant of Greek mythology, is about to take physical form in the mountains of North Carolina. In October, an array of 38 small telescopes will begin monitoring a slice of visible sky 1700 times the size of the full Moon. Known as the Argus Array Pathfinder, it will register changes in the stars second by second, essentially making a nightlong celestial movie. Its developers hope it will pave the way for a much larger Argus Array with 900 telescopes that by 2025 could watch the entire visible night sky.

The Argus telescopes join others aiming to capture short-lived or rapidly changing astrophysical events, known as transients, including exploding stars, ravenous black holes, neutron star mergers, and maybe even stars briefly eclipsed by the long-postulated hidden planet in our Solar System. The full Argus Array would watch the sky with more mirror area than all other transient telescopes put together, says team leader Nicholas Law of the University of North Carolina, Chapel Hill.

"The potential is enormous," says Igor Andreoni of the University of Maryland, College Park, who is not involved in the project. As well as catching real-time events, Argus will build an archive of images showing objects before they explode or change. "We'll know the history of anything that happens in the sky above a certain brightness," Andreoni says. "We're entering a new era of time-domain astronomy with an explosion of different sorts of telescope design," adds Carole Mundell of the University of Bath.

Argus aims to achieve its unique vision with hundreds of off-the-shelf telescopes, each just 20 centimeters across and watching a different patch of sky. The final array will match the light-gathering power of a telescope with a single 5-meter mirror, which typically costs hundreds of millions of dollars, but cheap components should keep Argus's cost below $20 million, Law says. The challenge will come in stitching together the array's 900 images into a single, seamless movie of the night sky. "We've spent an awful lot of time on the data pipeline," Law says.

In 2015, his team built a smaller instrument called Evryscope (*Science*, 3 July 2015, p. 14). That had 27 telescopes, each 7 centimeters across, looking outward from the surface of a hemispherical dome. Its successes included spotting a stellar flare—larger than any seen before—from our nearest neighbor star Proxima Centauri, but the team wanted to scale up to see objects outside our Galaxy.

Instead of looking out from a dome's surface, the Argus telescopes will sit in a 10-meter-wide bowl, all aiming out a single skylightlike window in a dome. Over the

The Argus Array's 900 telescopes will each watch a different patch of sky for rapid changes, from supernovae to the passing shadow of the hypothetical Planet 9.

course of the night, the bowl and telescopes will pivot slowly to follow the stars as Earth rotates. To capture quick-fire images, designers plan to replace the charge-coupled device (CCD) light sensors used in most telescopes with complementary metal-oxide-semiconductor detectors, which can read out data in less than a second compared with many seconds for CCDs.

Grants totaling $1.3 million from the National Science Foundation (NSF) and Schmidt Futures, a private foundation, funded the 38-scope prototype. Law and colleagues expect to test it in the coming weeks before transferring it first to a site i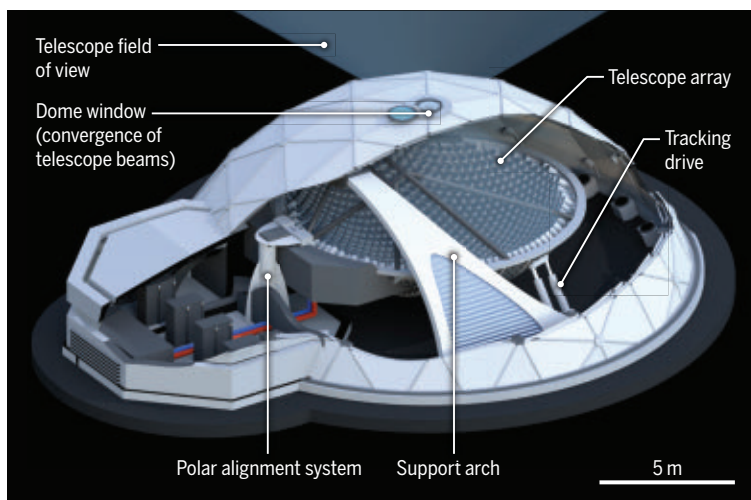n the Appalachian Mountains near Chapel Hill for debugging and later to Mount Laguna Observatory in California. The team hopes to show off its capabilities before seeking NSF funding for the full Argus Array after the turn of the year.

Data from Argus Pathfinder and its successor will be freely available in real time, and the software will issue automatic alerts when it detects an event. That will allow other, larger telescopes to quickly swivel to the same spot in the sky and collect more detailed data, a boon for astronomers probing stellar outbursts such as flares, supernovae, and gamma ray bursts.

Observers normally don't spot supernovae, for example, until hours after the event. "Getting closer in time means you get closer to the source" of the explosion, says Shrinivas Kulkarni of the California Institute of Technology, a pioneer in efforts to capture transients. If the progenitor star is bright enough, Argus might also record any sudden brightening or belches of gas before its death—possible precursors of the blast. "It makes history available in a very comprehensive way," Kulkarni says.

If Argus had been up and running in 2017, it might have given an early glimpse of the light flash from the first ever recorded kilonova—a merger of two neutron stars—and enabled other telescopes to home in on it quickly. As it happened, gravitational wave detectors were the first to sense the merger, but they can't pinpoint locations accurately and guide other telescopes. "We need simultaneous observations," Mundell says.

Argus might even spot the elusive Planet 9, hypothesized to lurk in the outer Solar System. It may be too cold and faint to be seen directly. But as it moves across the sky it should make background stars briefly blink out. "Occultations are certainly a promising avenue when it comes to Planet 9," says Konstantin Batygin of Caltech, who with colleague Mike Brown proposed its existence in 2016 from gravitational influences on other distant bodies. If Argus pulls off that discovery, it will certainly have lived up to its formidable namesake. ∎

SPARKLING WATERS

Tiny Caribbean crustaceans and their bioluminescent mating displays are shining new light on evolution

By **Elizabeth Pennisi**

In the 18th century, the French naturalist Godeheu de Riville was sailing across the Indian Ocean when he came upon a remarkable sight. The sea "was covered over with small stars; every wave which broke about us dispersed a most vivid light, in complexion like that of a silver tissue electrified in the dark," he recounted in his journal. When de Riville examined the sparkling water with his microscope, he discovered that the "small stars" were tiny crustaceans now known as ostracods.

Centuries later, in 1980, marine biologist James Morin was scuba diving just after sunset in the Virgin Islands when he noticed bright blue dots blinking on and off several meters away. When he shone his flashlight through the water, he saw scores of ostracods flitting across its beam. After multiple dives, he discerned that the flashes weren't random. The ostracods lit up in specific patterns in space and time, much like the courtship flashes of fireflies that light up summertime meadows. The realization changed the course of Morin's career.

Now a professor emeritus at Cornell University, Morin has spent the past 4 decades working with a small, dedicated group of colleagues to unravel the mysteries of what they describe as the most spectacular natural wonder that most people will never see. Male ostracods only display for about an hour, shortly after sunset on moonless nights in warm Caribbean seas. Most recreational divers don't dive at night, and those who do tend to use lights, which prompt the creatures to switch off for the evening.

No bigger than a grain of sand, ostracods abound in fresh and saltwater. "They are very cute but also sort of bizarre—like a cross between a crab and a tiny spaceship," says Timothy Fallon, an evolutionary biochemist at the University of California (UC), San Diego.

A long exposure captures ostracods in motion on a Bonaire reef, driven in part by currents.

PHOTO: KYLE MCBURNIE

Only seagoing ostracods are bioluminescent, and it's not their bodies that glow. Rather they spew out glowing mucus. In most of the world's oceans, ostracods do this for defense—to startle and distract would-be predators. But in the Caribbean, and only in the Caribbean, as Morin and colleagues discovered, those bright blue dots can double as mating calls. Today, thousands of dives later, they believe those signals have driven Caribbean ostracods to diversify into more than 100 species.

With modern genetic tools, they've been using these creatures to investigate the factors that wedge species apart, including sexual selection, driven by female preferences; geographic isolation; and genetic drift—the accumulation of random genetic changes. In just the past 2 years, researchers have figured out how to grow ostracods in the lab, a development that will allow them to dissect the molecular mechanisms of evolution in a way once possible only in more conventional lab animals such as nematodes and fruit flies.

"The ability to ask interesting questions about evolutionary patterns across multiple species is a powerful tool," says Christopher Cratsley, a behavioral ecologist at Fitchburg State University who works on fireflies. Ostracods are an "elegant system" for doing so, he says. The mechanics and biochemistry of their light flashes are relatively simple, and many species of ostracods overlap in small areas. Compared with other animals with complex mating rituals—songbirds, say—they may more readily yield clues about the forces that generate biological diversity.

IN JAPAN, dried ostracods are popular as curiosities because they glow when rehydrated. They're called *umi-hotaru*—"sea fireflies"—and in the first half of the 20th century, they caught the eye of Princeton University biochemist E. Newton Harvey. He used dried ostracods to work out the basic biochemistry of bioluminescence, which has evolved independently about 100 times. Organisms as disparate as bacteria, fungi, fish, and insects use it to evade predators, attract prey, or communicate with their own kind. For several, such as fireflies, it's a means of courtship.

In the Caribbean, the light show takes place underwater. When male ostracods sense the water is dark enough, they take off from the reef or seagrass bed where they spend most of their time and begin their display. Females swim toward the flashes, as do nonflashing males racing to intercept them.

To watch the spectacle, sea firefly researchers in scuba gear position themselves on the sea floor just after dark, using red lights to find their way. It's an eerie experience. At night, shallow reefs resound with snapping shrimp and the crunch of parrot fish chomping on coral. Deeper waters are spookily quiet.

In the early days, biologists used a night vision monocular attached to a VHS camera to capture the displays. The images were grainy and had a limited field of view. "It was very hard to see a whole display," says Gretchen Gerrish, one of Morin's first sea firefly graduate students and now an evolutionary ecologist at the University of Wisconsin, Madison. The video equipment has improved, but even now researchers often take waterproof notes by writing on pieces of PVC pipe with a mechanical pencil. A rubber band, rolled down a finger's width after each line, helps them keep their place. After documenting a display, they swim to the flashes and scoop up the creatures with a net.

Back in the lab—often a makeshift setup in a hotel room—they sort through their catch and examine their collected ostracods under a microscope to identify the species. Sometimes a subtle difference in the shape and size of the reproductive organs or in the relative proportions of body
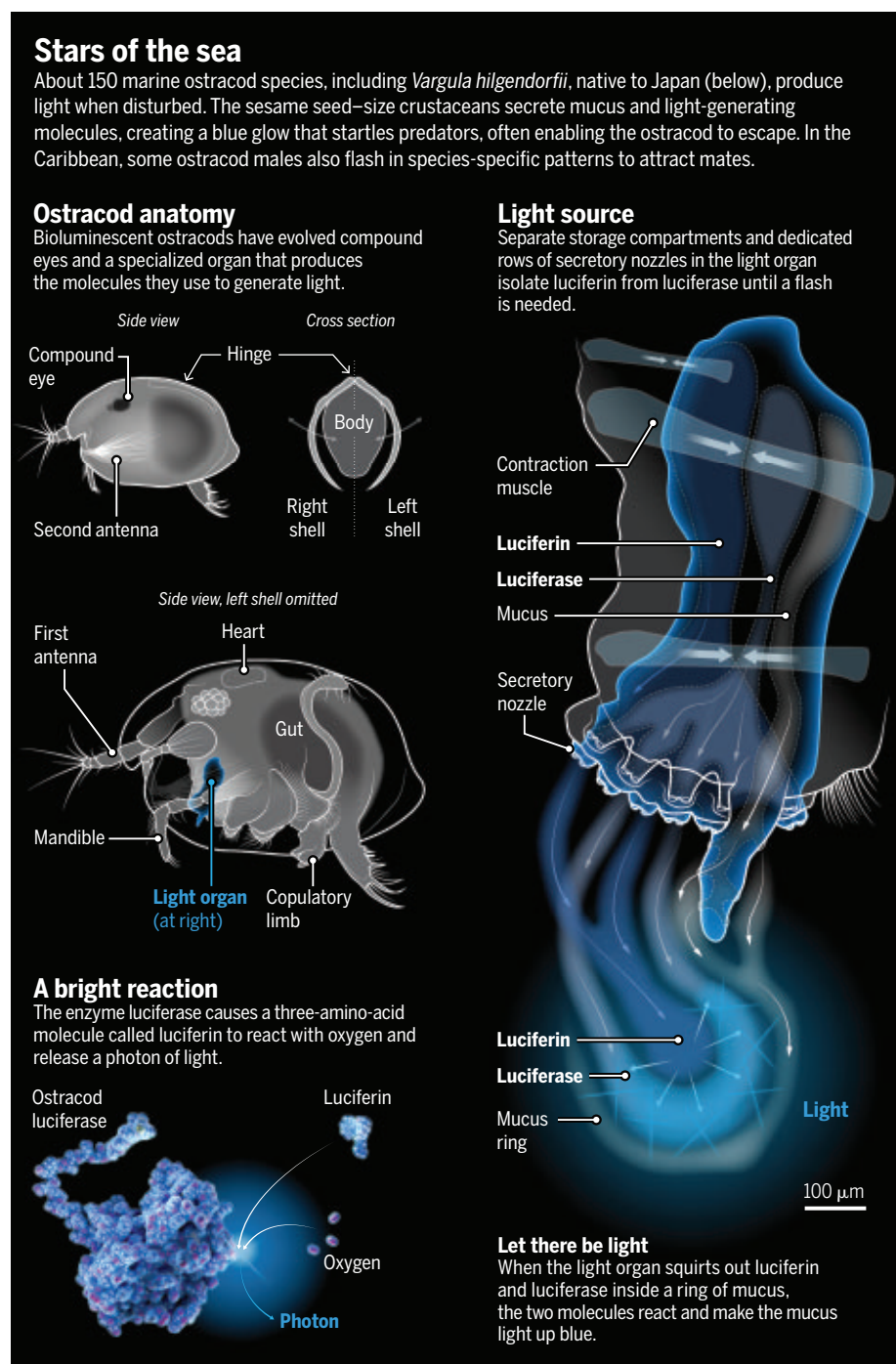
parts is all that distinguishes one species from another. So far, they've named more than 20 species; about 100 more await formal description.

By the early 2000s the work had revealed that the behavior of courting ostracods is surprisingly complex: Flashes can be dim, bright, or even different tints. They last from milliseconds to multiple seconds. And while generating them the ostracods move in species-specific ways—up, down, or on a slant—creating strings of flashes that range in length from less than 1 meter up to 30 meters. Everywhere Morin and his colleagues went they found new species and new behaviors. "It was really hard to comprehend the scale of unknown knowledge we were stumbling upon," recalls Nicholai Hensley, an integrative evolutionary biologist at Cornell.

TO DELVE MORE DEEPLY into sea firefly biology, Gerrish recruited nearly all the other sea firefly researchers to study the creatures, in a project that extended across five sites in the Caribbean between 2015 and 2019. They teamed up with Martin Dohrn, a filmmaker known for capturing nature in poorly lit places, to develop an underwater camera system that records visible and infrared light at the same time. That enabled the researchers to see the blue flashes as well as the animals themselves. The flashes show up as visible light, but the only way to see the ostracods without drowning out the flashes is to use infrared. "It transformed our abilities to document the displays in the field," Morin says.

The group also began to tease apart relationships among ostracod species. Todd Oakley, an evolutionary biologist at UC Santa Barbara, and his team used RNA samples to sequence the "transcriptome," or set of expressed genes, for Caribbean ostracod species and compare them with the transcriptomes of other ostracods, including those of the Pacific and Indian oceans, which don't use bioluminescence for courtship. Based on the degree of similarity in the transcriptomes, they arranged each species on a family tree and used the numbers of genetic differences between species as a "molecular clock" to determine when each originated.

This work revealed that the ability to generate light, presumably for defense at first, evolved about 197 million years ago, Oakley reported in a preprint posted on 13 April. The ostracod family tree indicated evolution co-opted this defense mechanism for mating displays only once, about 151 million years ago. The early date came as a surprise to Oakley and others, who had assumed this behavior was a relatively recent innova-

tion that arose after the Isthmus of Panama formed 3 million years ago, separating Caribbean ostracods from their Pacific kin. It's not clear why glowing courtship displays didn't spread to the Pacific before the barrier formed, but one possibility is that ostracods simply don't disperse widely. Another is that visual signals don't work as well in murky Pacific waters.

The consortium is now using ostracods as a new lens on one of the biggest questions in evolutionary biology: What drives the formation of new species? Female

choosiness about mates is one candidate. Such sexual selection can drive the evolution of brighter colors or bigger horns in males, but there has been little evidence it can actually split one species into two. Oakley thinks his studies of bioluminescence provide some of the first proof. He and his student Emily Ellis compared the rates at which new species form in ostracods that use their flashes as courtship displays with the rate in those that don't. In principle, new species should arise more frequently in populations where sexual selection is at

Stars of the sea

About 150 marine ostracod species, including *Vargula hilgendorfii*, native to Japan (below), produce light when disturbed. The sesame seed–size crustaceans secrete mucus and light-generating molecules, creating a blue glow that startles predators, often enabling the ostracod to escape. In the Caribbean, some ostracod males also flash in species-specific patterns to attract mates.

Ostracod anatomy
Bioluminescent ostracods have evolved compound eyes and a specialized organ that produces the molecules they use to generate light.

Side view

Compound eye
Hinge
Second antenna

Cross section

Body
Right shell
Left shell

Side view, left shell omitted

First antenna
Heart
Gut
Mandible
Light organ (at right)
Copulatory limb

A bright reaction
The enzyme luciferase causes a three-amino-acid molecule called luciferin to react with oxygen and release a photon of light.

Ostracod luciferase
Luciferin
Oxygen
Photon

Light source
Separate storage compartments and dedicated rows of secretory nozzles in the light organ isolate luciferin from luciferase until a flash is needed.

Contraction muscle
Luciferin
Luciferase
Mucus
Secretory nozzle
Luciferin
Luciferase
Mucus ring
Light

100 µm

Let there be light
When the light organ squirts out luciferin and luciferase inside a ring of mucus, the two molecules react and make the mucus light up blue.

play. And they do, Oakley's team reported in 2016—not only in Caribbean ostracods, but also in insects, fish, and octopuses with bioluminescent courtship displays.

Gerrish, too, has found evidence in ostracods that sexual selection can drive diversity. She and others had observed that when multiple ostracod species live close together, individual species' displays become more distinctive than when the same species are found on their own, which maintains diversity by making coexisting species less likely to crossbreed.

At a study site in Belize, Gerrish and her graduate student Nick Reda have also found evidence that distinctive displays might be pushing one species to divide into two. Most males of the species *Photeros annecohenae* swoop upward as they flash, painting their string of glowing dots in a consistent direction. But a few swoop downward, and this tendency seems to be increasing, suggesting enough females prefer this behavior to cause it to proliferate. In one seagrass bed along the reef where Gerrish has been working, 50% of the males now exhibit this odd behavior, and in an adjacent bed that percentage has grown to 70%, she and Reda plan to report in a paper later this year. As this mating display becomes more common, it's more likely to isolate this population, a key step toward speciation.

On that same reef, Gerrish and Reda see hints that other well-known evolutionary forces are at play. Multiple populations of *P. annecohenae* that live along the reef exhibit a genetic gradient, with quite distinct populations at either end, she, Reda, and colleagues plan to report later this year. They think random genetic drift is driving some of the differences. But geographic isolation also seems to contribute. In places where storms have created short breaks in the reef, isolating populations on either side, genetic differences are greater than expected from the gradient.

INCREASINGLY, ostracod researchers are delving into how evolution shaped the animals' most distinctive feature—their flashes. Oakley and Hensley, in collaboration with Elizabeth Torres, an evolutionary biologist at California State University, Los Angeles, have sequenced the ostracod genes for luciferase, the enzyme that adds oxygen to a molecule called luciferin to make light in all bioluminescent organisms. "Every new species we look at, it is a new gene," Oakley says. Moreover, those tiny differences in the ostracod luciferase "correlate with different types of signals," as this enzyme's activity can dictate the brightness, duration, and other features of each flash. The findings show how novelty at the molecular level can lead to behavioral changes that could foster the emergence of new species.

Such studies would be easier in the lab, but ostracods "are notoriously difficult to culture," says Trevor Rivers, a behavioral ecologist at the University of Kansas, Lawrence, who was an early student of Morin's. The animals are very picky about temperature and light and dark regimens, and

In this image from Panama, vertical strings of flashes, each created by an individual male ostracod, linger in the water. When one male begins to display, others join in, aiming to lure females.

researchers aren't even sure what most species eat. And their relatively slow life cycle, on the order of months, means a long wait to see whether the animals will breed in a particular setup.

To tackle this challenge, Oakley and Jessica Goodheart, then a postdoc in his lab, focused on *Vargula tsujii*, a California species that is a close relative of the Caribbean ostracods but does not use its glow for mating. For more than 2 years, their team tweaked the aquaria and the water flow, tried different feeding regimens (chicken livers proved better than white fish), and adjusted the number of ostracods per tank. In 2020, the researchers finally succeeded in getting a reproducing population. They and others hope to eventually do the same with Caribbean ostracods. But already, Gerrish says, "We're poised to run in a bunch of different directions" to learn more about these
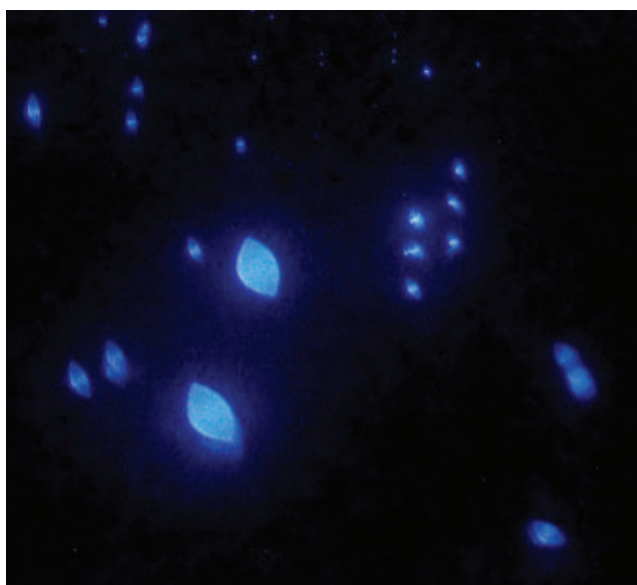
creatures and the evolutionary forces that shaped them.

Using lab-grown ostracods, Oakley's team has now uncovered evidence for a key idea about the evolution of novelty: that new traits often spring from modifications of existing ones. To control the secretion of the luminescent mucus, they found, ostracods rely on genes similar to those thought to be active in venom glands in centipedes and wasps, his graduate student Lisa Mesrop reported at a meeting this winter. Thus, when ostracod bioluminescence arose 197 million years ago, it wasn't newly invented, but rather a novel application for an existing gene network.

Another student in Oakley's lab, Emily Lau, has found ostracods and terrestrial fireflies evolved the same mechanism for regulating light-generating luciferin, most likely because chemical constraints limit what cells can do to control this very reactive molecule. Both sets of organisms stabilize luciferin by adding sulfur to its chemical structure, even though the sulfur-adding proteins are very different, she has found. Evolution appears to be "constrained" to one solution, Lau says, suggesting the same mechanism is at work in other bioluminescent organisms as well.

With ostracods now reproducing in the lab, researchers hope to finally sequence the entire genome. The ostracod genome is longer than our own and has repetitive regions and other complexities that make it challenging to sequence from single specimens snared at sea. Success in the lab would pave the way for genetic engineering not yet possible in most multicellular bioluminescent organisms, Hensley says. He's interested in why ostracods have hundreds of luciferase-like genes. By modifying these genes, he hopes to learn how they might fine-tune light production and whether they have additional functions.

The genome might also enable researchers to track down the enzymes that make luciferin and modulate its release. Comparing those enzymes with their counterparts in other bioluminescent organisms could provide "an opportunity to figure out what's truly necessary to make bioluminescence," Hensley says. That's just one of many insights de Riville could never have imagined centuries ago when he marveled at those shining stars in the sea. ∎

S **HTTPS://SCIM.AG/OSTRACODS**
See videos of ostracod mating displays.

FOOD WEBS

Machine learning ecological networks

Deep-learning tools can help to construct historical, modern-day, and future food webs

By **Eoin J. O'Gorman**

I t is perhaps unsurprising that apex predators, such as whales, sharks, leopards, and tigers, also tend to be the rarest species (*1*). This is largely because of the imperfect transfer of energy through each level in a food chain (*2*), which makes these carnivores more susceptible to starvation than herbivores, detritivores, or omnivores. Their survival also depends on having a large home range for them to roam far and wide to find the mates and resources needed to sustain their populations (*3*). These vulnerabilities make them particularly susceptible to human activities, such as habitat loss or being targeted by hunters for their trophy status. On page

School of Life Sciences, University of Essex, Wivenhoe Park, Colchester CO4 3SQ, UK. Email: e.ogorman@essex.ac.uk

1008 of this issue, Fricke *et al.* (*4*) adopt a network-based approach to establish how humans have disrupted apex predators and other mammalian fauna over the past 130,000 years.

Just as the poet John Donne mused that "no man is an island," the same can be said for all animals on Earth—that none can exist in isolation, and all are part of a complex tangle of interacting consumers, resources, and competitors (*5*). These ecological networks have been the focus of ecosystem ecologists for many decades, often requiring years of observation, stomach-content analyses, and experiments to quantify their complex structures. Describing the interactions in ecological networks is crucial for understanding the ecological surprises that may occur in ecosystems after environmental change or human intervention. For example, the overhunting of sea otters led to

an explosion of their sea urchin prey, whose overgrazing of kelp eliminated a swathe of other species that rely on these underwater forests for food and shelter (*6*). Such "trophic cascades" have been described in many ecosystems, where the loss of one species triggers biomass fluctuations across several trophic levels (*6*). Food webs are a central tool for tracking or anticipating changes along dominant pathways of energy flow, whereas network analysis helps to quantify the overall stability or resilience of an ecosystem and to identify key hubs or vulnerabilities (*7*, *8*).

Some of the findings by Fricke *et al.* are unsurprising. For instance, their analysis shows that there are fewer mammal species today than there were in the Late Pleistocene around 130,000 years ago. However, some of their other findings are more transformative. They find that there

Fricke *et al*. found that species with more connections in a food web, such as an apex predator like the lion, are more vulnerable to extinction.

has been a systematic demise of mammals with more connections in the food web, which can be explained by the greater susceptibility to extinction and range contraction of larger predators than smaller prey. This change has resulted in much-less-connected food webs than if the same number of species had been extinguished at random from the networks. Simpler food webs are typically shown to be less stable because they are more susceptible to further extinctions through energetic limitation (*7*) or a lack of redundancy in the choice of available prey (*9*). Furthermore, these food web "collapses" were particularly prominent after the arrival of humans to the region. Of further concern is the observation that currently endangered mammals share this same characteristic of being the most highly connected organisms in the network, which would lead to further food web collapses if they became extinct.

Fricke *et al*. also provide a valuable template for studying ecological networks in the past, present, and future. The complexity of food webs and the laborious task of describing their underlying connections have prevented their large-scale use in conservation and biomonitoring of ecosystems (*5*, *10*). Recent calls for incorporating ecological networks into biomonitoring have proposed ways of circumventing this obstacle by taking the species lists obtained from routine sampling and inferring the links from established databases, filling the gaps with modeling approaches (*10*, *11*). This "guesswork" is often built on the principle that body size is a key determinant of which species can interact with one another or that predators will consume phylogenetically related prey or share the diet of a phylogenetically related predator. Fricke *et al*. demonstrate how machine-learning techniques can be applied to a broad suite of traits to identify which species are likely to interact. Their deep-learning algorithm outperforms the allometric and phylogenetic models in common use by increasing the accuracy with which feeding interactions can be predicted. Although using machine-learning methods to study and model complex food web structures is not a new endeavor (*8*, *12*), it is yet to become a standard tool within the field.

Historical networks can no longer be observed, but their structure has been elucidated using ancient DNA, inferences from morphology, and models based on body size (*13*). Integration of machine-learning methods should progressively improve the reconstruction of paleo networks, enhancing the understanding of how ecosystems functioned in the past, how they differed from today, and how they responded to catastrophes.

For studying modern-day ecosystems, automation of deep-learning algorithms would increase the accessibility of network science for conservationists and monitoring agencies, helping to identify critical nontarget species or bioindicators of harmful change to an ecosystem. The approach could also be used to detect "potential prey" that are underrepresented in current food webs (*12*). For instance, DNA analysis of fish diets has revealed that gelatinous salps (a tunicate) could be a key alternative resource to declining krill in Southern Ocean food webs, despite years of underappreciation due to the rapid digestion of their soft bodies in fish stomachs (*14*).

Looking to the future, a major limitation at present is the inability to accurately forecast network responses to species extinctions or climate change. Now, it is typically assumed that a predator will go extinct if its primary prey disappears from the network, when it may instead shift its diet to other resources (*15*). Machine-learning opens avenues for anticipating how networks will rewire in response to global change by identifying resources with combinations of traits that would make certain prey suitable alternatives for predators. Similarly, knowledge of how a perturbation will alter the traits that underpin deep-learning algorithms would facilitate predictions of how the connections in the network, and not just the nodes, should respond. The accuracy and precision of these predictions may increase with the help of big data, transforming the power of network science for anticipating future ecological surprises from lofty aspiration to tangible reality. ∎

REFERENCES AND NOTES

1. G. Woodward *et al*., *Trends Ecol. Evol*. **20**, 402 (2005).
2. C. Barnes, D. Maxwell, D. C. Reuman, S. Jennings, *Ecology* **91**, 222 (2010).
3. W. Jetz, C. Carbone, J. Fulford, J. H. Brown, *Science* **306**, 266 (2004).
4. E. C. Fricke *et al*., *Science* **377**, 1008 (2022).
5. R. M. Thompson *et al*., *Trends Ecol. Evol*. **27**, 689 (2012).
6. J. A. Estes *et al*., *Science* **333**, 301 (2011).
7. L. Zhao *et al*., *Ecol. Lett*. **19**, 1032 (2016).
8. A. Ma *et al*., *Nat. Ecol. Evol*. **3**, 260 (2019).
9. D. Sanders, E. Thébault, R. Kehoe, F. J. Frank van Veen, *Proc. Natl. Acad. Sci. U.S.A*. **115**, 2419 (2018).
10. C. Gray *et al*., *J. Appl. Ecol*. **51**, 1444 (2014).
11. D. A. Bohan *et al*., *Trends Ecol. Evol*. **32**, 477 (2017).
12. D. A. Bohan, G. Caron-Lormier, S. Muggleton, A. Raybould, A. Tamaddoni-Nezhad, *PLOS ONE* **6**, e29028 (2011).
13. M. M. Pires *et al*., *Proc. R. Soc. London Ser. B* **282**, 20151367 (2015).
14. N. Henschke, J. D. Everett, A. J. Richardson, I. M. Suthers, *Trends Ecol. Evol*. **31**, 720 (2016).
15. X. Lu *et al*., *Nat. Clim. Change* **6**, 875 (2016).

10.1126/science.add7563

Interpreting thoughts during sleep

Rapid eye movements during sleep are a readout of thoughts during mouse dreams

By **Chris I. De Zeeuw**[1,2] and **Cathrin B. Canto**[1,2]

Have you ever noticed someone's eyes move rapidly under their eyelids during sleep? Owing to technical challenges in measuring eye movements in freely moving animals with their eyes half closed, this phenomenon has remained enigmatic. Sleep-related rapid eye movements occur during a specific sleep phase called rapid eye movement (REM) sleep, which is associated with vivid dreams (*1*). If rapid eye movements reflect thoughts during sleep, reading the eye movements of others, while observing them sleep, would open a window for reading and potentially manipulating their thoughts during dreams. On page 999 of this issue, Senzai and Scanziani (*2*) reveal that in mice, rapid eye movements during sleep are a readout of the internal sense of direction.

During the awake state, head direction (HD) cells in the thalamus form a circuit that functions as a compass, and HD cell activity can be read out as the neuronal correlate for physical head movement (*3*). HD cells, together with other cells that encode physical location in space, have been suggested to be important for the encoding of cognitive processes, such as the memorization of a certain episode in life, possibly linking spatial and temporal aspects of a particular event. Mice and other species, including humans, use a combination of alterations in heading and changes in eye movements to learn how to stabilize their gaze (*4*). In the awake situation, mammals make occasionally fast eye movements, called saccades, with alternating periods of fixation. This "saccade and fixate" gaze pattern is closely linked to rotational head movements. When a subject moves the head, the semicircular canals of the inner

[1]Netherlands Institute for Neuroscience, Amsterdam, Netherlands. [2]Department of Neuroscience Erasmus MC, Rotterdam, Netherlands. Email: c.canto@nin.knaw.nl

ear sense three-dimensional head rotations, and the angular vestibulo-ocular reflex opposes the rotational head movements to fix the gaze (5). In line with the evolutionary tight coupling between eye and head movements, Senzai and Scanziani found that the amplitude and speed of saccadic eye movements can predict physical head movements in awake and freely moving mice. At the same time, information from brain activity through recordings of the HD circuit allows predictions of the actual physical heading.

Moving the eyes in the same direction as the head can be particularly advantageous when the environment is being scanned. For example, by combining head and eye movements, mice can quickly sample the sky for

Senzai and Scanziani looked at whether REM sleep–related rapid eye movements encode daytime visual information by reading eye movements and concurrently decoding the internal representation of heading through simultaneously recorded HD cell activity. They found that the mouse brain processes visual and head movement information at the same time during REM sleep and that these information streams are congruent in that the direction encoded by the activity of the HD cells corresponds to that of the actual rapid eye movements. They found that REM sleep–related eye movements can be subdivided into two phases: "leading" eye movements, which predict the magnitude and directionality of the internal heading,

fest in muscle activity during the non-REM sleep phase. It will be important to find out to what extent activity in the HD system during REM sleep is internally generated or driven by a common "stimulus" that activates both the HD cells and the eye muscle system, akin to the coupling mechanism that occurs during the vestibulo-ocular reflex. Given that the speed of replay of HD cells during REM sleep is similar to that of the awake state and thus substantially lower than that of non-REM sleep, it is parsimonious to hypothesize that peripheral inputs differentially impinge on an internally organized network during different arousal states (12). Investigating whether cognitive processes that involve head and eye movement depend on sleep, and specifically REM sleep, will clarify whether the recorded rapid eye movements are not just the result of random brain waves leading to coupled HD circuit activity but also indeed fulfill a functional role that is similar to that suggested for neuronal replay (13).

Interpreting rapid eye movements during sleep may open opportunities for improving, interfering with, and/or deleting unwanted memories by inhibiting or stimulating eye movements during the dream phase. Perhaps vestibular stimulation with a certain frequency and amplitude could be used to improve memory for such movements while sleeping. Muscle twitches, which also frequently occur during REM sleep, might be related to the internal heading cues provided by rapid eye movements, and analyses of these might give further information about dreams. During the early development of mice, these muscle twitches have been shown to be important for healthy brain function (14), but whether the twitches that occur during REM sleep in adulthood also form a readout of dreams remains unknown. Indeed, the findings by Senzai and Scanziani may make dreams come true through studies of eye movements of sleeping mice. ∎

Dreaming of escape

Senzai and Scanziani found that rapid eye movements of mice encode daytime visual information and represent the internal sense of direction during sleep. This cognitive processing might entrain behavior when mice are awake, such as avoiding a bird of prey.

Awake
As a prey animal, a mouse uses its converging head and eye movements to actively explore the world for potential threats.

Head and eye movement

Vivid dream about escape from predator bird during REM sleep

Eye movement

Asleep
During subsequent sleep, the mouse goes through several cycles of non–rapid eye movement (NREM) sleep to rapid eye movement (REM) sleep. Rapid eye movements during REM sleep reveal an intentional or cognitive process, such as dreaming about when the mouse escapes from the predator bird. During this phase, the optimal avoidance behavior is also reflected in the activity of head direction cells, which corresponds to the direction of the rapid eye movements.

predator birds (6, 7). Training such lifesaving actions during sleep might increase the chances for survival (see the figure). Yet, with the rapid eye movements during REM sleep, most muscles are paralyzed. Is it possible to train a goal-directed behavior largely internally in the networks of the brain without making physical movements or making them only partially? Previously it was shown that brain activity that encodes places that have been experienced during daytime can reoccur at an accelerated rate during non-REM sleep and that this replay, as well as sleep in general, may facilitate memory formation and storage (8–10). Whether mice and other species use REM sleep-specific rapid eye movements for memorizing daytime visual information, such as detecting and escaping a predator, is an unsolved problem.

and sleep-specific "follower" eye movements, which likely mediate recentering of the eye.

This is fascinating because vestibular head movement information from the semicircular canals is absent during sleep. At the same time, rapid eye movements indicate the ongoing virtual representation of the HD circuit as if the mouse dreams about a particular physical head movement. This suggests that the rapid eye movements reflect cognitive processes that occur during sleep, such as manifesting the memory of a short episode in life that is critical for survival.

What still needs to be determined is whether these eye movements and HD circuit activity also come with a subconscious process that requires entrainment of a critical readiness to act (11). It is also unclear why such dreams about movement do not mani-

REFERENCES AND NOTES

1. E. Aserinsky, N. Kleitman, *J. Neuropsychiatry Clin. Neurosci.* **15**, 454 (2003).
2. Y. Senzai, M. Scanziani, *Science* **377**, 999 (2022).
3. J. S. Taube, *J. Neurosci.* **15**, 70 (1995).
4. A. F. Meyer *et al.*, *Curr. Biol.* **30**, 2116 (2020).
5. A. M. van Alphen *et al.*, *Brain Res.* **890**, 296 (2001).
6. M. Yilmaz, M. Meister, *Curr. Biol.* **23**, 2011 (2013).
7. A. M. Michaiel *et al.*, *eLife* **9**, e57458 (2020).
8. J. O'Neill *et al.*, *Science* **355**, 184 (2017).
9. A. K. Lee, M. A. Wilson, *Neuron* **36**, 1183 (2002).
10. C. I. De Zeeuw, C. B. Canto, *Neurobiol. Learn. Mem.* **170**, 107165 (2020).
11. L. Bina *et al.*, *Cell Rep.* **37**, 110116 (2021).
12. A. Peyrache *et al.*, *Nat. Neurosci.* **18**, 569 (2015).
13. G. Buzsáki, *Neuroscience* **31**, 551 (1989).
14. M. S. Blumberg *et al.*, *Curr. Biol.* **30**, R38 (2020).

GRAPHIC: K. K. HOLOSKI/SCIENCE

Two nanoparticles dancing as a pair

Lasers induce and control interactions between two nanoparticles

By **Julen Simon Pedernales**

That light can move matter should not come as a surprise to anyone. Scientists have considered this since 1619, when Johannes Kepler suggested that the tails of comets are pointing away from the Sun because of the force exerted on them by the sunlight. By the 1970s, scientists had figured out how to use laser beams to push, pull, and trap nano- and microscale objects. Using the same physical principles, light can also induce interactions between particles that would not otherwise "sense" the presence of each other. On page 987 of this issue, Rieser *et al.* (*1*) report an experimental demonstration of such a light-induced interaction between two silica nanoparticles suspended in a vacuum and show that the trapping laser beams can be used as a control to tune the form and strength of the coupling.

A dielectric nanoparticle embedded in a laser field with a wavelength much larger than the size of the particle can be treated as a point-sized object in calculations. The electric field from the laser induces an inhomogeneous distribution of charges in the nanoparticle, which can be considered as a point-like electric dipole that oscillates together with the laser field. If the electric field is not uniform, the dipole will experience a force pushing it toward where the electric field is more intense. Because a laser beam is more intense at its focal point, a nanoparticle is attracted to this point and can be held in place against gravity. This is the working principle behind optical tweezers (*2*).

Consider a second laser beam travelling parallel to the first beam and containing its own nanoparticle. The two nanoparticles suspended in the two laser beams can then interact through electric dipole-dipole interaction. This results in what is known as the optical binding force (*3*), which only occurs when the particles are illuminated. Although the force is called a binding force, it can be attractive or repulsive and can vary in magnitude. This depends on the relative orientation and phase of the dipoles, as well as the distance between the

Institut für Theoretische Physik, Universität Ulm, Ulm, Germany. Email: julen.pedernales@uni-ulm.de

dipoles, all of which can be controlled by tuning the laser beams.

Rieser *et al.* take advantage of this dependence and show that by adjusting certain parameters of the trapping laser fields, it is possible to control how the two particles interact, thus turning the trapping laser beams into control handles for adjusting the interparticle coupling. This opens the door to engineering arrays of

A one-way force on two nanoparticles

Levitated nanoparticles scatter light in phase with their trapping laser fields. The interference between the waves radiated by each nanoparticle can result in the total scattered light having a preferential direction of propagation.

Light scattered by each nanoparticle

Interference between the two light fields

The combined light field

— Total scattered field (■ + ■)

levitated solids with tunable couplings for the study of many-body physics in regimes otherwise inaccessible using previously existing methods.

Notably, the force that the dipoles exert on each other does not need to be reciprocal. At first sight, this might seem to violate Newton's third law of the equivalence between action and reaction. Nevertheless, one can untangle this paradox using the following logic. The optical binding is mediated by the electromagnetic waves from the laser that, after impinging on one nanoparticle, are scattered toward the second nanoparticle. However, the radiation scattered by each of the two nanoparticles will also interfere. For certain configurations of the particle positions and the laser phases, the combined light will increase in intensity in one direction while decreasing, or even canceling out, in the opposite direction (see the figure). This results in a preferential direction for the total light scattered from the incoming laser beams. Because light carries momentum, this deflection of light implies a change in momentum of the incident laser field, which needs to be compensated by the two nanoparticles by acquiring momentum in the opposite direction. Therefore, the two-particle system experiences a force acting on its center of mass in addition to the forces acting on the particles by each other, which accounts for the apparent nonreciprocity.

With an exquisite degree of control, Reiser *et al.* could discriminate the contribution of such a nonreciprocal component in the total optical binding force. Such a technical ability enhances the type of interactions that can be engineered among quantum systems. The phenomenon of optical binding between optically trapped particles is not new. It was reported soon after the discovery of optical tweezers (*4*) and has since been reported numerous times for different setups, including particles levitated in a vacuum (*5*, *6*). However, in their experiment, Rieser *et al.* go beyond the observation of the phenomenon and reach an unprecedented degree of control over the interaction. In this way, they have turned the knowledge into a tool for manipulating levitated optomechanical systems. Gaining increased control over the dynamics of mesoscopic objects can help
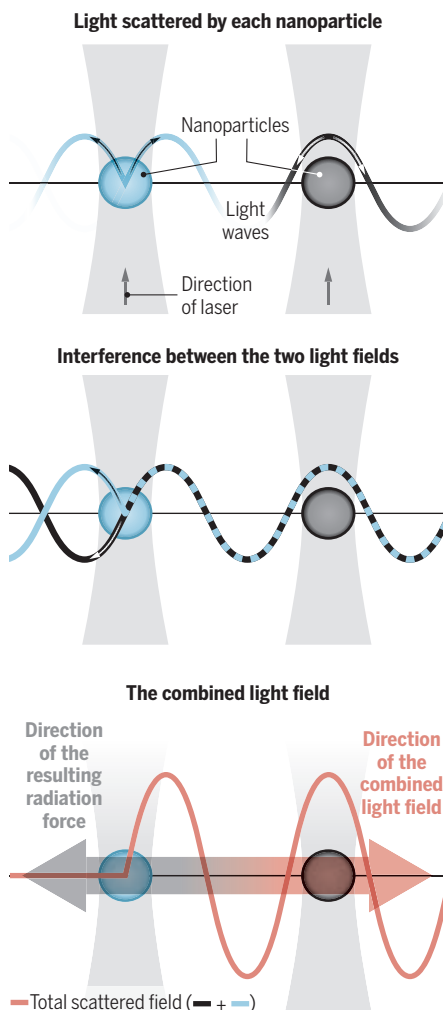
the exploration of macroscopic quantum mechanics.

Although quantum mechanics is often regarded as a theory of the microscopic world, its postulates do not indicate any particular scale at which they should cease to play a dominant role. Quantum properties like the superposition principle have thus far been observed for systems of up to some thousands of atoms (7). Thus, the range of applicability of quantum mechanics remains a matter of scientific debate. The answer to this puzzle should ultimately come from an experiment, and the field of levitodynamics (8) suggests that nanoparticles levitated in vacuum might be the right platform for testing this unseen boundary of where the quantum "rules" apparently become weak (9–11).

Future research efforts may look to combine the tunable optical binding demonstrated by Rieser et al. with the already established ground-state cooling of a levitated nanoparticle (12). In doing so, this type of experiment would usher in the regime of quantum coherent interactions between levitated nanoparticles, opening the door for the generation of entanglement between them (13, 14). One can imagine the possibilities offered by a programmable, many-body platform, where particles are solids with rotational degrees of freedom and masses that allow them to interact gravitationally with each other and with the environment. In just one decade, the field of levitated optomechanics has gone from being proposed as a theory for the cooling of a levitated nanoparticle to its experimental demonstration. Rieser et al. added a technique to the toolbox of this nascent field and may be regarded as a milestone on the path toward realizing the once niche theoretical endeavor in applications. ■

REFERENCES AND NOTES

1. J. Rieser et al., Science 377, 987 (2022).
2. A. Ashkin, J. M. Dziedzic, J. E. Bjorkholm, S. Chu, Opt. Lett. 11, 288 (1986).
3. K. Dholakia, P. Zemánek, Rev. Mod. Phys. 82, 1767 (2010).
4. M. M. Burns, J.-M. Fournier, J. A. Golovchenko, Phys. Rev. Lett. 63, 1233 (1989).
5. Y. Arita, E. M. Wright, K. Dholakia, Optica 5, 910 (2018).
6. V. Svak et al., Optica 8, 220 (2021).
7. Y. Y. Fein et al., Nat. Phys. 15, 1242 (2019).
8. C. Gonzalez-Ballestero, M. Aspelmeyer, L. Novotny, R. Quidant, O. Romero-Isart, Science 374, eabg3027 (2021).
9. O. Romero-Isart et al., Phys. Rev. Lett. 107, 020405 (2011).
10. C. Wan et al., Phys. Rev. Lett. 117, 143003 (2016).
11. J. S. Pedernales, G. W. Morley, M. B. Plenio, Phys. Rev. Lett. 125, 023602 (2020).
12. U. Delić et al., Science 367, 892 (2020).
13. T. Weiss, M. Roda-Llordes, E. Torrontegui, M. Aspelmeyer, O. Romero-Isart, Phys. Rev. Lett. 127, 023601 (2021).
14. F. Cosco, J. S. Pedernales, M. B. Plenio, Phys. Rev. A 103, L061501 (2021).

10.1126/science.add1374

PHOTO: LEEMAGE/CORBIS/GETTY IMAGES

EVOLUTION

Ancient genomes and West Eurasian history

Storytelling with ancient DNA reveals challenges and potential for writing new histories

By **Benjamin S. Arbuckle** *and* **Zoe Schwandt**

Innovations in the sequencing of ancient (>100 years old) DNA have provided a new source of historical information that is complementary to ancient texts, oral traditions, and the archaeological record. The geographic application of this new technology has been uneven, focusing largely on Western and Northern Europe. On pages 939, 940, and 982 of this issue, Lazaridis et al. (1–3) report leveraging newly sequenced ancient DNA from the remains of 777 humans from across West Eurasia. They describe the genomic history of the "Southern Arc," the region surrounding the Black Sea and including Southeastern and Eastern Europe, the Anatolian peninsula, the Pontic steppe, and the Caucasus. Focusing on the relative contributions of five ancestral West Eurasian populations, they reveal shifting proportions of these lineages, which are used to reconstruct population movements extending from the Neolithic (10,000 BCE) to the Ottoman (~1700 CE) periods and representing the demographic foundations of the modern West Eurasian world.

Once thought to represent a revolution emanating from a single "hearth" in the Euphrates river valley, Lazaridis et al. analyze ancient genomes from five populations (ancient Anatolian and Levantine farmers and Eastern, Balkan, and Caucasus hunter-gatherers) and show that the origins of farming in the Neolithic instead involved complex networks of communication and reproduction that connected populations in Anatolia, the Levant, Mesopotamia, and Iran (1–3). They also focus their powerful analytical tools on genomes associated with the expansionary Yamnaya archaeological culture emanating from the Pontic steppe in the Bronze Age (third millennium BCE) (4). Associating the Yamnaya with distinctive Eastern hunter-gatherer ancestry and the spread of Indo-European languages, Lazaridis et al. explore details of the expansion of steppe populations into Southeastern Europe and Armenia, two regions with ancient Indo-European lan-

Department of Anthropology, University of North Carolina at Chapel Hill, Chapel Hill, NC, USA. Email: bsarbu@email.unc.edu

The Crater of Warriors terracotta vase from Mycenae, an archaeological site in Greece, is dated to ~1200 BCE. It depicts Mycenaean warriors on the march.

guages (*1–3*). In Southeastern Europe, they show that steppe ancestry is associated with some but not all individuals from high-status tombs in Mycenaean Greece, indicating complex cultural (and biological) dynamics between the local Minoan population and incoming steppe migrants. They also use genomic evidence to evaluate events described in ancient texts. They highlight the variable patterns of ancient Greek colonization, discover that Anatolian migrants transformed the demographic composition of Imperial Rome, and show that ancient DNA can identify the expansion of Slavic and Turkic speakers into Eastern Europe and Anatolia in the medieval period (~500 to 1100 CE).

Although Lazaridis *et al.* address an extraordinarily wide range of topics and provide insights into the Eurasian past (*1–3*), several issues common to ancient DNA research are evident in the framing of the data, especially with regard to the stories that are chosen (or not) for explication. In ancient genome research, DNA sequences are often presented as revealing a "true" history of humanity in contrast to historical and archaeological records that are prone to untruthfulness and imprecision. Although base pairs do not lie or exaggerate (though they do decay), neither do they tell stories, and storytelling that is used to interpret ancient genome analyses inevitably projects specific worldviews (*5*).

Many of the narratives explored in the studies of Lazaridis *et al.* reflect a Eurocentric worldview. For example, the naming of the Southern Arc conjures a map projection that centers on the western tip of Eurasia rather than the Anatolian peninsula—a more intuitive geographic center of the research area. Moreover, in terms of scale, narratives based on genomes often project a high-altitude view of history (*6*), mostly devoid of individuals despite being derived from its most personal components. Neolithic farmer or steppe Yamnaya genetic material moves abstractly on its way from central Anatolia to the Balkans or from the Don to the Danube and the Peloponnese.

This approach to history-making offers a sanitized version of the past that avoids engaging with bodily experiences, including sexual violence, which was probably involved in the movement of genetic material through time and space (*7*). Sexual reproduction itself is reduced to a process motivated by competition and survival and carried out primarily by men. Thus, with this approach, history is made through vague processes of migration

and admixture, but the social mechanisms remain uncharted (*8*).

In constructing the history of the Southern Arc, Lazaridis *et al.* focus on Y chromosome lineages, especially to link populations in Southeastern Europe, the Aegean, and the southern Caucasus to the Bronze Age Yamnaya through shared patrilines (*1–3*). Ostensibly, there are technical reasons for this—Y chromosomes allow for precise reconstructions of lineages and divergence times. However, the resulting emphasis on patrilineal descent and the absence of discussions of parallel networks of matrilines (or of XX chromosome humans at all) creates a strong sense that the events of history are carried forward by "great men"—especially those bearing Eastern hunter-gatherer ancestry and buried under mounds of earth and stone. This emphasis on Y chromosome networks inadvertently projects gender stereotypes into the past, perpetuating an androcentric narrative of dominance and competition that equates chromosomes to gender and gender to behavior. Conversely, approaches that explore maternal markers and sex-neutral kinship coefficients have recently been used, showing that alternate methods that overcome sex biases are possible (*9, 10*).

Lazaridis *et al.* also present a dataset that estimates the phenotype, in terms of hair, eye, and skin pigmentation, for humans in the Southern Arc and Europe over the past 15,000 years (*1–3*). They show that brown hair and eyes and "intermediate" skin pigmentation was the most common phenotype in the region through time and that, despite common stereotypes, Bronze Age steppe populations were not dominated by blonde and blue-eyed individuals. They also document an increase in "light" pigmentation over time in West Eurasia, although potential reasons for selection of these traits are not addressed.

Despite the authors' intention of dispelling stereotypes, this brief presentation of phenotypes instead amplifies a Eurocentric worldview that highlights light pigmentation (*5*). Genomics scholars should think carefully about the political ramifications of presenting sensitive data such as these because they are consumed by a wide audience, and some may repurpose them (*11*). Other ways of presenting the data are possible. For example, it is equally interesting that southern Mesopotamians sometimes called themselves the "black-headed people," perhaps to contrast their own phenotype with the abundance of brown hair in adjacent regions (*12*).

Lazaridis *et al.* have produced an astounding dataset, unimaginable in its scale just a decade ago (*1–3*). It is important to

acknowledge that the narrative scaffolding used to interpret these data inevitably represents worldviews that center certain people and places (*13*). Other narratives and scales of inquiry are also possible. For example, one of the most interesting alternative interpretations emerging from the studies of Lazaridis *et al.* is the resilience of hunter-gatherer genomes in regions outside the Fertile Crescent region of Southwest Asia, where farming first emerged. In particular, and despite documenting large-scale incursions of exogenous populations into the Balkans in the Neolithic and Bronze Age, the authors show the surprising resilience of local Balkan hunter-gatherer ancestry in the region that continues to the present day. This finding complicates previous narratives of linear population replacements and further highlights the need to explore the complex social interactions associated with ancient population movements.

Moving forward, the growing corpus of ancient genomic data will continue to transform views of human history. This work can be particularly effective if researchers recognize their lack of neutrality and embrace their role in constructing narratives while allowing room for diverse perspectives that shine light onto people and places whose histories are less well known. Lazaridis *et al.* do an excellent job of this, for example, by exploring the genomic diversity of the poorly known kingdom of Biainili (known as Urartu to their Assyrian neighbors) in the mountains of Transcaucasia (*1–3*). Rather than presenting history from a traditional top-down view, genomic scholars can leverage the high resolution of their data to pivot between different scales—from the continental to the individual—and can address historical networks of interaction involving both patrilines and matrilines. The studies by Lazaridis *et al.* represent an important milestone for ancient genomic research, providing a rich dataset and diverse observations that will drive the next iteration of interpretations of the human history of West Eurasia. ∎

REFERENCES AND NOTES

1. I. Lazaridis *et al.*, *Science* **377**, eabm4247 (2022).
2. I. Lazaridis *et al.*, *Science* **377**, 940 (2022).
3. I. Lazaridis *et al.*, *Science* **377**, 982 (2022).
4. W. Haak *et al.*, *Nature* **522**, 207 (2015).
5. A. Källén *et al.*, *Curr. Swed. Archaeol.* **27**, 69 (2019).
6. D. Haraway, *Fem. Stud.* **14**, 575 (1988).
7. B. L. Voss, *Am. Anthropol.* **110**, 191 (2008).
8. R. J. Crellin, O. J. T. Harris, *Archaeol. Dialogues* **27**, 37 (2020).
9. R. Yaka *et al.*, *Curr. Biol.* **31**, 2455 (2021).
10. N. E. Altınışık *et al.*, bioRxiv 10.1101/2022.01.31.478487 (2022).
11. S. E. Hakenbeck, *World Archaeol.* **51**, 517 (2019).
12. M. Karlsson, *Akkadica* **141**, 127 (2020).
13. M. de la Cadena, M. Blaser, Eds., in *A World of Many Worlds* (Duke Univ. Press, 2018), pp. 1–22.

LIGHT TRAPPING

Absorbing light using time-reversed lasers

Laser cavities can be reverse engineered to create an efficient light trap

By **Jacopo Bertolotti**

n 2019, researchers from the Massachussetts Institute of Technology made headlines when they created the "blackest" material to date, which had the ability to absorb 99.995% of incident light (*1*). More than aesthetics, there are many technologies that can benefit from maximizing light absorption—for example, in photovoltaics because of the need to absorb and convert as much light as possible into electricity, or on the interior surface of a light sensor because of the need to minimize unwanted stray light. Although there are many ways to create something that can absorb some light, the endeavor gets more and more difficult the closer it gets to 100% absorption. On page 995 of this issue, Slobodkin *et al.* (*2*) report on a design principle that can absorb light on the basis of "coherent perfect absorption" (*3*), which can theoretically absorb 100% of the light incident on the device.

Intuitively, one might assume that a material with a larger absorption coefficient would lead to it being a better light absorber, but this is not always the case. For example, a sharp change in the value of the absorption coefficient will lead to the reflection of a large fraction of the incident light, which sends the light away instead of letting it be absorbed. This is why many metals make for very good mirrors despite having a decent absorption coefficient (*4*). One possible solution to this conundrum of absorption versus reflection is to use a material with a low absorption coefficient. This allows light to enter the medium without being reflected away, and consequently, the light remains in the medium for a long time and is gradually absorbed. This phenomenon can be observed in the darkness at the bottom of the ocean, where most of the sunlight has been absorbed by water, which itself is nearly transparent.

However, the obvious practical problem with this approach is the amount of space it requires, which limits its usefulness for most applications. A well-established approach to obtaining a similar absorption in a smaller volume is to trap the light in-side the medium. This is achieved in those "ultrablack" paints by using diffusive materials, in which the light is scattered many times and thus takes a long time to exit the medium (*1*). Although this approach works well to remove unwanted light, many applications aim to absorb light for use as energy (such as a solar panel). It can thus be difficult to integrate, for example, the photovoltaic material with the black paint to improve the overall efficiency of the device.

One way to help a functional absorber, such as a photovoltaic cell, to absorb light is to create an environment that can trap light for the absorber. This is the purpose of the cavity used by Slobodkin *et al.* Electrodynamic phenomena are invariant under time reversal, which means that if a certain electrodynamic effect exists, then there should also exist a time-reversed equivalent (*5*). Because the time-reversed equivalent of light emission is light ab-sorption, any system that emits light can, in principle, also be used to absorb light. In particular, lasers use a cavity to trap the light around a light emitter to control and amplify it. Replacing an emitter with an absorber (even a poor one) will make the system operate in reverse and absorb the light very efficiently (*3*). However, the problem with this design approach is that a laser cavity traps only specific patterns of light (modes), and thus time reversal can be used only to absorb light that happens to be in one of the specific modes. Any other mode, such as beams coming at a different angle or having a different shape, will not be stable in the cavity and will not be absorbed as much. What is needed is a cavity that traps all possible modes.

Slobodkin *et al.* designed a system that can trap all modes of light by using so-called "degenerate" optical cavities (*6*). An optical cavity is said to be "degenerate"

Department of Physics and Astronomy, University of Exeter, Stocker Road, Exeter EX4 4QL, UK. Email: j.bertolotti@exeter.ac.uk

As amplification, so absorption

Inside a degenerate optical cavity, light rays are reflected and refracted so that they always follow the same trajectory, which keeps all light modes circulating in the cavity. Although this design was originally devised to amplify light in a laser, it can be adapted for light absorption. f, focal length of lens.

For amplification
Light is kept circulating in the cavity and is amplified at each passage by the gain medium. However, a small fraction of light escapes the cavity as the laser emission.
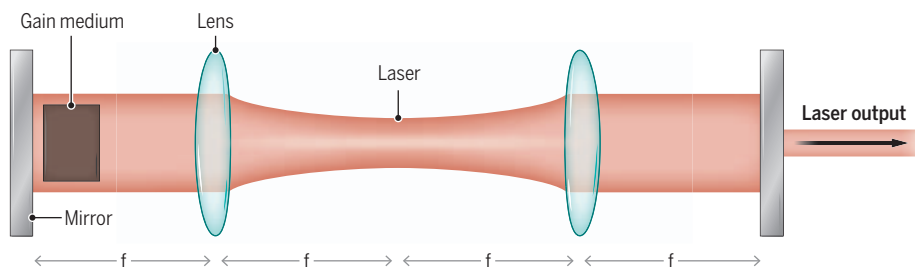
For absorption
When the gain medium is swapped for an absorber, the trapped light will gradually be absorbed. This makes the degenerate cavity a universal light absorber.

GRAPHIC: A. MASTIN/*SCIENCE*
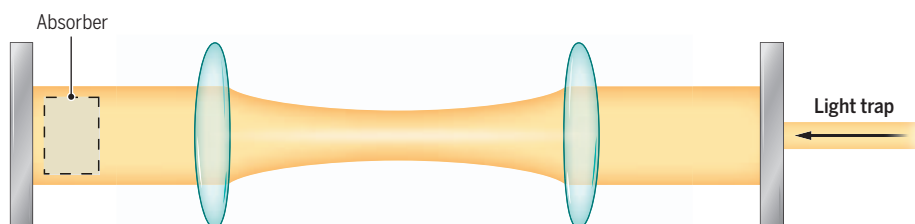
when any ray of light will eventually retrace its own path in the cavity. The simple design by Slobodkin et al. uses two mirrors on the outside and two lenses on the inside (see the figure). The light is trapped between the mirrors, and the addition of lenses helps guide the rays to always hit the same spot on the mirrors after each reflection, making the system degenerate. As a result, any light trapped between the two mirrors and the two lenses is kept circulating inside the cavity and absorbed at each reflection (7).

Although the experimental implementation of Slobodkin et al. is just a proof-of-principle device, it points to what can be done with this method in the future. Albeit only achieving around 95% absorption in their demonstration, their design strategy—known as "massively degenerated coherent perfect absorption"—can in principle absorb 100% of the incident light.

Their proof-of-concept device is also surprisingly robust to imperfections in its

> "...any system that emits light can, in principle, also be used to absorb light."

fabrication. This is somewhat unusual for a method that relies on wave interference because it is not uncommon for a misalignment of just a few tens of nanometers to destroy the desired effect.

Although the exact design of the device may not be ready for immediate applications, it provides the distinctive advantage of enhancing the absorption of any other device without modifying it, which could be used to improve the efficiency of photodetectors or photovoltaic units. The use of a cavity also opens the way to very sophisticated manipulations of absorption. By exploiting the techniques developed for lasers, it should be possible to design cavities that only trap certain frequencies. This would allow frequency-dependent absorption or the use of different frequencies of light to accumulate different phase retardations to generate time-dependent absorption. ∎

REFERENCES AND NOTES
1. K. Cui, B. L. Wardle, *ACS Appl. Mater. Interfaces* **11**, 35212 (2019).
2. Y. Slobodkin et al., *Science* **377**, 995 (2022).
3. Y. D. Chong et al., *Phys. Rev. Lett.* **105**, 053901 (2010).
4. D. Griffiths, *Introduction to Electrodynamics* (Pearson, 2014).
5. A. D. Boozer, *Am. J. Phys.* **81**, 585 (2013).
6. J. A. Arnaud, *Appl. Opt.* **8**, 189 (1969).
7. M. Nixon et al., *Opt. Lett.* **38**, 3858 (2013).

Wildlife trade is likely the source of SARS-CoV-2

Multiple transmissions from wildlife at a market in Wuhan probably led to SARS-CoV-2 emergence

By **Xiaowei Jiang** *and* **Ruoqi Wang**

Almost all pandemic viruses have zoonotic origins, including severe acute respiratory syndrome coronavirus (SARS-CoV) and SARS-CoV-2 (1). During SARS outbreaks between 2002 and 2003, a live animal source of SARS-like viruses was identified at a market in Guangdong, China, providing unequivocal understanding of its zoonotic origin. Although the most probable reservoir animal for SARS-CoV-2 is *Rhinolophus* bats (2, 3), zoonotic spillovers likely involve an intermediate animal. Various SARS-CoV-2–susceptible intermediate animals were sold at the Huanan Seafood Wholesale Market in Wuhan, such as raccoon dogs, foxes, and mink. But these were unavailable for testing, so direct evidence of an animal source is lacking. Thus, it remains unknown exactly how SARS-CoV-2 emerged and led to the COVID-19 pandemic. On pages 951 and 960 of this issue, Worobey et al. (4) and Pekar et al. (5), respectively, provide quantitative evidence that SARS-CoV-2 emergence was likely caused by multiple zoonotic transmissions due to wildlife trading at the Huanan Market.

The search for the origin of SARS-CoV-2 resulted in numerous discoveries of SARS-CoV-2–related viruses in bats and other susceptible animals, with implications for virus evolution. The most closely related bat coronaviruses to SARS-CoV-2, which were sampled in Laos, share an ancestor from ~30 years ago (3). At the genomic level, two of these viruses (BANAL-103 and BANAL-52) harbor a nearly identical receptor binding motif (responsible for human cell entry) to SARS-CoV-2 (see the figure). However, 30 years of evolution could have led to substantial mutational changes in the viral genome (2). Therefore, continual sampling of SARS-CoV-2–related viruses in bats and other susceptible animals in Southeast Asia and China may still help characterize the evolution and origin of SARS-CoV-2, even if the intermediate animals from the Huanan

Department of Biological Sciences, Xi'an Jiaotong–Liverpool University (XJTLU), Suzhou, China. Email: xiaowei.jiang@xjtlu.edu.cn

Market that carry the direct ancestor of the SARS-CoV-2 strains isolated in COVID-19 patients in Wuhan are no longer available.

Even without the intermediate animal, likely because Huanan Market was cleared from 1 January 2020, it is still possible to learn how SARS-CoV-2 may have emerged. Available epidemiological, genomic, and human demographic data from the location where human infections first emerged, which is not necessarily the place of virus evolutionary origin, can be analyzed to understand the beginning of the pandemic. To test whether Huanan Market is the source of the COVID-19 pandemic, Worobey et al. provide epidemiological evidence that the early cases were centered around the market, not other places frequently visited by people in Wuhan. Moreover, subsequent human-to-human transmissions shifted from the market and its neighborhood to more populated areas of Wuhan, particularly those with susceptible elderly people.

Was wildlife trading the origin of the early COVID-19 outbreak at Huanan Market? Worobey et al. provide evidence that there was trading of SARS-CoV-2–susceptible wildlife spanning several years immediately before December 2019. This created opportunities for close, sustained contacts between these animals and humans at the market, laying the foundation for potential zoonotic spillover. Moreover, Worobey et al. find that the market stalls that sold susceptible wildlife species are spatially correlated with SARS-CoV-2–positive environmental samples. Some of these sampled objects were used to handle wildlife, such as a metal cage and carts (6). At the beginning of the pandemic, two viral lineages of SARS-CoV-2 (termed S and L) were revealed from the viral genomes of early cases (7) and later termed A and B. These strains only differ by two mutations. However, how these lineages relate to an early zoonotic spillover was unclear owing to the lack of a direct ancestor virus for comparison. Worobey et al. established epidemiological links of early cases of the two viral lineages A and B to the market, and these lineages were present in the positive environmental samples from the market (6).

How could zoonotic transmission lead to the emergence of two viral lineages at

Wildlife farming and SARS-CoV-2–related viruses

Major wildlife farming and sourcing provinces for the Huanan Seafood Wholesale Market in Wuhan are shown with molecular dating of known severe acute respiratory syndrome coronavirus 2 (SARS-CoV-2)–related sarbecoviruses. The phylogenetic tree indicates the estimated time of divergence (2, 3). Provinces that supply wildlife to Huanan Market, according to the World Health Organization (WHO) SARS-CoV-2 origin report (8), are shown in dark gray. Hypothetical wildlife trading paths for lineage A/B SARS-CoV-2 ancestral viruses and other failed zoonotic transmissions at the Huanan market are indicated with red arrows.
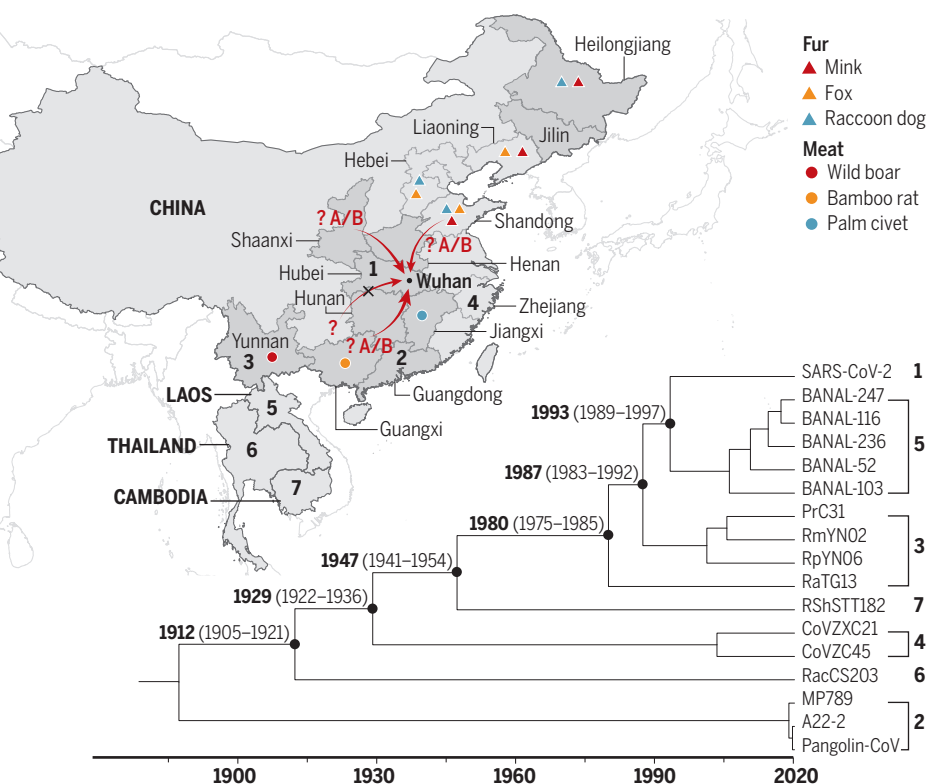
Maritime borders are not shown. Base map was made with data from naturalearthdata.com.

Huanan Market? Pekar *et al.* hypothesize that these two strains result from two independent zoonotic transmissions. Zoonotic events are stochastic in nature, so a spillover with successful onward transmission between humans normally involves a series of failed attempts by the virus, allowing it to establish sustained transmissions. For two independent zoonotic spillovers to be successful, sustained contacts and multiple zoonotic transmissions between people and the animals carrying SARS-CoV-2 at the Huanan Market would have been required. By using simulations—involving a predicted closely related SARS-CoV-2–like virus, the viral phylogenetic trees, and epidemiological data of early COVID-19 cases—Pekar *et al.* show that the two viral lineages can only be explained by two independent zoonotic transmissions. They determine that proposed intermediate forms of the two lineages with one mutation are sequencing artifacts. The likelihood that there are two independent lineages of the virus suggests that these could only come from the source animals and that the most recent common ancestors are in animals.

Further analysis suggests that transmissions from animals sold at the Huanan Market happened in a short period, likely between 1 and 2 months. The genetic diversity of the virus in the animals that led to the COVID-19 outbreak is likely low. This implies that the animals could be sourced from a local wildlife farm because multiple independent transmissions that would have resulted in an outbreak require multiple infected animals at the market during those months. These infected animals could also have come from provinces other than the local Hubei region, as implied in the World Health Organization SARS-CoV-2 origin report (8). But these are all speculations because the supply chain for these susceptible animals to the Huanan Market has not been investigated.

The zoonotic origins of the SARS and COVID-19 pandemics are very similar. Both likely involved trading of susceptible live wildlife at local markets and people who work and live in and around these markets. Developing real-time outbreak surveillance systems that are better at predicting risks would need to consider the supply chains at the human-animal interface. For example, wildlife trading

for fur, skin, and human food is usually supported by different farm sizes for socio-economic reasons, such as small farms in rural areas in an effort to reduce poverty (9). Wild animals harbor various pathogens, including potentially pandemic-causing coronaviruses, and only a fraction of virus diversity is being sampled (10, 11). Farming large numbers of wildlife inevitably provides opportunities for spillover events and so poses unprecedented threats to human health.

When farmed wildlife population sizes are large [at the scale of tens of millions or even larger (9)] and the underlying infrastructure for zoonosis control is lacking, farmed wild animals become reservoirs for pathogen genetic diversity to accumulate (9, 12). The diversity and scale of wildlife farming make zoonosis control almost impractical. Spillovers are destined to happen, particularly when there are changing driver events, such as altered demand owing to meat or food shortages or because of cost increases (9, 13). For example, since early 2022 there has been increased demand in Thailand for cheaper meat from crocodile, a widely farmed wild animal for its skin, during the African swine fever virus pandemic that resulted in high pig and pork prices (9, 14). Although applying existing livestock regulations to wildlife farming may minimize such risks, its effectiveness remains to be seen (15). When the science underlying multiple-host pathogen evolutionary dynamics is still not fully understood (12), it is challenging to establish effective zoonosis control infrastructure. Although Worobey *et al.* and Pekar *et al.* reveal the likely details of early zoonotic and epidemiological events that led to the COVID-19 pandemic, without knowing the exact animal origin of SARS-CoV-2 the threat posed by another similar virus from wildlife farming is looming. ■

REFERENCES AND NOTES

1. E. C. Holmes *et al.*, *Cell* **184**, 4848 (2021).
2. S. Temmam *et al.*, *Research Square* 10.21203/rs.3.rs-1803095/v1 (2022).
3. S. Lytras *et al.*, *Genome Biol. Evol.* **14**, evac018 (2022).
4. M. Worobey *et al.*, *Science* **377**, 951 (2022).
5. J. E. Pekar *et al.*, *Science* **377**, 960 (2022).
6. G. Gao *et al.*, *Research Square* 10.21203/rs.3.rs-1370392/v1 (2022).
7. X. Tang *et al.*, *Natl. Sci. Rev.* **7**, 1012 (2020).
8. WHO, "WHO-convened global study of origins of SARS-CoV-2: China Part" (2021); https://bit.ly/3JXJY5a.
9. W. Xia *et al.*, *Preprints* 10.20944/preprints202102.0590.v2 (2022).
10. W.-T. He *et al.*, *Cell* **185**, 1117 (2022).
11. W. Wang *et al.*, *Virus Evol.* **8**, veac046 (2022).
12. M. E. J. Woolhouse *et al.*, *Science* **292**, 1109 (2001).
13. S. Lytras *et al.*, *Science* **373**, 968 (2021).
14. V. Duangdee, South China Morning Post 21 January 2022; https://bit.ly/3AbYCCJ.
15. L. P. Koh *et al.*, *Nat. Sustain.* **4**, 2 (2021).

James Lovelock (1919–2022)

Father of Earth system science

By **Timothy M. Lenton**

James E. ("Jim") Lovelock died on 26 July, his 103rd birthday. An independent scientist and prolific inventor, Jim transformed our view of Earth and the impact of humans upon it. His Gaia hypothesis revealed that the thin film of life, air, water, soil, and sediments at the planet's surface is a remarkable, self-regulating system. Jim also showed how we are disrupting that system, discovering important trace gases with his own instruments—including ozone-depleting chlorofluorocarbons. He was the original Earth system scientist.

Born in Letchworth, UK, in 1919 and raised in Brixton, Jim hated doing homework but loved scientific books and nature walks with his father. While attending Birkbeck College at night, Jim learned his craft as an apprentice chemist for a consulting firm. War took him to Manchester University, where he earned his bachelor's degree in chemistry in 1941. A conscientious objector, Jim then joined the National Institute for Medical Research at Mill Hill. He received a PhD in medicine from the London School of Hygiene and Tropical Medicine in 1948 and a DSc in biophysics from the University of London in 1959. In 1961, an invitation to consult for NASA inspired him to ditch tenure and spend his life as an independent scientist.

Jim made deep and diverse contributions to science, with a passionate disregard for conventional disciplinary boundaries. At Mill Hill, he gained a reputation as a master inventor of precision instruments, most notably the exquisitely sensitive electron capture detector. He was a pioneer of cryobiology, including the freezing and resuscitation of small mammals, which gave him a keen sense of the resilience of life.

Working for NASA at the Jet Propulsion Laboratory in 1965, Jim was tasked with detecting whether there was life on Mars. He reasoned that the presence of abundant life on any planet would show up as a remotely detectable disequilibrium in the chemistry of its atmosphere (a method still foundational to contemporary efforts to detect life on exoplanets). A predominance of atmospheric

Global Systems Institute, University of Exeter, Exeter, UK.
Email: t.m.lenton@exeter.ac.uk

carbon dioxide strongly suggested that Mars was lifeless. Looking at Earth's atmosphere, Jim saw an extraordinarily improbable, yet remarkably stable, chemical cocktail created by life. He realized that life must play a role in regulating the composition of both the atmosphere and the climate. Later he teamed up with evolutionary biologist Lynn Margulis, who put microbiological flesh on the chemical bones of the hypothesis, which novelist William Golding named "Gaia."

In the early 1970s, Jim predicted that oceanic life would make atmospheric gases that return essential elements to the land. Using his own instruments, he discovered the biogenic gases methyl iodide and dimethyl sulfide in the remote marine atmosphere. He

PHOTO: COLIN MCPHERSON/CORBIS/GETTY IMAGES
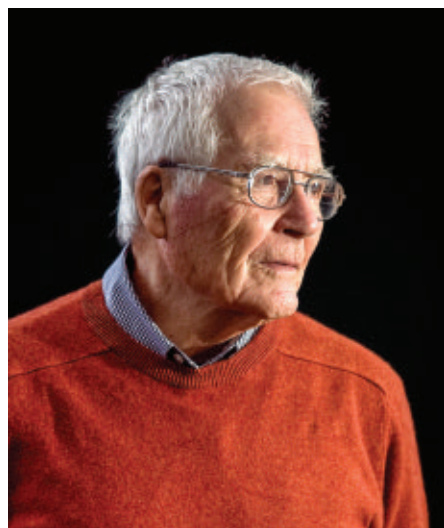
also discovered chlorofluorocarbons everywhere, providing critical evidence that they threatened the ozone layer. Subsequently, Jim realized that dimethyl sulfide produced by marine algae oxidized to form cloud condensation nuclei, that more small water droplets make clouds brighter, and that the resulting cooling of the surface would affect the algae producing dimethyl sulfide. Such linking of biology, chemistry, and physics in feedback loops gave us a new understanding of Earth as a dynamic system.

Gaia provoked strong reactions, particularly after Jim's popular first book on the subject in 1979. Evolutionary biologists argued either that global regulation required consciousness or that natural selection could never produce it. In response, Jim in-

vented "Daisyworld," a model parable that demonstrated how feedbacks involving life could give rise to automatic climate regulation at a planetary scale. It also showed that when regulation breaks down, it does so catastrophically. Daisyworld influenced a generation of climate modelers and informed Jim's follow-up book, *The Ages of Gaia*, which gave a new view of Earth history as a series of distinct regulatory regimes interspersed by periods of turmoil.

In 1992, at age 18, I wrote to Jim to answer his call for "practitioners of planetary medicine." He had the humility to invite me to visit his home and laboratory at Coombe Mill, where we walked the grounds at his signature breakneck speed. I marveled at his laboratory in a converted barn, which upstairs housed the homemade dilution chamber he used to calibrate his instruments. Jim became my mentor, unofficial supervisor, and close friend. His wicked sense of humor was always testing people's limits. On one memorable visit to the lab, he opened an old ice cream tub to reveal an orange puttylike substance, asking me what I thought it was. "Plasticene?" I ventured. "Semtex!" he replied. Jim was regularly employed by the UK Ministry of Defence, in this case to improve methods of sniffing out explosives. He was proud to have worked with explosives like Semtex throughout his life and still be in possession of his fingers, a tribute to his care in the lab, despite a professed loathing for "health and safety."

Jim had an amazing intuition for how things worked, often arriving at a working solution or invention without knowing how he got there. He was also an incredibly creative thinker who could make connections that no one else saw. Although wonderfully generous to his friends, Jim took a dim view of humanity's collective potential, writing, "I would sooner expect a goat to succeed as a gardener as expect humans to become stewards of the Earth." After sparking the environmental movement, Jim warned of the existential risk of climate change in his book *The Revenge of Gaia*. In recognition of his services to global environmental science, he was made a Companion of Honour in 2003.

The world has lost a genius and iconoclast of immense intellectual courage. Never afraid to lambast the establishment and challenge convention, Jim Lovelock transformed our view of the world, started the new field of Earth system science, and inspired generations of researchers. As we are confronted by complexity and volatility, from the pandemic to climate extremes, we need his unique perspective now more than ever before. ∎

PRIVACY

Policy impacts of statistical uncertainty and privacy

Funding formula reform may help address unequal impacts of uncertainty from data error and privacy protections

By **Ryan Steed,**[1] **Terrance Liu,**[2] **Zhiwei Steven Wu,**[2] **Alessandro Acquisti**[1]

Differential privacy (*1*) is an increasingly popular tool for preserving individuals' privacy by adding statistical uncertainty when sharing sensitive data. Its introduction into US Census Bureau operations (*2*), however, has been controversial. Scholars, politicians, and activists have raised concerns about the integrity of census-guided democratic processes, from redistricting to voting rights. The debate raises important issues, yet most analyses of trade-offs around differential privacy overlook deeper uncertainties in census data (*3*). To illustrate, we examine how education policies that leverage census data misallocate funding because of statistical uncertainty, comparing the impacts of quantified data error and of a possible differentially private mechanism. We find that misallocations due to our differentially private mechanism occur on the margin of much larger misallocations due to existing data error that particularly disadvantage marginalized groups. But, we also find that policy reforms can reduce the disparate impacts of both data error and privacy mechanisms.

Differential privacy is the cornerstone of the Census Bureau's updated disclosure avoidance system (DAS) (*2*). Designed to rigorously prevent reconstruction, reidentification, and other attacks on personal data, differential privacy formally guarantees that published statistics are not sensitive to the presence or absence of any individual's data by injecting transparently structured statistical uncertainty (noise) (*1*). But even before differential privacy is applied, estimates from the decennial census, surveys such as the American Community Survey (ACS), and other Census Bureau data products used for critical policy decisions already contain many kinds of statistical uncertainty, including sampling, measurement, and other kinds of nonsampling error (*4*). Some amount of those errors is quantified, but numerous forms of error are not (*5*), including some nonresponses, misreporting, collection errors, and even hidden distortions introduced by previous disclosure avoidance measures such as data swapping (*6*). If quantified and unquantified errors alike are not acknowledged and accounted for, policies that rely on census data sources may not distribute the impacts of uncertainty equally.

In 2021, the US federal government appropriated over $16.5 billion in Title I funds (including several special grants not

> "...misallocations due to our differentially private mechanism occur on the margin of much larger misallocations due to existing data error..."

analyzed here) to distribute to over 13,000 local education agencies (LEAs)—typically school districts—using a formula that takes as input census estimates of the number of children and children in poverty. School districts qualify for Title I grants on the basis of the number or share of children in poverty (*7*). However, the formula does not account for deviations in the poverty estimates that could cause misallocations—cases where the funding amount allocated to a school district differs from its entitlement in an imaginary (*3*), noise-free world.

Researchers have recognized Title I as an important case study of policy-relevant privacy-utility trade-offs (*8*), including misallocation after noise injection for differential privacy (*9*). We extend this work by comparing the policy impacts of noise injected for privacy to the impacts of existing statistical uncertainty, contextualizing preliminary error analyses by Census Bureau scientists (*2*). Our results empirically investigate analytical predictions and proposals from previous work on statistical estimation and federal funding formulas (*10–12*).

We focus specifically on the way Title I implicitly concentrates the negative impacts of statistical uncertainty on marginalized groups. Weakening privacy protection will do little to help the most vulnerable—for these communities, participating in a census survey can be especially risky, despite the benefits of voting rights protection and school funding. Historically, abuse of census data facilitated internment of Japanese Americans and other injustices (*3*). Today, a parent with a restrictive lease may not mention their children to a census worker because they fear being kicked out by their landlord if their responses are reidentified (*13*).

SIMULATING NOISE IN TITLE I ALLOCATIONS

Prior work on differential privacy in the context of Title I is purely analytical, analyzes abstracted components of funding formulas, or focuses only on basic grants (*8*, *9*). By contrast, we fully replicate the Title I provisions for allocating more than $11.6 billion in basic, targeted, and concentration grants using the same data sources and procedures as the Department of Education, which is responsible for calculating the official Title I grant amounts each year (*7*). We measure the impact of data and privacy deviations on the 2021 allocations to 13,190 LEAs across the United States. The primary data input is the Census Small Area Income and Poverty Estimates (SAIPE) from 2019—a table of counts of total population, children, and children in poverty in school districts from all 50 states (excluding Puerto Rico and other territories) that incorporates weighted survey estimates from the ACS [see supplementary materials (SM) section 2 for details].

In a given year, the SAIPE may vary due to several sources of error, including relative error in the county-level estimate, error from other data sources used (e.g., tax data), and errors from raking and recombination methods used to convert county estimates to school district estimates (*4*). To simulate the effects of these "data deviations"—quantified data errors (*14*)—we generate alternative poverty estimates for each school district from a normal distribution around the published estimate of children in poverty in that district from the 2019 SAIPE, following prior work and Census Bureau guidance (*4*) (SM section 2).

We then add "privacy deviations"—noise deliberately injected to achieve differential privacy. The Census Bureau has not yet an-

[1]Heinz College of Information Systems and Public Policy, Carnegie Mellon University, Pittsburgh, PA, USA. [2]School of Computer Science, Carnegie Mellon University, Pittsburgh, PA, USA. Email: ryansteed@cmu.edu

nounced any concrete plans for updated disclosure avoidance in the ACS, and the SAIPE currently does not inject noise for privacy on top of its inputs. To illustrate how privacy deviations might affect these and similar products, and to guide policymakers as the Census Bureau develops new disclosure avoidance measures, we follow prior work (8, 9) in applying the Laplace mechanism, a commonly used noise-injection procedure that is provably differentially private (1). Our hypothetical mechanism does not include the complex postprocessing applied to the discrete Gaussian mechanism used in the decennial census; we only round negative numbers to zero (2).

The strength of differential privacy (described by the parameter ε) determines the magnitude of privacy deviations (lower ε implies stronger privacy and generally more noise). ε measures how much an individu-

provision (20 U.S.C. §6332) limits funding losses to between 5 and 15% per year and the "state minimum" provision (20 U.S.C. §6333) sets a formulaic floor on the total amount received by each state. We treat the allocations generated without these provisions as the official formula-based "entitlements" for each district. Later, we compare these entitlements and the real allocations produced with these provisions. For each privacy setting, we compute the misallocation due to deviations by comparing the simulated allocations after deviations to the official entitlements. We repeat this procedure 1000 times, drawing new data and privacy deviations in each trial. Our metric of group-weighted misallocation describes the expected misallocation borne by the average formula-eligible child in a given group nationwide, assuming that misallocation to a district is borne equally by all its eligible students.

ginal impact is small because—as in the 2020 Decennial Census (2)—the magnitude of privacy deviations is comparable to the magnitude of data deviations only in the least populous districts, even at a relatively strong privacy setting (ε = 0.1) (SM section 7).

These costs are geographically asymmetrical. Certain population-sparse school districts, especially in the Northwest, benefit greatly on average from data deviations (fig. S3a)—their small sample sizes induce proportionally larger data deviations, and, because of their low absolute numbers of children in poverty (though poverty rates may still be high), they have more room to gain funding than to lose funding. Then, because the federal appropriation is fixed and allocations are zero sum, more populous districts, especially in the Southeast, pay for that proportional increase in funding with a small "tax" (9). Less populous districts gain even more as they qualify for new grants (10) (fig. S4). Notably, although less populous, usually rural districts gain funding on average from data deviations, their allocations are more volatile (9) (fig. S7).

When we add privacy deviations (for relatively strong privacy, ε = 0.1), gains by small districts are even more exaggerated (fig. S3b). Unlike data deviations, where the absolute variance increases with population size, our privacy deviations have the same variance in every district, exceeding data deviations in magnitude only in the least populous districts. Still, the marginal increase in cost to districts due to privacy deviations is much less than the base-level misallocations resulting from data deviations, and the marginal change reduces total misallocation about half the time.

DIVERSION FROM MARGINALIZED GROUPS

Owing to Title I's distribution of quantified data deviations alone, Black students and Asian students can expect to lose around $5 and $8 per eligible student, respectively, whereas white students gain over $2 per eligible child on average (see the second figure). (The average district receives $1120 per eligible student.) Likewise, school districts with large Cuban, Puerto Rican, and other Hispanic communities expect to lose funding (between $3 and $14 per eligible student), whereas non-Hispanic districts gain (fig. S9). For a child in a particular district in an unlucky year, the disparity may be worse. Whether a demographic group loses funding depends on whether its members tend to live in high- or low- poverty districts. Often, this happens because the poverty rate in the group itself is high. Groups that tend to live in denser, usually urban districts with more children in poverty lose

Expected lost entitlements due to data error and privacy protections

Out of a total of $11.7 billion in Title I basic, concentration, and targeted grants in 2021, we show expected sum of lost entitlements over 1000 trials due to quantifiable data error alone ("data deviations"; blue), and with the addition of noise injected for privacy ("privacy deviations"; blue plus red). Noise is injected with the ε-differentially private Laplace mechanism. The margins of error at 99% confidence are too small to be depicted—less than $4 million for all three bars. Note that for ε = 1.0, the additional funding loss due to privacy deviations falls within the 90% margin of error for the impact of data deviations alone.

Loss due to quantifiable data error
$1.06 billion

Additional loss due to noise injected for privacy (less noise, ε = 1.0)
$771 thousand

Additional loss due to noise injected for privacy (more noise, ε = 0.1)
$50 million

11.7   10   8   6   4   2   0
2021 Total funding for Title I grants ($ billions)
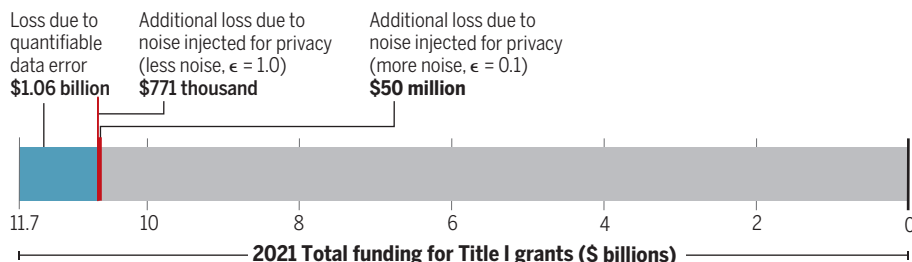
al's decision to respond to a census survey increases their risk of unwanted disclosure. It is not yet clear whether or how privacy deviations would be added to a statistical product like the SAIPE in practice, and because the SAIPE incorporates weighted survey estimates from the ACS, its sensitivity to changes in an individual's response is unclear. Instead, we try several reasonable privacy settings to provide an upper bound on the magnitude of privacy deviations that might be added in practice (8) (SM section 2). We focus on ε = 0.1 and ε = 1 (SM section 7 additionally varies ε from 0.001 to 10). Previous work on Title I (8) suggests ε ≥ 2.52; many applications use similarly high values (2), whereas differential privacy advocates often prefer ε < 1.

The Title I legislation includes two post-formula provisions to achieve secondary policy goals. The "hold harmless"

SUBSTANTIAL MISALLOCATIONS
Of the roughly $11.7 billion distributed nation-wide in 2021, districts in our simulation expect to lose a total of $1.06 billion (summing all losses in each simulation, then averaging summed losses across 1000 simulations; SD = $0.04 billion) in entitlements to other districts due to the Title I formula's handling of existing (before differential privacy) data deviations alone (see the first figure). The standard deviation in misallocation (computed by averaging over 1000 trials) is about $835,000 (the average district receives around $880,000)—$237 per student. When we add privacy deviations (for a relatively strong privacy setting ε = 0.1), the expected total entitlement loss only increases by $50 million (4.7%; marginal SD = $2.9 million). For a less strong privacy setting (smaller privacy deviations; ε = 1), the increase is negligible. The mar-

out, whereas groups that live in sparse, often rural districts with fewer children in poverty (though the rate of poverty may be higher) gain. Geographically concentrated groups—such as tribal nations or racial subgroups (SM section 4)—experience more volatility in outcomes across trials, which depend on the population density and poverty rates where they live.

In a relatively strong privacy setting (ϵ = 0.1), our differential privacy mechanism aggravates these disparities, especially for Black students, who lose more than twice as much funding on average after noise is injected—possibly because Black students are more likely to attend populous school districts where the costs of privacy deviations accumulate. But in less strong privacy settings ($\epsilon \geq 1$), disparities change very little from the status quo when privacy deviations are added (SM section 7).

To assess the impacts on noncategorical demographics, we also fit a generalized additive model (GAM) to the school district-level combined misallocations (ϵ = 0.1) using district population characteristics: population density, median household income, proportion white, proportion Hispanic, proportion renter-occupied housing, and racial homogeneity (the Herfindahl-Hirschman index). Fitting the GAM on a sample of 100 trials, we find that districts with a median income between approximately $25,000 and $75,000 (about 56% of districts) can expect to lose out because of deviations, whereas most other districts gain (fig. S6). The 40% most population-dense districts can also expect to lose funding. Conversely, districts that are less than 5% Hispanic tend to benefit from data and privacy deviations.

SIMPLE REFORMS

Simple changes to the formula—including additional provisions currently required by law—can alleviate or aggravate disparities. For example, adding the hold harmless provision reduces the standard deviation in misallocation (relative to the formula entitlement) but drastically increases disparities in outcomes for racial minorities (see the second figure). Hold harmless prevents small districts from losing funding to data or privacy deviations, thereby increasing the tax on more populous districts and their non-white residents. The state minimum provision has a similar but smaller effect. Typically received by low population states, the state minimum slightly increases the amount of grants to low population districts, exacerbating disparities.

This result illustrates a tension in evidence-based formula funding: Because estimates for less populous geographies have higher variance in both privacy and data deviations relative to their populations and entitlements, measures that overwhelmingly benefit those small areas burden larger areas.

We tested proposed policy changes that could alleviate this tension (SM section 6). We find that using multiyear averages with windows of increasing size decreases both overall misallocation and outcome disparities compared to when we use the averaged poverty estimates as a baseline (figs. S14 and S15). In general, using an average diminishes both data deviations and the privacy deviations required to achieve differential privacy, limiting both increases in expected funding for less populous districts and alleviating worst-case outcomes. Averaging may even be just as effective at stabilizing funding year to year as the hold harmless provision (10). We also tested requiring repeated years of ineligibility before disqualifying districts from funding, which did not change overall misallocation—likely because it permits more marginally wealthy districts to receive funding—but did reduce disparities (figs. S14 and S15).

Expected misallocation by racial group

Expected misallocation borne by the average formula-eligible child in a given census group nationwide is shown (assuming each child in a district is affected by misallocation equally). Specifically, bars depict the nationwide sum of each district's misallocation multiplied by the proportion of respondents of a given census single race category in that district, divided by the total nationwide number of eligible children of that race (SM section 2). Averaged over 1000 trials. The colored bars indicate the race-weighted misallocation due to data deviations (data error) alone, with an error bar spanning a 90% normal confidence interval for this quantity. The additional impact of privacy deviations is significantly different ($P < 0.01$) for all groups, according to a two-sample z-test.

Census race category:

Tribal grouping, White, Pacific islander, Two or more races, Asian, Black or African American, Some other race

Data deviations alone
- Funding formula only (baseline)
- "State minimum": post-formula provision that sets a floor on the total amount received by each state
- "Hold harmless": post-formula provision that limits funding losses to between 5 and 15% per year
- Both "state minimum" and "hold harmless" provisions

Data deviations + privacy deviations
- ϵ = 0.1

Race-weighted misallocation per eligible child ($)

PAYING FOR (PRIVATE) DATA

Simple policy changes can alleviate disparities in the impact of statistical uncertainty, but precisely targeted funding formulas will still have costs. Policy-makers could ensure that no school district expects to lose money because of the underlying data deviations quantified in our simulation by assigning just $107 million (SD = $31 million) in targeted payments to individual districts that lose funding on average across 1000 simulations. The cost of stronger privacy (using our simplified mechanism) could be much less: To compensate districts for only the expected additional lost funding due to privacy deviations, policy-makers need only distribute an extra $41 million (SD = $3.8 million) for stronger privacy ($\epsilon = 0.1$), or $1.7 million (SD = $601,000) for less added privacy ($\epsilon = 1$) (SM section 7). Still, a district's actual loss in any given year often greatly exceeds its expected loss, especially for less populous districts. To compensate districts for both data and privacy deviations in all but the worst 5% of our simulations, an additional $4.7 billion would be needed in the stronger privacy setting ($\epsilon = 0.1$). The cost is greater if policy-makers wish to also compensate for the many other forms of error not quantified here, or for a stronger privacy mechanism.

It may be difficult to justify or legislate funding increases to just the districts expected to lose funding. Simply increasing the total federal appropriation to Title I (benefiting all districts unequally) by $135 million (the combined total expected loss) would only compensate for about half of expected losses. However, a $4.7 billion increase (95% loss coverage) would compensate for nearly all total expected losses and cut total 5% quantile misallocation roughly in half. The White House's proposed 2022 allocation—a $20 billion increase, since reduced to $1 billion in Congress—would completely compensate for privacy and data deviations incurred under the 2019 budget, but inequalities would remain. An overall budget increase would provide "no-penalty" compensation (9) for data and privacy deviations but would not solve issues of relative equity (though budget increases do reduce the number of held harmless districts).

UNCERTAINTY-AWARE POLICY DESIGN

The addition of noise for differential privacy exposes epistemic issues with formula design predicted by early work on census-guided federal funding even before differential privacy was first proposed (3, 10–12). Indeed, our results suggest that the impacts of differential privacy relative to other sources of error in census data could be minimal. But current legislation holds few allowances for the impacts of statistical uncertainty. Use of census data for the Title I formula is mandated "unless the Secretary and the Secretary of Commerce determine that some or all of those data are unreliable or … otherwise inappropriate" (20 U.S.C. §6333). National Research Council studies, commissioned by the Department of Education before ACS estimates were first incorporated in the SAIPE after 2005, warned against hard thresholds and hold harmless provisions (11, 12)—but these provisions are still in effect. Recently, the Biden administration proposed a new Title I budget that includes funding to improve the poverty estimates—but there are still no measures to update the formula to

> ## "…policy reforms can reduce the…impact of both data error and privacy mechanisms."

handle uncertain inputs. Simply acknowledging the effects of data error could improve future policy design for both formula funding and disclosure avoidance.

Our findings come with limitations. Injected noise is just the tip of the iceberg: Many other unquantified forms of statistical uncertainty—including previous disclosure avoidance methods—affect poverty estimates in different ways (5). No confidentiality measures are directly applied to the SAIPE, but its inputs (mainly ACS and IRS data) may have hidden or unintended distortions due to swapping and other ad hoc disclosure avoidance techniques (6). By replacing other methods of disclosure avoidance, differential privacy could even reduce the amount of overall misallocation due to uncertainty. Lacking an alternative source of poverty data, we do not assess the impacts of systematic biases, including undercounts of marginalized groups. Our analysis of the Title I allocation process also leaves out several elements that could affect the applicability of our findings to the real-world distribution of funds, including small-district appeals (20 U.S.C. §6333) and district-level heterogeneity in use of funds. Temporal trends in funding, in combination with provisions like hold harmless, could compound the effects of deviations (10).

Data error—from undercounts to sampling error to noise injection—will always affect evidence-based policy to some degree. In 2017, 316 federal spending programs relied on US census data to distribute over $1.5 trillion in federal funding across states, cities, and school districts (15). Uncertainty in census data—including intentionally added error for privacy—will incur costs for stakeholders in those programs. But at least the quantifiable portion of those costs can be mitigated with uncertainty-aware policy design and budget increases—an avenue for compromise between targeted policy, equity, and also additional privacy. ∎

REFERENCES AND NOTES

1. C. Dwork, F. McSherry, K. Nissim, A. Smith, "Calibrating Noise to Sensitivity in Private Data Analysis" in *Theory of Cryptography*, S. Halevi, T. Rabin, Eds., Lecture Notes in Computer Science (Springer, 2006), pp. 265–284.
2. J. Abowd *et al.*, The 2020 Census Disclosure Avoidance System TopDown Algorithm, *Harvard Data Science Review* (2022).
3. d. boyd, J. Sarathy, Differential Perspectives: Epistemic Disconnects Surrounding the U.S. Census Bureau's Use of Differential Privacy, *Harvard Data Science Review* (2022).
4. US Census Bureau, Quantifying Relative Error in the School District Estimates (2020).
5. R. M. Groves, L. Lyberg, *Public Opin. Q.* **74**, 849 (2010).
6. M. Christ, S. Radway, S. M. Bellovin, Differential Privacy and Swapping: Examining De-Identification's Impact on Minority Representation and Privacy Preservation in the U.S. Census, *2022 IEEE Symposium on Security and Privacy (SP)* (IEEE Computer Society, 2022), pp. 1564–1564.
7. T. Snyder, R. Dinkes, W. Sonnenberg, S. Cornman, Study of the Title I, Part A Grant Program Mathematical Formulas, *Statistical Analysis Report 2019-016*, US Department of Education (2019).
8. J. M. Abowd, I. M. Schmutte, *Am. Econ. Rev.* **109**, 171 (2019).
9. D. Pujol *et al.*, Fair decision making using privacy-protected data, FAT* 2020 - Proceedings of the 2020 Conference on Fairness, Accountability, and Transparency (Association for Computing Machinery, 2020), pp. 189–199.
10. A. M. Zaslavsky, A. L. Schirm, *J. Off. Stat.* **18**, 371 (2002).
11. National Research Council, *Small-Area Income and Poverty Estimates: Priorities for 2000 and Beyond* (National Academies Press, 2000).
12. National Research Council, *Statistical Issues in Allocating Funds by Formula* (National Academies Press, 2003).
13. Panel Discussion on Key Privacy Issues, Privacy and Census Participation, *2020 Census Data Products: Data Needs and Privacy Considerations: Proceedings of a Workshop*, D. L. Cork, C. F. Citro, N. J. Kirkendall, Eds. (The National Academies Press, 2020), pp. 129–133.
14. B. D. Spencer, *J. Am. Stat. Assoc.* **80**, 815 (1985).
15. A. Reamer, Comprehensive Accounting of Census-Guided Federal Spending (FY2017), *Brief 7A*, George Washington Institute of Public Policy (2020).

BOOKS *et al.*

A visitor observes a robot writing a Bible in Lutherstadt Wittenberg, Germany, in 2017.

ARTIFICIAL INTELLIGENCE

The new storytellers

Computer-crafted tales offer insight into human creativity

By **Stephanie Dick**

Storytelling is an essential feature of the human condition, propose Mike Sharples and Rafael Pérez y Pérez in *Story Machines*. It allows us to make meaning in the world and in our lives, to communicate with one another, to teach, to learn, and to explore. The book, which provides a readable, engaging, and instructive introduction to the mechanisms according to which computers have been made to produce "stories," also confronts more fundamental questions: What constitutes our own creativity? Can stories do their cultural work without connecting a reader to a human writer? If computers cannot understand, appreciate, or intend the meaning of their compositions, does that limit their creative potential and the work they might do?

The landscape of artificial intelligence (AI) literature so often tends toward overconfidence, even hubris, but Sharples and Pérez y Pérez, refreshingly, do not claim to answer these questions in the book, although they remain at the heart of the project, nor do the pair pronounce what the future will or should be for computerized

The reviewer is at the School of Communication, Simon Fraser University, Burnaby, BC V5A 1S6, Canada. Email: stephanie_dick@sfu.ca

writing. The authors are as interested in what can be learned about people as storytellers and meaning-makers as they are in the automation of literary composition.

The book begins with an engaging survey of historical, cognitive, and cultural perspectives on human storytelling and a discussion of the long tradition of attempts to automate the production of compelling stories. Readers are then taken through a detailed exploration of the main approaches to AI-driven story production, which doubles as an accessible introduction to different approaches to AI in general.

We meet researchers who have sought to identify a set of rules, or grammars, informed by both linguistics and the formal study of myths, fairy tales, and novels, that could be translated into computer programs. As with most other domains of AI research that seek to convincingly simulate complex human behavior according to a set of rules in this fashion, the stories produced by rule-bound generators tend to be disappointing.

The authors then introduce more-advanced strategies, such as neural networks, which are trained on massive datasets (in this case, of existing stories and prose). Such approaches—which empower

algorithms to generate their own protocols on the basis of patterns and correlations they identify in the data, allowing for predictions about how to construct effective sentences, plots, characters, and structures—can produce far more compelling stories, but they often come at the cost of our access and understanding.

For Sharples and Pérez y Pérez, the goal of automation is not just to find any means to produce compelling computer story generation; they seek automated tools that can report on themselves, thereby facilitating a refined understanding of human creativity. This, they believe, could allow for new forms of storytelling, creative collaboration, and readership. The authors praise methods of story automation that are based on both active models of human creativity and the construction of what they call "story worlds," which consist of places, characters, and constraints that a computer might explore and tell stories within and about.

One of the most valuable features of the book is its rich presentation of examples. Readers come away having read nearly 100 instances of mechanically and computationally generated stories, which provide a clear sense of the variety of approaches and the kind of story they produce. Readers are even invited at several moments to experiment with these methods themselves. The authors also integrate computer-generated prose into the book's text, which serves as a frequent reminder that the act of reading may shift and transform as automation and authorship converge in different ways.

Story Machines
Mike Sharples and Rafael Pérez y Pérez
Routledge, 2022.
194 pp.

The book largely frames automated storytelling as a benign, creative, intellectual, and exciting field. However, it also hints at darker and deeply concerning possibilities. The authors mention believable computer generation of fake news stories, targeted custom narrative production that could infiltrate our internet browsing, fabricated texts made to convincingly read like those written by specific people, and many other potentially exploitative and extractive applications. Indeed, the most powerful tools for automated story production described in the book have been developed by entities such as Microsoft's OpenAI and Facebook, which have a reputation for prioritizing power, control, and profit over all else. The main drawback of the book is that it attends only in passing, and almost hesitantly, to these realities. ■

10.1126/science.adc9237

PHOTO: DPA PICTURE ALLIANCE/ALAMY STOCK PHOTO

When utility providers fall short

Pacific Gas and Electric's abysmal track record highlights the company's failings and our own

By **Gretchen Bakke**

Pacific Gas and Electric (PG&E) is no one's favorite utility provider. Failures of the company's electrical equipment have been implicated in fire after fire in Northern California. Its gas network, meanwhile, caused an explosion that destroyed a full block of a suburban San Francisco neighborhood in 2010. PG&E is perhaps best known, however, for its role in the fire that wiped the town of Paradise, California, from the map in 2018. In addition to causing tremendous property damage, that fire killed 85 people, the vast majority of whom were found dead in their homes or in cars, trapped by the fast-moving, wind-whipped flames that engulfed the valley.

Katherine Blunt starts her copiously researched account of PG&E's checkered history here, at the moment a century-old hook on a remote transmission line failed, dropping the line to the ground and igniting what would become known as the Camp Fire. The deadliest fire in California history, the Camp Fire was neither the first nor the last to be sparked by PG&E, a utility company with such a poor track record that only a careful excavation such as Blunt's can chart the thin course between wrongdoing, simple incompetence, poor governance, and bad luck.

PG&E—like every other utility provider—has never existed in a vacuum; it has been swayed by American cultural values from the start. Blunt introduces readers to these values via a long list of mustachioed and variously quaffed characters across the centuries—men whose visions for the company (or against it) pushed and pulled PG&E through California as it grew from a gold-rush frontier to the drought-riven, climate-concerned global economic actor it is today. It was a rollicking century to be sure, one about which PG&E has managed to lose a truly momentous number of technical records while becoming mired in even more scandals than Blunt details (*1*).

PG&E's service territory covers about 70,000 square miles, home to some of the richest people in America and to some of the country's wildest remaining lands—the Sierras, the Pacific coast, grasslands, and (today) thousands of acres of bone-dry forests. By one estimation, to effectively control wildfires, PG&E would not only need to upgrade all its rural electrical infrastructure but also regularly trim more than 8 million trees "in strike distance" of its lines. This work is both expensive and thankless; trees never stop growing, and a lot of the company's infrastructure is very old.

Should such a company—especially one whose equipment sparks as a part of its normal operations, because all electrical systems do spark and short and fail occasionally—even exist in the tinderbox that is Northern California today? This question stands at the heart of Blunt's book and plagues PG&E's current leadership. And it is masked by another: Could any company provide such services while also meeting expectations for uninterrupted energy supply, delivering promised returns to investors, and repaying fire and gas explosion victims, all while using renewables such as wind and solar to produce more than 30% of its electricity? Seemingly not, except that both of California's other investor-owned utilities,

California Burning
Katherine Blunt
Portfolio, 2022. 368 pp.

Southern California Edison and San Diego Gas and Electric, have a much better, if still imperfect, track record.

Blunt argues that PG&E is a failed company that nevertheless remains a major energy provider because no one—not the courts, not regulators, not legislators, not consultants, not the company's serially replaced CEOs, and not fire victims or their lawyers—has come up with a better way to provide reliable electricity and gas to 4.8 million residential customers. As PG&E roils from bankruptcy proceeding to bankruptcy proceeding, as it is convicted (twice) of willfully disregarding safety regulations that have led to the deaths of a hundred people and destroyed the homes and livelihoods of thousands of others, Blunt asks an even bigger question: If a corporation is a person in the eyes of the law, what does the death penalty look like for such an entity?

Blunt's story is not only a tale of the mostly undeserved second chances granted to PG&E but also of the failings of California's politicians, regulators, and judiciary to mandate a new route forward that prioritizes the safe and reliable provision of energy. There are better solutions available than the ones PG&E is offering. That we continue turning to PG&E again and again to provide what the company has proven it cannot is a failing that falls on us. ∎

REFERENCES AND NOTES

1. PG&E remains in defiance of a 20th-century Supreme Court judgment related to the use of the Hetch Hetchy dam.

10.1126/science.add4661

The reviewer is a senior fellow at the Institute for Advanced Sustainability Studies, 14467 Potsdam, Germany, and is at the Max Planck Institute for the History of Science, 14195 Berlin, Germany. Email: gretchen.bakke@iass-potsdam.de

---

PODCAST

The Blue Revolution: Hunting, Harvesting, and Farming Seafood in the Information Age
Nicholas P. Sullivan
Island Press, 2022. 272 pp.

Large-scale commercial fishing has depleted fish stocks around the world, but new technologies are increasingly being deployed to improve the efficiency and sustainability of this enterprise. This week on the *Science* podcast, Nicholas Sullivan unpacks the current state of fishing, explores the promise of aquaculture and fish farming, and discusses the future of seafood.
https://bit.ly/3Q8lcBq

A vendor sells crabs in an open-air market in Washington, DC.

10.1126/science.ade2202

Workers sort plastic waste at Yongin Recycling Center in Yongin, South Korea, during the COVID-19 pandemic.

Edited by **Jennifer Sills**

Paths to sustainable plastic waste recycling

The outbreak of COVID-19 has driven increased use of medical personal protective equipment, packaged take-out meals, and home-delivered groceries, exacerbating the accumulation of waste plastics (1, 2). The adoption of inappropriate management strategies such as local burning, incineration, and landfilling has also increased, leading to the leakage of waste plastics into the environment and hindering the mitigation of micro- and nanoplastics (3). Approximately 6% of the world's annual oil production is devoted to plastics, and 850 million metric tons of greenhouse gases was associated with new plastics production and incineration of waste plastics in 2019, which is equivalent to the annual emissions from 189 500-megawatt coal-fired power plants (4, 5). In the face of these challenges, it is imperative to develop strategies to recycle waste plastics more sustainably.

Some national and regional governments are taking action toward this goal. The European Commission has marked plastic recycling as a key priority for the new Circular Economy Action Plan and is planning to introduce a range of quotas for minimum recycled content in new plastic products (6). Some states in the United States have proposed minimum recycled content mandates to end plastic pollution. For example, California has required thermoform plastic containers to contain no less than 20% or 30% (depending on the recycling rate) postconsumer recycled plastic by 2030 (7). These efforts will help mitigate plastic pollution.

Coordinated global actions are also needed. In June, a United Nations Environment Assembly working group began planning for the development of an international legally binding instrument, which 175 nations committed to completing by the end of 2024, to shift away from single-use plastics and ensure the achievement of the UN Sustainable Development Goals (8). The treaty should include recycling standards of practice and require commitments to implement them.

Joint development efforts should work toward technologies that can recycle waste plastics [e.g., (9, 10)]. Designing catalytic processes to recover plastic monomers or valuable alkane products from waste plastic could potentially close the plastic use loop and bring a new and profitable branch to the plastic recycling industry (11, 12). Collective efforts to recycle plastic waste could substantially contribute to achieving an economy with net-zero greenhouse gas emissions by 2050 and limiting global warming to less than 1.5°C by 2100.

Leilei Dai[1], Roger Ruan[1]*, Siming You[2], Hanwu Lei[3]

[1]University of Minnesota, Saint Paul, MN 55108, USA. [2]University of Glasgow, Glasgow, UK. [3]Washington State University, Richland, WA 99354, USA.
*Corresponding author. Email: ruanx001@umn.edu

REFERENCES AND NOTES

1. J. Prata *et al.*, *Environ. Sci. Technol.* **54**, 7760 (2020).
2. S. Bengali, "The COVID-19 pandemic is unleashing a tidal wave of plastic waste," *Los Angeles Times* (2020).
3. M. Shams *et al.*, *Environ. Adv.* **5**, 100119 (2021).
4. The Ellen MacArthur Foundation, "The new plastics economy: Rethinking the future of plastics" (2016); https://ellenmacarthurfoundation.org/the-new-plastics-economy-rethinking-the-future-of-plastics.
5. Center for International Environmental Law, "Plastic & climate: The hidden costs of a plastic planet" (2019); www.ciel.org/wp-content/uploads/2019/05/Plastic-and-Climate-FINAL-2019.pdf.
6. European Commission, "New Circular Economy Action Plan for a cleaner and more competitive Europe" (2020); www.eumonitor.eu/9353000/1/j9vvik7m1c3gyxp/vl6vh7khf4n9.
7. California Legislative Information, "AB-478 solid waste: Thermoform plastic containers: Postconsumer thermoform recycled plastic: Commingled rates" (2021); https://leginfo.legislature.ca.gov/faces/billNavClient.xhtml?bill_id=202120220AB478.
8. United Nations Environment Assembly, "Ad hoc Open-ended Working Group to Prepare for the Intergovernmental Negotiating Committee to End Plastic Pollution" (2022); https://enb.iisd.org/working-group-intergovernmental-negotiating-committee-end-plastic-pollution-oewg-inc-summary.
9. L. Dai *et al.*, *Prog. Energ. Combust. Sci.* **93**, 101021 (2022).
10. H. Li *et al.*, "Expanding Plastics Recycling Technologies: Chemical Aspects, Technology Status and Challenges" *ChemRxiv* 10.26434/chemrxiv-2022-9wqz0-v2 (2022).
11. Y. Jing *et al.*, *Angew. Chem. Int. Educ.* **60**, 5527 (2021).
12. X. Wu *et al.*, *J. Am. Chem. Soc.* **144**, 5323 (2022).

10.1126/science.ade2221

News story miscasts Alzheimer's science

As experienced researchers in the Alzheimer's disease field, we have serious concerns about the News story "Blots on a field?" (C. Piller, 22 July, https://scim.ag/3T1evDh). The article summarizes the apparent manipulation of data in a 2006 study (1) and suggests that coauthor Sylvain Lesné committed egregious scientific misconduct when preparing figures supporting a central role for the specific amyloid-β (Aβ) peptide, Aβ*56, in memory loss in mouse models of Alzheimer's disease. Such investigative reporting is important to correct potential

PHOTO: SEONGJOON CHO/BLOOMBERG/GETTY IMAGES

fraud. However, the article overstates and distorts the effect of this paper on the Alzheimer's field.

Lesné's alleged malfeasance does not threaten the "reigning theory" of Alzheimer's pathobiology, known as the "amyloid hypothesis." The tone and content of the News story and the sensationalized media coverage it generated could derail Alzheimer's drug discovery and development based on the amyloid hypothesis, which is supported by a vast body of well-conducted research.

By 2008, 2 years after the Lesné paper, Alzheimer's researchers determined that the findings supporting Aβ*56's role in cognitive decline could not be replicated. Several, including one of us (D.S.), tried (2, 3). Although unaware of malfeasance, the field policed itself by not confirming these findings. Rather than being a "key element" of today's theory supporting the association between Aβ accumulation and cognitive decline, Lesné's "star suspect" rapidly became history as the science of Aβ oligomers moved ahead. Simply put, the 2006 Lesné et al. study had minimal, if any, impact on the evolution of the amyloid hypothesis.

Today, approximately 16% of Alzheimer's drugs in development are predicated on the amyloid hypothesis. Only a few of these directly target Aβ oligomers, and none targets Aβ*56 specifically. No patients have been misled and entered trials based on the Aβ*56 observation. Targeting Aβ-associated neuronal dysfunction represents one of the field's most promising approaches to prevent and treat Alzheimer's disease.

Dennis Selkoe[1]* and Jeffrey Cummings[2]
[1]Ann Romney Center for Neurologic Diseases, Department of Neurology, Brigham and Women's Hospital, Harvard Medical School, Boston, MA 02115, USA. [2]Chambers-Grundy Center for Transformative Neuroscience, Pam Quirk Brain Health and Biomarker Laboratory, Department of Brain Health, School of Integrated Health Sciences, University of Nevada Las Vegas, Las Vegas, NV 89052, USA.
*Corresponding author.
Email: dselkoe@bwh.harvard.edu

REFERENCES AND NOTES
1. S. Lesné et al., Nature **440**, 352 (2006).
2. G. M. Shankar et al., Nat. Med. **14**, 837 (2008).
3. M. B. Rogers, "Sylvain Lesné, who found Aβ*56, accused of image manipulation," Alzforum (2022); www.alzforum.org/news/community-news/sylvain-lesne-who-found-av56-accused-image-manipulation.

Alzheimer's target still viable but untested

In his News story "Blots on a field?" (22 July, https://scim.ag/3T1evDh), C. Piller inaccurately describes my scientific thesis. He implied that my work has misled researchers in the Alzheimer's disease field by encouraging the development of therapies targeting amyloid plaques, which are composed of amyloid beta protein (Aβ). Rather, for more than 20 years, I have consistently expressed concerns that drugs targeting plaques were not likely to be effective.

My published work independent of Lesné (1, 2) indicates that there are two classes of toxic Aβ oligomers based on quaternary protein structure: type 1 and type 2. One particular form of type 1 (referred to in our papers as Aβ*56) is found both within and outside amyloid plaques and was shown by my lab and several others to impair memory function in mice (3–5) and to be associated with memory loss in humans with probable Alzheimer's disease (6). The type 2 form is found encased within amyloid plaques, and thus entrapped it has a limited effect on cognition. It is this form (type 2) that drug developers have repeatedly but unsuccessfully targeted. I am unaware of any clinical trials targeting the type 1 form of Aβ—the form that my research has suggested is more relevant to dementia. Piller seems to conflate these two forms of toxic oligomers.

Piller's story suggests that the pursuit of Aβ-targeted therapies for Alzheimer's disease—which I agree has been frustratingly negative and expensive—was somehow ignited or fueled by the 2006 Nature paper (7). This is not true. Decades of human genetics research and studies of mouse models from many labs had already led drug developers to conclude that Aβ was a plausible target.

In the story, Piller confounds two distinct issues: the frustrations regarding the difficulties of drug development in Alzheimer's disease and a specific allegation of scientific misconduct relating to a set of papers about one particular subset of type 1 Aβ oligomers. To imply that the latter bears a heavy burden of responsibility for the former, as Piller did, condemns potentially fruitful avenues of the Aβ hypothesis.

Having worked for decades to understand the cause of Alzheimer's disease so that better treatments can be found for patients, it is devastating to discover that a co-worker may have misled dozens of coauthors, including me, and the scientific community through the doctoring of images. However, Piller's implication that this development invalidates my work is untrue and unfair.

Karen H. Ashe
Department of Neurology, N. Bud Grossman Center for Memory Research and Care, University of Minnesota Medical School, Minneapolis, MN 55455, USA. Email: hsiao005@umn.edu

REFERENCES AND NOTES
1. P. Liu et al., Cell Rep. **11**, 1760 (2015).
2. K. Ashe, Alzheimer's Dementia **16**, 1561 (2020).
3. I. Cheng et al., J. Biol. Chem. **282**, 23818 (2007).
4. L. Billings et al., J. Neurosci. **27**, 751 (2007).
5. W. Meilandt et al., J. Neurosci. **29**, 1977 (2009).
6. S.-J. Yoo et al., Sci. Rep. **10**, 11234 (2020).
7. S. Lesné et al., Nature **440**, 352 (2006).

10.1126/science.ade4073

Editor's note

We thank Selkoe and Cummings for their supportive words about our investigative reporting, but we disagree with their contention that the suspect work by Sylvain Lesné had minimal impact. The 2006 Nature paper discussed in the Letter—only one of nearly two dozen papers now in doubt—was cited at least 90 times annually as recently as 2021, according to Springer Nature. Over the past 5 years, Cummings and Selkoe continued to cite it and other work by Lesné on the amyloid-β (Aβ) Aβ*56 molecule. The story's assertion that the suspect work may have misdirected other Alzheimer's research was not ours alone; multiple experts in the field told us that it jump-started the search for soluble forms of amyloid-β that might explain neuron death and cognitive decline in Alzheimer's. Those efforts have not yielded any effective therapies to date. As for the broader amyloid hypothesis, to which both authors have devoted decades of effort, it does not depend on Lesné's work, and our story quotes Selkoe to that effect. But the doubts about work that once seemed a milestone in the effort to link amyloid to cognitive decline in Alzheimer's are surely a setback for the field.

Ashe misstates what we said about the influence of her work with Lesné. The idea that Alzheimer's might be treated by targeting amyloid deposits predated their 2006 paper by many years, as the story explains. But that and multiple other suspect papers did fuel the search for specific toxic forms of amyloid and for drugs that could target them, the line of research Ashe continues to pursue. She acknowledges the concerns about image manipulation that our story raises but downplays their importance and assumes no responsibility as Lesné's mentor and senior author of dubious studies.

Tim Appenzeller
News Editor

10.1126/science.ade2733

RESEARCH

IN *SCIENCE* JOURNALS

Edited by
Michael Funk

MATERIALS SCIENCE
An irregular plan

Materials with irregular microstructures are common in the natural world and often have interesting properties. Liu *et al.* devised a growth-inspired program for generating irregular materials from a limited number of basic elements. Using building blocks with arbitrary complexity, the authors stochastically connected them subject to a set of local rules. The results echoed the diversity of natural systems with a large range of functional properties. —BG *Science,* abn1459, this issue p. 975

Artist's conception of an illuminated, three-dimensional building block adding to a growing microstructure

MATERIALS SCIENCE
Carbon-based filter capacitors

Filter capacitors are used in filter circuits to convert alternating current into direct current by smoothing out ripples in the incoming supply. They have been dominated by aluminum electrolytic capacitors and are typically the largest component in an electronic circuit because of their low areal capacitances, thus limiting the potential for miniaturization. Using three-dimensional porous anodic aluminum oxide (AAO) templates, Han *et al.* constructed a network of carbon tubes in which they deposited nickel catalyst nanoparticles and grew vertically aligned carbon nanotubes using chemical vapor deposition. After removal of the AAO, a flexible film was obtained. The films show a 25% improvement in areal capacitance at 120 hertz and can be connected in series without affecting their electrochemical performance. —MSL
Science, abh4380, this issue, p. 1004

AUTOIMMUNITY
Livers beware T and B cells!

Diets high in fat and sugar are known to contribute to chronic inflammation in the liver and subsequent autoimmune reactions, yet the immune responses behind this phenomenon are not well characterized. Studying mice given a high-fat, high-glucose diet, Clement *et al.* identified PDIA3, a protein involved in immunogenic cell death, as a peptide presented by cell surface proteins that led to pathogenic T and B cell responses. PDIA3-specific T cells and PDIA3-specific antibodies were sufficient to induce liver toxicity in mice. Anti-PDIA3 was also detected at high levels in the serum of patients with chronic inflammatory liver conditions, suggesting that this mechanism may also be operative in humans. —DAE
Sci. Immunol. **7**, eabl3795 (2022).

MOLECULAR BIOLOGY
Minimally invasive cancer classification

Molecular characterization of hormone-responsive cancers by mapping tumor-specific transcription factor–binding locations holds promise for tracking the progression of cancers. However, invasive biopsies and labor-intensive chromatin immunoprecipitation and sequencing (ChIP-seq) techniques limit the reach of these approaches. Rao *et al.* developed a minimally invasive methodology that relies on sequencing the cell-free DNA circulating in plasma to generate an accurate map of transcription factor binding in estrogen receptor–positive breast cancer. The authors successfully used this mapping method to classify tumors associated with different types of estrogen receptor expression and mortality. —JHD
Sci. Adv. 10.1126/sciadv.abm4358 (2022).

NEUROSCIENCE
The meaning of rapid eye movement

Sleep includes phases characterized by rapid eye movement (REM) that are known to be associated with dreaming. But are these eye movements related to the contents of consciousness in that sleep state? Senzai and Scanziani recorded head direction cells in the anterior dorsal nucleus of the thalamus in mice during wake and sleep (see the Perspective by De Zeeuw and Canto). The direction and amplitude of eye movements encoded the direction and amplitude of the heading of mice in their virtual environment during REM sleep. It was possible to predict the actual heading in the real and virtual world of the mice during wake and REM sleep, respectively, using saccadic eye movements. —PRS

Science, abp8852, this issue p. 999; see also add8592, p. 919

METASURFACES
Another twist

Metasurfaces are specially designed arrays of dielectric components that transform the function of bulk optical components into thin films. Exploiting the physics of bulk states in the continuum for the highly efficient trapping of light, Santiago-Cruz *et al.* demonstrate metasurfaces that operate as sources of quantum and chiral light, respectively. Patterned in gallium arsenide, the quantum source can provide entangled pairs of
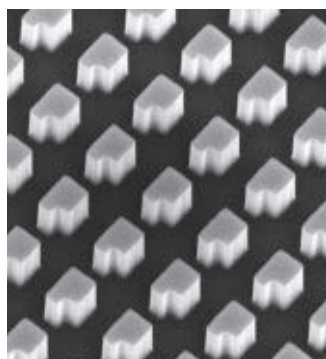
Scanning electron microscope image of a metasurface with an array of symmetry-breaking resonators

photons across a broad range of wavelengths, allowing for the formation of complex quantum states. The authors also used a dielectric metasurface doped with emitting molecules to produce chiral light and lasing. Both approaches will be useful for the development of integrated optical and quantum optical devices. —ISO

Science, abq8684, this issue, p. 991

FAUNAL DECLINE
Depauperate webs

Over the past 50 years, 60% of animal populations have been pushed to extinction. Although already tragic, such losses also have profound impacts on the ecological integrity of biological systems. Fricke *et al.* looked across mammalian communities globally over the past 130,000 years and found that more than half of the links, or connections, within these communities have been lost (see the Perspective by O'Gorman). This loss is due to extinction of species but also to a reduction in the ranges of extant species, because the total numbers of individuals within a species have also declined. Such losses could have profound impact on the long-term persistence and function of ecosystems. —SNV

Science, abn4012, this issue p. 1008; see also add7563, p. 918

SYNTHETIC BIOLOGY
Designer chromosomes

One of the goals in synthetic biology is to generate complex multicellular life with designed DNA sequences. Being able to manipulate DNA at large scales, including at the chromosome level, is an important step toward this goal. So far, chromosome-level genetic engineering has been accomplished only in haploid yeast. By applying gene editing to haploid embryonic stem cells, Wang *et al.* achieved whole-chromosome ligations in mice and successfully derived animals with 19 pairs of chromosomes, one pair fewer than is standard in this species. —DJ

Science, abm1964, this issue p. 967
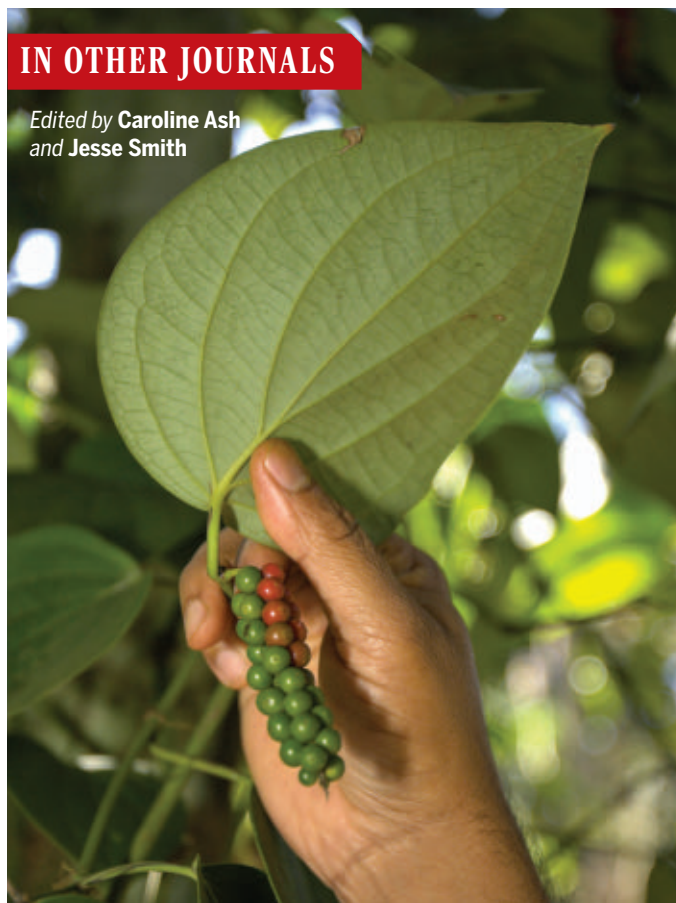
PLANT SCIENCE
Perisperm piperine biosynthesis

The pungent taste of black pepper is due in part to 1-piperoyl piperidine (piperine) in the dried fruits of the *Piper nigrum* plant. Piperine quantity increases as the fruit matures. Jäckel *et al.* show that the final step in piperine biosynthesis takes place in the perisperm, which supports the embryos of the black pepper fruit and is where the relevant enzymes and their products are colocalized. The aromatic flavor compound accumulates in specialized storage cells of the maturing fruit. If not harvested for our dinner tables, more than 95% of piperine remains in the dried seed shell as the young seedling germinates, itself mostly lacking piperine. —PJH   *Plant J.* **111**, 731 (2022).

Black pepper fruits accumulate the aromatic compound piperine as they mature.

CORONAVIRUS
Children protect against severe COVID-19

During the current COVID-19 outbreak, children are less likely than adults to develop severe disease, and the causes for this are obscure. One hypothesis is that early in life, children are exposed to other coronaviruses, which strengthens their immunity to this virus family. Solomon *et al.* show that adults with children are also protected. The authors analyzed data from millions of patients in a health care system and discovered that although adults with children have a higher risk of getting

BIOGEOGRAPHY
Good traits for travel

Species' abilities to establish in new locations depend on traits such as body size, life history, and current distribution. Among reptiles, species that reproduce early and often (i.e., those with a "fast" life history strategy) are more likely to become invasive. Weil *et al.* investigated whether life history strategy and other traits can explain the spread of chameleons, a group of lizards that originated in Africa. Chameleons have dispersed through multiple events to India, Arabia, and Europe. Phylogenetic analyses showed that both fast and slow life histories can be advantageous: Species with extreme life histories were more likely to have moved between regions. Large-bodied and coastal species were also more likely to have spread, especially when these traits were combined with extreme life histories. —BEL   *Ecography* 10.1111/ecog.06323 (2022).

Chameleons dispersed out of Africa to Arabia, Europe, and India.

COVID, they are less likely to develop serious disease. The authors could not obtain direct evidence of preexisting immunity to coronaviruses, but suggest that parents are likely exposed to endemic coronaviruses when their children are young, providing them with partial immunity against COVID-19. —YN

Proc. Natl. Acad. Sci. U.S.A. **119**, e2204141119 (2022).

AGING
Mitigating mitochondrial defects

Mitochondrial DNA mutations accumulate during aging, but the underlying mechanisms remain obscure. Eukaryotic cells contain a mixed complement of mitochondria, some of which may contain deleterious mutations. In the fruit fly, *Drosophila*, Tsai *et al*. found that quality control mechanisms such as purifying selection ensure that deleterious mutations are at a competitive disadvantage. However, with age, purifying selection becomes ineffective. Enhancing quality control, either genetically to enhance purifying selection or pharmacologically using kinetin, mitigated the age-associated increase of mutant

genomes, improved fly vigor, and reduced neural degeneration. Similar pharmacological treatment of aged wild-type mice reversed age-associated accumulation of a mitochondrial DNA deletion mutation. Thus, future therapies designed to modify the progression of mitochondrial disease could allay age-associated degeneration. —SMH

Proc. Natl. Acad. Sci. U.S.A. **119**, e2119009119 (2022).

SCIENCE EDUCATION
A CURE for museum exhibits

Course-based undergraduate research experiences (CUREs) are becoming abundant in undergraduate education. Donegan *et al.* explored what a CURE would look like outside of a classroom. Working with a university museum, and centered on the topic of desert biodiversity, students were given autonomy and access to the museum's biodiversity collections to identify a researchable question that could be explored using relevant data collection tools and analytical approaches. The experience culminated in the development of the

museum exhibit rather than a final exam. Students reported positive shifts in engaging in the implementation and evaluation of museum exhibits and on the relevancy of scientific work and museum education to broad audiences, highlighting the value of museums as a novel avenue for expanding upon the broader relevance of CUREs. —MMc

J. Biol. Educ. 10.1080/ 00219266.2022.2103168 (2022).

BIOMATERIALS
Optimizing the environment for healing

The delivery of growth factors can enhance chronic wound repair, but challenges remain in optimizing growth factor activity over time. Hwang *et al.* developed a hydrogel made of hyaluronic acid and collagen that incorporated electrostatically complexed DNA and polyethylenimine polyplexes using collagen mimetic peptide–based tethers. The authors looked at how changes in the fraction of collagen mimetic peptides enhanced the retention of the polyplexes to enable growth factor delivery over many days and how the

incorporation of hyaluronic acid in the hydrogel created a localized environment that enhanced gene transfection efficiency. —MSL

Acta Biomater. 10.1016/ j.actbio.2022.07.039 (2022).

ORGANIC SYNTHESIS
Anaerobic oxidation of alkenes

Carbonyl compounds can be synthesized from alkenes through aerobic routes such as ozonolysis or with a combination of osmium tetroxide and sodium periodate. Control of stoichiometry, the formation of waste products, and the need for highly oxidizing conditions limit the scope of alkene reactants. Wise *et al*. report an anaerobic route in which the visible light photoexcitation of a nitroarene (4-cyanonitrobenzene) generates pairs of oxygen radicals that undergo nonspecific cycloaddition with the double bonds. A wide variety of alkenes bearing functional groups that would not tolerate oxidizing conditions formed carbonyl compounds through this reaction. —PDS

J. Am. Chem. Soc. 10.1021/ jacs.2c05648 (2022).

PHOTO: DINODIA PHOTO/GETTY IMAGES

ALSO IN *SCIENCE* JOURNALS

Edited by **Michael Funk**

HUMAN GENETICS
Connecting genes and history

Stories about the peopling—and people—of Southern Europe and West Asia have been passed down for thousands of years, and these stories have contributed to our historical understanding of populations. Genomic data provide the opportunity to truly understand these patterns independently from written history. In a trio of papers, Lazaridis *et al.* examined more than 700 ancient genomes from across this region, called the Southern Arc, spanning 11,000 years from the earliest farming cultures to post-Medieval times (see the Perspective by Arbuckle and Schwandt). On the basis of these results, the authors suggest that earlier reliance on modern phenotypes and ancient writings and artistic depictions provided an inaccurate picture of early Indo-Europeans, and they provide a revised history of the complex migrations and population integrations that shaped these cultures. —SNV

Science, abm4247, abq0755, abq0762, this issue p. 939, 940, 982; see also add9059, p. 922

CORONAVIRUS
Pandemic epicenter

As 2019 turned into 2020, a coronavirus spilled over from wild animals into people, sparking what has become one of the best-documented pandemics to afflict humans. However, the origins of the pandemic in December 2019 are controversial. Worobey *et al.* amassed a variety of evidence from the City of Wuhan, China, where the first human infections were reported. These reports confirm that most of the earliest human cases centered around the Huanan Seafood Wholesale Market. Within the market, the data statistically located the earliest human cases to one section where vendors of live

wild animals congregated and where virus-positive environmental samples concentrated. In a related report, Pekar *et al.* found that genomic diversity before February 2020 comprised two distinct viral lineages, A and B, which were the result of at least two separate cross-species transmission events into humans (see the Perspective by Jiang and Wang). The precise events surrounding virus spillover will always be clouded, but all of the circumstantial evidence so far points to more than one zoonotic event occurring in Huanan market in Wuhan, China, likely during November–December 2019. —CA

Science, abp8337, abp8715, this issue p. 951, p. 960; see also add8384, p. 925

NANOPHYSICS
Levitated interactions

The ability to trap macroscopic objects in vacuum, levitating them with optical fields, and cooling them to their motional ground state, provides access to highly sensitive sensors for applications in metrology. Rieser *et al.* demonstrate the trapping of two silica nanoparticles and explore the light-induced dipole-dipole interactions between them (see the Perspective by Pedernales). The results provide a route to developing a fully tunable and scalable platform to study entanglement and topological quantum matter with nanoscale objects. —ISO

Science, abp9941, this issue p. 987; see also add1374, p. 921

OPTICS
Perfecting absorption

The absorption of light is important in many natural processes and device applications. Although absorbing a little bit of light is easy, absorbing all of it is generally difficult to achieve. However, the process of coherent perfect absorption, an interferometric effect,

showed that light of a very specific spatial mode could be perfectly absorbed if it was matched precisely to the properties of a cavity. Slobodkin *et al.* now extend the concept to multimode coherent perfect absorption (see the Perspective by Bertolotti). Using a self-imaging cavity design, the authors demonstrate that complex spatial modes can be absorbed almost perfectly. —ISO

Science, abq8103, this issue p. 995; see also add3039, p. 924

ALZHEIMER'S DISEASE
Determining behavior by following tau

Although some of the symptoms of Alzheimer's disease are conserved among patients, multiple phenotypes exist, including amnestic, visuospatial, language, and behavioral/dysexecutive symptoms. Understanding the mechanisms mediating the different behavioral phenotypes of Alzheimer's disease will help in the development of specific treatments. Therriault *et al.* studied the pattern of tau pathology spreading in multiple cohorts of patients with different phenotypes and showed that each phenotype was associated with a specific connectivity-based pattern of tau aggregation. The results suggest that intrinsic brain connectivity drives tau aggregation patterns, thus determining the behavioral phenotype of the disease. —MM

Sci. Transl. Med. **14**, eabc8693 (2022).

NEUROSCIENCE
Spiraling into neurodegeneration

Activating mutations in the kinase LRRK2 can cause Parkinson's disease (PD). Mutant LRRK2 promotes the processing of amyloid precursor protein (APP) into its transcriptionally active form, the APP intracellular domain. Zhang *et*

al. linked these proteins in a feed-forward cycle. In cultured neurons and brain tissue from mouse models of PD, LRRK2-mediated phosphorylation of APP up-regulated the APP intracellular domain, which then directly mediated *LRRK2* transcription. Pathological markers in LRRK2-mutant PD models were reduced by the APP intracellular domain inhibitor itanapraced, which is currently in trials to treat Alzheimer's disease. —LKF

Sci. Signal. **15**, eabk3411 (2022).

HUMAN GENETICS

The genetic history of the Southern Arc: A bridge between West Asia and Europe

Iosif Lazaridis, Songül Alpaslan-Roodenberg *et al.*

INTRODUCTION: For thousands of years, humans moved across the "Southern Arc," the area bridging Europe through Anatolia with West Asia. We report ancient DNA data from 727 individuals of this region over the past 11,000 years, which we co-analyzed with the published archaeogenetic record to understand the origins of its people. We focused on the Chalcolithic and Bronze Ages about 7000 to 3000 years ago, when Indo-European language speakers first appeared.

RATIONALE: Genetic data are relevant for understanding linguistic evolution because they can identify movement-driven opportunities for language spread. We investigated how the changing ancestral landscape of the Southern Arc, as reflected in DNA, corresponds to the structure inferred by linguistics, which links Anatolian (e.g., Hittite and Luwian) and Indo-European (e.g., Greek, Armenian, Latin, and Sanskrit) languages as twin daughters of a Proto-Indo-Anatolian language.

RESULTS: Steppe pastoralists of the Yamnaya culture initiated a chain of migrations linking Europe in the west to China and India in the East. Some people across the Balkans (about 5000 to 4500 years ago) traced almost all their genes to this expansion. Steppe migrants soon admixed with locals, creating a tapestry of diverse ancestry from which speakers of the Greek, Paleo-Balkan, and Albanian languages arose.

The Yamnaya expansion also crossed the Caucasus, and by about 4000 years ago, Armenia had become an enclave of low but pervasive steppe ancestry in West Asia, where the patrilineal descendants of Yamnaya men, virtually extinct on the steppe, persisted. The Armenian language was born there, related to Indo-European languages of Europe such as Greek by their shared Yamnaya heritage.

Neolithic Anatolians (in modern Turkey) were descended from both local hunter-gatherers and Eastern populations of the Caucasus, Mesopotamia, and the Levant. By about 6500 years ago and thereafter, Anatolians became more genetically homogeneous, a process driven by the flow of Eastern ancestry across the peninsula. Earlier forms of Anatolian and non–Indo-European languages such as Hattic and Hurrian were likely spoken by migrants and locals participating in this great mixture.

Anatolia is remarkable for its lack of steppe ancestry down to the Bronze Age. The ancestry of the Yamnaya was, by contrast, only partly local; half of it was West Asian, from both the Caucasus and the more southern Anatolian-Levantine continuum. Migration into the steppe started by about 7000 years ago, making the later expansion of the Yamnaya into the Caucasus a return to the homeland of about half their ancestors.

CONCLUSION: All ancient Indo-European speakers can be traced back to the Yamnaya culture, whose southward expansions into the Southern Arc left a trace in the DNA of the Bronze Age people of the region. However, the link connecting the Proto-Indo-European–speaking Yamnaya with the speakers of Anatolian languages was in the highlands of West Asia, the ancestral region shared by both. ∎

S **READ THE FULL ARTICLE AT**
https://doi.org/10.1126/science.abm4247

Genetic History of the Southern Arc

1. Around 7000–5000 years ago, people with ancestry from the Caucasus (blue) moved west into Anatolia and north into the steppe. Some of these migrants may have spoken ancestral forms of Anatolian and Indo-European languages.

2. Beginning ~5000 years ago, Yamnaya expansions introduced Eastern European ancestry (red) west into the Balkans and Greece and east across the Caucasus into Armenia. However, they made no detectable impact on Anatolia.

Many partings, many meetings: How migration and admixture drove early language spread. Westward and northward migrations out of the West Asian highlands split the Proto-Indo-Anatolian language into Anatolian and Indo-European branches. Yamnaya pastoralists, formed on the steppe by a fusion of newcomers and locals, admixed again as they expanded far and wide, splitting the Proto-Indo-European language into its daughter languages across Eurasia. Border colors represent the ancestry and locations of five source populations before the migrations (arrows) and mixture (pie charts) documented here.

HUMAN GENETICS

The genetic history of the Southern Arc: A bridge between West Asia and Europe

Iosif Lazaridis[1,2]*†, Songül Alpaslan-Roodenberg[2,3]*†, Ayşe Acar[4], Ayşen Açıkkol[5], Anagnostis Agelarakis[6], Levon Aghikyan[7], Uğur Akyüz[8], Desislava Andreeva[9], Gojko Andrijašević[10], Dragana Antonović[11], Ian Armit[12], Alper Atmaca[13], Pavel Avetisyan[7], Ahmet İhsan Aytek[14], Krum Bacvarov[15], Ruben Badalyan[7], Stefan Bakardzhiev[16], Jacqueline Balen[17], Lorenc Bejko[18], Rebecca Bernardos[2], Andreas Bertsatos[19], Hanifi Biber[20], Ahmet Bilir[21], Mario Bodružić[22], Michelle Bonogofsky[23], Clive Bonsall[24], Dušan Borić[25], Nikola Borovinić[26], Guillermo Bravo Morante[3], Katharina Buttinger[3], Kim Callan[2,27], Francesca Candilio[28], Mario Carić[29], Olivia Cheronet[3], Stefan Chohadzhiev[30], Maria-Eleni Chovalopoulou[19], Stella Chryssoulaki[31], Ion Ciobanu[32,33], Natalija Čondić[34], Mihai Constantinescu[35], Emanuela Cristiani[36], Brendan J. Culleton[37], Elizabeth Curtis[2,27], Jack Davis[38], Tatiana I. Demcenco[39], Valentin Dergachev[40], Zafer Derin[41], Sylvia Deskaj[42], Seda Devejyan[7], Vojislav Djordjević[43], Kellie Sara Duffett Carlson[3], Laurie R. Eccles[44], Nedko Elenski[45], Atilla Engin[46], Nihat Erdoğan[47], Sabiha Erir-Pazarcı[48], Daniel M. Fernandes[3,49], Matthew Ferry[2,27], Suzanne Freilich[3], Alin Frînculeasa[50], Michael L. Galaty[42], Beatriz Gamarra[51,52,53], Boris Gasparyan[7], Bisserka Gaydarska[54], Elif Genç[55], Timur Gültekin[56], Serkan Gündüz[57], Tamás Hajdu[58], Volker Heyd[59], Suren Hobosyan[7], Nelli Hovhannisyan[60], Iliya Iliev[16], Lora Iliev[2,27], Stanislav Iliev[61], İlkay İvgin[62], Ivor Janković[29], Lence Jovanova[63], Panagiotis Karkanas[64], Berna Kavaz-Kındığılı[65], Esra Hilal Kaya[66], Denise Keating[3], Douglas J. Kennett[37,67], Seda Deniz Kesici[68], Anahit Khudaverdyan[7], Krisztián Kiss[58,69], Sinan Kılıç[20], Paul Klostermann[70], Sinem Kostak Boca Negra Valdes[68], Saša Kovačević[71], Marta Krenz-Niedbała[72], Maja Krznarić Škrivanko[73], Rovena Kurti[74], Pasko Kuzman[75], Ann Marie Lawson[2,27], Catalin Lazar[76], Krassimir Leshtakov[77], Thomas E. Levy[78], Ioannis Liritzis[79,80], Kirsi O. Lorentz[81], Sylwia Łukasik[72], Matthew Mah[2,27,82], Swapan Mallick[2,27], Kirsten Mandl[3], Kristine Martirosyan-Olshansky[83], Roger Matthews[84], Wendy Matthews[84], Kathleen McSweeney[24], Varduhi Melikyan[7], Adam Micco[2], Megan Michel[1,2,27], Lidija Milašinović[85], Alissa Mittnik[1,2,86], Janet M. Monge[87], Georgi Nekhrizov[15], Rebecca Nicholls[88], Alexey G. Nikitin[89], Vassil Nikolov[15], Mario Novak[29], Iñigo Olalde[2,90], Jonas Oppenheimer[2,27], Anna Osterholtz[91], Celal Özdemir[13], Kadir Toykan Özdoğan[3], Nurettin Öztürk[65], Nikos Papadimitriou[92], Niki Papakonstantinou[93], Anastasia Papathanasiou[94], Lujana Paraman[95], Evgeny G. Paskary[96], Nick Patterson[1,82], Ilian Petrakiev[45], Levon Petrosyan[7], Vanya Petrova[77], Anna Philippa-Touchais[97], Ashot Piliposyan[98], Nada Pocuca Kuzman[75], Hrvoje Potrebica[99], Bianca Preda-Bălănică[59], Zrinka Premužić[100], T. Douglas Price[101], Lijun Qiu[2,27], Siniša Radović[102], Kamal Raeuf Aziz[103], Petra Rajić Šikanjić[29], Kamal Rasheed Raheem[103], Sergei Razumov[104], Amy Richardson[84], Jacob Roodenberg[105], Rudenc Ruka[74], Victoria Russeva[106], Mustafa Şahin[57], Ayşegül Şarbak[107], Emre Savaş[68], Constanze Schattke[3], Lynne Schepartz[108], Tayfun Selçuk[68], Ayla Sevim-Erol[109], Michel Shamoon-Pour[110], Henry M. Shephard[111], Athanasios Sideris[112], Angela Simalcsik[32,113], Hakob Simonyan[114], Vitalij Sinika[104], Kendra Sirak[2], Ghenadie Sirbu[115], Mario Šlaus[116], Andrei Soficaru[35], Bilal Söğüt[117], Arkadiusz Sołtysiak[118], Çilem Sönmez-Sözer[109], Maria Stathi[119], Martin Steskal[120], Kristin Stewardson[2,27], Sharon Stocker[38], Fadime Suata-Alpaslan[121], Alexander Suvorov[59], Anna Szécsényi-Nagy[122], Tamás Szeniczey[58], Nikolai Telnov[104], Strahil Temov[123], Nadezhda Todorova[77], Ulsi Tota[74,124], Gilles Touchais[125], Sevi Triantaphyllou[93], Atila Türker[126], Marina Ugarković[71], Todor Valchev[16], Fanica Veljanovska[123], Zlatko Videvski[123], Cristian Virag[127], Anna Wagner[3], Sam Walsh[128], Piotr Włodarczak[129], J. Noah Workman[2], Aram Yardumian[130,131], Evgenii Yarovoy[132], Alper Yener Yavuz[133], Hakan Yılmaz[20], Fatma Zalzala[2,27], Anna Zettl[3], Zhao Zhang[2], Rafet Çavuşoğlu[20], Nadin Rohland[2], Ron Pinhasi[3,134]*, David Reich[1,2,27,82]*

By sequencing 727 ancient individuals from the Southern Arc (Anatolia and its neighbors in Southeastern Europe and West Asia) over 10,000 years, we contextualize its Chalcolithic period and Bronze Age (about 5000 to 1000 BCE), when extensive gene flow entangled it with the Eurasian steppe. Two streams of migration transmitted Caucasus and Anatolian/Levantine ancestry northward, and the Yamnaya pastoralists, formed on the steppe, then spread southward into the Balkans and across the Caucasus into Armenia, where they left numerous patrilineal descendants. Anatolia was transformed by intra–West Asian gene flow, with negligible impact of the later Yamnaya migrations. This contrasts with all other regions where Indo-European languages were spoken, suggesting that the homeland of the Indo-Anatolian language family was in West Asia, with only secondary dispersals of non-Anatolian Indo-Europeans from the steppe.

The Balkans and Anatolia are often portrayed as being geographically peripheral to Europe and Asia rather than as central to an interconnected region spanning both continents. Here, we take a different view by providing a systematic genetic history of what we refer to as the "Southern Arc," a region (Fig. 1A) centered on the large Anatolian peninsula (Turkey), including in the west (in Europe) the Balkans and the Aegean, and in the south and east, Cyprus, Mesopotamia, the Levant, Armenia, Azerbaijan, and Iran. We present new genome-wide DNA data from 777 individuals from the Southern Arc: 727 previously unsampled and 50 previously published for which we report new data from 1094 newly generated ancient DNA libraries (1). As a resource to guide future sampling

efforts, we also report negative results for 476 samples that we screened using 537 libraries and that failed to yield ancient DNA data meeting the criteria for authenticity (1). Finally, we provide 239 new radiocarbon dates on the same skeletal elements analyzed for DNA (1). We studied these along with the previously published individuals for a total sample size of 1317 ancient individuals in the region (Fig. 1B) (1).

Our newly reported data fill many sampling gaps in space and time in the Southern Arc. In Turkey, our new sampling has a particular focus on the western (Aegean, Marmara), northern (Black Sea), and eastern (Eastern Anatolia, Southeastern Anatolia) regions connecting it with the rest of the Southern Arc. Another area of high-density sampling is Armenia, with sub-

stantial coverage of the Bronze and Iron Ages representing an order of magnitude more individuals than previously available. Many individuals of the Bronze-to-Iron Age time frame are also sampled from the Iranian highlands at Hasanlu, where only a single individual has previously been studied (2), and from Dinkha Tepe, neighboring Anatolia, Mesopotamia, Armenia, and the Caucasus. In the southern part of Southeastern Europe, we sample Mycenaean-era individuals from multiple regions of the Aegean. From the Southern Balkans, we present a full time transect of Albania; numerous individuals from North Macedonia, where previously data from only a single Neolithic individual had been published (3); and more than double the previously available body of ancient DNA data from Bulgaria. Farther north, at the western wing of the Southern Arc, we sample individuals from Croatia, Montenegro, and Serbia in the west and Romania and Moldova in the east, which interface with the extensively studied worlds of Central Europe and the Eurasian steppe. This dataset includes >100 Bronze Age individuals, including many from Cetina Valley and Bezdanjača Cave in Croatia, which add to only five previously published from the entire area (3, 4). Some of the Balkan individuals include culturally Yamnaya individuals from Serbia and Bulgaria,

allowing us to compare them with those of the Eurasian steppe. With this greatly enhanced dataset across the entire region, we are able to fill in major gaps in sampling in time, space, and cultural context. Our large sample sizes also allow us to identify main clusters as well as genetic outliers, providing insights about within-population patterns of variation and contact networks with neighboring groups. Details of all studied individuals can be found in (1) (figs. S5 to S21).

To discuss the geographic distribution of these individuals, we take a flexible approach, in some cases using the names of ecological or topographical regions and in others the names of present-day countries depending on how well these align with genetic patterns. In some cases, we also use more specific regional location information to add precision (5). In the interest of having a uniform nomenclature that is easily accessible to readers familiar with the current political map of the Southern Arc, we also refer to groups of individuals with labels prefixed with three-letter International Standards Organization (ISO) codes for countries, as in Fig. 1. Multiple toponyms have been used for the same sites during the Southern Arc's long history, and we typically choose labels appropriate for the period and/or present-day usage. To designate the period in which individuals lived, we use conventional archaeological designations for each region; e.g., Eneolithic and Chalcolithic both denote copper-using cultures in different parts of the archaeological literature. We caution that the transition between the Eneolithic or Chalcolithic and the Bronze Age did not occur simultaneously in different parts of the Southern Arc. Detailed archaeological information for each individual is presented in (1), specifying the analysis labels we use integrating information from chronology, geography, archaeology, and genetics.

[1]Department of Human Evolutionary Biology, Harvard University, Cambridge, MA 02138, USA. [2]Department of Genetics, Harvard Medical School, Boston, MA 02115, USA. [3]Department of Evolutionary Anthropology, University of Vienna, 1030 Vienna, Austria. [4]Department of Anthropology, Faculty of Letters, Mardin Artuklu University, 47510 Artuklu, Mardin, Turkey. [5]Department of Anthropology, Faculty of Letters, Sivas Cumhuriyet University, 58140 Sivas, Turkey. [6]Department of History, Adelphi University, Garden City, NY 11530, USA. [7]Institute of Archaeology and Ethnography, NAS RA, 0025 Yerevan, Armenia. [8]Samsun Museum of Archeology and Ethnography, Kale Mahallesi, Merkez, İlkadım, 55030 Samsun, Turkey. [9]Iskra Museum of History, 6100 Kazanlak, Bulgaria. [10]Historical Museum in Kotor, 85330 Kotor, Montenegro. [11]Institute of Archaeology, 11000 Belgrade, Serbia. [12]Department of Archaeology, University of York, York YO1 7EP, UK. [13]Amasya Archaeology Museum, Mustafa Kemal Paşa Caddesi, 05000 Amasya, Turkey. [14]Department of Anthropology, Faculty of Arts and Science, Burdur Mehmet Akif University, 15100 Burdur, Turkey. [15]National Institute of Archaeology and Museum, Bulgarian Academy of Sciences, 1000 Sofia, Bulgaria. [16]Yambol Regional Historical Museum, 8600 Yambol, Bulgaria. [17]Archaeological Museum in Zagreb, 10000 Zagreb, Croatia. [18]Department of Archaeology and Heritage Studies, University of Tirana, 1010 Tirana, Albania. [19]Department of Animal and Human Physiology, Faculty of Biology, School of Sciences, National and Kapodistrian University of Athens, 10679 Athens, Greece. [20]Department of Archaeology, Faculty of Humanities, Van Yüzüncü Yıl University, 65090 Tuşba, Van, Turkey. [21]Department of Archaeology, Faculty of Science and Letters, Düzce University, 81620 Düzce, Turkey. [22]Stratum Ltd., 21218 Seget Donji, Croatia. [23]Independent Researcher, Berkeley, CA 94720, USA. [24]School of History, Classics and Archaeology, University of Edinburgh, Edinburgh EH8 9AG, UK. [25]The Italian Academy for Advanced Studies in America, Columbia University, New York, NY 10027, USA. [26]Center for Conservation and Archaeology of Montenegro, 81250 Cetinje, Montenegro. [27]Howard Hughes Medical Institute, Harvard Medical School, Boston, MA 02115, USA. [28]Servizio di Bioarcheologia, Museo delle Civiltà, 00144 Rome, Italy. [29]Centre for Applied Bioanthropology, Institute for Anthropological Research, 10000 Zagreb, Croatia. [30]Department of Archaeology, University of Veliko Tarnovo "St. Cyril and St. Methodius," 5003 Veliko Tarnovo, Bulgaria. [31]Hellenic Ministry of Culture and Sports, Ephorate of Antiquities of Piraeus and the Islands, 10682 Piraeus, Greece. [32]"Orheiul Vechi" Cultural-Natural Reserve, Institute of Bioarchaeological and Ethnocultural Research, 3552 Butuceni, Moldova. [33]National Archaeological Agency, 2012 Chişinău, Moldova. [34]Archaeological Museum in Zadar, 23000 Zadar, Croatia. [35]"Francisc I. Rainer" Institute of Anthropology, 050711 Bucharest, Romania. [36]Department of Oral and Maxillo-Facial Sciences, Sapienza University of Rome, 00161 Rome, Italy. [37]Institutes of Energy and the Environment, The Pennsylvania State University, University Park, PA 16802, USA. [38]Department of Classics, University of Cincinnati, Cincinnati, OH 45221, USA. [39]Independent Researcher, Aberystwyth SY23 4UH, UK. [40]Center of Archaeology, Institute of Cultural Heritage, Academy of Science of Moldova, 2001 Chişinău, Moldova. [41]Department of Archaeology, Faculty of Letters, Ege University, 35100 Bornova-Izmir, Turkey. [42]Museum of Anthropological Archaeology, University of Michigan, Ann Arbor, MI 48109, USA. [43]Narodni muzej Pančevo, 26101 Pančevo, Serbia. [44]Human Paleoecology and Isotope Geochemistry Lab, Department of Anthropology, The Pennsylvania State University, University Park, PA 16802, USA. [45]Regional Museum of History – Veliko Tarnovo, 5000 Veliko Tarnovo, Bulgaria. [46]Department of Archaeology, Faculty of Science and Letters, Gaziantep University, 27310 Gaziantep, Turkey. [47]Mardin Archaeological Museum, Şar, Cumhuriyet Meydanı üstü, 47100 Artuklu, Mardin, Turkey. [48]Muğla İl Kültür ve Turizm Müdürlüğü, 48000 Muğla, Turkey. [49]Research Centre for Anthropology and Health (CIAS), Department of Life Sciences, University of Coimbra, 3000-456 Coimbra, Portugal. [50]Prahova County Museum of History and Archaeology, 100042 Ploieşti, Romania. [51]Institut Català de Paleoecologia Humana i Evolució Social, 43007 Tarragona, Spain. [52]Departament d'Història i Història de l'Art, Universitat Rovira i Virgili, 43002 Tarragona, Spain. [53]School of Archaeology and Earth Institute, University College Dublin, Belfield, Dublin 4, Ireland. [54]Department of Archaeology, Durham University, Durham DH1 3LE, UK. [55]Department of Archaeology, Faculty of Science and Letters, Çukurova University, 01330 Balçalı-Sarıçam-Adana, Turkey. [56]Department of Anthropology, Faculty of Humanities, Ankara University, 06100 Sıhhiye, Ankara, Turkey. [57]Department of Archaeology, Faculty of Science and Letters, Bursa Uludağ University, 16059 Görükle, Bursa, Turkey. [58]Department of Biological Anthropology, Institute of Biology, Eötvös Loránd University, 1053 Budapest, Hungary. [59]Department of Cultures, University of Helsinki, 00100 Helsinki, Finland. [60]Department of Ecology and Nature Protection, Yerevan State University, 0025 Yerevan, Armenia. [61]Regional Museum of History, 6300 Haskovo, Bulgaria. [62]Ministry of Culture and Tourism, İsmet İnönü Bulvarı, 06100 Emek, Ankara, Turkey. [63]Museum of the City of Skopje, 1000 Skopje, North Macedonia. [64]Malcolm H. Wiener Laboratory, American School of Classical Studies at Athens, 10676 Athens, Greece. [65]Department of Archaeology, Faculty of Letters, Atatürk University, 25100 Erzurum, Turkey. [66]Muğla Archaeological Museum and Yatağan Thermal Power Generation Company, Rescue Excavations, 48000 Muğla, Turkey. [67]Department of Anthropology, University of California, Santa Barbara, Santa Barbara, CA 93106, USA. [68]Bodrum Museum of Underwater Archeology, Çarşı Neighbourhood, 48400 Bodrum, Muğla, Turkey. [69]Department of Anthropology, Hungarian Natural History Museum, 1117 Budapest, Hungary. [70]Department of Anthropology, Natural History Museum Vienna, 1010 Vienna, Austria. [71]Institute of Archaeology, 10000 Zagreb, Croatia. [72]Faculty of Biology, Adam Mickiewicz University in Poznań, 61-614 Poznań, Poland. [73]Municipal Museum Vinkovci, 32100 Vinkovci, Croatia. [74]Prehistory Department, Albanian Institute of Archaeology, Academy of Albanian Studies, 1000 Tirana, Albania. [75]National Museum in Ohrid, 6000 Ohrid, North Macedonia. [76]ArchaeoSciences Division, Research Institute of the University of Bucharest, University of Bucharest, 050663 Bucharest, Romania. [77]Department of Archaeology, St. Kliment Ohridski University of Sofia, 1504 Sofia, Bulgaria. [78]Department of Anthropology, University of California, San Diego, La Jolla, CA 92093, USA. [79]Key Research Institute of Yellow River Civilization and Sustainable Development and the Collaborative Innovation Center on Yellow River Civilization of Henan Province, Laboratory of Yellow River Cultural Heritage, Henan University, 475001 Kaifeng, China. [80]European Academy of Sciences and Arts, 5020 Salzburg, Austria. [81]Science and Technology in Archaeology and Culture Research Center, The Cyprus Institute, 2121 Aglantzia, Nicosia, Cyprus. [82]Broad Institute of Harvard and MIT, Cambridge, MA 02142, USA. [83]Cotsen Institute of Archaeology, University of California, Los Angeles, Los Angeles, CA 90095, USA. [84]Department of Archaeology, University of Reading, Reading RG6 6AB, UK. [85]National Museum of Kikinda, 23300 Kikinda, Serbia. [86]Department of Archaeogenetics, Max Planck Institute for Evolutionary Anthropology, 04103 Leipzig, Germany. [87]University of Pennsylvania Museum of Archaeology and Anthropology, Philadelphia, PA 19104, USA. [88]School of Archaeological and Forensic Sciences, Faculty of Life Sciences, University of Bradford, Bradford BD7 1DP, UK. [89]Department of Biology, Grand Valley State University, Allendale, MI 49401, USA. [90]BIOMICs Research Group, University of the Basque Country UPV/EHU, 01006 Vitoria-Gasteiz, Spain. [91]Department of Anthropology and Middle Eastern Cultures, Mississippi State University, Mississippi State, MS 39762, USA. [92]Paul and Alexandra Canellopoulos Museum, 105-55 Athens, Greece. [93]Faculty of Philosophy, School of History and Archaeology, Aristotle University of Thessaloniki, 54124 Thessaloniki, Greece. [94]Ephorate of Paleoantropology and Speleology, Greek Ministry of Culture, 11636 Athens, Greece. [95]Trogir Town Museum, 21220 Trogir, Croatia. [96]Moldavian Historic-Geographical Society, 2044 Chişinău, Moldova. [97]French School of Archaeology at Athens, 10680 Athens, Greece. [98]Department of Armenian History, Armenian State Pedagogical University After Khachatur Abovyan, 0010 Yerevan, Armenia. [99]Department of Archaeology, Faculty of Humanities and Social Sciences, University of Zagreb, 10000 Zagreb, Croatia. [100]Independent Researcher, 10000 Zagreb, Croatia. [101]Laboratory for Archaeological Chemistry, University of Wisconsin–Madison, Madison, WI 53706, USA. [102]Institute for Quaternary Paleontology and Geology, Croatian Academy of Sciences and Arts, 10000 Zagreb, Croatia. [103]Sulaymaniyah Directorate of Antiquities and Heritage, 46010 Sulaymaniyah, Iraq. [104]Pridnestrovian University named after Taras Shevchenko, 3300 Tiraspol, Moldova. [105]The Netherlands Institute for the Near East, 2311 Leiden, Netherlands. [106]Institute of Experimental Morphology, Pathology and Archeology with Museum, Bulgarian Academy of Science, 1113 Sofia, Bulgaria. [107]Department of Anthropology, Faculty of Science and Letters, Hitit University, 19040 Çorum, Turkey. [108]School of Anatomical Sciences, The University of the Witwatersrand, 2193 Johannesburg, South Africa. [109]Department of Anthropology, Faculty of Language and History - Geography, Ankara University, 06100 Sıhhiye, Ankara, Turkey [110]Department of Anthropology, Binghamton University, Binghamton, NY 13902, USA. [111]Archaeological Institute of America, Boston, MA 02108, USA. [112]Institute of Classical Archaeology, Charles University, 11636 Prague, Czechia. [113]"Olga Necrasov" Centre of Anthropological Research, Romanian Academy Iaşi Branch, 2012 Iaşi, Romania. [114]Scientific Research Center of the Historical and Cultural Heritage, 0010 Yerevan, Armenia. [115]Thracology Scientific Research Laboratory of the State University of Moldova, Department of Academic Management, Academy of Science of Moldova, 2009 Chişinău, Moldova. [116]Anthropological Center of the Croatian Academy of Sciences and Arts, 10000 Zagreb, Croatia. [117]Department of Archaeology, Faculty of Science and Arts, Pamukkale University, 20070 Denizli, Turkey. [118]Faculty of Archaeology, University of Warsaw, 00-927 Warszawa, Poland. [119]Ephorate of Antiquities of East Attica, Ministry of Culture and Sports, 10682 Athens, Greece. [120]Austrian Archaeological Institute at the Austrian Academy of Sciences, 1190 Vienna, Austria. [121]Department of Anthropology, Faculty of Letters, Istanbul University, 34134 Istanbul, Turkey. [122]Institute of Archaeogenomics, Research Centre for the Humanities, Eötvös Loránd Research Network, 1097 Budapest, Hungary. [123]Archaeology Museum of North Macedonia, 1000 Skopje, North Macedonia. [124]Culture and Patrimony Department, University of Avignon, F-84029 Avignon, France. [125]Department of the History of Art and Archaeology, Université Paris 1 Panthéon-Sorbonne, 75006 Paris, France. [126]Department of Archaeology, Faculty of Science and Letters, Ondokuz Mayıs University, 55139 Atakum-Samsun, Turkey. [127]Satu Mare County Museum, 440031 Satu Mare, Romania. [128]School of Natural Sciences, University of Central Lancashire, Preston PR1 2HE, UK. [129]Institute of Archaeology and Ethnology, Polish Academy of Sciences, 31-016 Kraków, Poland. [130]Department of History and Social Sciences, Bryn Athyn College, Bryn Athyn, PA 19009, USA. [131]Penn Museum, University of Pennsylvania, Philadelphia, PA 19104, USA. [132]History of the Ancient World and Middle Ages Department, Moscow Region State University, Moscow Region, 141014 Mytishi, Russia. [133]Department of Anthropology, Burdur Mehmet Akif Ersoy University, Istiklal Campus, 15100 Burdur, Turkey. [134]Human Evolution and Archaeological Sciences, University of Vienna, 1030 Vienna, Austria.

*Corresponding author. Email: lazaridis@genetics.med.harvard.edu (I.La.); msglalpaslan@gmail.com (S.A.-R.); ron.pinhasi@univie.ac.at (R.P.); reich@genetics.med.harvard.edu (D.R.)
†These authors contributed equally to this work.

Fig. 1. Studied individuals and PCA analysis. (**A**) The geography of the Southern Arc. Sampling locations of previously published individuals are shown as gray circles, new data on published individuals are shown by pink squares, and new individuals are shown as yellow circles. Convex hulls of individuals from each present-day country are also shown. (**B**) Timeline of studied individuals (random uniform jitter applied to the vertical dimension). (**C**) Principal components analysis of ancient individuals projected on modern West Eurasian variation. Country names are represented by three-letter International Standards Organization (ISO) codes.

Overview of genetic variation in the Southern Arc

To understand genetic variation in the Southern Arc, we began with ADMIXTURE (fig. S1) analysis, which allowed us to detect individuals with non–West Eurasian–associated ancestry (6) and to appreciate the broad pattern of variation in terms of the four West Eurasian components that appear in the ADMIXTURE analysis: Iran/Caucasus-related, "Eastern hunter-gatherer," Anatolian/Levantine-related, and "Balkan hunter-gatherer." Principal components analysis (Fig. 1C) of Southern Arc individuals together with other West Eurasian individuals demonstrates the central position of the Southern Arc within the continuum of West Eurasian variation, with a long "bridge" of individuals joining Europe (left) to West Asia (right), but with individuals spread across the entire range of variation.

To quantify the ancestry of Southern Arc individuals, we developed a five-source modeling framework (using qpAdm and F4admix) (1) that allows a high-resolution description of the ancestry of the Southern Arc population as a whole and as individuals. To generate this model, we used an automated procedure that did not preselect a specific set of surrogates for the source populations, but instead explored many possible sets and identified those that, for as many individuals as possible, maximized the quality of the statistical fit of the model while minimizing the standard errors in inferences of ancestry proportions (tables S1 to S21 and figs. S22 to S27). After applying this procedure, the five sources of ancestry that we used are: Caucasus hunter-gatherers (CHG) (7), Eastern hunter-gatherers (EHG) from Europe (8, 9), Levantine Pre-Pottery Neolithic (10), Balkan hunter-gatherers from the Iron Gates in Serbia (3), and Northwestern Anatolian Neolithic from Barcın (9). These correspond to the four-source ADMIXTURE model, with further distinction between the Anatolian and Levantine ends of the "Mediterranean" interaction zone (11). These five sources should not be unduly emphasized beyond their utility as a descriptive convenience because (i) they could be swapped for related ones [e.g., Neolithic Iran captures much of the same deep ancestry as Caucasus hunter-gatherers do (10, 11)], (ii) they were themselves derived from earlier (more "distal") populations [e.g., Levantine Pre-Pottery Neolithic from earlier Natufian hunter-gatherers (10)], and (iii) they transmitted their ancestry through later (more "proximal") sources [e.g., Eastern hunter-gatherers through Yamnaya steppe pastoralists (8)]. The inferred proportions of ancestry for individuals are summarized in figs. S2 to S4 and figs. S28 to S76 and are discussed in detail in (1).

The Anatolian core of the Southern Arc

When we apply our five-way model to individuals from Anatolia (Fig. 2, A to E), it is
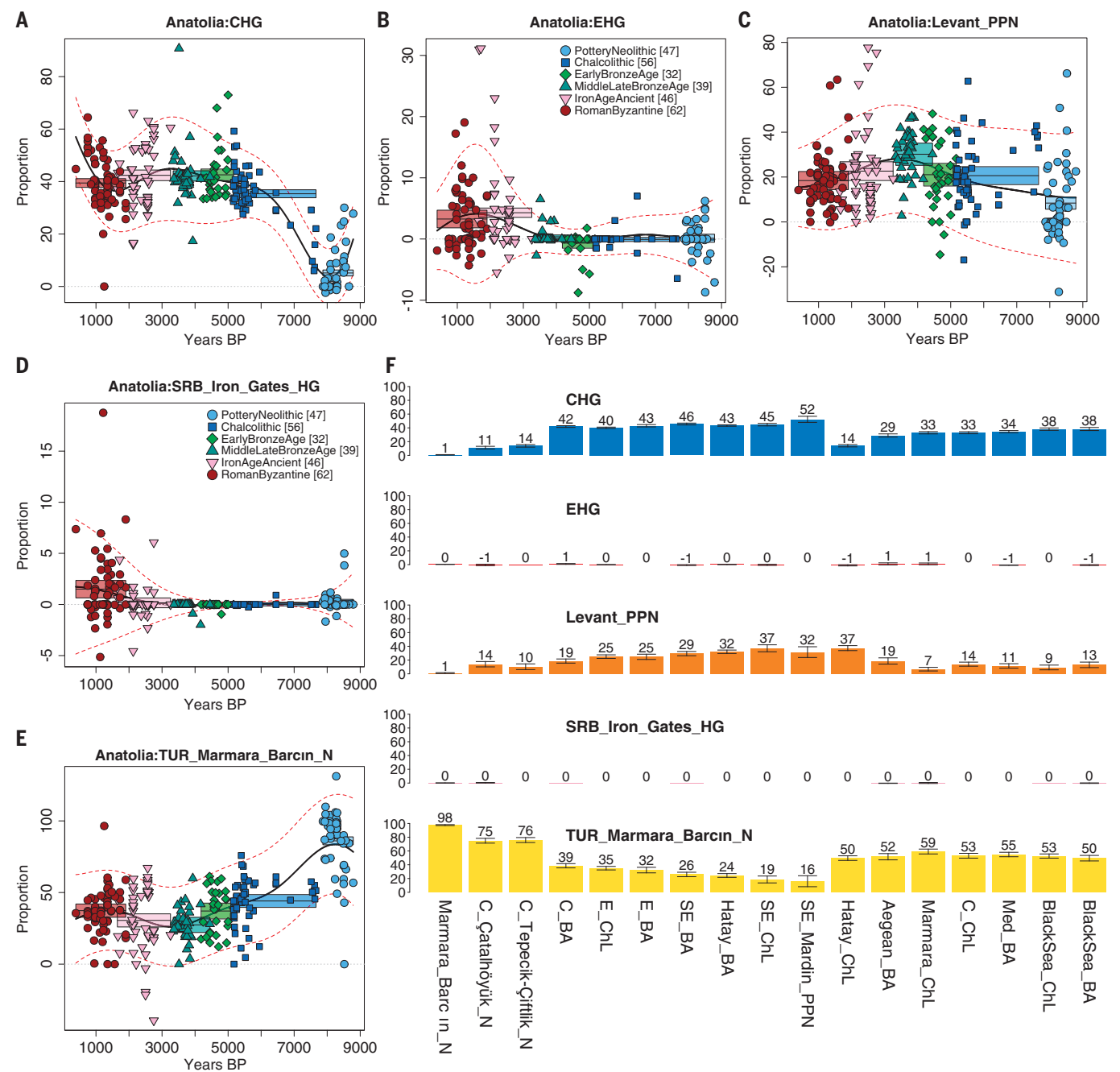
Fig. 2. The Anatolian heartland. (**A** to **E**) Five components of ancestry in Anatolia from the Pottery Neolithic to the Roman/Byzantine period. Boxes in this and subsequent figures indicate the temporal extent (horizontal) and 95% confidence interval (±1.96 SE) for each period; we also show the fit (solid line) and 5/95% (dotted lines) of the fit of a heteroskedastic Gaussian process (53) on the individuals without any assignment to populations, which allows us to appreciate the degree of variation in ancestry in each time period (ancestry proportions for some individuals are shown as negative, reflecting statistical uncertainty in the estimates). Here and in subsequent figures, numbers in brackets are sample sizes. The results show that across the peninsula, the post-Neolithic period was characterized by

an expansion of CHG-related ancestry (A) and a dilution of Northwest Anatolian-related ancestry (E). EHG-related ancestry from both the steppe/Eastern Europe (B) and the Balkans (D) was insignificant until the past 3000 years. (**F**) A detailed look at the Chalcolithic/Bronze Age period showing that populations had ancestry intermediate between early farmers from Western/Central Anatolia [Barcın (9), Tepecik-Çiftlik (13), and Çatalhöyük (12)] and Southeastern Anatolia (Northern Mesopotamia at Mardin) on the other, the result of admixture between the preceding Neolithic populations, without discernible external influences (that would have elevated any of the five components above their Neolithic levels). PPN, Pre-Pottery Neolithic. ±1 SE shown.

immediately apparent that before ~3000 years ago, virtually all ancestry is drawn from local West Asian sources (Northwest Anatolian Neolithic, hereafter called "Anatolian," Levantine, Caucasus), with negligible contribution

from the two European (Balkan and Eastern hunter-gatherer) sources of our model. Broadly speaking, the temporal trend is one of increasing Caucasus/Levantine–related ancestry between the Neolithic and Chalcolithic periods,

with a corresponding decrease of the Anatolian-related ancestry. To better understand this process in the Anatolian peninsula, we examined geographical subpopulations of the Chalcolithic and Bronze Age compared with

the Neolithic ones that preceded them (Fig. 2F). We observed that Northwest Anatolian–related ancestry varied between ~100% (at Barcın, Menteşe, and Ilıpınar in the Marmara region; we use the high-quality data we have from Barcın to define this component of ancestry) to ~16% (the Pre-Pottery Neolithic individual from Mardin in Southeast Anatolia/North Mesopotamia). Conversely, Caucasus/Levantine ancestry varied between ~50 and ~32% in North Mesopotamia to ~0% in Northwest Anatolia.

The Chalcolithic period in Anatolia has a wide temporal range (Fig. 2) that spans from the end of the Neolithic (~6000 BCE) to the beginning of the Bronze Age (~3000 BCE). Individuals in our analysis are mostly from the Late Chalcolithic (after ~4500 BCE) and from the entirety of the Bronze Age (down to 1300 BCE). Both Chalcolithic and Bronze Age populations from all regions generally had intermediate admixture proportions within the Neolithic ranges of ancestry. This suggests that they could be modeled as drawn from mixtures of the preceding Neolithic populations. In the Marmara region, Caucasus hunter-gatherer ancestry increased from ~0 to ~33% between the Neolithic and Chalcolithic periods [to define the Chalcolithic, we added four individuals from Ilıpınar to a single one from Barcın previously published (10)]. In the Central region, we document an increase from ~10 to 15% at Neolithic Çatalhöyük (12) and Tepecik-Çiftlik (13) to a similar ~33% at Chalcolithic Çamlıbel Tarlası (14) and ~42% at Bronze Age Kalehöyük and Ovaören (15). In the Mediterranean region (Southwest Anatolia), the same approximate one-third proportion was present at Harmanören Göndürle (16) in the Bronze Age. In the Aegean region (Western Anatolia), we observe a similar ~29% in the Bronze Age. Thus, individuals from more western regions of Anatolia (Marmara, Aegean, Central, and Mediterranean) all had more Caucasus-related ancestry (and correspondingly less Anatolian-related ancestry) during the Chalcolithic and Bronze Age than the preceding Neolithic populations of the area, suggesting that a spread of this ancestry westward across the peninsula occurred after the Neolithic, a pattern also observed in the Levant (11). In the more eastern regions of Anatolia [East, in Arslantepe (14); Southeast, from Batman, Gaziantep, Kilis, and Şırnak (new data) and Titriş Höyük (14); Black Sea, from Devret Höyük in Amasya and Samsun (new data) and İkiztepe (14)], populations of the Chalcolithic and Bronze Age periods had, conversely, more Western Anatolian Neolithic–related, and less Caucasus-related ancestry, than the Pre-Pottery Neolithic individual from Mardin. This pattern is also observed when we compare the Chalcolithic with the Bronze Age. Differences are small but all in the direction

of more Western Anatolian Neolithic-related ancestry (an increase of ~3 to 7% in the East, Southeast, and Black Sea regions) except in the Hatay Province (14), where Western Anatolian Neolithic-related ancestry decreased and Caucasus-related ancestry increased (from ~14 to 43%) between the Early Chalcolithic (~5500 BCE) and the Middle to Late Bronze Age (after ~2000 BCE).

Taken as a whole, the genetic history of Anatolia during the Chalcolithic and Bronze Age can be characterized as one of homogenization. Neolithic populations differed by as much as ~80% in terms of Western Anatolian Neolithic–related and by ~50% in terms of Caucasus-related ancestry. In the Chalcolithic and Bronze Age, the range of these differences narrowed substantially. That of Western Anatolian Neolithic–related ancestry halved to ~40% (becoming ~20 to 60%) and that of Caucasus-related ancestry to ~15% (becoming ~30 to 45% except in the Hatay Province). Despite this homogenization, some ancestry differences persisted. The eastern regions retained more Caucasus-related ancestry than the western ones, but the overall pattern was one of attenuated differentiation after intra-Anatolian gene flow stemming from the highly differentiated Neolithic populations of Western/Central Anatolia on the one hand and Northern Mesopotamia on the other (as well as hitherto unsampled others).

Homogenization in Anatolia was coupled by impermeability to exogenous gene flow from Europe, which could be explained by either a large and stable population base that attenuated the demographic impact of external immigration or cultural factors impeding it. The asymmetry of gene flow between Anatolia and its neighbors is evident, for example, in the fact that Caucasus hunter-gatherer–related ancestry flowed westward across Anatolia into the Balkans and northward into the Eurasian steppe, but Balkan hunter-gatherer ancestry did not flow into Anatolia or further eastward, and Eastern hunter-gatherer ancestry entered West Asia only as far south as Armenia and, to a lesser extent, Iran (as we will see below). This was true even down to the Urartian period of the Iron Age, when a population lacking Eastern hunter-gatherer ancestry still existed in the center of the Kingdom of Van (6).

The origin and expansion of steppe pastoralists

The absence of European hunter-gatherer admixture in Anatolia during the Chalcolithic and Bronze Age periods contrasts with developments to the north of the Southern Arc and north of the Black and Caspian Seas, which saw the formation of Eneolithic (a term used instead of Chalcolithic for this area) and Bronze Age pastoralist populations that harbored a mixture of populations from Eastern Europe and the Southern Arc (8, 9, 17). Examining

individuals from the steppe (Fig. 3), we observe that in the post–5000 BCE period, Caucasus-related ancestry is added to the previous Eastern hunter-gatherer population, forming the Eneolithic populations at Khvalynsk (9) and Progress-2 (17); this ancestry persisted in the Steppe Maykop population of the 4th millennium BCE (17). However, all of these populations before ~3000 BCE lack any detectible Anatolian/Levantine–related ancestry, contrasting with all contemporaneous ones from the Southern Arc, which have at least some such ancestry at least since the Neolithic (11). In all later periods in the Southern Arc, Caucasus hunter-gatherer–related ancestry is never found by itself but rather is always admixed, to various degrees, with Anatolian/Levantine ancestry. This suggests that whatever the source of the Caucasus-related ancestry in the Eneolithic steppe, it cannot have been from the range of variation sampled in the Southern Arc because this would have introduced Anatolian/Levantine–related ancestry. This implies that the proximal source of the Caucasus-related ancestry in the Eneolithic steppe should be sought in an unsampled group that did not experience Anatolian/Levantine–related gene flow until the Eneolithic. Plausibly, this population existed in the North Caucasus, from which Caucasus hunter-gatherer–related, but not Anatolian/Levantine–related, ancestry could have entered the Eneolithic steppe.

The Eneolithic steppe population contrasts with that of the Yamnaya cluster of individuals ~3000 BCE, which does have significant Anatolian (3 ± 1%)–and Levantine (3.5 ± 1%)–related ancestry [Fig. 3A; steppe individuals in this analysis are listed in (1)]. This inference is further supported by detailed analysis of Yamnaya ancestry at different time depths (tables S22 to S28) (1), which indicates that they derived from at least two southern sources. The first source dates to the Eneolithic and includes Caucasus hunter-gatherer ancestry only. The second source dates to before the formation of the Yamnaya cluster and includes Anatolian/Levantine–related ancestry in addition to Caucasus hunter-gatherer (as deep sources), ancestry related to Neolithic people of Armenia (more proximally), or ancestry related to Chalcolithic people of the Caucasus to Southeast Anatolia (even more proximally). A more direct and geographically proximate source in the Maykop population of the North Caucasus of the 4th millennium BCE has also been proposed (18). Although the exact source cannot at present be determined (all of the candidates have different combinations of the same Anatolian/Levantine/Caucasus ancestry; fig. S1), it was people drawn from this metapopulation in the Chalcolithic Caucasus, Armenia, and East/Southeast Anatolia that must have been responsible for the second pulse of Southern Arc ancestry into the precursors of Yamnaya
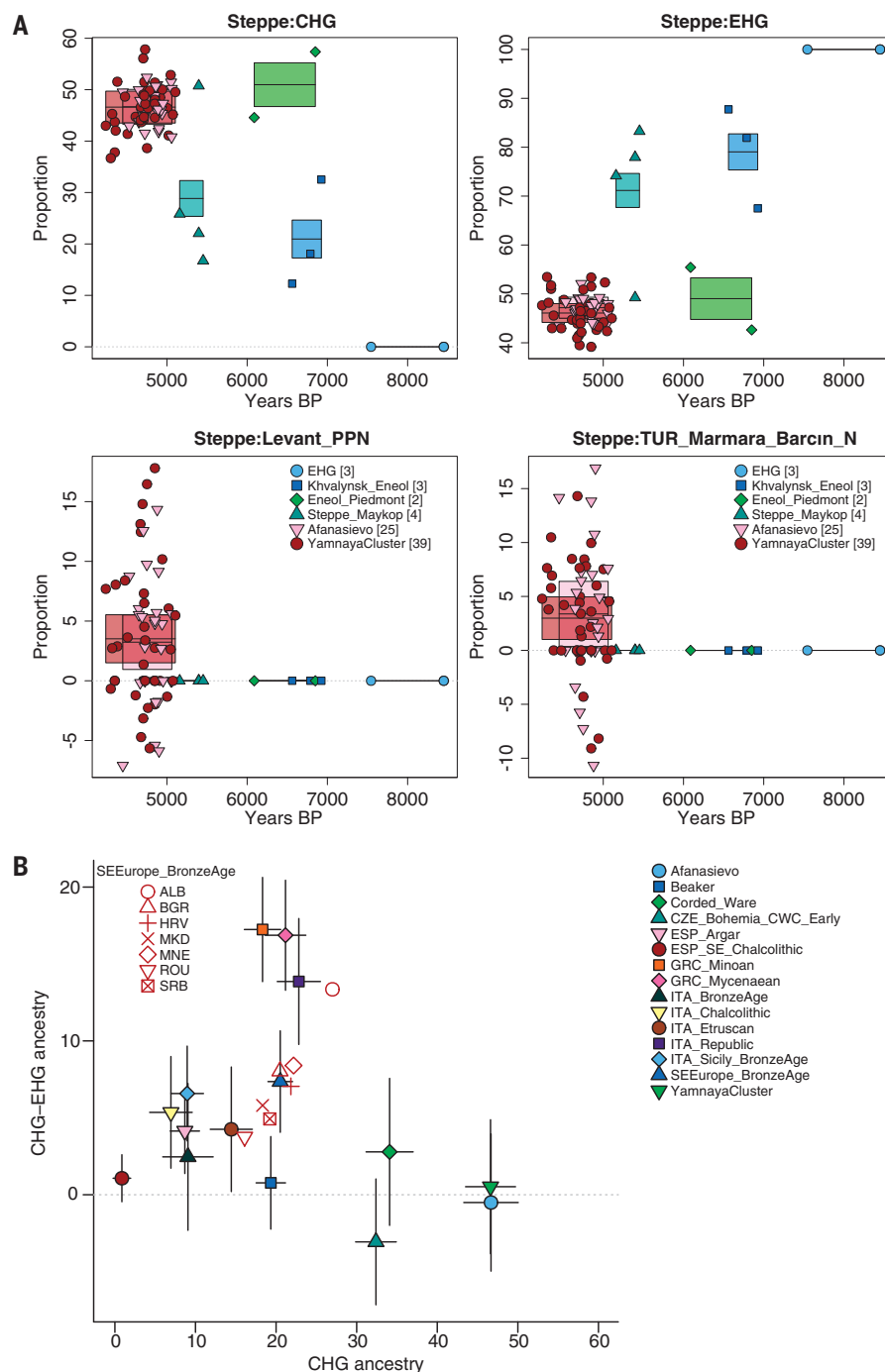
Fig. 3. Yamnaya origins and expansions. (**A**) The earliest inhabitants of the steppe (EHG) were followed by CHG-admixed populations by ~5000 BCE and by Anatolian/Levantine–admixed populations by ~3000 BCE with the emergence of the Yamnaya-Afanasievo genetic cluster. The proportion of Balkan hunter-gatherer–related ancestry (not shown) is 0.8 ± 0.6% in the Yamnaya cluster and −0.5 ± 0.5% in the Afanasievo. (**B**) The Yamnaya had nearly half their ancestry from CHG, higher than any Bronze Age Europeans from the Balkans, Italy, or Central/Northern Europe, but their CHG-EHG balance was equal, similar to the Corded Ware/Beaker clusters of Central/Northern Europe and contrasting with Southeastern and Mediterranean Europe, where CHG was significantly higher than EHG. 95% confidence intervals of ±1.96 SE are shown.

steppe pastoralists. The genetic contribution of the second pulse may have been as low as 6.5%, the sum of Anatolian and Levantine ancestry in the Yamnaya, or as high as 53.1%, the totality of the combined Caucasus hunter-gatherer and Anatolian/Levantine ancestry. The low end is unlikely because Caucasus hunter-gatherer ancestry was ubiquitous in

West Asia during the Chalcolithic period and some of it should be added to the 6.5% figure. The high end is also unlikely because it suggests that all Caucasus hunter-gatherer ancestry flowed northward with the second pulse, thus ignoring the evidence for its independent flow into the Eneolithic steppe. Our modeling suggests intermediate values of ~21 to 26% (table S28), in the middle of the 6.5 to 53.1% range, an estimate that may be updated in the future as better proximate sources in both West Asia and the steppe come to light.

Archaeological evidence documents how western steppe populations interacted with European farmer groups such as the Cucuteni-Trypillia and Globular Amphora cultures, and it was previously suggested that ancestry from such groups contributed to the ancestry of the Yamnaya (*17*). Our genetic results contradict this scenario because European farmers were themselves a mixture of Anatolian Neolithic and European hunter-gatherer ancestry, but the Yamnaya lacked the European hunter-gatherer ancestry differentiating European from West Asian farmers, and had an ~1:1 ratio of Levantine-to-Anatolian ancestry in our five-way model, contrasting with the over-whelming predominance of Anatolian ancestry in European farmers. The Caucasus hunter-gatherer/Eastern hunter-gatherer/Western hunter-gatherer/Anatolian Neolithic model of (*17*) fails ($P < 1 \times 10^{-10}$) because it under-estimates shared genetic drift with Levantine farmers ($Z = 5.6$), whose contribution into the Yamnaya cannot be explained under that model. These results shift the quest for the ancestral origins of a component of Yamnaya ancestry firmly to the south of the steppe and the eastern wing of the Southern Arc. Determining the proximate source of the two move-ments into the steppe from the south will depend on further sampling across the Anatolia-Caucasus-Mesopotamia-Zagros area where populations with variations of the three com-ponents existed. Similarly, on the steppe side, study of Eneolithic (pre-Yamnaya) individuals could disclose the source dynamics of Caucasus hunter-gatherer infiltration northward and identify the likely geographical region for the emergence of the distinctive Yamnaya cluster, which we show has an autosomal signal of admixture dating to the mid-5th millennium BCE [fig. S5 and (*19*)], coinciding with the direct evidence of the first southern influence pro-vided by the Eneolithic individuals of the steppe.

The role of Yamnaya-like populations in spreading both Eastern hunter-gatherer and West Asian ancestry into mainland Europe has been previously recognized (*8*), but it has also become apparent that some of the latter entered Europe independently of steppe ex-pansions into the Aegean (*9, 16*), Sicily (*20*), and even as far west as Iberia (*21*) by the Bronze Age. We observe that the Caucasus

minus Eastern hunter-gatherer ancestry difference in the Yamnaya is ~0% (Fig. 4B), and this allows us to both test whether steppe migrants into mainland Europe may have originated from a different steppe population (with a nonequal balance of Caucasus and Eastern hunter-gatherer components) and whether additional migrations (with either more Eastern or Caucasus hunter-gatherer ancestry, thus shifting the difference away from zero) occurred. We find that the Corded Ware and Bell Beaker complex individuals from Europe are all consistent with a balanced presence of the two components (consistent with having been transmitted through a Yamnaya-like population). Even in the early Corded Ware from Bohemia, where a third "northern" source has been suggested to have been substantially involved (22), the difference is one of a small 3.1 ± 2.1% excess of Eastern hunter-gatherer ancestry, which is entirely consistent with being transmitted entirely by the Yamnaya to

the limits of the resolution of our statistical analysis. This is not the case for Southeastern Europe, where Bronze Age individuals had an excess of Caucasus over Eastern hunter-gatherer ancestry not only in the Aegean (~17% in both Minoans and Mycenaeans) (16), but throughout the Balkan peninsula (Fig. 3B), where the overall Bronze Age excess is 7.4 ± 1.7% (with by-country estimates of ~4 to 13%). A possible explanation for this excess is the existence of a small 5.2 ± 0.6% Caucasus hunter-gatherer component in the Neolithic substratum of Southeastern Europe (Fig. 4A); we estimated that this proportion is ~0 to 1% in four separate Early Neolithic populations from Hungary (Starčevo-Körös cultural complex), France, Spain, and the Linearbandkeramik of Austria, Germany, and Hungary (3, 23–30). Thus, the Bronze Age Caucasus hunter-gatherer ancestry in Southeastern Europe compared with Central/Northern/Western Europe may replicate this contrast from the Neolithic. However,

the even higher levels observed in the Aegean [Fig. 3B and (6)] suggest additional gene flow after the Neolithic by the time of the Early Bronze Age (31).

Interplay of local, steppe, and West Asian ancestries in Southeastern Europe

Southeastern Europe interfaces geographically with both the Eurasian steppe and Anatolia, and its genetic history (Fig. 4) bears traces of both connections, starting from the partial replacement of its local Balkan hunter-gatherers by Anatolian Neolithic farmers beginning ~8500 years ago, followed by the expansion of Eastern hunter-gatherer-ancestry–bearing steppe populations ~5000 years ago (3). Although the Bronze Age was a period of partial homogenization in Anatolia, as we have seen, in Southeastern Europe, it was a time of substantial contrasts.

One aspect of this heterogeneity was the retention of the local Balkan hunter-gatherer
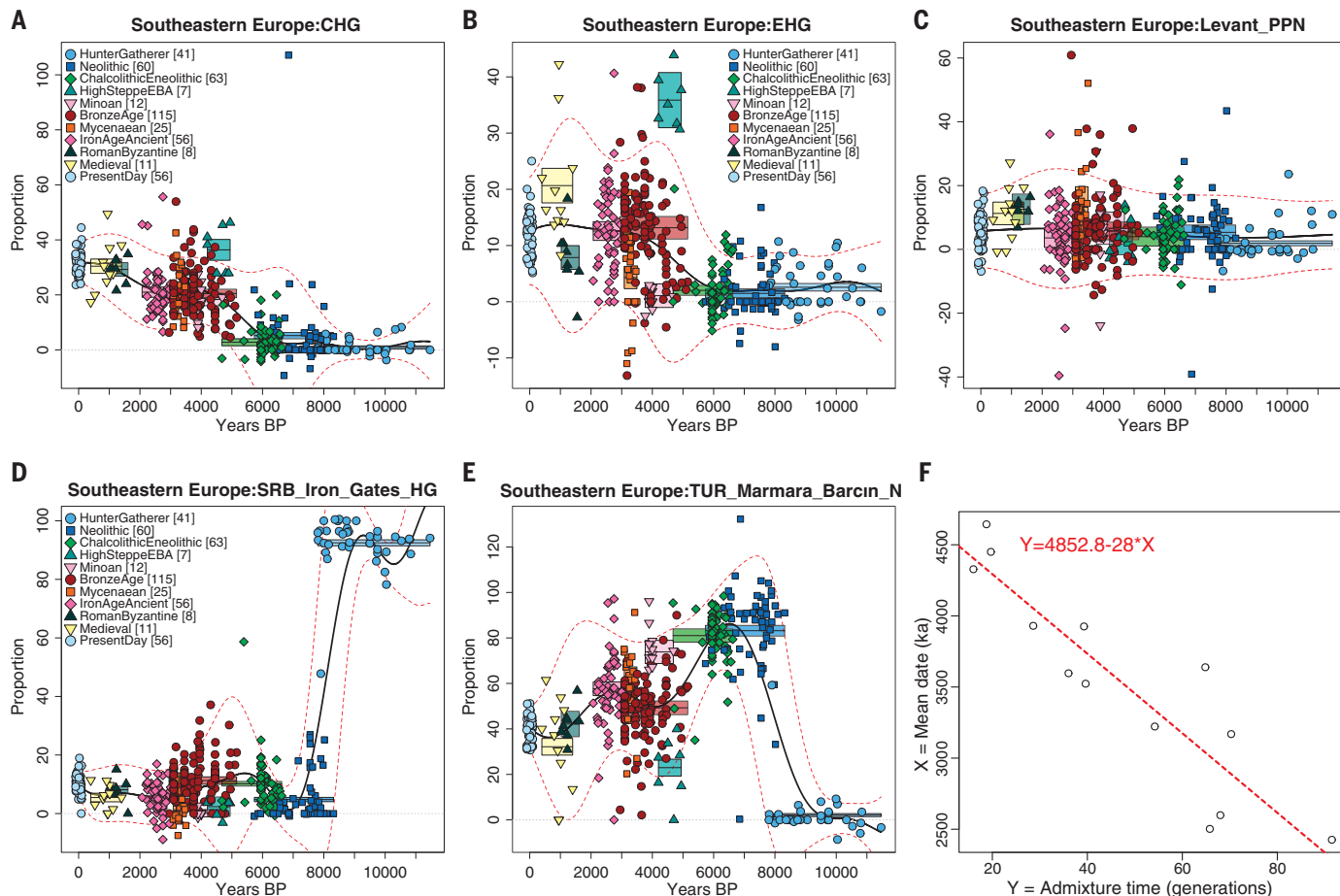
Fig. 4. Genetic heterogeneity in Southeastern Europe after the Yamnaya expansion. (**A** to **E**) Five components of ancestry in Southeastern Europe. The replacement of hunter-gatherer by early farmer ancestry [(D) and (E)] was followed by the rise of CHG and EHG ancestry over the past 5000 years [(A) and (B)], with Levantine ancestry being relatively unimportant and showing no discernible temporal pattern (C). In (**F**), we show a linear regression of population

dates (using directly radiocarbon-dated individuals for each population) on admixture times in generations; more recent populations have older admixture times, and the regression places admixture between populations related to the Southeast European Neolithic and Yamnaya at 4853 ± 205 years ago and the generation length at 28 ± 4 years, virtually identical to its independent empirical estimation of 28 years.

ancestry itself, which was detected only in the Balkans (within the Southern Arc), thus precluding any substantial migration from the area to the rest of the Southern Arc. Balkan hunter-gatherer ancestry was variable during the Bronze Age and related to geography. A marked contrast is found within Romania, where our new data show that it makes up ~12% of the ancestry of 42 individuals from the Bodrogkeresztúr Chalcolithic and ~24 to 30% in 10 Bronze Age individuals from Cârlomăneşti (Arman) and from Ploieşti and Târgşoru Vechi south of the Carpathian Mountains. Together with another Bronze Age individual from Padina in Serbia [2460 to 2296 calibrated (cal) BCE] near the Iron Gates, whose Balkan hunter-gatherer ancestry was ~37%, these results prove substantial hunter-gatherer ancestry preservation in the North Balkans postdating the arrival of both Anatolian Neolithic and steppe ancestry in the region. This contrasts with the southern end of the Balkan peninsula in the Aegean (6), where neither the Neolithic nor the Bronze Age populations had any significant Balkan hunter-gatherer ancestry, raising the question of whether the region's pre-Neolithic population was more similar to that of the North Balkans (Balkan hunter-gatherer-like) or Western Anatolia (and thus similar to the Neolithic population).

The key driver of the Bronze Age heterogeneity was the appearance of Eastern hunter-gatherer ancestry that became ubiquitous in Southeastern Europe after its sporadic Chalcolithic appearance (3). This is most evident (~31 to 44%) in Moldova at several Bronze Age sites, including those of the Catacomb and Multi-cordoned Ware cultures, and individuals from Romania (Trestiana and Smeeni) on the eastern/southeastern slopes of the Carpathians, which contrast with the high-Balkan hunter-gatherer group from Arman. We also detect a contrast between Catacomb culture individuals from Moldova and those from the Caucasus (17), driven by an individual from Purcari with substantial (17 ± 4%) Anatolian Neolithic ancestry, suggesting some heterogeneity within this culture on opposite sides of the Black Sea. For the rest of the Balkans, the amount of Eastern hunter-gatherer ancestry is ~15% and drops to ~4% in Mycenaean Greece and to negligible levels in Minoan Crete (6, 16).

Our study identifies a "high-steppe ancestry" set of individuals, a term we use to refer to individuals from the Balkans during the Early Bronze Age who had unusually high proportions of Eastern hunter-gatherer ancestry compared with their contemporaries (Fig. 4B). This includes two previously published individuals from Nova Zagora in Bulgaria and Vucedol in Croatia (3), as well as five newly reported individuals, including an Early Bronze Age individual from Çinamak in Albania (2663 to 2472 calBCE) and four that are culturally

Yamnaya: one from Vojlovica-Humka in Serbia, two from Boyanovo, and one from Mogila in Bulgaria. In aggregate, this group of Balkan individuals has 35.9 ± 2.5% Eastern hunter-gatherer, 36.4 ± 1.9% Caucasus hunter-gatherer, and 23.0 ± 1.9% Anatolian Neolithic ancestry compared with the Yamnaya cluster individuals (46.1 ± 1.0%, 46.6 ± 1.6%, and 3.0 ± 1.0%, respectively), i.e., the same Caucasus/Eastern hunter-gatherer balance as the Yamnaya but diluted by about one-fifth by local Neolithic ancestry of ultimately Anatolian origin.

When we use DATES (19) to date the admixture of steppe ancestry in populations of Southeastern Europe (Fig. 5F and fig. S6), we arrive at an estimate that this took place ~4850 years ago, i.e., precisely after the Yamnaya expansion, and within the time frame of our "high-steppe" cluster individuals. This suggests that (as a first approximation) steppe ancestry in Southeastern Europe from the Bronze Age onward was largely mediated by descendants of Yamnaya and local Balkan populations and not by earlier waves out of the steppe that affected the region sporadically. This admixture need not have taken place in one locality, as indicated by the presence of Yamnaya-like individuals in several regions of the Balkans, spatially beyond both the cultural transition zone between steppe pastoralist and settled populations (32), and the geographical one from the Eastern European flatlands into mountainous areas.

Armenia: Fluctuating steppe ancestry against a persistent West Asian genetic background

Armenia is situated in the highlands of West Asia to the east of Anatolia and to the south of the Caucasus mountains separating West Asia from the Eurasian steppe to the north. When we examine the trajectory of ancestry there (Fig. 5), we observe that the local Caucasus hunter-gatherer–related ancestry (Fig. 5A) has always been the most important component of the population from the Neolithic to the present, making up ~50 to 70% of ancestry over the past 8000 years. As in Anatolia, the two other components of West Asian ancestry had a strong presence as well, making up most of the remainder.

The most noticeable feature of the history of Armenia compared with all other Asian regions of the Southern Arc is the tentative appearance of Eastern hunter-gatherer ancestry in the Chalcolithic at Areni-1 Cave (10) ~6000 years ago (Fig. 5B), followed by its disappearance ~5000 years ago with the Early Bronze Age Kura-Araxes culture and its reappearance at the Middle Bronze Age, when a level of ~14% was followed by ~10% in the Late Bronze Age and Iron Age and then diluted to ~7% by the Urartian period of the first half of the 1st millennium BCE and to the ~1 to 3% levels observed since the second half of that millen-

nium at sites such as Aghitu and through the medieval period (at Agarak) down to present-day Armenians. When we compare the Middle/Late Bronze Age individuals from Armenia (when Eastern hunter-gatherer ancestry was highest and from which we have individuals from >20 sites) with other West Asian European and steppe populations (Fig. 5E), it is evident that Armenia is an outlier. Populations from Armenia have significantly more such ancestry than all surrounding populations: Anatolia and the Levant, where this ancestry is undetected during the Bronze Age; Iran, where it makes up ~2% overall; and even the Maykop cluster populations of the North Caucasus (17), where it reaches ~3%. These analyses in Armenia show that Eastern hunter-gatherer ancestry flowed from the steppe not only west of the Black Sea into Southeastern Europe, attaining its minimum in the Aegean and east of it, but also across the Caucasus into Armenia. However, substantial proportions of steppe ancestry spread no further into Anatolia from either west or east.

The appearance of Eastern hunter-gatherer ancestry at Areni-1 Cave is the first known genetic influence of peoples of the Eurasian steppe on West Asia, although with our current sparse sampling of the Eneolithic steppe, we do not know the precise geographical source of this ancestry within the steppe. The Areni individuals date to the same 5th millennium BCE, in which we saw that the Eneolithic steppe came to be influenced by Caucasus hunter-gatherer–related ancestry from the south and to which our admixture dating of Yamnaya origins also points. However, it was only during the Middle/Late Bronze Age that Eastern hunter-gatherer ancestry became entrenched in Armenia, at least for a while, forming an "enclave" of steppe influence in West Asia that eventually dissipated during the 1st millennium BCE. This period of relatively high-steppe ancestry corresponds to the "Lchashen-Metsamor" culture of the Bronze-to-Iron Age (1). Linkage disequilibrium dating of steppe admixture (Fig. 5F) in our extensive set of individuals of average late 2nd millennium BCE date suggests it occurred a millennium and a half earlier, at the middle of the 3rd millennium BCE, and thus in parallel to the transformation of mainland Europe and the Balkans. In Armenia itself, the mid-3rd millennium BCE corresponds to the demise of the Kura-Araxes culture and its succession by the "Early Kurgan" culture, followed during the end of that millennium by the "Trialeti-Vanadzor" complex from which an individual from Tavshut (2127 to 1900 calBCE) already has the ~10% Eastern hunter-gatherer ancestry of the Lchashen-Metsamor population, the first documented steppe descendant in Armenia two millennia after the Chalcolithic. The analysis of Y chromosomes to which we now turn provides an independent line of evidence
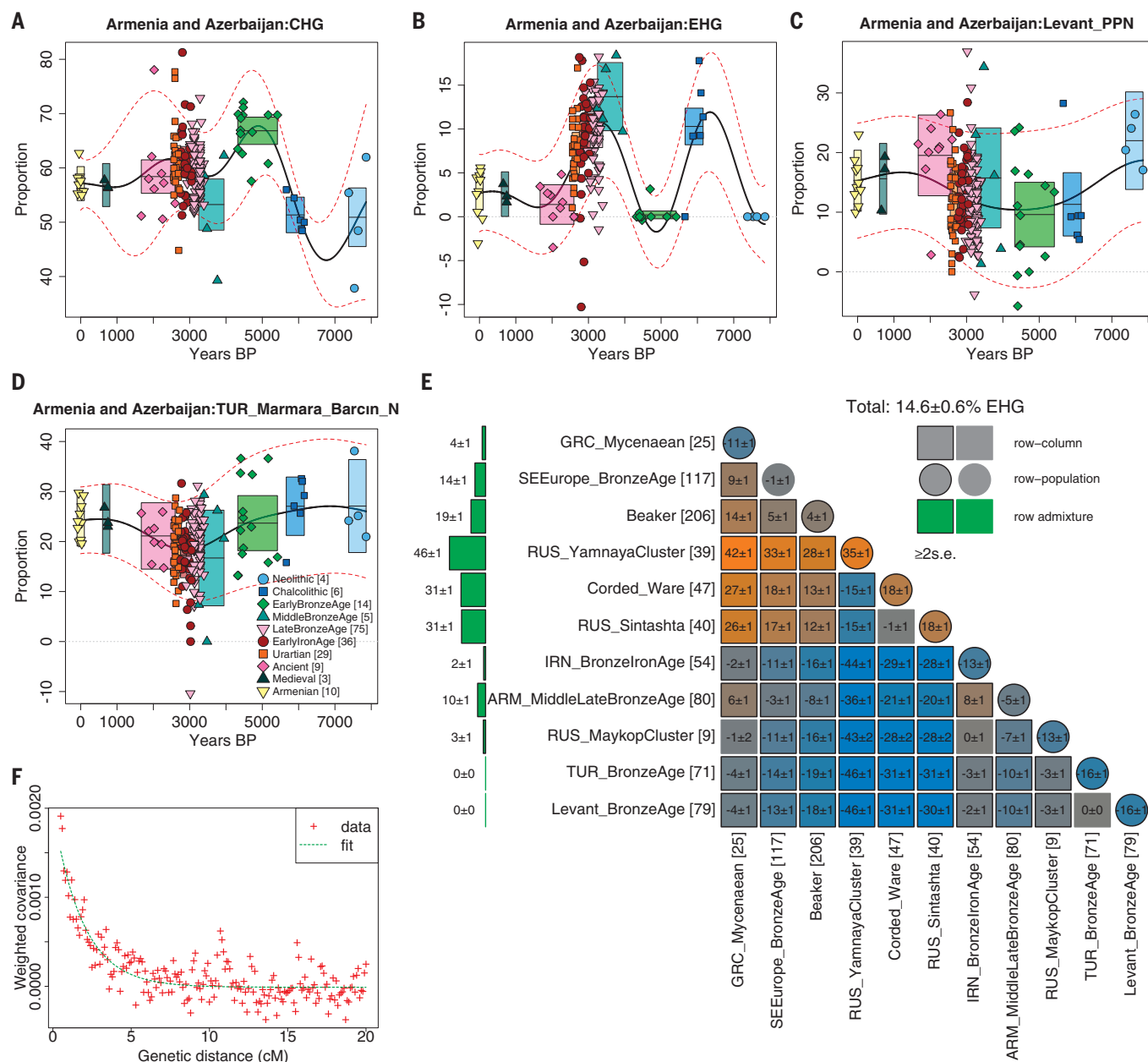
Fig. 5. A genetic history of Armenia. Shown are changes in the four components of ancestry. (**A**) CHG is the most important component in all ages, rising to its maximum in the Kura-Araxes culture of the Early Bronze Age. (**B**) EHG ancestry first appears in the Chalcolithic at Areni Cave, disappears during the Kura-Araxes period, reappears strongly in the Middle-to-Late Bronze Age period, and decreases to about one-third of its peak value by ~2000 years ago. (**C** and **D**) Levantine and Anatolian ancestry were present in all periods as minority components. Balkan hunter-gatherer ancestry (not shown) is <1% in all periods. All individuals shown are from Armenia save for two Neolithic and a Chalcolithic individual previously published from Azerbaijan. (**E**) During the Middle-to-Late Bronze Age peak, Armenia had more EHG ancestry than its neighbors in West Asia (Anatolia, the Levant, and Iran). (**F**) C[14]-dated Bronze-to-Iron Age individuals from Armenia admixed 52.2 ± 8.0 generations (1460 ± 224 years) before their average date of 1119 BCE, or ~2579 BCE (mid-3rd millennium BCE), assuming a generation length of 28 years (*54*). We use Early Bronze Age Armenia and Yamnaya cluster individuals from Russia as proxy sources.

for a link between the Yamnaya and populations of Armenia after this 3rd millennium BCE reappearance of Eastern hunter-gatherer ancestry.

Y-chromosome links between the steppe and West Asia in their genome-wide context

Y-chromosome variation (tables S29 to S34 and figs. S77 and S79) (*1*) can be used to pro-

vide confident upper bounds on the date when two populations shared ancestors because the large number of mutations that can be analyzed over almost 10 million nucleotides of alignable sequence means that the split times in the genealogy are accurately known. The ancient individuals' Y-chromosome analysis also has the potential to provide insight into social processes.

Subclades of Y-chromosome haplogroup R-L389 are particularly informative for tracing connections between the Southern Arc and the Eurasian steppe (Fig. 6). First, haplogroup R-V1636, with an inferred common ancestor in the 5th millennium BCE, documents gene flow between the steppe and the Southern Arc in the Eneolithic/Chalcolithic period (Fig. 6B). R-V1636 is present in two individuals
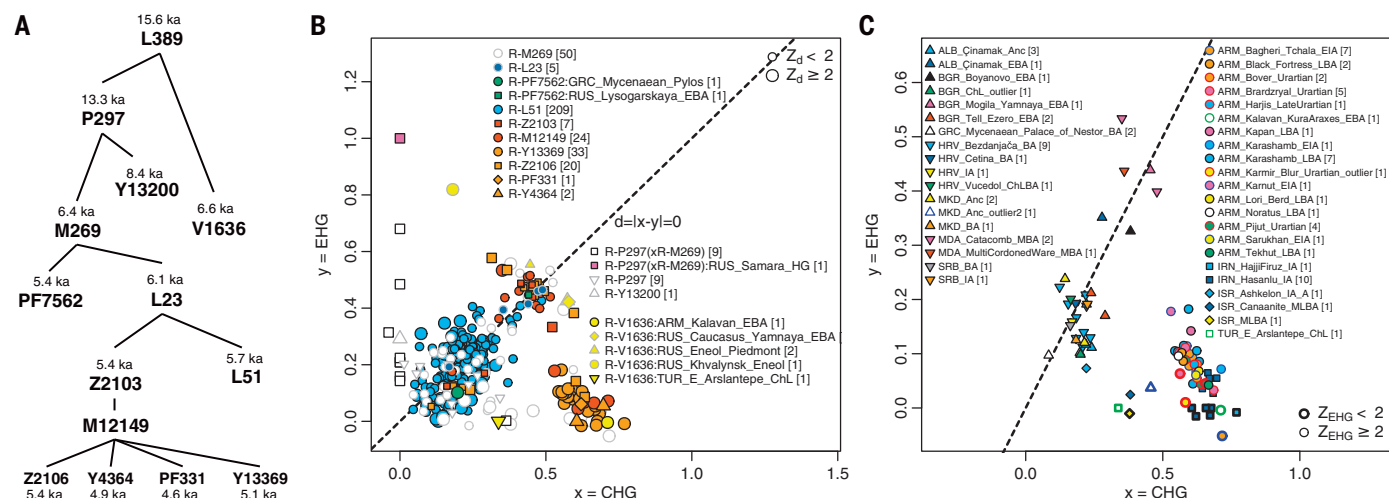
Fig. 6. Y-chromosome links between the Southern Arc and the Eurasian steppe. (**A**) Phylogeny of haplogroup R-L389 (R1b1a1) with TMRCA estimates of yfull. com. (**B**) CHG/EHG ancestral composition of R-L389 Y-chromosome individuals. (**C**) R-L389 individuals from the Southern Arc, representing a subset of the individuals plotted in (B). Individuals >2000 years old are shown. ka, thousand years ago.

from the Late Chalcolithic at Arslantepe (Turkey) (*14*) and the Early Bronze Age in Armenia at Kalavan (*10*). It is also found in the piedmont of the North Caucasus at Progress-2 (*17*), the open steppe at Khvalynsk II (*9*), and the Single Grave Culture of Northern Europe (Gjerrild) (*33*). The individuals from Armenia and Arslantepe lack any detectible Eastern hunter-gatherer autosomal ancestry (Fig. 6C), which is maximized in the Khvalynsk individuals, an observation that provides some evidence for a southern origin for the R-V1636 haplogroup (we caution, however, that the haplogroup occurs earlier in several sites in the north, which could be consistent with an alternative scenario in which male migrants from the steppe introduced it into Southern Arc populations during the Chalcolithic, but their autosomal genetic legacy was diluted by the much more numerous locals). The earliest individuals from the R-L389 clade belong to the R-P297 sister clade of R-V1636, including the hunter-gatherer from Lebyazhinka IV (*8, 9*) and hunter-gatherers from the Baltic region (*3*), both without Caucasus hunter-gatherer ancestry, suggesting an Eastern European origin of this clade that would eventually give rise to the R-M269 clade that spread extremely widely in the Bronze Age.

Haplogroup R-M269, which is inferred to have a shared common ancestor in the 5th millennium BCE, is crucial for understanding steppe expansions because it was the dominant lineage of the Yamnaya-Afanasievo group (*4, 8, 34*) in its 4th millennium BCE R-Z2103→R-M12149 sublineage. In the Balkans, a group of six Bronze Age individuals from the 3rd millennium BCE carrying R-M269 (Fig. 6C) are associated with >30% Eastern hunter-gatherer ancestry, and this includes not only Catacomb and Multi-cordoned Ware individuals from Moldova, adjacent to the steppe, but also

from farther south, including two Yamnaya males from Bulgaria (Boyanovo and Mogila, the latter associated with Yamnaya burial custom and with the R-Z2103 haplogroup typical of the steppe Yamnaya) and one from Albania (Çinamak) belonging to the high-steppe ancestry group. By the Late Bronze Age (late 2nd millennium BCE) and later, no high-steppe ancestry individuals are observed, but steppe-associated Y chromosomes persist, including R-Z2106, a lineage that links North Macedonia (Ulanci-Veles), Albania (Çinamak), the steppe, and Armenia. The population of Southeastern Europe contrasts strongly with those of the Central/Northern Europe and Eurasian steppe archaeological cultures of ~3000 to 2000 BCE that were strongly associated with particular Y-chromosome lineages: Afanasievo (*4, 34*) with the same R-Z2103 as the Yamnaya, Corded Ware/Fatyanovo/Sintashta (*4, 8, 34, 35*) with R-M417, and Beaker (*36*) with R-L51. In Southeastern Europe during the Bronze Age, we detect 32/30/21/11 Y chromosomes belonging to haplogroups R/J/I/G linking it with Central/Northern Europe and the steppe/West Asia/local hunter-gatherers/Anatolian-European Neolithic farmers, respectively. Together with the extraordinary heterogeneity in autosomal ancestry in the Balkans, a picture emerges of a fragmented genetic landscape that may well parallel the poorly understood linguistic diversity in the ancient Balkans, which among Indo-European languages includes Paleo-Balkan speakers before the spread of Latin and Slavic, with Albanian as the only surviving representative. Did the early Indo-European language become successful in Southeastern Europe because it functioned as a "lingua franca," facilitating communication among speakers of the diverse languages of previous farmer and hunter-gatherer populations?

Our newly reported data reveal that a large proportion of individuals in Armenia and Northwest Iran belonged to the R-Z2103→R-M12149 haplogroup during the 2nd and early 1st millennium BCE, providing a genetic link with the Yamnaya in these regions where no archaeological presence of the Yamnaya culture itself is attested. It definitely represents a more direct link than either R-V1636 or the early appearance of Eastern hunter-gatherer ancestry at Areni-1 cave in Armenia (*10*) during the Chalcolithic at the end of the 5th millennium BCE, which provides evidence of converse movement of Caucasus hunter-gatherer ancestry into the steppe Eneolithic.

Despite the Y-chromosome movement southward attested by our data, any association between R-haplogroup bearers and Eastern hunter-gatherer ancestry was lost south of the steppe because these had similar proportions of Eastern hunter-gatherer ancestry as I-Y16419 bearers (the second most prevalent lineage in Armenia). Two Bronze-to-Iron Age sites with substantial sample sizes [unrelated males from Bagheri Tchala (*n* = 7) and Noratus (*n* = 12)] have contrasting haplogroup distributions dominated by R-M12149 and I-Y16419, respectively (Fisher's exact test *P* < 0.001), suggesting founder events, high genetic drift, or a patrilocal mating system ~1000 BCE in Armenia. During the same period at Hasanlu in Northwest Iran, many individuals have no trace of Eastern hunter-gatherer ancestry at all despite the presence of R-M12149 there (*6*), suggesting that the initial association of this lineage with Eastern hunter-gatherer ancestry on the steppe had vanished as R-M12149 bearers reproduced with Southern Arc individuals without Eastern hunter-gatherer ancestry (Fig. 6C).

We observe that, on the steppe, R-M12149 Y chromosomes (within haplogroup R1b) at

the beginning of the 3rd millennium BCE, associated with the Yamnaya, were replaced by the beginning of the next millennium by R-Z93 Y chromosomes (within haplogroup R1a), associated with Corded Ware/Fatianovo (35) steppe descendants such as those of the Sintashta culture (34). Genetic data cannot distinguish whether this Y-chromosome replacement was the result of competition between patrilineal groups from the steppe, one of which may have had cultural adaptations such as usage of an improved variety of domesticated horse (37), or whether one group simply filled an ecological niche vacated by earlier groups. A fuller understanding of the reason for this profound genetic change requires combined analysis of genetic and archaeological data.

Whatever the reason for their demise on the steppe itself, the Yamnaya-descended R-Z2103 patrilineages survived in Armenia down to the present day, where this clade is present in appreciable frequencies in all studied Armenian groups (38) despite the substantial dilution of autosomal steppe ancestry documented in our study. The persistent and lasting presence of Yamnaya patrilineal descendants in Armenia contrasts with mainland Europe and South Asia, where steppe ancestry was introduced by people who were not patrilineal descendants of the dominant R-M12149 lineage of the Yamnaya population. Instead, they belonged to different descent groups who had received autosomal steppe admixture while carrying different predominant Y-chromosome lineages. Armenia also contrasts with Anatolia, for which no R-M269 Y-chromosomes are observed at all during the Chalcolithic, Bronze Age, or Ancient (pre-Roman) periods [$n = 80$ unrelated individuals; 95% confidence interval (CI): 0 to 4.5%] and in which haplogroups J (36 individuals) and G (17 individuals) are most common. Haplogroup J is still common at a frequency of about one-third in present-day people from Turkey (39), having achieved such prominence despite occurring in only in one in 18 Neolithic male individuals from Barcın and Ilıpınar in the Marmara region during the pre-Chalcolithic period. A likely explanation for the haplogroup J increase is that it accompanied the spread of Caucasus hunter-gatherer ancestry inferred by our admixture analysis (Fig. 2). This inference is made plausible by the fact that both Caucasus hunter-gatherer individuals from Kotias and Satsurblia (7) and a Mesolithic individual from Hotu Cave (10, 34) in Iran belonged to this lineage, suggesting its very old presence in the Caucasus/Iran region, and in contrast with haplogroup G, which occurred in the majority (10/18) of individuals from the Neolithic Marmara region. By the Chalcolithic, haplogroups G and J were ubiquitous in Anatolia, each making up 10/28 males from that period, paralleling the homogenization that had occurred by that time.

The Indo-Hittite hypothesis in the light of genetic data

We discuss the implications of our genetic findings for hypotheses about the origins and spread of Indo-European and Anatolian languages. We also highlight a caveat: In contrast to findings about movements of people, the relevance of genetics to debates about language origins is more indirect because languages can be replaced with little or no genetic change and populations can migrate and mix with little or no linguistic change. Nevertheless, the detection of migration is important because it identifies a plausible vector for language change (40).

The discoveries of massive migrations from the steppe both westward into Central and Western Europe (4, 8), and eastward into South Siberia (4) and Central/South Asia (34), have provided powerful evidence for the theory of steppe Indo-European origins by linking populations all the way from Northwest Europe (36) to India and China through common steppe ancestry. The present study adds further support to the theory by the discovery of ubiquitous ancestry from the steppe in the Bronze Age Balkans [where, indubitably, Indo-European Paleo-Balkan languages such as Thracian and Illyrian (41) were spoken], including individuals of predominantly steppe ancestry; by documenting the ubiquity of steppe ancestry in Bronze and Iron Age Armenia where Armenian is first attested and links between Armenia, the steppe, and the Balkans; and by the further documentation of steppe ancestry in the Aegean (6) during the Mycenaean period when the Greek language is first attested, albeit at lower levels. All ancient and present-day branches of the Indo-European language family can be derived or at least linked to the early Bronze Age Yamnaya pastoralists of the steppe or genetically similar populations.

A link to the steppe cannot be established for the speakers of Anatolian languages because of the absence of Eastern hunter-gatherer ancestry in Anatolia (4, 10, 14, 16), which our study reinforces in three ways: (i) by documenting its paucity in ~100 new Anatolian individuals from the Chalcolithic to pre-Roman antiquity, (ii) by contrasting western parts of Anatolia with its immediate Aegean-Balkan neighbors to the west, and (iii) by contrasting eastern/northern parts of Anatolia with its neighbors in Armenia in the east. Certainly, the absence of Eastern hunter-gatherer ancestry in Anatolia can never be categorically proven (because more sampling can always disclose some such ancestry); however, at present, and despite extensive sampling, such ancestry is not detected either at possible entry points (west and east by land or even north by sea) or in the population as a whole.

The Indo-Hittite hypothesis, first proposed by E. H. Sturtevant in 1926 (42), has been partially supported by more modern phylolinguistic analyses, indicating that Anatolian languages such as Hittite are basal to the rest of the Indo-European family tree (43) and suggesting an early split between the two. We have shown that Anatolia was indeed transformed by the Late Chalcolithic through the spread of Caucasus hunter-gatherer–related ancestry to its westernmost edges, as were apparently Eneolithic populations of the steppe, which included also Anatolian/Levantine–related ancestry by the time of the formation of the Yamnaya pastoralists. It is premature to identify the proximate sources of these movements before all the candidate source populations of Anatolia, North Mesopotamia, Western Iran, Armenia, Azerbaijan, and the Caucasus have been adequately sampled.

Our analyses show that there were at least two gene flows from two groups related to West Asians into the steppe, which transformed the steppe's population and may have induced linguistic change there. The reverse movement is more tentative, with early influences from the north such as at Areni Cave (10) or possibly associated with R-V1636 Y-chromosomes, not making a sizable genetic impact on the population of Anatolia. The evidence is consistent with two hypotheses.

Hypothesis A postulates that Proto-Indo-Anatolian (including both Anatolian languages and Proto-Indo-European) was spoken by a population with high Eastern hunter-gatherer ancestry that had a disproportionate linguistic impact on Anatolia while contributing little if any ancestry. In the post–Bronze Age landscape of Anatolia, we do find outliers marked by European or steppe influence (6), but this is a period when Anatolia is influenced by numerous linguistically non-Anatolian Indo-European populations, including Phrygians, Greeks, Persians, Galatians, and Romans, to name only a few. However, in individuals from Gordion, a Central Anatolian city that was under the control of Hittites before becoming the Phrygian capital and then coming under the control of Persian and Hellenistic rulers, the proportion of Eastern hunter-gatherer ancestry is only ~2%, a tiny fraction for a region controlled by at least four different Indo-European–speaking groups. In medieval times, Central Asian ancestry associated with Turkic speakers was added (6), and it persists to the present. Clearly, Anatolia has not been impervious to linguistic change during its recorded history, and the harbingers of that change are also detected genetically, even if as outliers. By contrast, the complete absence of Eastern hunter-gatherer ancestry in the Chalcolithic and Bronze Age either as isolated outliers or as a general low-level presence challenges the steppe theory to suggest a plausible mechanism of how a population that made little, if any, genetic impact could nonetheless effect

large-scale linguistic change. A common vocabulary for wheeled vehicles is not attested for both Anatolian languages and the rest of the Indo-European languages (*44*), thus potentially removing a technological advantage regarded as potentially crucial in the dissemination of Indo-European languages (*45*).

Hypothesis B postulates that Proto-Indo-Anatolian was spoken by a population of West Asia and the Caucasus with low or no Eastern hunter-gatherer ancestry, which affected both Anatolia and the steppe. Hypothesis B may help to explain the linguistic diversity observed in Bronze Age Anatolia in which both Anatolian (Hittite, Luwian, and Palaic) speakers, as well as speakers of other languages including Hattic (a non–Indo-European linguistic isolate of Central/Northern Anatolia) and Hurrian [a non–Indo-European language from Eastern Anatolia and North Mesopotamia related to the later Iron Age Urartian language (*6*)], coexisted. The non–Indo-European Hattic language, attested only in Anatolia, would most economically represent the linguistic substratum, spoken by a population of high Anatolian-related ancestry, whereas the Indo-European Anatolian languages would be spoken by a population of high Caucasus hunter-gatherer–related ancestry. The spread of people of high Caucasus hunter-gatherer ancestry across the peninsula from the east, at least some of whom may have spoken early forms of Anatolian languages, would simultaneously explain both the genetic homogenization before the Late Chalcolithic (Fig. 2) and the coexistence of the two linguistic groups. How many of the peoples associated with the spread of Caucasus hunter-gatherer ancestry spoke Anatolian languages? People speaking other languages related to the diverse non–Indo-European language families of the Caucasus, such as Kartvelian and Northwest/Northeast Caucasian, may have also participated in the westward movements.

As for the steppe, at least two streams of migration from the south (Eneolithic and Yamnaya-specific) present the opportunity for an early (Chalcolithic) split of Yamnaya linguistic ancestors from the Anatolian linguistic ancestors, followed 1000 to 2000 years later by the dispersal of Indo-European languages from the steppe with the expansion of the Yamnaya culture. Linguistic borrowings (*46*) between Proto-Indo-European and other language families such as Kartvelian (spoken primarily in Georgia) could be useful for localizing the Proto-Indo-Anatolian homeland, but these may have alternatively come about by long-range mobility since the Chalcolithic, proven by such evidence as the presence of R-V1636 descendants ~3000 km apart from Khvalynsk to Anatolia during this period. Contributions of Indo-European to Uralic languages (spoken in the forest zone of Eastern Europe and Siberia)

appear to have involved only Indo-Iranian speakers ~4200 years ago (*47*). This is important because it constrains the migratory history of Proto-Indo-Iranian, consistent with genetic evidence (*34*) that it spread through the steppe to South Asia and ruling out the possibility that it spread from West Asia to South Asia over the Iranian plateau. However, the contribution of Indo-Iranian to Uralic languages does not shed light on the deeper question of early Indo-Anatolian origins. A challenge for the theory that Proto-Indo-Anatolian was formed in the south in a Caucasus hunter-gatherer–rich population will be to trace the origins of the autosomal ancestry of the Yamnaya in the Caucasus or West Asia [where some existing proposals place the Proto-Indo-Anatolian homeland (*32*, *48*, *49*)] and to identify the place from which the R-M269 ancestral lineage expanded, because this will be a most plausible secondary homeland of Indo-European expansion outside of Anatolia.

The scenario of a West Asian source of Proto-Indo-Anatolian is consistent with a linguistic analysis (*50*) that places the split of Tocharian from the remaining (Inner Indo-European) languages ~3000 BCE associated with the Yamnaya expansion and the disintegration of the remaining languages during the 3rd millennium BCE, consistent with our inferences of major steppe admixture into the Balkans and Armenia for the subset of Indo-European languages of these regions. The Anatolian split is placed by that study at ~3700 BCE (4314 to 3450 BCE, 95% highest posterior density interval), a period during which the Caucasus hunter-gatherer ancestry first appears as far west as the Chalcolithic individuals from Northwest Anatolia (at Ilıpınar) sampled in our study and during which the flow of Caucasus hunter-gatherer ancestry into the steppe had already commenced.

Overall, we suggest that a scenario in which Anatolian and Indo-European languages are descended from a common West Asian progenitor matches the evidence of population change provided by ancient DNA for four reasons. First, the genetic transformation of Anatolia after the Neolithic and before the Late Chalcolithic (Fig. 2) was a clear opportunity for linguistic spread resulting in the coexistence of Hattic and Anatolian languages. Second, the two transformations of steppe populations during the Eneolithic and before the Bronze Age, with their strong south-north directionality (Fig. 3), were opportunities for linguistic spread and match exactly the Anatolia/Indo-European split inferred by linguists. Third, steppe migrations into regions where Indo-European daughter languages were spoken, such as the Balkans (Fig. 4), Armenia (Fig. 5), Central/Northern Europe (*4*, *8*, *36*), and Central/South Asia (*4*, *34*), were clear opportunities for the disintegration of

Proto-Indo-European and the dispersal of its daughter languages across Eurasia. Fourth, the absence of such migrations into Anatolia (Fig. 2F), in contrast to both neighboring Armenia and Southeastern Europe [Figs. 4 and 5 and (*6*)], makes Anatolia the only exception in the association of steppe ancestry with Indo-Anatolian languages.

This outline of events points toward a concrete research program of investigating the archaeological cultures of West Asia, the Caucasus, and the Eurasian steppe to identify a population driving transformations of both the steppe and Anatolia, linking the two regions. The discovery of such a "missing link" (corresponding to Proto-Indo-Anatolians if our reconstruction is correct) would bring to an end the centuries-old quest for a common source binding through language and some ancestry many of the peoples of Asia and Europe (*41*, *51*).

REFERENCES AND NOTES

1. Detailed information is provided in the supplementary materials.
2. F. Broushaki *et al.*, Early Neolithic genomes from the eastern Fertile Crescent. *Science* **353**, 499–503 (2016). doi: 10.1126/science.aaf7943; pmid: 27417496
3. I. Mathieson *et al.*, The genomic history of Southeastern Europe. *Nature* **555**, 197–203 (2018). doi: 10.1038/nature25778; pmid: 29466330
4. M. E. Allentoft *et al.*, Population genomics of Bronze Age Eurasia. *Nature* **522**, 167–172 (2015). doi: 10.1038/nature14507; pmid: 26062507
5. S. Eisenmann *et al.*, Reconciling material cultures in archaeology with genetic data: The nomenclature of clusters emerging from archaeogenomic analysis. *Sci. Rep.* **8**, 13003 (2018). doi: 10.1038/s41598-018-31123-z; pmid: 30158639
6. I. Lazaridis *et al.*, A genetic probe into the ancient and medieval history of Southern Europe and West Asia. *Science* **377**, 940–951 (2022).
7. E. R. Jones *et al.*, Upper Palaeolithic genomes reveal deep roots of modern Eurasians. *Nat. Commun.* **6**, 8912 (2015). doi: 10.1038/ncomms9912; pmid: 26567969
8. W. Haak *et al.*, Massive migration from the steppe was a source for Indo-European languages in Europe. *Nature* **522**, 207–211 (2015). doi: 10.1038/nature14317; pmid: 25731166
9. I. Mathieson *et al.*, Genome-wide patterns of selection in 230 ancient Eurasians. *Nature* **528**, 499–503 (2015). doi: 10.1038/nature16152; pmid: 26595274
10. I. Lazaridis *et al.*, Genomic insights into the origin of farming in the ancient Near East. *Nature* **536**, 419–424 (2016). doi: 10.1038/nature19310; pmid: 27459054
11. I. Lazaridis *et al.*, Ancient DNA from Mesopotamia suggests distinct Pre-Pottery and Pottery Neolithic migrations into Anatolia. *Science* **377**, 982–987 (2022).
12. R. Yaka *et al.*, Variable kinship patterns in Neolithic Anatolia revealed by ancient genomes. *Curr. Biol.* **31**, 2455–2468.e18 (2021). doi: 10.1016/j.cub.2021.03.050; pmid: 33857427
13. G. M. Kılınç *et al.*, The demographic development of the first farmers in Anatolia. *Curr. Biol.* **26**, 2659–2666 (2016). doi: 10.1016/j.cub.2016.07.057; pmid: 27498567
14. E. Skourtanioti *et al.*, Genomic history of Neolithic to Bronze Age Anatolia, Northern Levant, and Southern Caucasus. *Cell* **181**, 1158–1175.e28 (2020). doi: 10.1016/j.cell.2020.04.044; pmid: 32470401
15. P. de Barros Damgaard *et al.*, The first horse herders and the impact of early Bronze Age steppe expansions into Asia. *Science* **360**, eaar7711 (2018). doi: 10.1126/science.aar7711; pmid: 29743352
16. I. Lazaridis *et al.*, Genetic origins of the Minoans and Mycenaeans. *Nature* **548**, 214–218 (2017). doi: 10.1038/nature23310; pmid: 28783727
17. C.-C. Wang *et al.*, Ancient human genome-wide data from a 3000-year interval in the Caucasus corresponds with eco-geographic regions. *Nat. Commun.* **10**, 590 (2019). doi: 10.1038/s41467-018-08220-8; pmid: 30713341

18. K. Kristiansen, "The archaeology of Proto-Indo-European and Proto-Anatolian: Locating the split," in *Dispersals and Diversification: Linguistic and Archaeological Perspectives on the Early Stages of Indo-European*, M. Serangeli, T. Olander, Eds. (Brill, 2019), pp. 157–165.

19. M. Chintalapati, N. Patterson, P. Moorjani, Reconstructing the spatiotemporal patterns of admixture during the European Holocene using a novel genomic dating method. bioRxiv 2022.2001.2018.476710 (2022). doi: 10.1101/2022.01.18.476710

20. D. M. Fernandes *et al.*, The spread of steppe and Iranian-related ancestry in the islands of the Western Mediterranean. *Nat. Ecol. Evol.* **4**, 334–345 (2020). doi: 10.1038/s41559-020-1102-0; pmid: 32094539

21. V. Villalba-Mouco *et al.*, Genomic transformation and social organization during the Copper Age-Bronze Age transition in southern Iberia. *Sci. Adv.* **7**, eabi7038 (2021). doi: 10.1126/sciadv.abi7038; pmid: 34788096

22. L. Papac *et al.*, Dynamic changes in genomic and social structures in third millennium BCE central Europe. *Sci. Adv.* **7**, eabi6941 (2021). doi: 10.1126/sciadv.abi6941; pmid: 34433570

23. S. Brunel *et al.*, Ancient genomes from present-day France unveil 7,000 years of its demographic history. *Proc. Natl. Acad. Sci. U. S. A.* **117**, 12791–12798 (2020). doi: 10.1073/pnas.1918034117; pmid: 32457149

24. R. Fregel *et al.*, Ancient genomes from North Africa evidence prehistoric migrations to the Maghreb from both the Levant and Europe. *Proc. Natl. Acad. Sci. U. S. A.* **115**, 6774–6779 (2018). doi: 10.1073/pnas.1800851115; pmid: 29895688

25. I. Lazaridis *et al.*, Ancient human genomes suggest three ancestral populations for present-day Europeans. *Nature* **513**, 409–413 (2014). doi: 10.1038/nature13673; pmid: 25230663

26. M. Lipson *et al.*, Parallel palaeogenomic transects reveal complex genetic history of early European farmers. *Nature* **551**, 368–372 (2017). doi: 10.1038/nature24476; pmid: 29144465

27. I. Olalde *et al.*, A common genetic origin for early farmers from Mediterranean Cardial and Central European LBK Cultures. *Mol. Biol. Evol.* **32**, 3132–3142 (2015). doi: 10.1093/molbev/msv181; pmid: 26337550

28. M. Rivollat *et al.*, Ancient genome-wide DNA from France highlights the complexity of interactions between Mesolithic hunter-gatherers and Neolithic farmers. *Sci. Adv.* **6**, eaaz5344 (2020). doi: 10.1126/sciadv.aaz5344; pmid: 32523989

29. C. Valdiosera *et al.*, Four millennia of Iberian biomolecular prehistory illustrate the impact of prehistoric migrations at the far end of Eurasia. *Proc. Natl. Acad. Sci. U. S. A.* **115**, 3428–3433 (2018). doi: 10.1073/pnas.1717762115; pmid: 29531053

30. V. Villalba-Mouco *et al.*, Survival of Late Pleistocene hunter-gatherer ancestry in the Iberian Peninsula. *Curr. Biol.* **29**, 1169–1177.e7 (2019). doi: 10.1016/j.cub.2019.02.006; pmid: 30880015

31. F. Clemente *et al.*, The genomic history of the Aegean palatial civilizations. *Cell* **184**, 2565–2586.e21 (2021). doi: 10.1016/j.cell.2021.03.039; pmid: 33930288

32. C. Renfrew, *Archaeology and Language: The Puzzle of Indo-European Origins* (CUP Archive, 1990).

33. A. F.-H. Egfjord *et al.*, Genomic Steppe ancestry in skeletons from the Neolithic Single Grave Culture in Denmark. *PLOS ONE* **16**, e0244872 (2021). doi: 10.1371/journal.pone.0244872; pmid: 33444387

34. V. M. Narasimhan *et al.*, The formation of human populations in South and Central Asia. *Science* **365**, eaat7487 (2019). doi: 10.1126/science.aat7487; pmid: 31488661

35. L. Saag *et al.*, Genetic ancestry changes in Stone to Bronze Age transition in the East European plain. *Sci. Adv.* **7**, eabd6535 (2021). doi: 10.1126/sciadv.abd6535; pmid: 33523926

36. I. Olalde *et al.*, The Beaker phenomenon and the genomic transformation of Northwest Europe. *Nature* **555**, 190–196 (2018). doi: 10.1038/nature25738; pmid: 29466337

37. P. Librado *et al.*, The origins and spread of domestic horses from the Western Eurasian steppes. *Nature* **598**, 634–640 (2021). doi: 10.1038/s41586-021-04018-9; pmid: 34671162

38. O. Balanovsky *et al.*, Genetic differentiation between upland and lowland populations shapes the Y-chromosomal landscape of West Asia. *Hum. Genet.* **136**, 437–450 (2017). doi: 10.1007/s00439-017-1770-2; pmid: 28281087

39. C. Cinnioğlu *et al.*, Excavating Y-chromosome haplotype strata in Anatolia. *Hum. Genet.* **114**, 127–148 (2004). doi: 10.1007/s00439-003-1031-4; pmid: 14586639

40. P. S. Bellwood, *The Encyclopedia of Global Human Migration* (Wiley, 2013), vol. 1, *Prehistory*.

41. J. P. Mallory, *In Search of the Indo-Europeans: Language, Archaeology, and Myth* (Thames and Hudson, 1989).

42. E. H. Sturtevant, On the position of Hittite among the Indo-European languages. *Language* **2**, 25–34 (1926). doi: 10.2307/408784

43. D. Ringe, T. Warnow, A. Taylor, Indo-European and computational cladistics. *Trans. Philol. Soc.* **100**, 59–129 (2002). doi: 10.1111/1467-968X.00091

44. M. J. Kümmel, "Wheel and chariot in early IE: What exactly can we conclude from the linguistic data?" paper presented at the 25th Annual Meeting of the European Association of Archaeologists, Bern, Switzerland, 4–7 September 2019 (abstract #374).

45. D. W. Anthony, *The Horse, the Wheel, and Language: How Bronze-Age Riders from the Eurasian Steppes Shaped the Modern World* (Princeton Univ. Press, 2010).

46. D. W. Anthony, D. Ringe, The Indo-European homeland from linguistic and archaeological perspectives. *Annu. Rev. Linguist.* **1**, 199–219 (2015). doi: 10.1146/annurev-linguist-030514-124812

47. J. Nichols, The origin and dispersal of Uralic: Distributional typological view. *Annu. Rev. Linguist.* **7**, 351–369 (2021). doi: 10.1146/annurev-linguistics-011619-030405

48. T. V. Gamkrelidze, V. V. Ivanov, R. Jakobson, N. Johanna, *Indo-European and the Indo-Europeans, A Reconstruction and Historical Analysis of a Proto-Language and Proto-Culture* (Mouton de Gruyter, 1995).

49. S. A. Grigoriev, *Ancient Indo-Europeans* (RIFEI, 2002).

50. A. S. Kassian *et al.*, Rapid radiation of the inner Indo-European languages: An advanced approach to Indo-European lexicostatistics. *Linguistics* **59**, 949–979 (2021). doi: 10.1515/ling-2020-0060

51. W. Jones, *Discourses Delivered Before the Asiatic Society: And Miscellaneous Papers, on the Religion, Poetry, Literature, Etc., of the Nations of India* (C. S. Arnold, 1824).

52. S. Alpaslan-Roodenberg *et al.*, Ethics of DNA research on human remains: Five globally applicable guidelines. *Nature* **599**, P.41–44 (2021). doi: 10.1038/s41586-021-04008-x; pmid: 34671160

53. M. Binois, R. B. Gramacy, hetgp: Heteroskedastic Gaussian process modeling and sequential design in R. *J. Stat. Softw.* **98**, 1–44 (2021). doi: 10.18637/jss.v098.i13

54. P. Moorjani *et al.*, A genetic method for dating ancient genomes provides a direct estimate of human generation interval in the last 45,000 years. *Proc. Natl. Acad. Sci. U. S. A.* **113**, 5652–5657 (2016). doi: 10.1073/pnas.1514696113; pmid: 27140627

SUPPLEMENTARY MATERIALS

Where Science Gets Social.

AAAS.ORG/COMMUNITY

AAAS' Member Community is a one-stop destination for scientists
and STEM enthusiasts alike. It's "Where Science Gets Social":
a community where facts matter, ideas are big and there's
always a reason to come hang out, share, discuss and explore.

Member COMMUNITY
AAAS

AMERICAN ASSOCIATION FOR THE ADVANCEMENT OF SCIENCE

HUMAN GENETICS

A genetic probe into the ancient and medieval history of Southern Europe and West Asia

Iosif Lazaridis[1,2]*†, Songül Alpaslan-Roodenberg[2,3]*†, Ayşe Acar[4], Ayşen Açıkkol[5], Anagnostis Agelarakis[6], Levon Aghikyan[7], Uğur Akyüz[8], Desislava Andreeva[9], Gojko Andrijašević[10], Dragana Antonović[11], Ian Armit[12], Alper Atmaca[13], Pavel Avetisyan[7], Ahmet İhsan Aytek[14], Krum Bacvarov[15], Ruben Badalyan[7], Stefan Bakardzhiev[16], Jacqueline Balen[17], Lorenc Bejko[18], Rebecca Bernardos[2], Andreas Bertsatos[19], Hanifi Biber[20], Ahmet Bilir[21], Mario Bodružić[22], Michelle Bonogofsky[23], Clive Bonsall[24], Dušan Borić[25], Nikola Borovinić[26], Guillermo Bravo Morante[3], Katharina Buttinger[3], Kim Callan[2,27], Francesca Candilio[28], Mario Carić[29], Olivia Cheronet[3], Stefan Chohadzhiev[30], Maria-Eleni Chovalopoulou[19], Stella Chryssoulaki[31], Ion Ciobanu[32,33], Natalija Čondić[34], Mihai Constantinescu[35], Emanuela Cristiani[36], Brendan J. Culleton[37], Elizabeth Curtis[2,27], Jack Davis[38], Tatiana I. Demcenco[39], Valentin Dergachev[40], Zafer Derin[41], Sylvia Deskaj[42], Seda Devejyan[7], Vojislav Djordjević[43], Kellie Sara Duffett Carlson[3], Laurie R. Eccles[44], Nedko Elenski[45], Atilla Engin[46], Nihat Erdoğan[47], Sabiha Erir-Pazarcı[48], Daniel M. Fernandes[3,49], Matthew Ferry[2,27], Suzanne Freilich[3], Alin Frînculeasa[50], Michael L. Galaty[42], Beatriz Gamarra[51,52,53], Boris Gasparyan[7], Bisserka Gaydarska[54], Elif Genç[55], Timur Gültekin[56], Serkan Gündüz[57], Tamás Hajdu[58], Volker Heyd[59], Suren Hobosyan[7], Nelli Hovhannisyan[60], Iliya Iliev[16], Lora Iliev[2,27], Stanislav Iliev[61], İlkay İvgin[62], Ivor Janković[29], Lence Jovanova[63], Panagiotis Karkanas[64], Berna Kavaz-Kındığılı[65], Esra Hilal Kaya[66], Denise Keating[3], Douglas J. Kennett[37,67], Seda Deniz Kesici[68], Anahit Khudaverdyan[7], Krisztián Kiss[58,69], Sinan Kılıç[20], Paul Klostermann[70], Sinem Kostak Boca Negra Valdes[68], Saša Kovačević[71], Marta Krenz-Niedbała[72], Maja Krznarić Škrivanko[73], Rovena Kurti[74], Pasko Kuzman[75], Ann Marie Lawson[2,27], Catalin Lazar[76], Krassimir Leshtakov[77], Thomas E. Levy[78], Ioannis Liritzis[79,80], Kirsi O. Lorentz[81], Sylwia Łukasik[72], Matthew Mah[2,27,82], Swapan Mallick[2,27], Kirsten Mandl[3], Kristine Martirosyan-Olshansky[83], Roger Matthews[84], Wendy Matthews[84], Kathleen McSweeney[24], Varduhi Melikyan[7], Adam Micco[2], Megan Michel[1,2,27], Lidija Milašinović[85], Alissa Mittnik[1,2,86], Janet M. Monge[87], Georgi Nekhrizov[15], Rebecca Nicholls[88], Alexey G. Nikitin[89], Vassil Nikolov[15], Mario Novak[29], Iñigo Olalde[2,90], Jonas Oppenheimer[2,27], Anna Osterholtz[91], Celal Özdemir[13], Kadir Toykan Özdoğan[3], Nurettin Öztürk[65], Nikos Papadimitriou[92], Niki Papakonstantinou[93], Anastasia Papathanasiou[94], Lujana Paraman[95], Evgeny G. Paskary[96], Nick Patterson[1,82], Ilian Petrakiev[45], Levon Petrosyan[7], Vanya Petrova[77], Anna Philippa-Touchais[97], Ashot Piliposyan[98], Nada Pocuca Kuzman[75], Hrvoje Potrebica[99], Bianca Preda-Bălănică[59], Zrinka Premužić[100], T. Douglas Price[101], Lijun Qiu[2,27], Siniša Radović[102], Kamal Raeuf Aziz[103], Petra Rajić Šikanjić[29], Kamal Rasheed Raheem[103], Sergei Razumov[104], Amy Richardson[84], Jacob Roodenberg[105], Rudenc Ruka[74], Victoria Russeva[106], Mustafa Şahin[57], Ayşegül Şarbak[107], Emre Savaş[68], Constanze Schattke[3], Lynne Schepartz[108], Tayfun Selçuk[68], Ayla Sevim-Erol[109], Michel Shamoon-Pour[110], Henry M. Shephard[111], Athanasios Sideris[112], Angela Simalcsik[32,113], Hakob Simonyan[114], Vitalij Sinika[104], Kendra Sirak[2], Ghenadie Sirbu[115], Mario Šlaus[116], Andrei Soficaru[35], Bilal Söğüt[117], Arkadiusz Sołtysiak[118], Çilem Sönmez-Sözer[109], Maria Stathi[119], Martin Steskal[120], Kristin Stewardson[2,27], Sharon Stocker[38], Fadime Suata-Alpaslan[121], Alexander Suvorov[59], Anna Szécsényi-Nagy[122], Tamás Szeniczey[58], Nikolai Telnov[104], Strahil Temov[123], Nadezhda Todorova[77], Ulsi Tota[74,124], Gilles Touchais[125], Sevi Triantaphyllou[93], Atila Türker[126], Marina Ugarković[71], Todor Valchev[16], Fanica Veljanovska[123], Zlatko Videvski[123], Cristian Virag[127], Anna Wagner[3], Sam Walsh[128], Piotr Włodarczak[129], J. Noah Workman[2], Aram Yardumian[130,131], Evgenii Yarovoy[132], Alper Yener Yavuz[133], Hakan Yılmaz[20], Fatma Zalzala[2,27], Anna Zettl[3], Zhao Zhang[2], Rafet Çavuşoğlu[20], Nadin Rohland[2], Ron Pinhasi[3,134]*, David Reich[1,2,27,82]*

Literary and archaeological sources have preserved a rich history of Southern Europe and West Asia since the Bronze Age that can be complemented by genetics. Mycenaean period elites in Greece did not differ from the general population and included both people with some steppe ancestry and others, like the Griffin Warrior, without it. Similarly, people in the central area of the Urartian Kingdom around Lake Van lacked the steppe ancestry characteristic of the kingdom's northern provinces. Anatolia exhibited extraordinary continuity down to the Roman and Byzantine periods, with its people serving as the demographic core of much of the Roman Empire, including the city of Rome itself. During medieval times, migrations associated with Slavic and Turkic speakers profoundly affected the region.

T he works of ancient writers provide powerful insights into the ancient world, recording information on different groups, their political organizations, customs, relations, and military conflicts. The manuscript tradition has been augmented by the archaeological record, which also includes the discovery of texts of past Mediterranean and West Asian civilizations. In this work, we leverage the power of ancient DNA to provide a third source of information about the people inhabiting the states and empires of the past. Many of these aspects have been recorded, or hinted at, in ancient texts composed close to the time of the events they describe. However, no text is fully objective, and all texts are inevitably shaped by authors' biases and world views. Ancient DNA provides independent evidence, with its own strengths and weaknesses, and cannot paint a picture of the past on its own. Nonetheless, it complements the ancient texts and evidence from archaeology. By using genetic data, we can hope to obtain a more nuanced impression of past processes—especially with regards to movements of people and biological phenotypes—than would be possible without such data.

This study is a part of a comprehensive archaeogenetic analysis of the genetic history of the populations of the Southern Arc, spanning a trio of papers. For a description of the full dataset and analysis framework and characterization of the population history of the Chalcolithic and Bronze Age periods, see (1). For analysis of the population history of the Neolithic, see (2). The present paper focuses on peoples for which there is also information from written texts. A main theme is to test the extent to which textual insights are supported or not supported by the genetic data and furthermore to explore what complementary information genetics can provide. When we reference ancient literature, we use standard abbreviations for locating passages in online repositories of texts, such as the Perseus Digital Library (3). Our study begins at the end of the Bronze Age and traces the region's history through the first millennium BCE, through the Roman Empire and up to the present, a time span of >3000 years.

The Bronze Age Aegean world

Previous work has demonstrated that the Bronze Age civilizations of Greece of the

periods labeled Minoan (on the island of Crete; spanning the entirety of the Bronze Age, ~3500 to 1100 BCE) and Mycenaean (on the Greek mainland and its islands; spanning the latter part of the Bronze Age since the last phase of the Middle Helladic period to the end of the Late Helladic period, ~1750 to 1050 BCE) (4) were inhabited by genetically similar populations that traced most of their ancestry to the Neolithic inhabitants of the region, who, in turn, were related to the farmers of Anatolia (4–7).
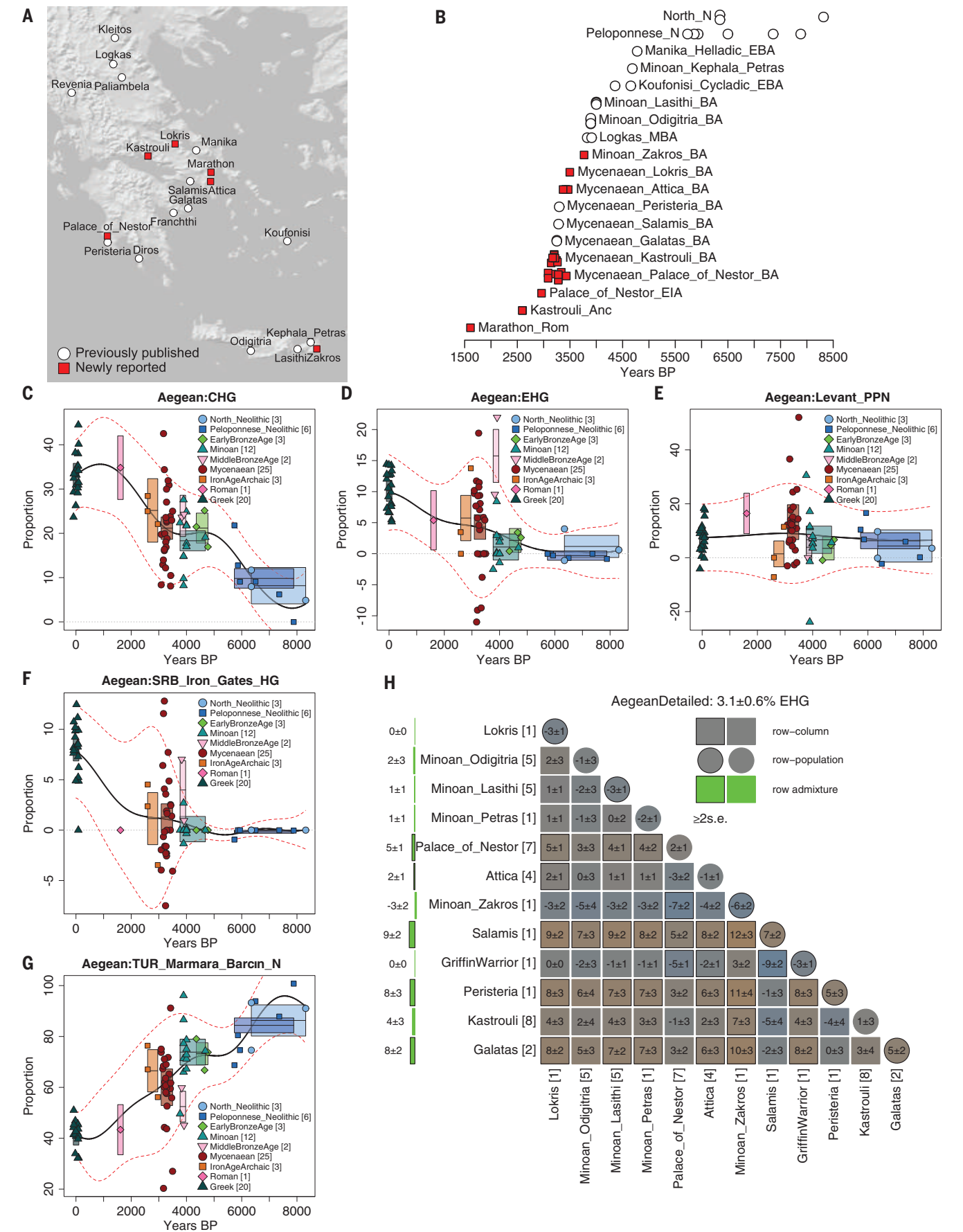
We refer to people associated with these archaeological contexts as Minoan and Mycenaean, recognizing that the people themselves would almost certainly not have considered themselves as belonging to two groups divided according to this framework defined by archaeology and that there was in fact extensive genetic variation in ancestry among people associated with such cultures, as we prove here. Both Mycenaeans and Minoans had extra "eastern" Caucasus-related ancestry compared

with that of the Neolithic inhabitants of Greece, but they differed from each other in that the Mycenaeans taken as a group had some steppe ancestry that Minoans lacked (4). In this work, we extend the geographical sampling to multiple sites without previously reported ancient DNA data, complementing published Mycenaean data from the Peloponnese and Salamis and Minoan data from Lasithi and Moni Odigitria (4). From Crete, we report a Middle Minoan individual from Zakros. From

[1]Department of Human Evolutionary Biology, Harvard University, Cambridge, MA 02138, USA. [2]Department of Genetics, Harvard Medical School, Boston, MA 02115, USA. [3]Department of Evolutionary Anthropology, University of Vienna, 1030 Vienna, Austria. [4]Department of Anthropology, Faculty of Letters, Mardin Artuklu University, 47510 Artuklu, Mardin, Turkey. [5]Department of Anthropology, Faculty of Letters, Sivas Cumhuriyet University, 58140 Sivas, Turkey. [6]Department of History, Adelphi University, Garden City, NY 11530, USA. [7]Institute of Archaeology and Ethnography, NAS RA, 0025 Yerevan, Armenia. [8]Samsun Museum of Archeology and Ethnography, Kale Mahallesi, Merkez, İlkadım, 55030 Samsun, Turkey. [9]Iskra Museum of History, 6100 Kazanlak, Bulgaria. [10]Historical Musem in Kotor, 85330 Kotor, Montenegro. [11]Institute of Archaeology, 11000 Belgrade, Serbia. [12]Department of Archaeology, University of York, York YO1 7EP, UK. [13]Amasya Archaeology Museum, Mustafa Kemal Paşa Caddesi, 05000 Amasya, Turkey. [14]Department of Anthropology, Faculty of Arts and Science, Burdur Mehmet Akif University, 15100 Burdur, Turkey. [15]National Institute of Archaeology and Museum, Bulgarian Academy of Sciences, 1000 Sofia, Bulgaria. [16]Yambol Regional Historical Museum, 8600 Yambol, Bulgaria. [17]Archaeological Museum in Zagreb, 10000 Zagreb, Croatia. [18]Department of Archaeology and Heritage Studies, University of Tirana, 1010 Tirana, Albania. [19]Department of Animal and Human Physiology, Faculty of Biology, School of Sciences, National and Kapodistrian University of Athens, 10679 Athens, Greece. [20]Department of Archaeology, Faculty of Humanities, Van Yüzüncü Yıl University, 65090 Tuşba, Van, Turkey. [21]Department of Archaeology, Faculty of Science and Letters, Düzce University, 81620 Düzce, Turkey. [22]Stratum Ltd., 21218 Seget Donji, Croatia. [23]Independent Researcher, Berkeley, CA 94720, USA. [24]School of History, Classics and Archaeology, University of Edinburgh, Edinburgh EH8 9AG, UK. [25]The Italian Academy for Advanced Studies in America, Columbia University, New York, NY 10027, USA. [26]Center for Conservation and Archaeology of Montenegro, 81250 Cetinje, Montenegro. [27]Howard Hughes Medical Institute, Harvard Medical School, Boston, MA 02115, USA. [28]Servizio di Bioarcheologia, Museo delle Civiltà, 00144 Rome, Italy. [29]Centre for Applied Bioanthropology, Institute for Anthropological Research, 10000 Zagreb, Croatia. [30]Department of Archaeology, University of Veliko Tarnovo "St. Cyril and St. Methodius," 5003 Veliko Tarnovo, Bulgaria. [31]Hellenic Ministry of Culture and Sports, Ephorate of Antiquities of Piraeus and the Islands, 10682 Piraeus, Greece. [32]"Orheiul Vechi" Cultural-Natural Reserve, Institute of Bioarchaeological and Ethnocultural Research, 3552 Butuceni, Moldova. [33]National Archaeological Agency, 2012 Chișinău, Moldova. [34]Archaeological Museum in Zadar, 23000 Zadar, Croatia. [35]"Francisc I. Rainer" Institute of Anthropology, 050711 Bucharest, Romania. [36]Department of Oral and Maxillo-Facial Sciences, Sapienza University of Rome, 00161 Rome, Italy. [37]Institutes of Energy and the Environment, The Pennsylvania State University, University Park, PA 16802, USA. [38]Department of Classics, University of Cincinnati, Cincinnati, OH 45221, USA. [39]Independent Researcher, Aberystwyth SY23 4UH, UK. [40]Center of Archaeology, Institute of Cultural Heritage, Academy of Science of Moldova, 2001 Chișinău, Moldova. [41]Department of Archaeology, Faculty of Letters, Ege University, 35100 Bornova-Izmir, Turkey. [42]Museum of Anthropological Archaeology, University of Michigan, Ann Arbor, MI 48109, USA. [43]Narodni muzej Pančevo, 26101 Pančevo, Serbia. [44]Human Paleoecology and Isotope Geochemistry Lab, Department of Anthropology, The Pennsylvania State University, University Park, PA 16802, USA. [45]Regional Museum of History – Veliko Tarnovo, 5000 Veliko Tarnovo, Bulgaria. [46]Department of Archaeology, Faculty of Science and Letters, Gaziantep University, 27310 Gaziantep, Turkey. [47]Mardin Archaeological Museum, Şar, Cumhuriyet Meydanı üstü, 47100 Artuklu, Mardin, Turkey. [48]Muğla İl Kültür ve Turizm Müdürlüğü, 48000 Muğla, Turkey. [49]Research Centre for Anthropology and Health (CIAS), Department of Life Sciences, University of Coimbra, 3000-456 Coimbra, Portugal. [50]Prahova County Museum of History and Archaeology, 100042 Ploiești, Romania. [51]Institut Català de Paleoecologia Humana i Evolució Social, 43007 Tarragona, Spain. [52]Departament d'Història i Història de l'Art, Universitat Rovira i Virgili, 43002 Tarragona, Spain. [53]School of Archaeology and Earth Institute, University College Dublin, Belfield, Dublin 4, Ireland. [54]Department of Archaeology, Durham University, Durham DH1 3LE, UK. [55]Department of Archaeology, Faculty of Science and Letters, Çukurova University, 01330 Balçalı-Sarıçam-Adana, Turkey. [56]Department of Anthropology, Faculty of Humanities, Ankara University, 06100 Sıhhiye, Ankara, Turkey. [57]Department of Archaeology, Faculty of Science and Letters, Bursa Uludağ University, 16059 Görükle, Bursa, Turkey. [58]Department of Biological Anthropology, Institute of Biology, Eötvös Loránd University, 1053 Budapest, Hungary. [59]Department of Cultures, University of Helsinki, 00100 Helsinki, Finland. [60]Department of Ecology and Nature Protection, Yerevan State University, 0025 Yerevan, Armenia. [61]Regional Museum of History, 6300 Haskovo, Bulgaria. [62]Ministry of Culture and Tourism, İsmet İnönü Bulvarı, 06100 Emek, Ankara, Turkey. [63]Museum of the City of Skopje, 1000 Skopje, North Macedonia. [64]Malcolm H. Wiener Laboratory, American School of Classical Studies at Athens, 10676 Athens, Greece. [65]Department of Archaeology, Faculty of Letters, Atatürk University, 25100 Erzurum, Turkey. [66]Muğla Archaeological Museum and Yatağan Thermal Power Generation Company, Rescue Excavations, 48000 Muğla, Turkey. [67]Department of Anthropology, University of California, Santa Barbara, Santa Barbara, CA 93106, USA. [68]Bodrum Museum of Underwater Archeology, Çarşı Neighbourhood, 48440 Bodrum, Muğla, Turkey. [69]Department of Anthropology, Hungarian Natural History Museum, 1117 Budapest, Hungary. [70]Department of Anthropology, Natural History Museum Vienna, 1010 Vienna, Austria. [71]Institute of Archaeology, 10000 Zagreb, Croatia. [72]Faculty of Biology, Adam Mickiewicz University in Poznań, 61-614 Poznań, Poland. [73]Municipal Museum Vinkovci, 32100 Vinkovci, Croatia. [74]Prehistory Department, Albanian Institute of Archaeology, Academy of Albanian Studies, 1000 Tirana, Albania. [75]National Museum in Ohrid, 6000 Ohrid, North Macedonia. [76]ArchaeoSciences Division, Research Institute of the University of Bucharest, University of Bucharest, 050663 Bucharest, Romania. [77]Department of Archaeology, St. Kliment Ohridski University of Sofia, 1504 Sofia, Bulgaria. [78]Department of Anthropology, University of California, San Diego, La Jolla, CA 92093, USA. [79]Key Research Institute of Yellow River Civilization and Sustainable Development and the Collaborative Innovation Center on Yellow River Civilization of Henan Province, Laboratory of Yellow River Cultural Heritage, Henan University, 475001 Kaifeng, China. [80]European Academy of Sciences and Arts, 5020 Salzburg, Austria. [81]Science and Technology in Archaeology and Culture Research Center, The Cyprus Institute, 2121 Aglantzia, Nicosia, Cyprus. [82]Broad Institute of Harvard and MIT, Cambridge, MA 02142, USA. [83]Cotsen Institute of Archaeology, University of California, Los Angeles, Los Angeles, CA 90095, USA. [84]Department of Archaeology, University of Reading, Reading RG6 6AB, UK. [85]National Museum of Kikinda, 23300 Kikinda, Serbia. [86]Department of Archaeogenetics, Max Planck Institute for Evolutionary Anthropology, 04103 Leipzig, Germany. [87]University of Pennsylvania Museum of Archaeology and Anthropology, Philadelphia, PA 19104, USA. [88]School of Archaeological and Forensic Sciences, Faculty of Life Sciences, University of Bradford, Bradford BD7 1DP, UK. [89]Department of Biology, Grand Valley State University, Allendale, MI 49401, USA. [90]BIOMICs Research Group, University of the Basque Country UPV/EHU, 01006 Vitoria-Gasteiz, Spain. [91]Department of Anthropology and Middle Eastern Cultures, Mississippi State University, Mississippi State, MS 39762, USA. [92]Paul and Alexandra Canellopoulos Museum, 105-55 Athens, Greece. [93]Faculty of Philosophy, School of History and Archaeology, Aristotle University of Thessaloniki, 54124 Thessaloniki, Greece. [94]Ephorate of Paleoantropology and Speleology, Greek Ministry of Culture, 11636 Athens, Greece. [95]Trogir Town Museum, 21220 Trogir, Croatia. [96]Moldavian Historic-Geographical Society, 2044 Chișinău, Moldova. [97]French School of Archaeology at Athens, 10680 Athens, Greece. [98]Department of Armenian History, Armenian State Pedagogical University After Khachatur Abovyan, 0010 Yerevan, Armenia. [99]Department of Archaeology, Faculty of Humanities and Social Sciences, University of Zagreb, 10000 Zagreb, Croatia. [100]Independent Researcher, 10000 Zagreb, Croatia. [101]Laboratory for Archaeological Chemistry, University of Wisconsin–Madison, Madison, WI 53706, USA. [102]Institute for Quaternary Paleontology and Geology, Croatian Academy of Sciences and Arts, 10000 Zagreb, Croatia. [103]Sulaymaniyah Directorate of Antiquities and Heritage, 46010 Sulaymaniyah, Iraq. [104]Pridnestrovian University named after Taras Shevchenko, 3300 Tiraspol, Moldova. [105]The Netherlands Institute for the Near East, 2311 Leiden, Netherlands. [106]Institute of Experimental Morphology, Pathology and Archeology with Museum, Bulgarian Academy of Science, 1113 Sofia, Bulgaria. [107]Department of Anthropology, Faculty of Science and Letters, Hitit University, 19040 Çorum, Turkey. [108]School of Anatomical Sciences, The University of the Witwatersrand, 2193 Johannesburg, South Africa. [109]Department of Anthropology, Faculty of Language and History - Geography, Ankara University, 06100 Sıhhiye, Ankara, Turkey [110]Department of Anthropology, Binghamton University, Binghamton, NY 13902, USA. [111]Archaeological Institute of America, Boston, MA 02108, USA. [112]Institute of Classical Archaeology, Charles University, 11636 Prague, Czechia. [113]"Olga Necrasov" Centre of Anthropological Research, Romanian Academy Iași Branch, 2012 Iași Romania. [114]Scientific Research Center of the Historical and Cultural Heritage, 0010 Yerevan, Armenia. [115]Thracology Scientific Research Laboratory of the State University of Moldova, Department of Academic Management, Academy of Science of Moldova, 2009 Chișinău, Moldova. [116]Anthropological Center of the Croatian Academy of Sciences and Arts, 10000 Zagreb, Croatia. [117]Department of Archaeology, Faculty of Science and Arts, Pamukkale University, 20070 Denizli, Turkey. [118]Faculty of Archaeology, University of Warsaw, 00-927 Warszawa, Poland. [119]Ephorate of Antiquities of East Attica, Ministry of Culture and Sports, 10682 Athens, Greece. [120]Austrian Archaeological Institute at the Austrian Academy of Sciences, 1190 Vienna, Austria. [121]Department of Anthropology, Faculty of Letters, Istanbul University, 34134 Istanbul, Turkey. [122]Institute of Archaeogenomics, Research Centre for the Humanities, Eötvös Loránd Research Network, 1097 Budapest, Hungary. [123]Archaeology Museum of North Macedonia, 1000 Skopje, North Macedonia. [124]Culture and Patrimony Department, University of Avignon, 84029 Avignon, France. [125]Department of the History of Art and Archaeology, Université Paris 1 Panthéon-Sorbonne, 75006 Paris, France. [126]Department of Archaeology, Faculty of Science and Letters, Ondokuz Mayıs University, 55139 Atakum-Samsun, Turkey. [127]Satu Mare County Museum, 440031 Satu Mare, Romania. [128]School of Natural Sciences, University of Central Lancashire, Preston PR1 2HE, UK. [129]Institute of Archaeology and Ethnology, Polish Academy of Sciences, 31-016 Kraków, Poland. [130]Department of History and Social Sciences, Bryn Athyn College, Bryn Athyn, PA 19009, USA. [131]Penn Museum, University of Pennsylvania, Philadelphia, PA 19104, USA. [132]History of the Ancient World and Middle Ages Department, Moscow Region State University, Moscow Region, 141014 Mytishi, Russia. [133]Department of Anthropology, Burdur Mehmet Akif Ersoy University, Istiklal Campus, 15100 Burdur, Turkey. [134]Human Evolution and Archaeological Sciences, University of Vienna, 1030 Vienna, Austria.

*Corresponding author. Email: lazaridis@genetics.med.harvard.edu (I.La.); msglalpaslan@gmail.com (S.A.-R.); ron.pinhasi@univie.ac.at (R.P.); reich@genetics.med.harvard.edu (D.R.)
†These authors contributed equally to this work.

Fig. 1. Genetic heterogeneity in the Aegean. (**A**) A map of Aegean sites. (**B**) Timeline of Aegean individuals, with vertical jitter added to distinguish contemporaneous individuals. BP, before the present. (**C** to **G**) Ancestry changes of five components show an increase of Caucasus hunter-gatherer (CHG) and Eastern European hunter-gatherer (EHG) ancestry over time and a dilution of Anatolian Neolithic ancestry. (**H**) During the Minoan and Mycenaean periods of the Bronze Age, Eastern European hunter-gatherer ancestry was variable, absent in Minoan individuals of Crete, and present in most but not all Mycenaean individuals of the mainland. s.e., standard error.

mainland contexts, we report the first Mycenaean data from Central Greece—that is, the previously unsampled region north of the Isthmus of Corinth—including Attica, Kastrouli near Delphi in Phokis, and Lokris in Phthiotis. South of the Isthmus in the Peloponnese, we report data from many individuals from the "Palace of Nestor" at Pylos and its environs, including the elite "Griffin Warrior," a young (30 to 35 years old) male buried in a large stone-built tomb with hundreds of precious artifacts, many of them made in Minoan Crete (*8*).

To contextualize the transformations in the Bronze Age Aegean, it is critical to characterize the pre–Bronze Age genetic landscape (Fig. 1). We begin with the Neolithic inhabitants (*4*, *6*, *7*), estimating proportions of ancestry using a five-source model that we developed for Southern Arc Holocene populations (*1*), which includes as proxies for the sources Caucasus hunter-gatherers (*9*), Eastern European hunter-gatherers (*5*, *10*), Levantine Pre-Pottery Neolithic (*11*), Balkan hunter-gatherers from the Iron Gates in Serbia (*7*), and Northwestern Anatolian Neolithic from Barcın (*5*). We infer that not only Neolithic Greeks from the Peloponnese (*7*) but also those from Northern Greece (*6*) had ~8 to 10% Caucasus hunter-gatherer–related ancestry (Fig. 1C). We find small amounts of Caucasus hunter-gatherer–related ancestry in Southeastern Europe and Neolithic populations in general, which is different from the pattern in Central/Western Europe where there is none (*1*). This provides proof of multiple streams of migration from different Anatolian Neolithic populations into Europe.

Both Caucasus and Eastern European hunter-gatherer–related ancestry increased in the Bronze Age in the Aegean just as the Anatolian-related ancestry decreased (Fig. 1), with Mycenaean Greeks having 21.2 ± 1.3% Caucasus hunter-gatherer ancestry and 4.3 ± 1.0% Eastern European hunter-gatherer ancestry. Given the evenly balanced proportions of these components in the Yamnaya and the "high steppe" cluster from the Balkans (*1*), it can be assumed that the Eastern European hunter-gatherer component in the Aegean was not introduced there on its own but rather was accompanied by an approximately matching amount of Caucasus hunter-gatherer ancestry, thus leaving a remainder of ~21.2 – 4.3 = 16.9% Caucasus hunter-gatherer. This allows us to infer that steppe migrants admixed with a population whose composition must have

included $\frac{16.9}{100 - 2 \times 4.3}$ or ~18.5% Caucasus hunter-gatherer–related ancestry. Notably, the estimated proportion of Caucasus hunter-gatherer ancestry in Minoans is virtually identical at 18.3 ± 1.2%. Thus, our analyses resolve the question of the origins of the Late Bronze Age population by strongly supporting one of two previously proposed hypotheses (*4*)—that Mycenaeans were the outcome of admixture of descendants of Yamnaya-like steppe migrants with a Minoan-like substratum, rather than the hitherto plausible alternative scenario of an Anatolian Neolithic–like substratum admixing with an Armenian-like population from the east. This alternative scenario is further contradicted by the fact that pre–Mycenaean period individuals belonging to the Early Bronze Age from the islands of the Cyclades and Euboea in Southern Greece in ~2500 BCE (*12*) had 21.2 ± 1.7% Caucasus hunter-gatherer–related ancestry (*12*), consistent with our inferred proportion and providing direct evidence for the predicted Minoan-like substratum (*4*).

The fact that Mycenaeans can be modeled as a mixture in an ~1:10 ratio of a Yamnaya-like steppe-derived population and a Minoan- or Early Bronze Age–like Aegean population suggests that any contribution of geographically intermediate populations (between the steppe and the Aegean) to the formation of Mycenaeans was minor. This conclusion is further supported by the following: (i) the lower (~5%) Caucasus hunter-gatherer ancestry in the Neolithic of the Balkans compared with the ~20% inferred for the Aegean substratum (*1*), (ii) the near absence of Balkan hunter-gatherer (fig. S1) ancestry in the Aegean in contrast to other Southeastern European populations (~10%) (*1*), and (iii) the presence of Yamnaya-like individuals with minimal local ancestry—immediately to the north of the Aegean—in Albania and Bulgaria during the Early Bronze Age (*1*). Whatever the genetic makeup of people mediating the spread of steppe ancestry into the ancestors of Mycenaeans, the genetic impact of steppe on Aegean populations was quantitatively minor. We estimate the Yamnaya-related steppe ancestry proportion in Mycenaeans to be ~⅓ of the level of that in the Balkans to the north, ~½ of that in Armenia in the east, and ~⅕ to ⅛ of that of populations of Central/Northern Europe associated with the Bell Beaker and Corded Ware cultures (*1*).

Eastern European hunter-gatherer ancestry as a marker for Yamnaya steppe pastoralist

ancestry is absent in a newly reported Middle Minoan period individual from Zakros on the eastern edge of Crete. This individual's ancestry is generally similar to those previously published (*13*), but with significant Levantine admixture (30.5 ± 9.1%), which is consistent with her either being a migrant to the island from the east or part of a structured Cretan population whose past ethnic diversity was noted as early as the *Odyssey* of Homer (Hom. Od. 19.172-177).

We show that Eastern European hunter-gatherer ancestry was also absent in some Mycenaean individuals, which suggests that although the contrast between the mainland and Crete was significant (fig. S1), the penetration of Eastern European hunter-gatherer ancestry did not reach the totality of the mainland population during the Late Bronze Age and was even significantly variable within Mycenaean sites. The Griffin Warrior (*8*), the earliest individual (~1450 BCE) from the Palace of Nestor in Pylos, is genetically right in the middle of the general population of the Aegean and was thus plausibly of entirely local Aegean origin. He had no detectable Eastern European hunter-gatherer ancestry (compared with the average of 4.8 ± 1.1% for the rest of the Mycenaean-era individuals sampled at the Palace; Fig. 1H). This finding could be consistent with a Cretan origin of this individual or his ancestors; alternatively, he could be drawn from a mainland population that had not experienced Eastern European hunter-gatherer admixture, as could two later individuals from Pylos—one buried near the Palace in a chamber tomb and another in a cist grave. Variation in Eastern European hunter-gatherer ancestry is observed at short geographical distance scales and within the same time periods: We observe that four individuals (~1450 BCE) of the sample from Attica buried at Kolikrepi-Spata had only 2 ± 1% Eastern European hunter-gatherer ancestry that was significantly less (by more than two standard errors) than that of individuals from the neighboring island of Salamis and all sampling locations in the Peloponnese. This suggests that the classical Athenian claim (e.g., Plat. Menex. 237b) of having received fewer migrants than other Greek poleis in the remote past may have had an element of truth, although larger sample sizes will be necessary to definitively establish such geographic patterns.

Northern migrants made an impact throughout mainland Greece, even if it was a modest one. This is also attested in the male line, for
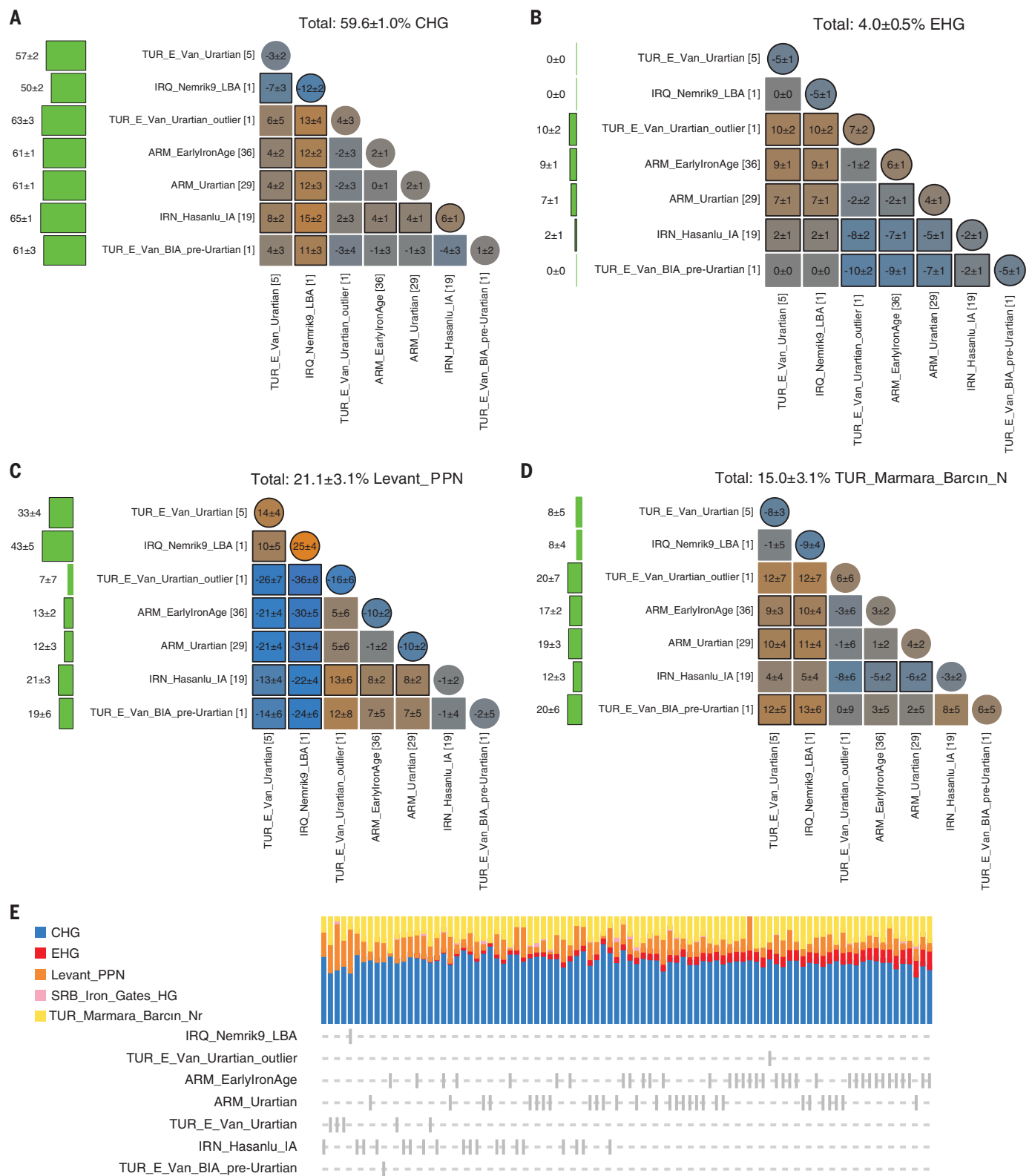
Fig. 2. The Kingdom of Urartu and its neighbors. (**A** to **D**) Comparisons of ancestry in four ancestral components [SRB_Iron_Gates_HG, the fifth component of the model of (*1*) is negligible]. This analysis shows a stark contrast between Armenia and the other populations in terms of Eastern European hunter-gatherer ancestry (B) and between Van and Assyrian Mesopotamia (represented by the site of Nemrik 9 in Iraq) in terms of Levantine ancestry (C). When unlabeled individuals are ordered in increasing Eastern European hunter-gatherer ancestry (**E**), Assyrian Mesopotamia and Van lack this ancestry (except for an outlier individual from Van), whereas individuals from Armenia mostly have it, and those from Hasanlu have a limited range from zero Eastern European hunter-gatherer ancestry to a maximum level that is less than that seen in Armenia.
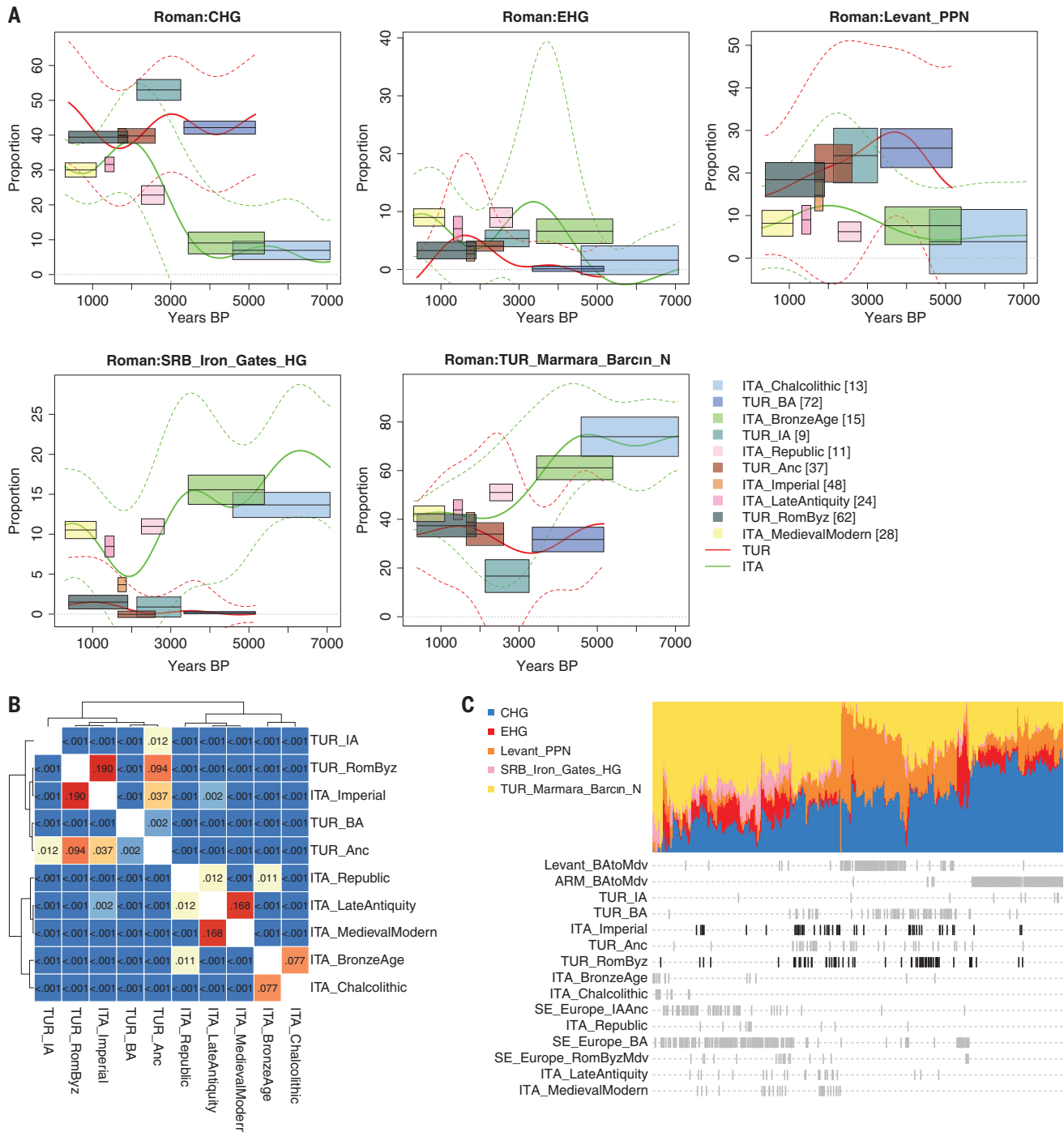
Fig. 3. The Roman Empire, east and west. (**A**) The Imperial period Romans from the vicinity of the city of Rome in Central Italy resembled Roman-Byzantine Anatolians in their average admixture proportions [95% confidence interval (CI) of ±1.96 standard errors shown as boxes, and a heteroskedastic Gaussian process is fitted to unlabeled Italian and Anatolian individuals; dashed lines indicate 5% and 95% quantiles]. (**B**) P values of the Baringhaus-Franz multivariate two-sample test (45) for pairs of populations indicate that Imperial Romans can be drawn from the same distribution as Roman-Byzantine ones ($P = 0.19$) but are significantly different ($P ≤ 2.16 × 10^{-3}$) from all other periods of Italy. (**C**) Hierarchical clustering of raw ancestry estimates of diverse individuals shows overlapping distributions of Imperial Roman and Anatolian Roman-Byzantine individuals (black) without knowledge of their ancestry labels and differentiated from the distributions of Southeastern Europe, Armenia, and the Levant.

example, by a Y chromosome match of the rare R-PF7562 haplogroup between a pair of patrilineal relatives from the Palace of Nestor, which links Late Bronze Age Mycenaean Greece with an Early Bronze Age individual of the

North Caucasus at Lysogorskyja that is genetically similar to the Yamnaya (14). This patrilineal connection to the Yamnaya should not be interpreted as a general association of steppe ancestry with elite burial status, as

the common people, making up most of our Mycenaean-era individuals, also had steppe ancestry, whereas some members of the elite (such as the Griffin Warrior) did not have significant evidence of it. A parallel example of an

elite individual with less steppe ancestry than others from the same cultural context during a period of steppe ancestry spread is given by the "Amesbury Archer," the most well-furnished grave in the Stonehenge mortuary landscape of Great Britain (15). These two examples highlight the pitfalls of conflating genetic ancestry with narratives of social dominance. Whatever the social role of early steppe migrants into the Aegean, they did not establish a system that precluded admixture with locals or prevented them from rising to positions of power. This inclusiveness may explain the substantial dilution of steppe ancestry in the Aegean, as migrants and locals blended to form the ancestors of the Mycenaean-era population, and may shed light on the genesis of the Greek language linked, on one hand, with the rest of Indo-Europeans through steppe ancestry (1) and, on the other, with the people of the Aegean who preceded the Proto-Greek speakers (16).

One of the two patrilineal relatives at Pylos (I13518) was almost certainly the offspring of first cousins; we document such close-kin unions not only in elite Mycenaean society but also in different localities of the Bronze Age Southern Arc (fig. S2) (17), including an individual from Bezdanjača in Croatia (I18717) who was likely the offspring of an uncle-niece pairing. This documents the later persistence of the practice of close-kin matings that had started with the Neolithic (18, 19), although whether this is the result of the burials we analyzed being a biased subset of a population or reflects society-wide cultural preferences cannot be resolved with our available sample. Did descriptions of such unions in classical mythological accounts of the "Heroic Age" reflect practices that persisted to the authors' own time? Ancient DNA studies from more locations would allow these patterns of mating preferences inferred from a handful of sites to be characterized at higher resolution.

The era of Greek colonization

We report a preliminary look at demographic patterns associated with the Greek colonial period (eighth to sixth centuries BCE) by identifying individuals from both the Southern Arc and outside of it who were genetically similar to Bronze Age individuals of the Mycenaean period (supplementary text S1 and fig. S3) (17). This identifies an Archaic period individual from Kastrouli near Delphi in Phokis on the Greek mainland and individuals at Empúries in Northeastern Spain who are genetically very similar to Mycenaean-era individuals from the Greek mainland (20). Empúries was an outpost colonized by Phocaeans from Western Anatolia, who were themselves said to be colonists from Phokis (Paus. 7.3.10). Thus, we capture the end points of a long chain of transmission, with little admixture, across the Mediterranean. Could the ancestry of the

Empúries individuals be traced back to the beginning of this chain, or was it drawn from another genetically similar source? Although we do not yet have rich sampling of the peoples of the Greek colonial world, systematic sampling of diverse Greek colonies spread over the Mediterranean and Black Sea coasts would make it possible to systematically test for evidence of specific metropolis-colony connections and document the extent to which migration, admixture with local populations, and genetic heterogeneity played a role in Greek colonization.

Ancestry typical of the Mycenaean period also spread to the Eastern Mediterranean, as in the case of an individual from Ashkelon associated with a Philistine archaeological context (21). We also show the similarity of some individuals from inland Thrace (at Kapitan Andreevo) with the Mycenaean genetic profile, which suggests that Mycenaeans were genetically similar to some Thracians from the East Balkans, outside the sphere of the Late Bronze Age Aegean. This provides a cautionary tale highlighting the dangers of conflating genetic and cultural similarity.

The coastal regions of Anatolia formed another area of Greek settlement, and much of the Anatolian peninsula was incorporated into the Hellenistic kingdoms established by the successors of Alexander the Great, providing opportunity for population transfer from Southeastern Europe to Anatolia. Yet, we do not find Mycenaean-like individuals either at first millennium BCE Greek colony sites, such as Halicarnassus (modern Bodrum), or Amisos (modern Samsun) in the Aegean and Black Sea regions, respectively. This pattern is qualitatively different from that at Empúries in Iberia and is consistent with the account of Herodotus that early Greek colonists of Anatolia married indigenous Carian women of Anatolia when they first settled there (Hdt. 1.146). It is also reminiscent of the marriages of Alexander himself and his companions with local women of the conquered Persian Empire (Arr. An. 7.4.4ff). Clearly, Greeks segregated themselves socially and reproductively from non-Greeks in some parts of the Greek world and not in others; an important topic for future research is to identify the factors that correlated with Greeks mixing with peoples from local communities.

The Urartian Kingdom and its neighbors in Iran and Mesopotamia

We have already seen how the Aegean was an area of limited Eastern European hunter-gatherer penetrance that nonetheless differentiates it from neighboring Anatolia, where Eastern European hunter-gatherer ancestry was negligible (1). An even more notable case is that of the Iron Age Kingdom of Urartu, situated in the mountainous and geographically fragmented regions of eastern Turkey

and Armenia, where the linguistic landscape must have been complex in the Bronze and Iron Ages. The people at the center of this kingdom in the Lake Van region of Turkey (Çavuştepe) and its northern extension in Armenia were strongly connected by material culture and were buried only ~200 km apart, yet they formed distinct genetic clusters with little overlap during the kingdom's early (ninth to eighth centuries BCE) period (Fig. 2). The Van cluster is in continuity with the pre-Urartian population (~1300 BCE) at neighboring Muradiye also in the Van region and is characterized by more Levantine ancestry and the absence of steppe ancestry. It contrasts with the cluster of Urartian period individuals from Armenia, who have less Levantine and some steppe ancestry, like the pre-Urartian individuals of the Early Iron Age (1). Our genetic results help to explain the formation of linguistic relationships in the region. Population continuity of the Lake Van core population with greater Levantine ancestry may well correspond to the Hurro-Urartian language family (22) that linked the non–Indo-European Urartian language of the kingdom with the earlier Bronze Age Hurrian language, whose more-southern distribution encompassed parts of Syria and Northern Mesopotamia. Into the periphery of this Hurro-Urartian linguistic sphere came a steppe-admixed population from the north, whose presence marks the southern edge of steppe expansion that we discussed above and whose proximity to the Urartian speakers would provide a mechanism for the incorporation of Urartian words into the Armenian lexicon.

When we compare (Fig. 2E) the Urartian individuals with their neighbors at Iron Age Hasanlu in Northwestern Iran (~1000 BCE), we observe that the Hasanlu population had some Eastern European hunter-gatherer ancestry but to a lesser degree than their contemporaries in Armenia. The population was also linked to Armenia by the presence of the same R-M12149 Y chromosomes (within haplogroup R1b), linking it to the Yamnaya population of the Bronze Age steppe (1). Which language was spoken in this case is not clear, but the population shows no connection with the high–Eastern European hunter-gatherer R-Z93 (within haplogroup R1a) haplogroup–bearing groups from Central and South Asia belonging to steppe populations ancestral to Indo-Aryan speakers (23)—the closest linguistic relatives of Iranian speakers (24). Present-day Iranians do have R-Z93 Y chromosomes (25) or the more general upstream R1a-M17 ones [observed in every one of 19 diverse populations from Iran (26), as well as in present-day Indians (27), and modern Iranians almost completely lack R1b Y chromosomes (<1% frequency)]. Thus, it appears that R1a haplogroup Y chromosomes represent a
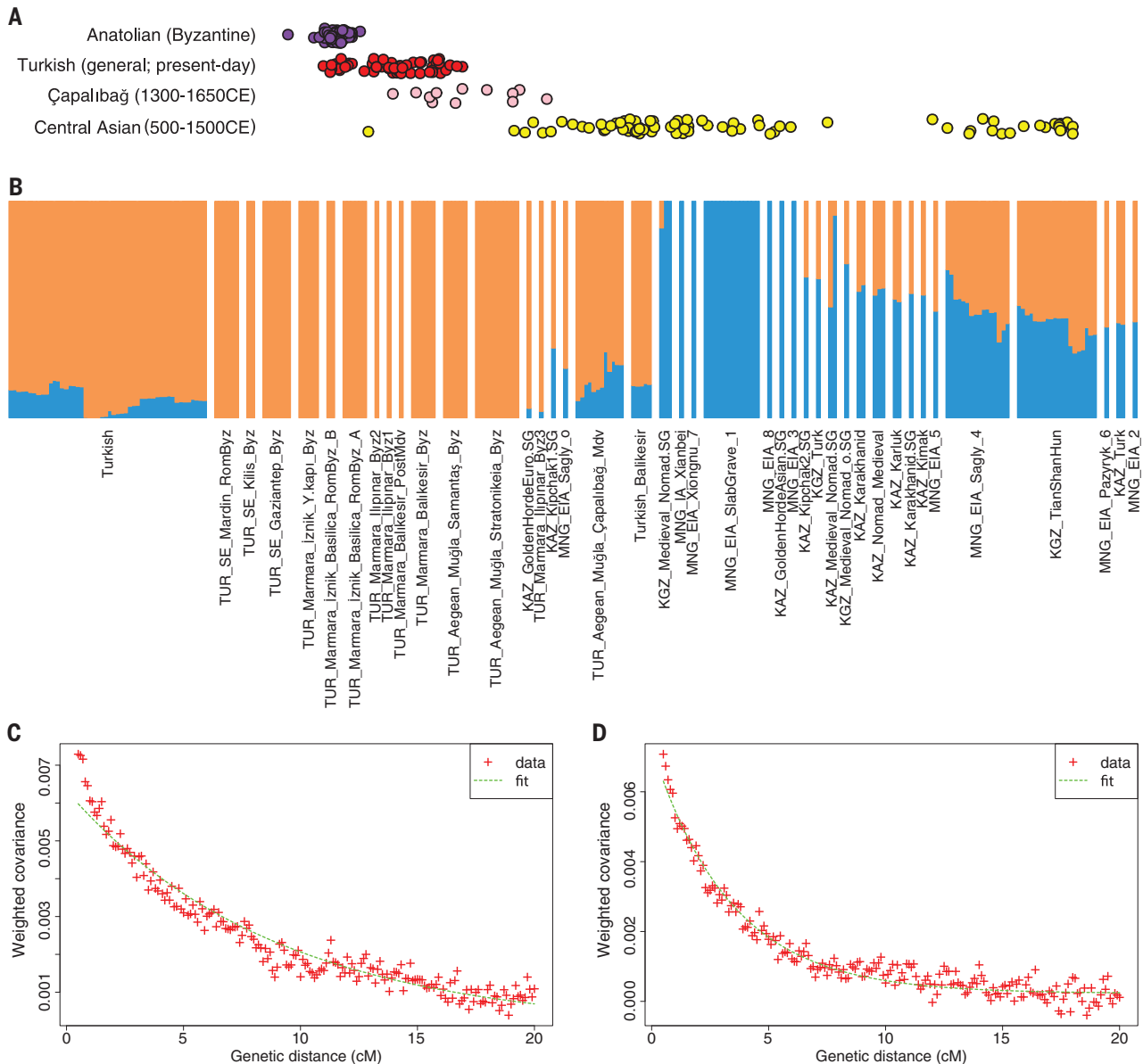
Fig. 4. Central Asian Turkic admixture in Anatolia. (**A**) Individuals from Çapalıbağ (1300 to 1650 CE) and present-day Turkish individuals are intermediate between Byzantine Anatolia and 500 to 1500 CE Central Asians along a global principal components analysis distinguishing West from East Eurasians (left-to-right on the horizontal dimension; noise added on the vertical dimension to distinguish points). (**B**) Two-way unsupervised ADMIXTURE analysis of eastern ancestry: Byzantine (0%); present-day Turkish (9%); Çapalıbağ (18%); and Central Asian individuals, who differ between 100% (in Mongolia) and 43% (some ancient populations of Kazakhstan and Kyrgyzstan). (**C**) Individuals from Çapalıbağ in Turkey admixed 12.2 ± 1.4 generations (342 ± 39 years) before their time using Byzantine Anatolians and Central Asians (from 500 to 1500 CE) as sources. cM, centimorgan. (**D**) Present-day Turkish people genotyped on the Human Origins array (*34*) admixed 30.6 ± 1.9 generations ago (857 ± 53 years ago) using the same sources as in (D).

common link between ancient and modern Indo-Iranians, whereas R1b haplogroup Y chromosomes (to which many of the Hasanlu males belonged) do not. The absence of any R1a examples among 16 males at Hasanlu, who are instead patrilineally related to individuals from Armenia, suggests that a non–Indo-Iranian (either related to Armenian or belonging to the non–Indo-European local population) language may have been spoken there and that Iranian languages may have been introduced to the Iranian plateau from

Central Asia only in the first millennium. Finally, a single individual from the Late Bronze Age of Assyrian Northern Mesopotamia (~1250 BCE) resembled the Urartian Van individuals in lacking Eastern European hunter-gatherer ancestry, had the highest amount of Levantine autosomal ancestry (42.8 ± 5.3%), and had a J-P58–derived Y chromosome with strong Levantine geographical associations (*1*) and may have plausibly been a speaker of a Semitic language, such as those that have been spoken and recorded in the region for

most of its history. Archaeology and historical texts have furnished a wealth of information about the political geography of the ancient Near East, and future genetic studies will elucidate changes of population that occurred either due to voluntary migration or forced movements of peoples implemented by state policies.

The Anatolian origins of the population of the Roman-Byzantine Empire

A paleogenomic time transect of the city of Rome in Central Italy (*28*) identified an ancestry
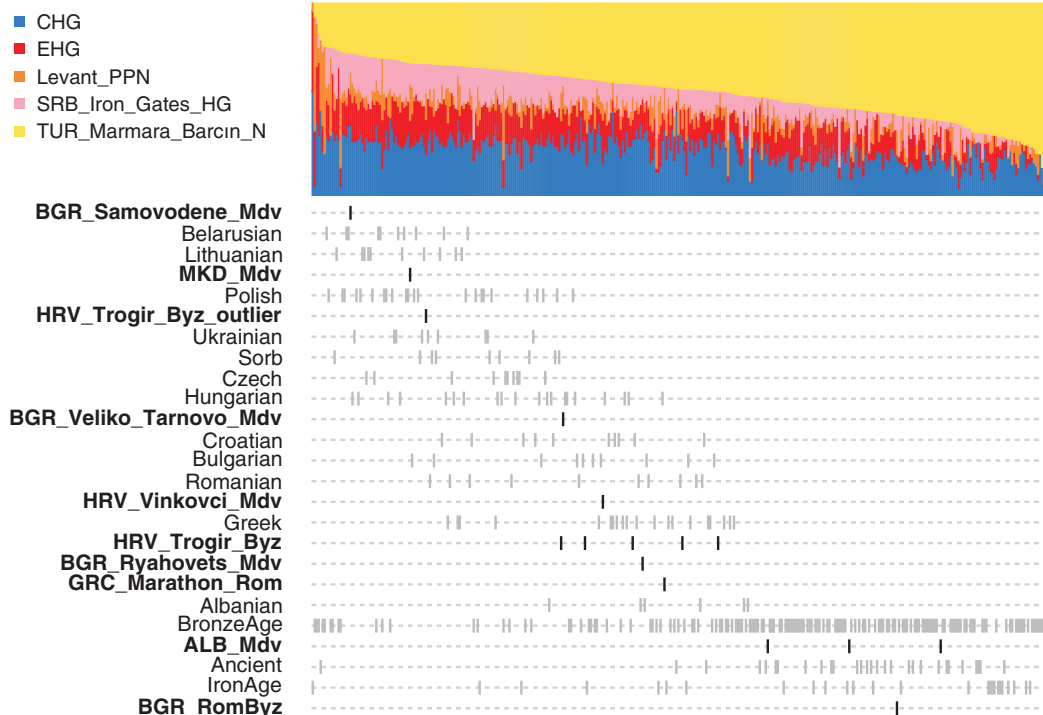
Fig. 5. Byzantine and medieval Southeastern Europe. We sorted admixture proportions of Anatolian Neolithic ancestry to investigate the dilution of this ancestry in present-day populations from Southeastern Europe. Roman-, medieval-, and Byzantine-era individuals are all indicated in bold. During the Bronze Age, the range of this ancestry was immense, as observed in (1), but present-day people from the Balkans have less of this ancestry than was the case in individuals from the Bronze Age through the Iron Age and down to classical antiquity (Ancient). Medieval and Byzantine people from the Balkans were diverse, with some (right) continuing the ancient pattern of high Anatolian Neolithic ancestry, several (middle) overlapping with the range of present-day people, and some (left) having as little of such ancestry as present-day Balto-Slavic people from Eastern Europe.

shift toward the Near East during the Imperial period (27 BCE to 300 CE) but was unable to localize the origin of the migrants driving this phenomenon. We sought to identify the geographic sources of these Imperial-era Romans by coanalyzing the data from Italy with data from the Southern Arc. Unexpectedly, the ancestry of the sample of people whose genomes were analyzed who lived around Rome in the Imperial period was almost identical to that of Roman and Byzantine individuals from Anatolia in both their mean (Fig. 3A) and pattern of variation (Fig. 3B), whereas Italians before the Imperial period had a very different distribution (28, 29). We clustered diverse Roman, Byzantine, and medieval individuals and their immediate predecessors without any knowledge of their population labels and found that the Italian and Anatolian individuals clustered together with those of pre-Roman Anatolia, whereas pre-Imperial people around the city of Rome were systematically different (Fig. 3C). This suggests that the Roman Empire in both its shorter-lived western part and the longer-lasting eastern centered on Anatolia had a diverse but similar population plausibly drawn, to a substantial extent, from Anatolian pre-Imperial sources. In an irony of history, although the Roman Republic prevailed in its existential military struggle against the Anatolians rallied by Mithridates VI of Pontus during the first century BCE, the final incorporation of Anatolia into the Roman Empire and the increased connectivity that ensued may have set the stage

for the very same Anatolians to become the demographic engine of Imperial Rome itself. This recreated, in historical time, the mythical journey of Aeneas and his Trojan exiles from Anatolia to the shores of Italy.

The Southern Arc was also a recipient of many immigrants from outside the region in the Historical period, such as two individuals sampled in Samsun in the Black Sea region from the Roman era in the second to third centuries CE (17). These individuals have both Eastern European hunter-gatherer and some East Eurasian ancestry that contrasts them with the local population of the Black Sea region that had been stable since the Chalcolithic (30), across the Early Bronze Age transition at Amasya, and down to the time of the Kingdom of Pontus (first century BCE). Broad genetic stability in Anatolia during the Roman-Byzantine period did not mean isolation, as outliers of likely Levantine, Northern European or Germanic, and Iberian origin are detected in the Marmara region (in the Basilica of Nicaea or present-day Iznik and the Virgin Mary Monastery at Zeytinliada, Erdek) close to the Imperial capital of Constantinople (present-day Istanbul), which may have attracted a more diverse set of foreigners. Other outliers are found at the periphery of the Southern Arc in the Iron Age, in Moldova and Romania, long after the early steppe migrants previously discussed. These are distinctive because of the East Eurasian admixture of Central Asian Scythian individuals (31–33).

Medieval migrations into Anatolia and the Balkans

East Eurasian ancestry also helps identify a noteworthy set of outliers at Çapalıbağ in the Aegean coast of Turkey dating from the 14th to 17th centuries (Fig. 4) (17). These have ~18% such ancestry, unlike Byzantine-era individuals from Turkey (Fig. 4B), which suggests a Central Asian influence. An admixture date estimate of 12.2 ± 1.4 generations before their time using Roman-Byzantine and Central Asian sources (Fig. 4C) suggests that the admixture occurred in the period surrounding the 11th century arrival and expansion of Seljuq Turks to Anatolia. Present-day Turkish individuals have an admixture date estimate of 30.6 ± 1.9 generations (Fig. 4D) and thus from the same early centuries of the 1000s CE, which coincided with the transfer of control of Anatolia from the Romans to the Seljuqs and eventually the Ottomans. The genetic contribution of Central Asian Turkic speakers to present-day people can be provisionally estimated by comparison of Central Asian ancestry in present-day Turkish people (~9%) and sampled ancient Central Asians (range of ~41 to 100%) to be between $\frac{9}{100}$ and $\frac{9}{41}$, or ~9 to 22%. Our sample of present-day Turkish people is broadly representative of the general population, as it derives from eight localities across the country (n = 58) (34). The genetic data point to Turkish people carrying the legacy of both ancient people who lived in Anatolia for thousands of years covered by our study and people coming from Central Asia bearing Turkic languages.
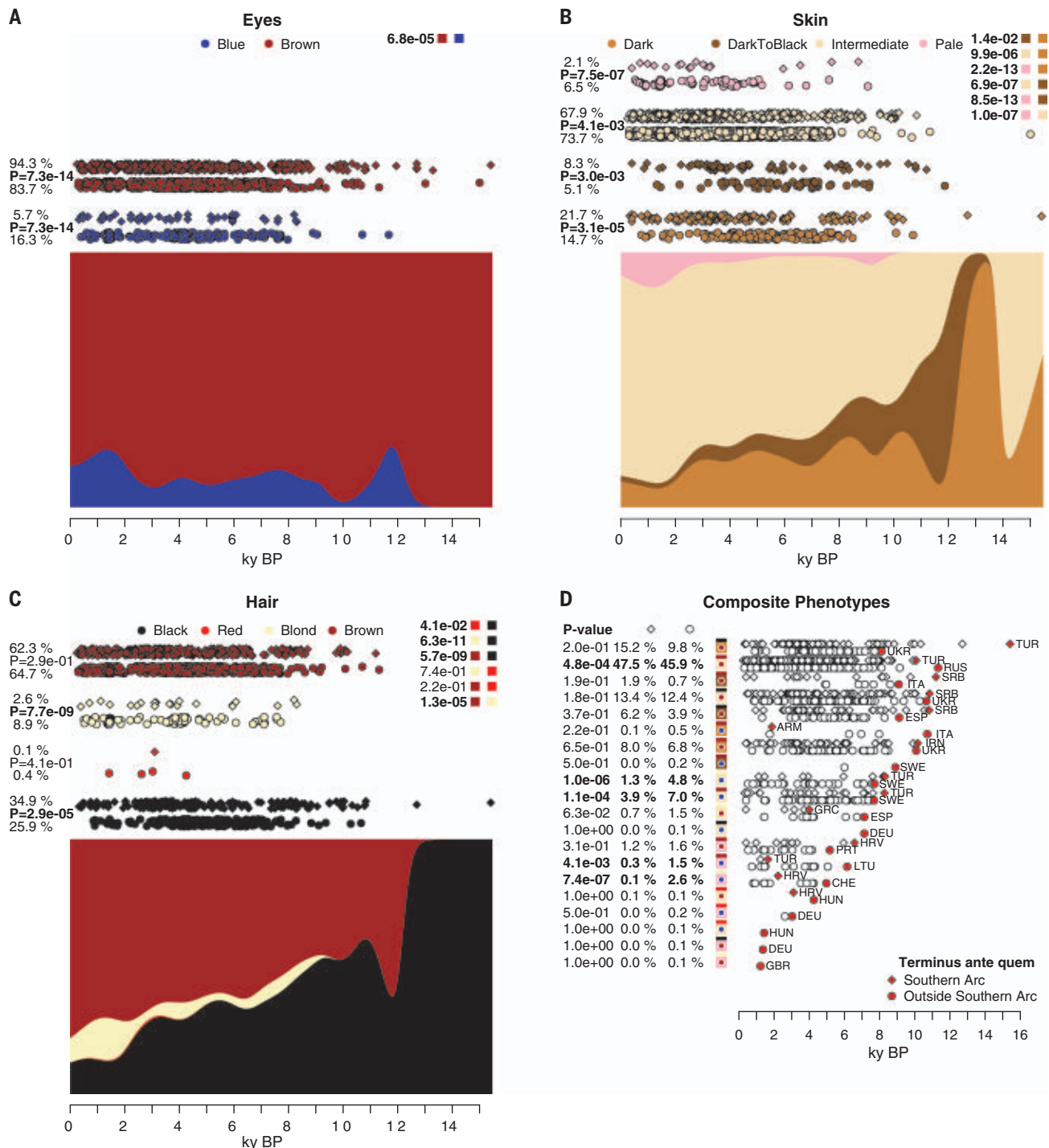
Fig. 6. Pigmentation in West Eurasia. (**A** to **C**) We show the temporal distribution of genetically predicted eye (A), skin (B), and hair (C) color in West Eurasians of the last 16,000 years; each point represents an individual, with the top row for each subphenotype corresponding to the Southern Arc and the bottom row corresponding to Northern, Central, and Western Europeans and people of the Eurasian steppe. ky BP, thousand years before the present. (**D**) Composite phenotypes of all three aspects of pigmentation using the same color scheme as (A) to (C) and denoted as eye color (circle), hair color (top), and skin color (bottom) in the composite phenotype symbols. The modal phenotype of West Eurasians had brown eyes, intermediate skin pigmentation, and brown hair, with the highest prevalence (Fisher's exact test) of low pigmentation outside the Southern Arc (in the rest of Europe and the Eurasian steppe).

The medieval period was marked by Slavic migrations into the Balkans on the basis of the genetic analysis of present-day populations (*35, 36*). It is also recorded in historical sources, such as those of Procopius (*37*) in the sixth century BCE, when Slavic groups came into contact with the Roman Empire (*38*). The South Slavs of today in the Balkans are one of the major groups of Slavic speakers, and the question of which migrations played a role in their origin is of interest for understanding how this group of languages, little-attested until medieval times, came to be so widespread across the greater part of Eastern Europe. We highlight Roman, Byzantine, and

medieval individuals from Albania, Bulgaria, Croatia, Greece, North Macedonia, and Serbia, which we studied in conjunction with those that preceded them in the Balkans and with published data from present-day people genotyped on the Human Origins array (*34, 39*) (Fig. 5). The reduction of Anatolian Neolithic ancestry was a long-term process in Southeastern Europe (*1*), which allows us to differentiate present-day populations from those preceding the Slavic migrations. When we order individuals along this component of ancestry (Fig. 5), we observe that present-day Slavs outside the Balkans have the least, whereas pre-Slavic inhabitants from the Balkans have the most of this type of ancestry, with present-day people from Southeastern Europe intermediate between the two extremes. Three individuals from Bulgaria (Samovodene), North Macedonia (Bitola), and an outlier individual from Trogir in Croatia (700 to 1100 CE) have the lowest levels of this ancestry. Most individuals from Trogir (a port city of the Adriatic in Croatia that was founded by Ancient Greek colonists and was part of the Byzantine Empire) overlapped with present-day people from ~700 to 900 CE, as did 12th century CE individuals from Veliko Tarnovo and Ryahovets in Bulgaria and a mid–fourth century CE Roman-era individual from Marathon in Greece, who, however, lacked the Balkan hunter-gatherer ancestry found consistently in the present-day population (Fig. 1). Finally, three medieval individuals from Albania (500 to 1100 CE) and a Late Antique (~500 CE) individual from Boyanovo in Bulgaria preceding the Slavic migrations, overlapped with the more ancient population, having high levels of Anatolian Neolithic ancestry. Among present-day people, Greeks and Albanians have more Anatolian Neolithic ancestry than their South Slavic neighbors. Slavic migrations have some echoes, ~3000 years later, to the spread of the descendants of Yamnaya steppe pastoralists into Southeastern Europe (*1, 7*). Although both events were transformative, any analogy should not be pushed too far. The medieval movements were carried out by large, organized communities engaging with complex states, such as the Avar Khaganate and Byzantine Empire, and no comparable polities existed in Yamnaya times. Collectively, our data suggest that although Balkan groups experienced a shift of ancestry in the medieval period, the fusion of locals and migrants was variable with individuals of diverse ancestry being present in medieval times and persisting up to the present.

Phenotypes of the Southern Arc in their West Eurasian context

Our survey of populations of the Southern Arc focuses on ancestry, but it also illuminates other aspects of biology. Superficial phenotypes, such as pigmentation, were remarked upon by ancient writers. We carried out a survey of predicted pigmentation and other phenotypes of West Eurasian populations across time (supplementary text S3 and Fig. 6) (*17*) to discover the extent to which ancient authors' perceptions (based on direct observation or through accounts of faraway peoples) might correspond to the genetic inference of their appearances (*40*). We find that the modal phenotype of eye, skin, and hair pigmentation in ancient West Eurasians was brown-eyed, of intermediate complexion, and brown-haired—even among Yamnaya steppe pastoralists—contradicting stereotypical characterizations of Steppe peoples as being blue-eyed, pale-skinned, and light-haired (*41, 42*). Note that when we use categorizations—such as intermediate—of the continuous skin tone phenotype, we refer to the scheme adopted by HIrisPlex-S (*40*); in that scheme, intermediate skin tones are commonly found in present-day Mediterranean populations and pale ones in present-day Northern European ones. A general depigmentation trend can be seen across time (Fig. 6), with a reduction of black hair and darker skin tones accompanying the increase of brown hair and intermediate skin tones. However, inhabitants of the Southern Arc had significantly darker pigmentation on average than those of the north (defined as Europe outside the Southern Arc and the Eurasian steppe) over all periods (Fig. 6), which provides support for the identification by ancient writers of light-pigmentation phenotypes as being more common in some groups of the north, such as the Celts and Scythians. Another contrast made by ancient writers was with people of Africa, such as Egyptians and Ethiopians, who were said to be of darker pigmentation (e.g., Hdt. 2.104); a comparison of people of the Southern Arc with their southern neighbors will become possible when genomic data from people living south of the Mediterranean become available. When examining composite pigmentation phenotypes (Fig. 6D), we observe that although average pigmentation did differentiate between populations of the Southern Arc and the north, light phenotypes were found in both areas at similar early dates, growing in parallel in the more recent millennia of history. Light pigmentation in West Eurasia was the result of selection across time, which continued into the Historical period (*43, 44*), and not of the survival of supposed ancient Indo-European phenotypes as some 19th and 20th century writers supposed (*41, 42*) or the product of the direct influence of climate that some Greco-Roman writers hypothesized to explain patterns they observed during their own time (*17*). The malleability of human phenotypes across time and the presence of diverse ones—whether dark, light, or intermediate—across space undermine prejudiced views of history that overemphasize superficial traits at the expense of the more meaningful aspects of human culture and biology.

This study illustrates the potential of archaeogenetic studies of people of the civilizations of the ancient world in conjunction with archaeological and textual evidence. Ancient writings are replete with the descriptions of little-known groups, such as the numerous tribes encountered by Xenophon the Athenian at the end of the fifth century BCE and recorded in his *Anabasis*, as he and his fellow mercenaries escaped from Mesopotamia northward to the Black Sea. To what extent did these and other named entities of antiquity correspond to ancestral groups that may one day be placed on the genetic landscape of the ancient world? Ancient DNA is bringing some of the stories of these forgotten peoples back to life and paying homage to their legacies.

REFERENCES AND NOTES

1. I. Lazaridis et al., Science 377, eabm4247 (2022).
2. I. Lazaridis et al., Science 377, 982–987 (2022).
3. G. R. Crane, Ed., Perseus Digital Library (Tufts University); http://www.perseus.tufts.edu.
4. I. Lazaridis et al., Nature 548, 214–218 (2017).
5. I. Mathieson et al., Nature 528, 499–503 (2015).
6. Z. Hofmanová et al., Proc. Natl. Acad. Sci. U.S.A. 113, 6886–6891 (2016).
7. I. Mathieson et al., Nature 555, 197–203 (2018).
8. J. L. Davis, S. R. Stocker, Hesperia 85, 627–655 (2016).
9. E. R. Jones et al., Nat. Commun. 6, 8912 (2015).
10. W. Haak et al., Nature 522, 207–211 (2015).
11. I. Lazaridis et al., Nature 536, 419–424 (2016).
12. F. Clemente et al., Cell 184, 2565–2586.e21 (2021).
13. D. Adamov, V. M. Gurianov, S. Karzhavin, V. Tagankin, V. Urasin, Russ. J. Genet. Geneal. 7, 1920–2997 (2015).
14. C.-C. Wang et al., Nat. Commun. 10, 590 (2019).
15. N. Patterson et al., Nature 601, 588–594 (2022).
16. M. B. Sakellariou, Les Proto-grecs (Ekdotikè Athenon, 1980).
17. Detailed information is provided in the supplementary materials.
18. R. Yaka et al., Curr. Biol. 31, 2455–2468.e18 (2021).
19. H. Ringbauer, J. Novembre, M. Steinrücken, Nat. Commun. 12, 5425 (2021).
20. I. Olalde et al., Science 363, 1230–1234 (2019).
21. M. Feldman et al., Sci. Adv. 5, eaax0061 (2019).
22. I. M. D'jakonov, S. A. Starostin, Hurro-Urartian as an Eastern Caucasian Language (R. Kitzinger, 1986).
23. V. M. Narasimhan et al., Science 365, eaat7487 (2019).
24. A. S. Kassian et al., Linguistics 59, 949–979 (2021).
25. P. A. Underhill et al., Eur. J. Hum. Genet. 23, 124–131 (2015).
26. V. Grugni et al., PLOS ONE 7, e41252 (2012).
27. S. Sengupta et al., Am. J. Hum. Genet. 78, 202–221 (2006).
28. M. L. Antonio et al., Science 366, 708–714 (2019).
29. T. Saupe et al., Curr. Biol. 31, 2576–2591.e12 (2021).
30. E. Skourtanioti et al., Cell 181, 1158–1175.e28 (2020).
31. M. Unterländer et al., Nat. Commun. 8, 14615 (2017).
32. P. B. Damgaard et al., Nature 557, 369–374 (2018).
33. M. Krzewińska et al., Sci. Adv. 4, eaat4457 (2018).
34. I. Lazaridis et al., Nature 513, 409–413 (2014).
35. P. Ralph, G. Coop, PLOS Biol. 11, e1001555 (2013).
36. G. B. J. Busby et al., Curr. Biol. 25, 2518–2526 (2015).
37. E. James, Europe's Barbarians: AD 200-600 (Pearson Longman, 2009).
38. I. Olalde et al., bioRxiv 2021.08.30.458211 [Preprint] (2021). https://doi.org/10.1101/2021.08.30.458211.
39. N. Patterson et al., Genetics 192, 1065–1093 (2012).
40. L. Chaitanya et al., Forensic Sci. Int. Genet. 35, 123–135 (2018).
41. L. Poliakov, Le Mythe Aryen: Essai sur les Sources du Racisme et du Nationalisme (Calmann-Levy, 1971).
42. J. V. Day, Indo-European Origins: The Anthropological Evidence (Institute for the Study of Man, 2001).
43. D. Ju, I. Mathieson, Proc. Natl. Acad. Sci. U.S.A. 118, e2009227118 (2021).
44. S. Wilde et al., Proc. Natl. Acad. Sci. U.S.A. 111, 4832–4837 (2014).

45. L. Baringhaus, C. Franz, *J. Multivariate Anal.* **88**, 190–206 (2004).
46. S. Alpaslan-Roodenberg *et al.*, *Nature* **599**, 41–46 (2021).

The Huanan Seafood Wholesale Market in Wuhan was the early epicenter of the COVID-19 pandemic

Michael Worobey[1]*, Joshua I. Levy[2], Lorena Malpica Serrano[1], Alexander Crits-Christoph[3], Jonathan E. Pekar[4,5], Stephen A. Goldstein[6], Angela L. Rasmussen[7,8], Moritz U. G. Kraemer[9], Chris Newman[10], Marion P. G. Koopmans[11,12], Marc A. Suchard[13,14,15], Joel O. Wertheim[16], Philippe Lemey[17,18], David L. Robertson[19], Robert F. Garry[18,20,21], Edward C. Holmes[22], Andrew Rambaut[23], Kristian G. Andersen[2,24]*

Understanding how severe acute respiratory syndrome coronavirus 2 (SARS-CoV-2) emerged in 2019 is critical to preventing future zoonotic outbreaks before they become the next pandemic. The Huanan Seafood Wholesale Market in Wuhan, China, was identified as a likely source of cases in early reports, but later this conclusion became controversial. We show here that the earliest known COVID-19 cases from December 2019, including those without reported direct links, were geographically centered on this market. We report that live SARS-CoV-2–susceptible mammals were sold at the market in late 2019 and that within the market, SARS-CoV-2–positive environmental samples were spatially associated with vendors selling live mammals. Although there is insufficient evidence to define upstream events, and exact circumstances remain obscure, our analyses indicate that the emergence of SARS-CoV-2 occurred through the live wildlife trade in China, and show that the Huanan market was the epicenter of the COVID-19 pandemic.

O n 31 December 2019, the Chinese government notified the World Health Organization (WHO) of an outbreak of severe pneumonia of unknown etiology in Wuhan, Hubei Province, China (*1–4*), a city of ~11 million people. Of the initial 41 people hospitalized with unknown pneumonia by 2 January 2020, 27 (66%) had direct exposure to the Huanan Wholesale Seafood Market (hereafter, "Huanan market") (*2, 5, 6*). These first cases were confirmed to be infected with a novel coronavirus, subsequently named severe acute respiratory syndrome coronavirus 2 (SARS-CoV-2), and were suffering from a disease later named coronavirus disease 2019 (COVID-19). The initial diagnoses of COVID-19 were made in several hospitals independently between 18 and 29 December 2019 (*5*). These early reports were free from ascertainment bias because they were based on signs and symptoms before the Huanan market was identified as a shared risk factor (*5*). A subsequent systematic review of all cases reported to China's National Notifiable Disease Reporting System by hospitals in Wuhan as part of the joint WHO-Chinese "WHO-convened global study of origins of SARS-CoV-2: China Part" (hereafter, "WHO mission report") (*7*) showed that 55 of 168 of the earliest known COVID-19 cases were associated with this market. However, the observation that the preponderance of early cases were linked to the Huanan market, alone, does not establish that the pandemic originated there.

Sustained live mammal sales during 2019 occurred at the Huanan market and three other markets in Wuhan, and included wild and farmed wildlife (*8*). Several of these species are known to be experimentally susceptible to SARS-related coronaviruses (SARSr-CoVs) such as SARS-CoV (hereafter, "SARS-CoV-1") and SARS-CoV-2 (*9–11*). During the early stages of the COVID-19 pandemic, animals sold at the Huanan market were hypothesized to be the source of the unexplained pneumonia cases (*12–19*) (data S1), consistent with the emergence of SARS-CoV-1 from 2002 to 2004 (*20*), as well as other viral zoonoses (*21–23*). This led to the decision to close and sanitize the Huanan market on 1 January 2020, with environmental samples also being collected from vendors' stalls (*7, 12, 24*) (data S1).

Determining the epicenter of the COVID-19 pandemic at the neighborhood level rather than at the city level could help to resolve whether SARS-CoV-2 had a zoonotic origin, similar to SARS-CoV-1 (*20*). In this study, we obtained data from a range of sources to test the hypothesis that the COVID-19 pandemic began at the Huanan market. Despite limited testing of live wildlife sold at the market, collectively, our results provide evidence that the Huanan market was the early epicenter of the COVID-19 pandemic and suggest that SARS-CoV-2 likely emerged from the live wildlife trade in China. However, events upstream of the market, as well as exact circumstances at the market, remain obscure, highlighting the need for further studies to understand and lower the risk of future pandemics.

Results

Early cases lived near to and centered on the Huanan market

The 2021 WHO mission report identified 174 COVID-19 cases in Hubei Province in December 2019 after careful examination of reported case histories (*7*). Although geographical coordinates of the residential locations of the 164 cases who

lived within Wuhan were unavailable, we were able to reliably extract the latitude and longitude coordinates of 155 cases from maps in the report (figs. S1 to S8).

Although early COVID-19 cases occurred across Wuhan, most clustered in central Wuhan near the west bank of the Yangtze River, with a high density of cases near to, and surrounding, the Huanan market (Fig. 1A). We used a kernel density estimate (KDE) to reconstruct an underlying probability density function from which the home locations for each case were drawn (25). Using all 155 of the December 2019 cases, the location of the Huanan market lies within the highest density contour that contains 1% of the probability mass (Fig. 1B). For a KDE estimated using the 120 cases with no known linkage to the market, the market remains within the highest density 1% contour (Fig. 1C). The clustering of COVID-19 cases in December around the Huanan market (Fig. 1, B and C, insets) contrasts with the pattern of widely dispersed cases across Wuhan by early January through mid-February 2020 (Fig. 1, D and E), which we mapped using location data from individuals who had used a COVID-19 assistance channel on Sina Weibo, a Chinese social media platform (26). Weibo-based data analyses showed that, unlike early COVID-19 cases, by January and February, many of the sick individuals who sought help resided in highly populated areas of the city, particularly in areas with a high density of older people (Fig. 1E and figs. S9 and S10).

We also investigated whether the December COVID-19 cases were closer to the market than expected based on an empirical null distribution of Wuhan's population density [data from WorldPop.org (27, 28)], with a median distance to the Huanan market of 16.11 km (25). To account for older individuals being more likely to be hospitalized and sick with COVID-19 (29), we age-matched the population data to the December 2019 COVID-19 case data. We considered three categories of cases, which were all significantly closer to the Huanan market than expected: (i) all cases (median distance 4.28 km; $P < 0.001$), (ii) cases linked directly to the Huanan market (median distance 5.74 km; $P < 0.001$), and (iii) cases with no evidence of

a direct link to the Huanan market (median distance 4.00 km; $P < 0.001$) (Fig. 2A). The cases with no known link to the market on average resided closer to the market than the cases with links to the market ($P = 0.029$). Furthermore, the distances between the center points (Fig. 2B) and the Huanan market were shorter than expected for all categories of December cases compared with the empirical null distribution of Wuhan's population density (Fig. 2A). For all December cases, the center point was located 1.02 km away ($P = 0.007$); for cases with market links, it was 2.28 km away ($P = 0.034$); and for the cases with no reported link to the market, it was 0.91 km away ($P = 0.006$). By comparison, the center point of age-matched samples drawn from the empirical null distribution was 4.65 km away from the market (Fig. 2A).

We tested the robustness of our results for the possibility of ascertainment bias (25). For all mapped cases ($n = 155$), under the "center-point distance to the Huanan market" test, the 38 cases residing closest to the market (within a radius of 1.6 km) could be removed from the dataset before losing significance at the $\alpha = 0.05$ level (fig. S12). For the "median distance to Huanan market" test, we could remove 98 cases (63%) ($r = 5.8$ km). For cases not directly linked to the Huanan market ($n = 120$), we could remove 36 (30%) ($r = 1.5$ km) and 81 (68%) ($r = 4.3$ km) cases for the two tests, respectively, before losing significance at the $\alpha = 0.05$ level (fig. S12).

We performed a spatial relative risk analysis (25) to compare December 2019 COVID-19 cases with January–February 2020 cases reported through Weibo (Fig. 2C). The Huanan market is located within a well-defined area with high case density that would be expected to be observed in <1 in 100,000 samplings of the Weibo data empirical distribution (the relative risk analysis is shown in Fig. 2C and the control distribution in Fig. 1D). No other regions in Wuhan showed a comparable case density.

Both early lineages of SARS-CoV-2 were geographically associated with the market

Two lineages of SARS-CoV-2 designated A and B (30) have co-circulated globally since early in

the COVID-19 pandemic (31). Until a report in a recent preprint (24), only lineage B sequences had been sampled at the Huanan market. The 11 lineage B cases from December 2019 for which we have location information resided closer than expected to the Huanan market compared with the age-matched Wuhan population distribution (median distance 8.30 km; $P = 0.017$) (25). The center point of the 11 lineage B cases was 1.95 km from the Huanan market, also closer than expected ($P = 0.026$). The two lineage A cases for which we have location information involved the two earliest lineage A genomes known to date. Neither case reported any contact with the Huanan market (7). The first case was detected before any knowledge of a possible association of the unexplained pneumonia in Wuhan with the Huanan market (5), and therefore could not have been a product of ascertainment bias in favor of cases residing near the market. The second case had stayed in a hotel near the market (32) for the 5 days preceding symptom onset (25). Relative to the age-matched Wuhan population distribution, the first individual resided closer to the Huanan market (2.31 km) than expected ($P = 0.034$). Although the exact location of the hotel near the market was not reported (32), there are at least 20 hotels within 500 m (table S1). Under the conservative assumption that the hotel could have been located as far as 2.31 km from the Huanan market (as was the residence of the other lineage A case), and assuming that this location is comparable to a residential location given the timing of the stay before symptom onset (25), it would be unlikely to observe both of the earliest lineage A cases this near to the Huanan market ($P = 0.001$ or less). The finding that both identified lineage A cases had a geographical connection to the market, in combination with the detection of lineage A within the market (24), support the likelihood that during the early epidemic, lineage A was, like lineage B, disseminating outward from the Huanan market into the surrounding neighborhoods.

Our statistical results were robust to a range of factors, for example, the use of an empirical control distribution that was based on presumptive COVID-19 cases locations later in the

[1]Department of Ecology and Evolutionary Biology, University of Arizona, Tucson, AZ 85721, USA. [2]Department of Immunology and Microbiology, The Scripps Research Institute, La Jolla, CA 92037, USA. [3]W. Harry Feinstone Department of Molecular Microbiology and Immunology, Johns Hopkins Bloomberg School of Public Health, Baltimore, MD 21205, USA. [4]Bioinformatics and Systems Biology Graduate Program, University of California San Diego, La Jolla, CA 92093, USA. [5]Department of Biomedical Informatics, University of California San Diego, La Jolla, CA 92093, USA. [6]Department of Human Genetics, University of Utah School of Medicine, Salt Lake City, UT 84112, USA. [7]Vaccine and Infectious Disease Organization, University of Saskatchewan, Saskatoon, SK S7N 5E3, Canada. [8]Center for Global Health Science and Security, Georgetown University, Washington, DC 20057, USA. [9]Department of Zoology, University of Oxford, Oxford OX1 3SZ, UK. [10]Wildlife Conservation Research Unit, Department of Zoology, The Recanati-Kaplan Centre, University of Oxford, Oxford OX13 5QL, UK. [11]Pandemic and Disaster Preparedness Centre, Erasmus University Medical Center, 3015 CE Rotterdam, Netherlands. [12]Department of Viroscience, Erasmus University Medical Center, 3015 CE Rotterdam, Netherlands. [13]Department of Biostatistics, Fielding School of Public Health, University of California Los Angeles, Los Angeles, CA 90095, USA. [14]Department of Human Genetics, David Geffen School of Medicine, University of California Los Angeles, Los Angeles, CA 90095, USA. [15]Department of Computational Medicine, David Geffen School of Medicine, University of California Los Angeles, Los Angeles, CA 90095, USA. [16]Department of Medicine, University of California San Diego, La Jolla, CA 92093, USA. [17]Department of Microbiology, Immunology and Transplantation, Rega Institute for Medical Research, KU Leuven, 3000 Leuven, Belgium. [18]Global Virus Network (GVN), Baltimore, MD 21201, USA. [19]MRC-University of Glasgow Center for Virus Research, Glasgow G61 1QH, UK. [20]Tulane University, School of Medicine, Department of Microbiology and Immunology, New Orleans, LA 70112, USA. [21]Zalgen Labs, Frederick, MD 21703, USA. [22]Sydney Institute for Infectious Diseases, School of Life and Environmental Sciences and School of Medical Sciences, The University of Sydney, Sydney, New South Wales 2006, Australia. [23]Institute of Evolutionary Biology, University of Edinburgh, Edinburgh EH9 3FL, UK. [24]Scripps Research Translational Institute, La Jolla, CA 92037, USA.
*Corresponding author. Email: worobey@arizona.edu (M.W.); andersen@scripps.edu (K.G.A.)

Wuhan epidemic (Weibo data); laboratory-confirmed versus clinically diagnosed cases; and uncertainty in case location or missing data (figs. S13 to S15) (*25*). For instance, we artificially introduced location uncertainty ("noise") in each case location in our dataset by randomly resampling each point within a circle of radius 1000 m centered on its original center point, and the conclusions were unaffected (fig. S13). The extraction method that we used actually introduced only up to ~50 m of noise in each case location estimate (fig. S7), ruling out the possibility that our overall results were affected by this source of error. The results were also robust when corrected for multiple-hypothesis testing (table S4).

Wild animal trading in Wuhan markets

In addition to selling seafood, poultry, and other commodities, the Huanan market was among four markets in Wuhan reported to consistently sell a variety of live wild-captured or farmed mammal species in the years and months leading up to the COVID-19 pandemic (*8*). There are, however, no prior reports of which species, if any, were sold at the Huanan market in the months leading up to the pandemic. Here, we report that multiple plausible intermediate wildlife hosts of SARS-CoV-2 progenitor viruses, including red foxes (*Vulpes vulpes*), hog badgers (*Arctonyx albogularis*), and common raccoon dogs (*Nyctereutes procyonoides*), were sold live at the Huanan market up until at least November 2019 (Table 1 and table S5). No reports are known to be available for SARS-CoV-2 test results from these mammals at the Huanan market. Despite a general slowdown in live animal sales during the winter months, we report that raccoon dogs, which are sold for both meat and fur, were consistently available for sale throughout the year, including at the Huanan market in November 2019 (Table 1 and table S5).

There were potentially many locations in Wuhan, a city of 11 million, that would have been equally or more likely than the Huanan market to sustain the first recognized cluster of a new respiratory pathogen had its introduction not been linked to a live animal market, including other shopping venues, hospitals, elder care facilities, workplaces, universities, and places of worship. To investigate possible sites, we compared the relative extent of intra-urban human traffic to the Huanan market versus other locations within the city of Wuhan using a location-specific dataset of social media check-ins in the Sina Visitor System (*25*, *33*). We found at least 70 other markets throughout the city of Wuhan that received more social media check-ins than the Huanan market (Fig. 3). To extend this analysis beyond only markets, we also used a subsequently published list of known SARS-CoV-2 superspreader locations (*34*) to identify 430 locations in Wuhan
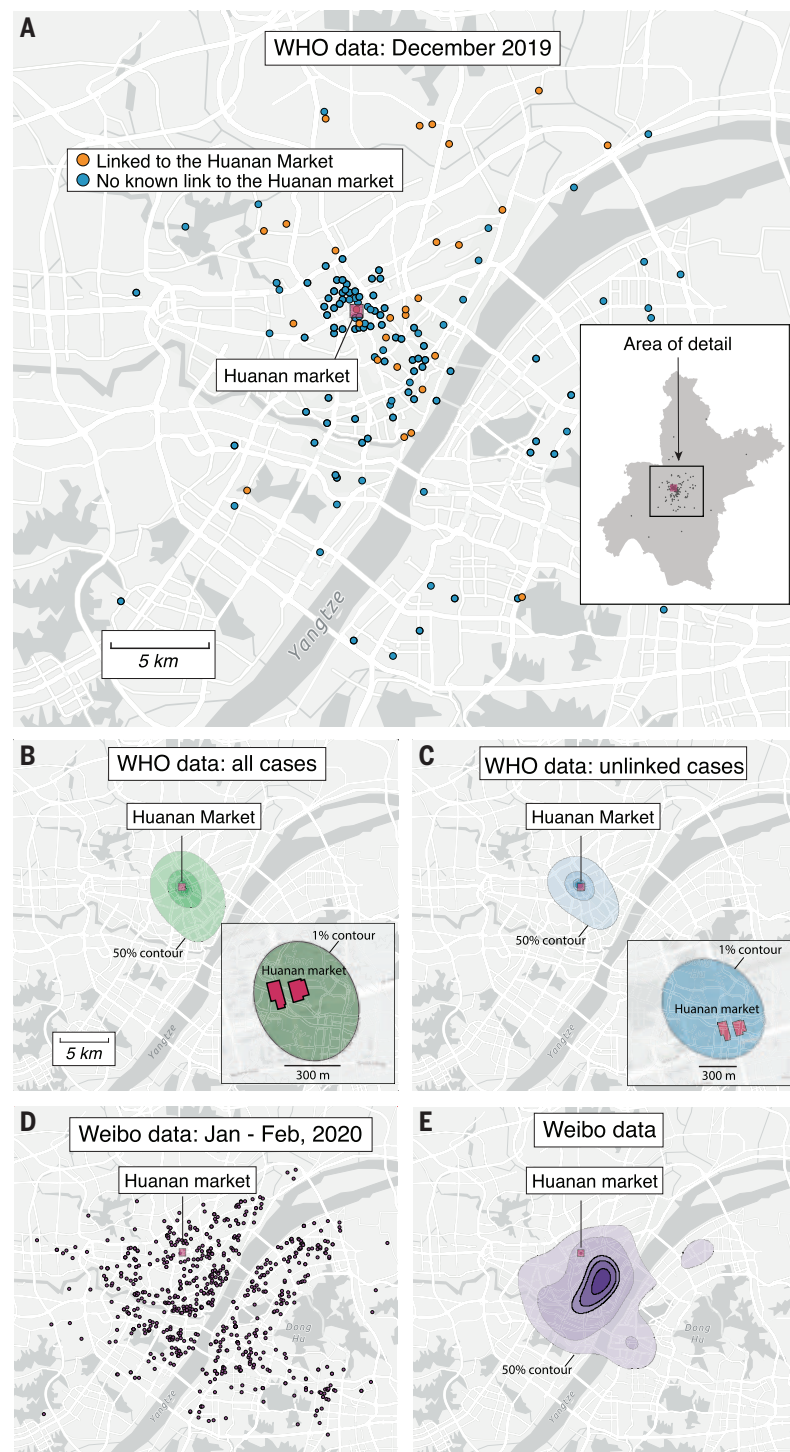
Fig. 1. Spatial patterns of COVID-19 cases in Wuhan in December 2019 and January–February 2020. (**A**) Locations of the 155 cases that we extracted from the WHO mission report (*7*). Inset: map of Wuhan with the December 2019 cases indicated with gray dots (no cases are obscured by the inset). In both the inset and the main panel, the location of the Huanan market is indicated with a red square. (**B**) Probability density contours reconstructed by a KDE using all 155 COVID-19 cases locations from December 2019. The highest density 50% contour marked is the area for which cases drawn from the probability distribution are as likely to lie inside as outside. Also shown are the highest density 25%, 10%, 5%, and 1% contours. Inset: expanded view and the highest density 1% probability density contour. (**C**) Probability density contours reconstructed using the 120 COVID-19 cases locations from December 2019 that were unlinked to the Huanan market. (**D**) Locations of 737 COVID-19 cases from Weibo data dating to January–February 2020. (**E**) The same highest probability density contours (50% through 1%) as shown in (B) and (C) for 737 COVID-19 case locations from Weibo data.

Fig. 2. Spatial analyses. (**A**) Inset: map of Wuhan, with gray dots indicating the 1000 random samples from the WorldPop.com null distribution. In the main panel, the median distance between Huanan market and the WorldPop.org null distribution is indicated by the outer black circle. December 2019 cases are indicated by concentric red circles (distances to Huanan market are described in the purple boxes). The center point of Wuhan population density data is indicated by a blue dot. Center points of December 2019 case locations are shown as follows: red dots indicate "all," "linked," and "unlinked" cases, and the yellow dot indicates lineage B cases. Distance from center points to Huanan market are described in orange boxes. (**B**) Schematic showing how cases can be near to, but not centered on, a specific location. We hypothesized that if the Huanan market were the epicenter of the pandemic, then early cases should fall not just unexpectedly near to it but should also be unexpectedly centered on it (see the materials and methods). The blue dots show how hypothetical cases quite near the Huanan market could nevertheless not be centered on it. (**C**) Tolerance contours based on relative risk of COVID-19 cases in December 2019 versus data from January–February 2020. The gray dots show the December case locations. The contours represent the probability of observing that density of December cases within the bounds of the given contour if the December cases had been drawn from the same spatial distribution as the January–February data.

respiratory disease might first be noticed in a large city.

A dataset from the Chinese Center for Disease Prevention and Control (CCDC) report dated 22 January 2020 (data S1) (*12, 13, 15, 16*) was made publicly available in June 2020 (*24, 35*). A total of 585 environmental samples were initially taken from various surfaces in the Huanan market on 1 and 12 January 2020 by the CCDC (tables S6 and S7 and data S1) (*12, 13, 15, 16, 24, 35*), with further samples taken throughout the market during January and February (*24*). We extended the analysis in the WHO mission report (*7*) by integrating public online maps and photographic evidence, data from public business registries (table S8 and data S2), information about which live mammal species were sold at the Huanan market in late 2019 (Table 1 and table S5), and the CCDC report (data S1). We reconstructed the floor plan of the market and integrated information from business registries of vendors at the market (fig. S16 and table S8), as well as an official report (*36*) recording fines to three business owners for illegal sales of live mammals (data S2) (*36*). From this, we identified an additional five stalls that were likely selling live or freshly butchered mammals or other unspecified meat products in the southwest corner of the western section of the market (Fig. 4A, figs. S16 and S17, and table S6).

Five of the SARS-CoV-2–positive environmental samples were taken from a single stall selling live mammals in late 2019 (table S6). Further, all five objects sampled showed an association with animal sales, including a metal cage, two carts (of the kind frequently used to transport mobile animal cages), and a hair and feather remover (table S6). No human COVID-19 cases were reported there (*7, 12*). The same stall was visited by one of us (E.C.H.) in 2014, and live raccoon dogs were observed housed in a metal cage stacked on top of a cage with live birds (Fig. 4A) (*37*). A recent report (*24*) identified that the grates outside of this stall, upon which animal cages were stacked (*37*), were positive for SARS-CoV-2.

Positive environmental samples linked both to live mammal sales and to human cases at the Huanan market

We used a spatial relative risk analysis to identify potential regions of the market with an increased density of positive environmental samples (*25*). We found evidence (*P* < 0.05) of a region in the southwest area of the market where live mammals were for sale (Fig. 4B). Although environmental sampling of the market was incomplete and spatially heterogeneous (data S1 and table S6), our analysis accounts for the empirical environmental sampling distribution, which was biased toward "stalls related to December cases," as well as "stalls that sold livestock, poultry, farmed wildlife"

that may have been at high risk for superspreader events and which received more check-ins than the Huanan market (Fig. 3, inset). The Huanan market accounted for 0.12% (120 of 98,146) of social media check-ins to markets in the dataset that received at least as many check-ins as the Huanan market. The market accounted for 0.04% (120 of 262,233) of all social media check-ins to the >400 sites in

Wuhan identified as especially likely to be potential superspreader locations and which received at least as many social media visits as the Huanan market. Considering the number of check-ins to all four markets selling live wild animals in Wuhan (combined), they accounted for 0.21% (206 of 98,146) of market visits and 0.079% (206 of 262,233) of visits to the 430 potential superspreader sites, where a new

(7) (Fig. 4, C and D). The "distance to the nearest vendor selling live mammals" and the "distance to the nearest human case" were independently predictive of environmental sample positivity (P = 0.004 and 0.014, respectively, for n = 6; table S9). To further investigate the robustness of these findings to possible sampling biases, we considered three scenarios: (i) oversampling of live mammal and unknown meat stalls, (ii) overcounting of positive samples, and (iii) exclusion of the seafood stand near the wildlife area of the market (with five positive samples) from our analysis (table S10). In each case, the distance to live mammal vendors remained predictive of environmental sample positivity, and the region of increased positive sample density in the southwest corner of the western section of the market remained consistent (fig. S18).

Finally, to analyze the spatial patterning of human cases within the Huanan market, we plotted cases as a function of symptom onset from the WHO mission report (7) (Fig. 5A and table S11) (25). All eight COVID-19 cases detected before 20 December 2019 were from the western side of the market, where mammal species were also sold (Fig. 5, B and C). Unlike SARS-CoV-2–positive environmental samples (Fig. 4, A and C), we found that COVID-19 cases were more diffuse throughout the building (Fig. 5).

Study limitations

There are several limitations to our study. We have been able to recover location data for most of the December-onset COVID-19 cases identified by the WHO mission (7) with sufficient precision to support our conclusions. However, we do not have access to the precise latitude and longitude coordinates of all of these cases. Should such data exist, they may be accompanied by additional metadata, some of which we have reconstructed, but some of which, including the date of onset of each case, would be valuable for ongoing studies. We also lack direct evidence of an intermediate animal infected with a SARS-CoV-2 progenitor virus either at the Huanan market or at a location connected to its supply chain, such as a farm. Additionally, no line list of early COVID-19 cases is available, and we do not have complete details of environmental sampling. However, compared with many other outbreaks, we have more comprehensive information on early cases, hospitalizations, and environmental sampling (7).

Discussion

Several lines of evidence support the hypothesis that the Huanan market was the epicenter of the COVID-19 pandemic and that SARS-CoV-2 emerged from activities associated with the live wildlife trade there. Spatial analyses within the market show that SARS-CoV-2–positive environmental samples, including cages, carts, and freezers, were associated with activities concentrated in the southwest corner of the market. This is the same section where vendors were selling live mammals, including raccoon dogs, hog badgers, and red foxes, immediately before the COVID-19 pandemic. Multiple positive samples were taken from one stall known to have sold live mammals, and the water drain proximal to this stall, as well as other sewerages and a nearby wildlife stall on the southwest side of the market, tested positive for SARS-CoV-2 (24). These findings suggest that infected animals were present at the Huanan market at the beginning of the COVID-19 pandemic; however, we do not have access to any live animal samples from relevant species. Additional information, including sequencing data and detailed sampling strategy, would be invaluable to test this hypothesis comprehensively.

In a related study, we inferred separate introductions of SARS-CoV-2 lineages A and B into humans from likely infected animals at the Huanan market (38). We estimated the first COVID-19 case to have occurred in November 2019, with few human cases and hospitalizations occurring through mid-December (38). A recent preprint (24) confirms the authenticity of the CCDC report (data S1) and records additional positive environmental samples in the southwestern area of the market selling live animals. This report also documents the early presence of the A lineage of SARS-CoV-2 in a Huanan market environmental sample. This, along with the lineage A cases that we report in close geographical proximity to the market in December 2019, challenges the suggestion that the market was

Table 1. Live mammals traded at the Huanan market in November and December 2019.

Species (susceptibility*)	Family (susceptibility*)	Order (susceptibility*)	Observed at Huanan market November 2019
Raccoon dog (*Nyctereutes procyonoides*) (Y)	Canidae (Y)	Carnivora (Y)	Y
Amur hedgehog (*Erinaceus amurensis*)	Erinaceidae	Eulipotyphla	Y
Hog badger (*Arctonyx albogularis*) (Y)	Mustelidae (Y)	Carnivora (Y)	Y
Asian badger (*Meles leucurus*)	Mustelidae (Y)	Carnivora (Y)	Y
Chinese hare (*Lepus sinensis*)	Leporidae (Y)	Lagomorpha (Y)	Y
Chinese bamboo rat (*Rhizomys sinensis*) (Y)	Spalacidae (Y)	Rodentia (Y)	Y
Malayan porcupine (*Hystrix brachyura*)	Hystricidae	Rodentia (Y)	Y
Chinese muntjac (*Muntiacus reevesi*)	Cervidae (Y)	Artiodactyla (Y)	Y
Marmot (*Marmota himalayana*)	Sciuridae	Rodentia (Y)	Y
Red fox (*Vulpes vulpes*) (Y)	Canidae (Y)	Carnivora (Y)	Y
Siberian weasel (*Mustela sibirica*)	Mustelidae (Y)	Carnivora (Y)	N†
Pallas's squirrel (*Callosciurus erythraeus*)	Sciuridae	Rodentia (Y)	N
Masked palm civet (*Paguma larvata*) (Y)	Viverridae (Y)	Carnivora (Y)	N
Coypu (*Myocastor coypus*)	Echimyidae	Rodentia (Y)	N
Mink (*Neovison vison*) (Y)	Mustelidae (Y)	Carnivora (Y)	N
Red squirrel (*Sciurus vulgaris*)	Sciuridae	Rodentia (Y)	N
Wild boar (*Sus scrofa*) (Y)	Suidae (Y)	Artiodactyla (Y)	N
Complex-toothed flying squirrel (*Trogopterus xanthipes*)	Sciuridae	Rodentia (Y)	N

*Based on live susceptibility findings, serological findings, or ACE2-binding assays. See table S5 for details and associated references.   †Animals listed as "N" (no) were, however, present at Wuhan market during the 2017–2019 study period (8).
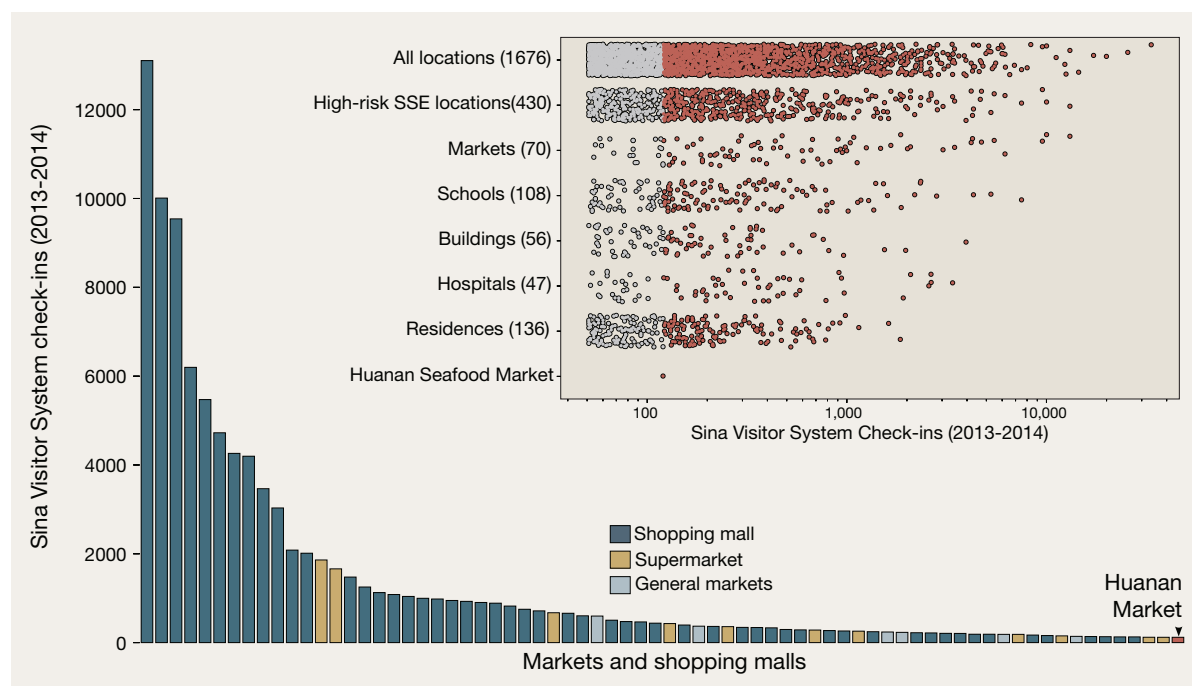
Fig. 3. Visitors to locations throughout Wuhan. Shown is the number of social media check-ins in the Sina Visitor System from 2013 to 2014 as shared by (*33*). The numbers of check-ins to individual markets throughout the city are shown in comparison with check-ins at the Huanan market. Inset: the total number of check-ins to all individual locations across the city of Wuhan grouped by category. Locations with >50 visitor check-ins are shown, and the locations that received more check-ins than the Huanan market in the same period are shown in red.

simply a superspreading event, which would be lineage specific. Rather, it adds to the evidence presented here that lineage A, like lineage B, may have originated at the Huanan market and then spread from this epicenter into the neighborhoods surrounding the market and beyond.

Several observations suggest that the geographic association of early COVID-19 cases with the Huanan market is unlikely to have been the result of ascertainment bias (see the supplementary text and tables S2 and S3) (*39*). These include that (i) few, if any, cases among Huanan market–unlinked individuals are likely to have been detected by active searching in the neighborhoods around the market, only in hospitals, because all of the cases analyzed here were hospitalized (*7*); (ii) public health officials simultaneously became aware of Huanan-linked cases both near and far from the Huanan market, not just the ones near it (fig. S11) (*5*); (iii) Huanan market–unlinked cases would not be expected to live significantly closer to the market than linked cases if they had been ascertained as contacts traced from those market-linked cases; and (iv) seroprevalence in Wuhan was highest in the districts around the market (*40*, *41*). It is also noteworthy that the December 2019 COVID-19 cases that we consider here were identified based on reviews of clinical signs and symptoms, not epidemiological factors such as where they

resided or links to the Huanan market (*7*), and that excess deaths from pneumonia rose first in the districts surrounding the market (*42*). Moreover, the spatial relationship with the Huanan market remains after removing the two-thirds of the unlinked cases residing nearest the market.

One of the key findings of our study is that "unlinked" early COVID-19 patients, i.e., those who did not work at the market, did not know someone who did, and had not recently visited the market, resided significantly closer to the market than patients with a direct link to it. The observation that a substantial proportion of early cases had no known epidemiological link had previously been used as an argument against the Huanan market being the epicenter of the pandemic. However, this group of cases resided significantly closer to the market than those who worked there, indicating that they had been exposed to the virus at or near the Huanan market. For market workers, the exposure risk was their place of work, not their residential locations, which were significantly farther afield than those cases not formally linked to the market.

Our spatial analyses show how patterns of COVID-19 cases shifted between late 2019, when the outbreak began (*43*), and early 2020, as the epidemic spread widely across Wuhan. COVID-19 cases in December 2019 were associated with the Huanan market in a manner

unrelated to Wuhan population density or demographic patterns, unlike the wide spatial distribution of cases observed during later stages of the epidemic in January–February 2020. This observation fits with the evidence from other sources that SARS-CoV-2 was not widespread in Wuhan at the end of 2019. For example, no SARS-CoV-2–positive sera or influenza-like illness reports were recorded among more 40,000 blood donor samples collected up to December 2019 (*44*, *45*), and none of thousands of samples taken from patients with influenza-like illness at Wuhan hospitals in October to December 2019 tested for SARS-CoV-2 RNA was positive (*7*).

The sustained presence of a potential source of virus transmission into the human population in late 2019, plausibly from infected live mammals sold at the Huanan market, offers an explanation of our findings and the origins of SARS-CoV-2. The pattern of COVID-19 cases reported for the Huanan market, with the earliest cases in the same part of the market as the wildlife sales and evidence of at least two introductions (*38*), resembles the multiple cross-species transmissions of SARS-CoV-2 subsequently observed during the pandemic from animals to humans on mink farms (*46*) and from infected hamsters to humans in the pet trade (*47*). There was an extensive network of wildlife farms in western Hubei Province, including hundreds of thousands of raccoon
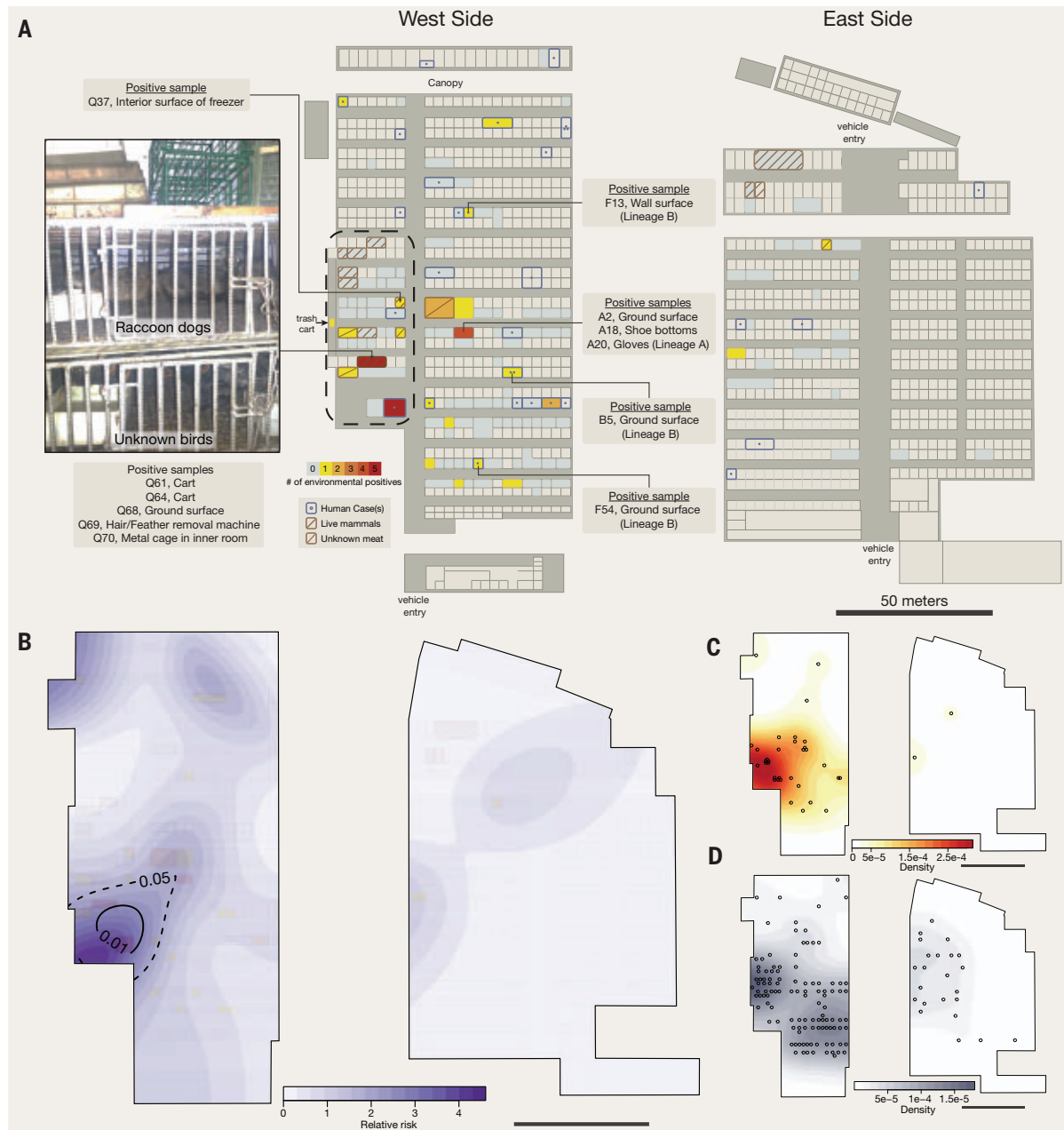
Fig. 4. Map of the Huanan market. (**A**) Aggregated environmental sampling and human case data from the Huanan market. Captions describe the types of SARS-CoV-2–positive environmental samples obtained from known live animal vendors (left) and from stalls with samples with known virus lineage (center). Lineage is unknown unless noted; sequencing data have not been released for some samples, and many samples were PCR-positive but not sequenced. Image at left shows raccoon dogs in a metal cage on top of caged birds from a business with five positive environmental samples (photo by E.C.H.). Center: Rectangle with dashed outline indicates the "wildlife" section of the market.

(**B**) Relative risk analysis of positive environmental samples. Tolerance contours enclose regions with statistically significant elevation in density of positive environmental samples relative to the distribution of sampled stalls. (**C**) Distribution of positive environmental samples. Sample locations (centroid of corresponding business) and quantity are shown as black circles. (**D**) Control distribution for relative risk analysis. All businesses investigated with environmental sampling are shown as black circles (there is one circle per business regardless of whether a positive sample was found). See table S12 for details on stalls that were SARS-CoV-2–negative.

dogs on farms in Enshi Prefecture, which supplied the Huanan market (48). This region of Hubei contains extensive cave complexes housing *Rhinolophus* bats, which carry SARSr-CoVs (49). SARS-CoV-1 was recovered from

farmed masked palm civets (*Paguma larvata*) from Hubei in 2003 and 2004 (20). The animals on these farms (nearly 1 million) were rapidly released, sold, or killed in early 2020 (48), apparently without testing for SARS-CoV-2

(7). Live animals sold at the market (Table 1) were apparently not sampled either. By contrast, during the SARS-CoV-1 outbreaks, farms and markets remained open for more than a year after the first human cases occurred,
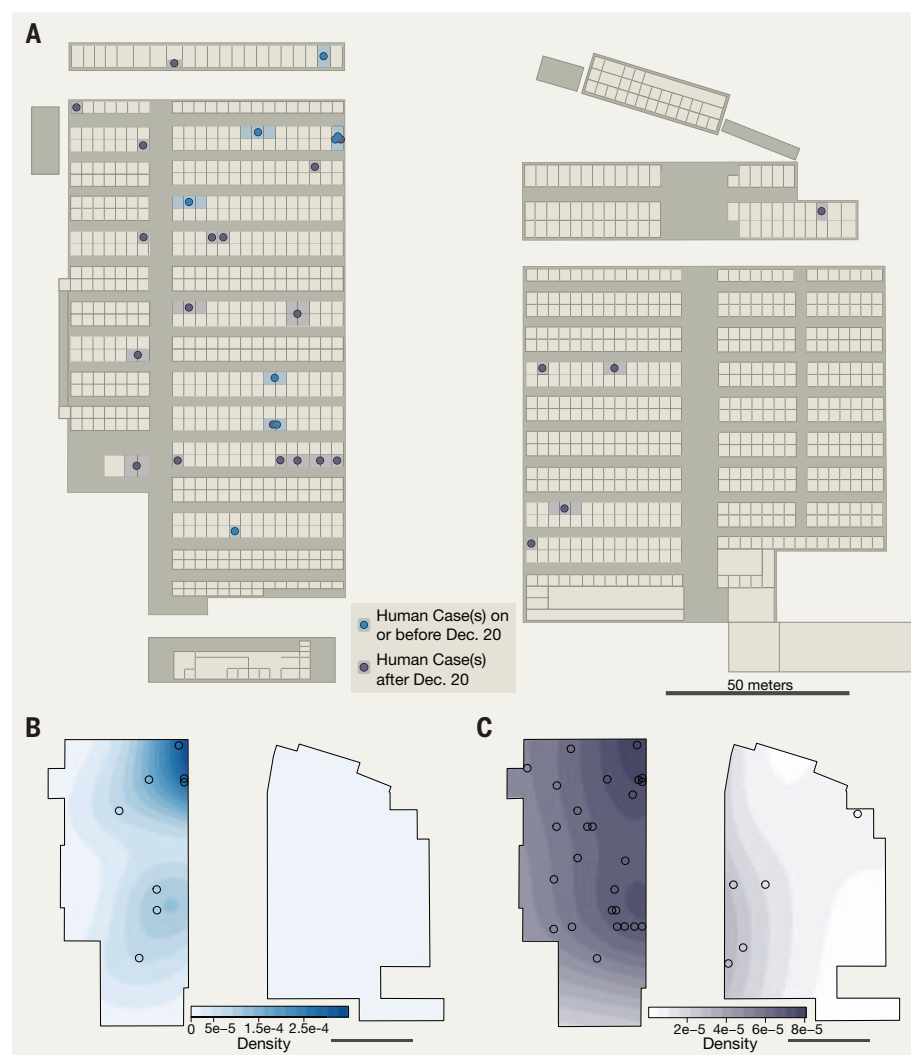
Fig. 5. Location and timing of human cases in Huanan market. (**A**) Outline colors correspond to the timing of the first known case in each business. Individual case timing is denoted by marker color and shown within the outlined business. (**B**) Distribution of known cases on or before 20 December 2019. Case locations are shown as black circles. (**C**) Distribution of all known human cases in Huanan market. See table S11 for details on SARS-CoV-2–positive human cases with the Huanan market.

allowing sampling of viruses from infected animals (20).

The live animal trade and live animal markets are a common theme in virus spillover events (21–23, 50), with markets such as the Huanan market selling live mammals being in the highest risk category (51). The events leading up to the COVID-19 pandemic mirror the SARS-CoV-1 outbreaks from 2002 to 2004, which were traced to infected animals in the Guangdong, Jiangxi, Henan, Hunan, and Hubei provinces in China (20). Maximum effort must now be applied to elucidate the upstream events that might have brought SARS-CoV-2 into the Huanan market, culminating in the COVID-19 pandemic. To reduce the risk of future pandemics, we must understand, and then limit, the routes and opportunities for virus spillover.

Methods summary
Ethics statement

This research was reviewed by the Human Subject Protection Program at the University of Arizona and the Institutional Review Board (IRB) at The Scripps Research Institute and determined to be exempt from IRB approval because it constitutes secondary research for which consent is not required.

Data sources

COVID-19 case data from December 2019 were obtained from the WHO mission report (7) and from our previous analyses (5). Location information was extracted and sensitivity analyses performed to confirm accuracy and assess potential ascertainment bias. Geotagged January–February 2020 data from Weibo COVID-19 help seekers was obtained from

the authors (26). Population density data were obtained from WorldPop.org (27). Sequencing- or quantitative polymerase chain reaction (PCR)–based environmental sample SARS-CoV-2 positivity from the Huanan market was obtained from a January 2020 CCDC report (data S1) (24).

Wildlife trading at the Huanan market

Animal sales from Wuhan wet markets immediately before the COVID-19 pandemic were previously reported (8), and in this study we report details about animals for sale at the Huanan market up until November 2019.

Spatial analyses of COVID-19 cases

Haversine distances to the Huanan market were calculated for each of the geolocated December 2019 cases. Center points and median distances from cases to the Huanan market were calculated separately for (i) all 155 cases, (ii) the 35 cases epidemiologically linked to the Huanan market, (iii) the 120 cases not epidemiologically linked to the market, (iv) the 11 lineage B cases, and (v) the earliest lineage A case. These distances were also calculated for the 737 Weibo help seekers from 8 January to 10 February 2020 (26). Empirical null distributions were generated from the population density data and the Weibo data. The population density–null distributions were age-matched to the December 2019 cases. KDEs were also generated for the market-linked cases, unlinked cases, and all cases to infer a probability density function from which the cases could have been drawn. Highest-density contours representing specific probability masses (0.5, 0.25, 0.1, 0.05, and 0.01) were inferred, and the location of the market was compared with these.

Mobility analyses

To estimate the relative amount of intra-urban human traffic to the Huanan market compared with other locations within the city of Wuhan, we used a location-specific dataset of social media check-ins in the Sina Visitor System as shared by Li et al. (33). This dataset is based on 1,491,499 individual check-in events across the city of Wuhan from the years 2013–2014 (5 to 6 years before the start of the COVID-19 pandemic), and 770,521 visits were associated with 312,190 unique user identifiers. Location names and categories were translated using a Python API for Google Translate.

Spatial analyses of environmental samples at the Huanan market

We used the official maps from the CCDC (12) (data S1) and the WHO map (7), as well as satellite photographs (Google Maps, Google Earth, Baidu Maps), aerial photographs, and images of the market in the public domain to reconstruct the floorplan of the market. Market stalls were assigned by categories of the types of

goods sold using official reports and data from the TianYanCha.com business directory (this company has since gone out of business; for screenshots, see table S8 and data S2). Final maps of the Huanan market were converted into geoJSON format for spatial analyses. Significance testing of live animal vendors and/or human SARS-CoV-2 cases on the number of positive environmental samples was performed using a binomial general linear model. Distances between businesses were defined as the distance between their respective center points, and spatial relative risk analysis was performed using the 'sparr' package in R, with linear boundary kernels for edge correction (52) and bandwidth selection performed using least-squares cross-validation.

REFERENCES AND NOTES

1. Sina Finance, "Wuhan pneumonia of unknown cause cases isolated, test results to be announced ASAP" (Sina Finance, 2019); https://finance.sina.cn/2019-12-31/detail-iihnzahk1074832.d.html?from=wap.
2. Wuhan Municipal Health Commission, "Wuhan Municipal Health Commission's briefing on the current situation of pneumonia in our city" (Wuhan Municipal Health Commission, 2019); https://web.archive.org/web/20200131202951/http://wjw.wuhan.gov.cn/front/web/showDetail/2019123108989.
3. World Health Organization, "COVID-19 – China" (WHO, 2020); https://www.who.int/emergencies/disease-outbreak-news/item/2020-DON229.
4. The Novel Coronavirus Pneumonia Emergency Response Epidemiology Team, *China CDC Wkly* **2**, 113–122 (2020).
5. M. Worobey, *Science* **374**, 1202–1204 (2021).
6. C. Huang et al., *Lancet* **395**, 497–506 (2020).
7. World Health Organization, "WHO-convened global study of origins of SARS-CoV-2: China Part" (WHO, 2021); https://www.who.int/publications/i/item/who-convened-global-study-of-origins-of-sars-cov-2-china-part.
8. X. Xiao, C. Newman, C. D. Buesching, D. W. Macdonald, Z.-M. Zhou, *Sci. Rep.* **11**, 11898 (2021).
9. C. M. Freuling et al., *Emerg. Infect. Dis.* **26**, 2982–2985 (2020).
10. W. K. Jo et al., *Transbound. Emerg. Dis.* **68**, 1824–1834 (2021).
11. I. R. Fischhoff, A. A. Castellanos, J. P. G. L. M. Rodrigues, A. Varsani, B. A. Han, *Proc. Biol. Sci.* **288**, 20211651 (2021).
12. W. Guizhen, "Chinese CDC disease control report" (see data S1).
13. Xinhua News, "Good news! Phased progress made in tracing the origin of the coronavirus" (Xinhua News, 2020); http://www.xinhuanet.com/politics/2020-01-26/c_1125503792.htm.
14. Beijing News, "Huanan Seafood Market in the pneumonia of unexplained incident" (Beijing News, 2020); http://www.bjnews.com.cn/feature/2020/01/02/669054.html.
15. Chinese Center for Disease Control and Prevention, "Chinese Center for Disease Control and Prevention detects large quantity of novel coronavirus in Wuhan Huanan Seafood Market" (Chinese CDC, 2020); https://www.chinacdc.cn/yw_9324/202001/t20200127_211469.html.
16. Yicai Global, "China detects large quantity of novel coronavirus at Wuhan Seafood Market" (Yicai Global, 2020); https://www.yicaiglobal.com/opinion/yicai.global/china-detects-large-quantity-of-novel-coronavirus-at-wuhan-seafood-market.
17. Chinese Center for Disease Control and Prevention, "China CDC calls on the public to protect themselves" (Chinese CDC, 2020); https://www.chinacdc.cn/yw_9324/202001/t20200128_211498.html.
18. Chinese Center for Disease Control and Prevention, "On the front line, disease control warriors race against the new coronavirus" (Chinese CDC, 2020); https://www.chinacdc.cn/yw_9324/202002/t20200201_212137.html.
19. Xinhua News, "China detects large quantity of novel coronavirus at Wuhan seafood market" (Xinhua News, 2020); https://web.archive.org/web/20200126230041/http://www.xinhuanet.com/english/2020-01/27/c_138735677.htm.
20. Z. Shi, Z. Hu, *Virus Res.* **133**, 74–87 (2008).
21. W. B. Karesh, R. A. Cook, E. L. Bennett, J. Newcomb, *Emerg. Infect. Dis.* **11**, 1000–1002 (2005).
22. N. D. Wolfe, P. Daszak, A. M. Kilpatrick, D. S. Burke, *Emerg. Infect. Dis.* **11**, 1822–1827 (2005).
23. C. K. Johnson et al., *Proc. Biol. Sci.* **287**, 20192736 (2020).
24. G. Gao et al., "Surveillance of SARS-CoV-2 in the environment and animal samples of the Huanan Seafood Market" [Preprint] (Research Square, 2022); https://www.researchsquare.com/article/rs-1370392/v1.
25. Material and methods are available as supplementary materials.
26. Z. Peng, R. Wang, L. Liu, H. Wu, *ISPRS Int. J. Geoinf.* **9**, 402 (2020).
27. WorldPop, "WorldPop: Open spatial demographic data and research" (2020); http://WorldPop.org.
28. A. J. Tatem, *Sci. Data* **4**, 170004 (2017).
29. M. O'Driscoll et al., *Nature* **590**, 140–145 (2021).
30. A. Rambaut et al., *Nat. Microbiol.* **5**, 1403–1407 (2020).
31. outbreak.info, "SARS-CoV-2 (hCoV-19) mutation reports: Lineage/mutation tracker" (outbreak.info, 2022); https://outbreak.info/situation-reports.
32. R. Lu et al., *Lancet* **395**, 565–574 (2020).
33. L. Li, L. Yang, H. Zhu, R. Dai, *PLOS ONE* **10**, e0135286 (2015).
34. D. Majra, J. Benson, J. Pitts, J. Stebbing, *J. Infect.* **82**, 36–40 (2021).
35. Epoch Times, "[Exclusive] The secret of Wuhan Huanan Seafood Market testing" (Epoch Times, 2020); https://www.epochtimes.com/gb/20/5/31/n12150755.htm.
36. Wuhan Municipal Bureau of Landscape Architecture and Forestry, "Administrative penalties in 2019" (Wuhan Municipal Bureau of Landscape Architecture and Forestry, 2019); https://web.archive.org/web/20211117124950/http://ylj.wuhan.gov.cn/zwgk/zwxxgkzl_12298/cfqz/xzcf/202011/t20201110_1499879.shtml.
37. Y.-Z. Holmes, E. C. Holmes, *Cell* **181**, 223–227 (2020).
38. J. E. Pekar et al., *Science* **377**, 960–966 (2022).
39. N. Chen et al., *Lancet* **395**, 507–513 (2020).
40. Z. Li et al., *Lancet Reg Health West Pac* **8**, 100094 (2021).
41. Z. He et al., *Lancet* **397**, 1075–1084 (2021).
42. E. C. Holmes et al., *Cell* **184**, 4848–4856 (2021).
43. J. Pekar, M. Worobey, N. Moshiri, K. Scheffler, J. O. Wertheim, *Science* **372**, 412–417 (2021).
44. L. Chang et al., *Nat. Commun.* **12**, 1383 (2021).
45. L. Chang et al., *Protein Cell* pwac013 (2019).
46. L. Lu et al., *Nat. Commun.* **12**, 6802 (2021).
47. H.-L. Yen et al., *Lancet* **399**, 1070–1078 (2022).
48. M. Standaert, E. Dou, "In search for coronavirus origins, Hubei caves and wildlife farms draw new scrutiny," *The Washington Post*, 11 October 2021; https://www.washingtonpost.com/world/asia_pacific/china-covid-bats-caves-hubei/2021/10/10/082eb8b6-1c32-11ec-bea8-308ea134594f_story.html.
49. X.-D. Lin et al., *Virology* **507**, 1–10 (2017).
50. Q. Li et al., *N. Engl. J. Med.* **370**, 520–532 (2014).
51. B. Lin, M. L. Dietrich, R. A. Senior, D. S. Wilcove, *Lancet Planet. Health* **5**, e386–e394 (2021).
52. T. M. Davies, J. C. Marshall, M. L. Hazelton, *Stat. Med.* **37**, 1191–1221 (2018).
53. Data and code for: M. Worobey et al., The Huanan Seafood Wholesale Market in Wuhan was the early epicenter of the COVID-19, Zenodo (2022); http://doi.org/10.5281/zenodo.6786454.

CORONAVIRUS

The molecular epidemiology of multiple zoonotic origins of SARS-CoV-2

Jonathan E. Pekar[1,2]*, Andrew Magee[3], Edyth Parker[4], Niema Moshiri[5], Katherine Izhikevich[5,6], Jennifer L. Havens[1], Karthik Gangavarapu[3], Lorena Mariana Malpica Serrano[7], Alexander Crits-Christoph[8], Nathaniel L. Matteson[4], Mark Zeller[4], Joshua I. Levy[4], Jade C. Wang[9], Scott Hughes[9], Jungmin Lee[10], Heedo Park[10,11], Man-Seong Park[10,11], Katherine Ching Zi Yan[12], Raymond Tzer Pin Lin[12], Mohd Noor Mat Isa[13], Yusuf Muhammad Noor[13], Tetyana I. Vasylyeva[14], Robert F. Garry[15,16,17], Edward C. Holmes[18], Andrew Rambaut[19], Marc A. Suchard[3,20,21]*, Kristian G. Andersen[4,22]*, Michael Worobey[7]*, Joel O. Wertheim[14]*

Understanding the circumstances that lead to pandemics is important for their prevention. We analyzed the genomic diversity of severe acute respiratory syndrome coronavirus 2 (SARS-CoV-2) early in the coronavirus disease 2019 (COVID-19) pandemic. We show that SARS-CoV-2 genomic diversity before February 2020 likely comprised only two distinct viral lineages, denoted "A" and "B." Phylodynamic rooting methods, coupled with epidemic simulations, reveal that these lineages were the result of at least two separate cross-species transmission events into humans. The first zoonotic transmission likely involved lineage B viruses around 18 November 2019 (23 October to 8 December), and the separate introduction of lineage A likely occurred within weeks of this event. These findings indicate that it is unlikely that SARS-CoV-2 circulated widely in humans before November 2019 and define the narrow window between when SARS-CoV-2 first jumped into humans and when the first cases of COVID-19 were reported. As with other coronaviruses, SARS-CoV-2 emergence likely resulted from multiple zoonotic events.

Severe acute respiratory syndrome coronavirus 2 (SARS-CoV-2) is responsible for the coronavirus disease 2019 (COVID-19) pandemic that caused more than 5 million confirmed deaths in the 2 years after its detection at the Huanan Seafood Wholesale Market (hereafter the "Huanan market") in December 2019 in Wuhan, China (1–3). As the original outbreak spread to other countries, the diversity of SARS-CoV-2 quickly increased and led to the emergence of multiple variants of concern, but the beginning of the pandemic was marked by two major lineages denoted "A" and "B" (4).

Lineage B has been the most common throughout the pandemic and includes all 11 sequenced genomes from humans directly associated with the Huanan market, including the earliest sampled genome, Wuhan/IPBCAMS-WH-01/2019, and the reference genome, Wuhan/Hu-1/2019 (hereafter "Hu-1") (5), sampled on 24 and 26 December 2019, respectively. The earliest lineage A viruses, Wuhan/IME-WH01/2019 and Wuhan/WH04/2020, were sampled on 30 December 2019 and 5 January 2020, respectively (6). Lineage A differs from lineage B by two nucleotide substitutions, C8782T and T28144C, which are also found in related coronaviruses from *Rhinolophus* bats (4), the presumed host reservoir (7). Lineage B viruses have a "C/T" pattern at these key sites (C8782 and T28144), whereas lineage A viruses have a "T/C" pattern (C8782T and T28144C). The earliest lineage A genomes from humans lack a direct epidemiological connection to the Huanan market but

were sampled from individuals who lived or had recently stayed close to the market (8). It has been hypothesized that lineages A and B emerged separately (9), but "C/C" and "T/T" genomes intermediate to lineages A and B present a challenge to that hypothesis because their existence suggests within-human evolution of one lineage toward the other by way of a transitional form.

Questions about these lineages remain: If lineage B viruses are more distantly related to sarbecoviruses from *Rhinolophus* bats, then (i) why were lineage B viruses detected earlier than lineage A viruses, and (ii) why did lineage B predominate early in the pandemic?

Answering these questions requires determining the ancestral haplotype, the genomic sequence characteristics of the most recent common ancestor (MRCA) at the root of the SARS-CoV-2 phylogeny. In this study, we combined genomic and epidemiological data from early in the COVID-19 pandemic with phylodynamic models and epidemic simulations. We eliminated many of the haplotypes previously suggested as the MRCA of SARS-CoV-2 and show that the pandemic most likely began with at least two separate zoonotic transmissions starting in November 2019.

Results

Erroneous assignment of haplotypes intermediate to lineages A and B

There are 787 near-full-length genomes available from lineages A and B sampled by 14 February 2020 (data S1 and S2). However, there are also 20 genomes of intermediate haplotypes from this period that contain either

T28144C or C8782T but not both mutations: C/C or T/T, respectively.

We identified numerous instances of C/C and T/T genomes sharing rare mutations with lineage A or lineage B viruses, often sequenced in the same laboratory, indicating that these intermediate genomes are likely artifacts of contamination or bioinformatics (10), similar to findings from our analysis of the emergence of SARS-CoV-2 in North America (fig. S1 and supplementary text) (11). We confirmed that a C/C genome from South Korea sharing three such mutations had low sequencing depth at position 28144 (≤10×), a T/T genome sampled in Singapore had low coverage at both 8782 and 28144 (≤10×), and three T/T genomes sampled in Wuhan had low sequencing depth and indeterminate nucleotide assignment at position 8782 (table S1). Further, the authors of 11 C/C genomes sampled in Wuhan and Sichuan confirmed that low sequencing depth at position 8782 led to the erroneous assignment of intermediate haplotypes.

C/C and T/T genomes continue to be observed throughout the pandemic as a result of convergent evolution, including T/T in the Diamond Princess cruise ship outbreak and subsequent COVID-19 waves in New York City

[1]Bioinformatics and Systems Biology Graduate Program, University of California, San Diego, La Jolla, CA 92093, USA. [2]Department of Biomedical Informatics, University of California, San Diego, La Jolla, CA 92093, USA. [3]Department of Human Genetics, David Geffen School of Medicine, University of California, Los Angeles, Los Angeles, CA 90095, USA. [4]Department of Immunology and Microbiology, The Scripps Research Institute, La Jolla, CA 92037, USA. [5]Department of Computer Science and Engineering, University of California, San Diego, La Jolla, CA 92093, USA. [6]Department of Mathematics, University of California, San Diego, La Jolla, CA 92093, USA. [7]Department of Ecology and Evolutionary Biology, University of Arizona, Tucson, AZ 85721, USA. [8]W. Harry Feinstone Department of Molecular Microbiology and Immunology, Johns Hopkins Bloomberg School of Public Health, Baltimore, MD 21205, USA. [9]New York City Public Health Laboratory, New York City Department of Health and Mental Hygiene, New York, NY 11101, USA. [10]Department of Microbiology, Institute for Viral Diseases, Biosafety Center, College of Medicine, Korea University, Seoul, South Korea. [11]BK21 Graduate Program, Department of Biomedical Sciences, Korea University College of Medicine, Seoul 02841, Republic of Korea. [12]National Public Health Laboratory, National Centre for Infectious Diseases, Singapore. [13]Malaysia Genome and Vaccine Institute, Jalan Bangi, 43000 Kajang, Selangor, Malaysia. [14]Department of Medicine, University of California, San Diego, La Jolla, CA 92093, USA. [15]Department of Microbiology and Immunology, School of Medicine, Tulane University, New Orleans, LA 70112, USA. [16]Zalgen Labs, Frederick, MD 21703, USA. [17]Global Virus Network (GVN), Baltimore, MD 21201, USA. [18]Sydney Institute for Infectious Diseases, School of Life and Environmental Sciences and School of Medical Sciences, The University of Sydney, Sydney, NSW 2006, Australia. [19]Institute of Evolutionary Biology, University of Edinburgh, King's Buildings, Edinburgh EH9 3FL, UK. [20]Department of Biomathematics, David Geffen School of Medicine, University of California, Los Angeles, Los Angeles, CA 90095, USA. [21]Department of Biostatistics, Fielding School of Public Health, University of California, Los Angeles, Los Angeles, CA 90095, USA. [22]Scripps Research Translational Institute, La Jolla, CA 92037, USA.
*Corresponding author. Email: jepekar@ucsd.edu (J.E.P.); msuchard@ucla.edu (M.A.S.); andersen@scripps.edu (K.G.A.); worobey@arizona.edu (M.W.); jwertheim@health.ucsd.edu (J.O.W.)

and San Diego (figs. S2 to S5 and supplementary text). Instances of convergent evolution are identifiable because SARS-CoV-2 phylogenies exist in "near-perfect" tree space, in which topology can be inferred with high accuracy (12). These findings cast doubt on the claim that transitional C/C or T/T haplotypes between lineages A and B circulated in humans, reopening the door to the hypothesis that lineages A and B represent separate introductions.

Progenitor genome reconstruction

To better understand SARS-CoV-2 mutational patterns, we reconstructed the genome of a hypothetical progenitor of SARS-CoV-2. Using maximum likelihood ancestral state reconstruction across 15 nonrecombinant regions of SARS-CoV-2 and closely related sarbecovirus genomes sampled from bats and pangolins (13), we inferred the genome of this recombinant common ancestor (recCA) (figs. S6 and S7 and supplementary text). The recCA differed from Hu-1 by just 381 substitutions, including C8782T and T28144C. It is more informative than an outgroup sarbecovirus because it accounts for the closest relative across all recombinant segments (figs. S8 to S14 and supplementary text) (14) and, as an internal node on the phylogeny, is more genetically similar to SARS-CoV-2 than any extant sarbecovirus.

Reversions across the early pandemic phylogeny

The ubiquity of SARS-CoV-2 reversions (mutations from Hu-1 toward the recCA) indicates that genetic similarity to related viruses is a poor proxy for the ancestral haplotype. We observe 23 distinct reversions and 631 distinct substitutions (excluding reversions) across the SARS-CoV-2 phylogeny from the COVID-19 pandemic up to 14 February 2020 (Fig. 1). Substitutions were overrepresented at the 381 sites separating the recCA from Hu-1 (23 of 381, 6.04%), compared with substitutions at all other sites (631 of 29,134, 2.17%).

Most reversions were C-to-T mutations (19 of 23, 82.6%), matching the mutational bias of SARS-CoV-2 (15–17). Genomes with C-to-T reversions can be found within lineage A, including C18060T (lineage A.1; for example, WA1) and C29095T (for example, 20SF012), as well as C24023T, C25000T, C4276T, and C22747T in mid-late January and February 2020. Hence, triple revertant genomes, such as WA1 and 20SF012, are neither unique nor rare. We also identified a lineage A genome (Malaysia/MKAK-CL-2020-6430/2020), sampled on 4 February 2020 from a Malaysian citizen traveling from Wuhan whose only four mutations from Hu-1 are all reversions (lineage A.1 +T6025C) (Fig. 1). Therefore, no highly revertant haplotype can automatically be assumed to represent the MRCA of SARS-CoV-2, especially when these reversions are most often the result of C-to-T mutations. We continue to observe these reversion patterns throughout the pandemic, including in the emergence of
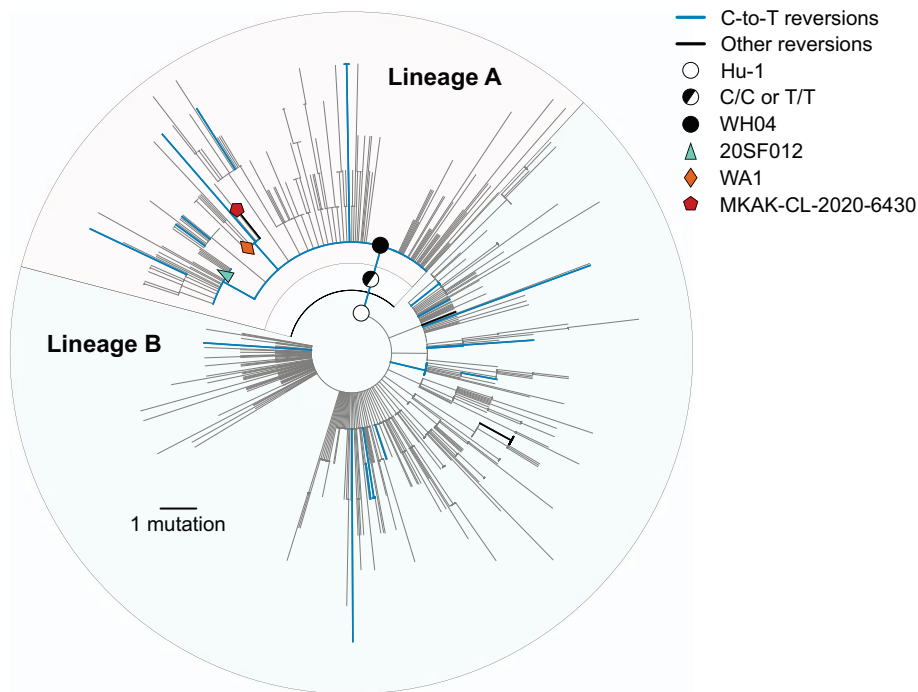
Fig. 1. Maximum likelihood phylogeny of the early SARS-CoV-2 pandemic, showing nucleotide reversions and putative candidates for the ancestral haplotype at the MRCA. Putative ancestral haplotypes are identified with colored shapes. Reversions from the Hu-1 reference genome to the recCA are colored. Blue indicates C-to-T reversions, and black indicates all other reversions. The tree is rooted on Hu-1 to show reversion dynamics to the recCA.

Table 1. Posterior probabilities of inferred ancestral haplotype at the MRCA of SARS-CoV-2. Positions 8782 and 28144 are indicated in parentheses. Representative genome is genome with sequence matching the haplotype. "No market" excludes 15 market-associated genomes (13 lineage B genomes associated with the Huanan market plus one lineage A and one lineage B genome not associated with the Huanan market). *BF > 10; **BF > 100; ***BF > 1000. BFs are in favor of hypothesis rejection.

Haplotype	Mutations from Hu-1 reference	Representative genome	Phylodynamic analysis		
			Unconstrained (%)	No market (%)	recCA (%)
B (C/T)	N/A	Hu-1	80.85[†]	62.96[†]	8.18
A (T/C)	C8782T+T28144C	WH04	1.68*	5.73*	77.28[†]
C/C	T28144C	N/A	10.32	23.02	10.49
T/T	C8782T	N/A	0.92*	1.68*	3.71*
A+C29095T (T/C)	C8782T+T28144C+C29095T	20SF012	<0.01***	<0.01***	0.20**
A.1 (T/C)	C8782T+T28144C+C18060T	WA1	<0.01***	<0.01***	0.04***

†Haplotype with greatest posterior probability; reference for BF.

A 47.5%	**B** 0.0%	**C** 0.5%

◆ MRCA
● Sampled taxon
◀ Clade
▰ Clade w/ ≥30% and ≤70% of taxa
— 1 mutation
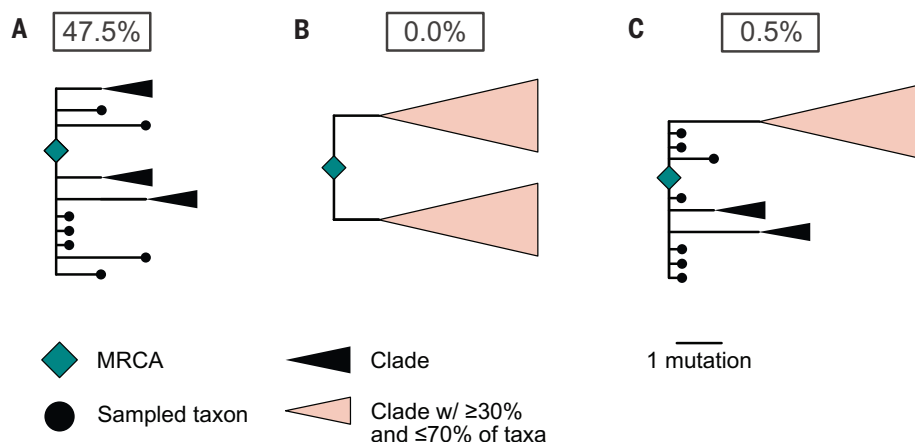
Fig. 2. Probability of phylogenetic structures arising from a single introduction of SARS-CoV-2 in epidemic simulations. (**A**) A large polytomy of at least 100 descendent lineages, which is consistent with the base of both lineages A and B. (**B**) Topology matching a C/C ancestral haplotype: two clades, each one mutation from the ancestor, both with polytomies of at least 100 descendent lineages. (**C**) Topology matching either a lineage A or lineage B ancestral haplotype: a basal polytomy with at least 100 descendent lineages, including a large clade separated by two mutations, also possessing a polytomy of at least 100 descendent lineages. Basal taxa have short branch lengths for clarity. The probability of each phylogenetic structure after a single introduction is reported in the respective boxes.

World Health Organization (WHO)–named variants (figs. S15 and S16).

Inferring the MRCA of SARS-CoV-2

To infer the ancestral SARS-CoV-2 haplotype, we developed a nonreversible, random-effects substitution process model in a Bayesian phylodynamic framework that simultaneously reconstructs the underlying coalescent processes and the sequence of the MRCA of the SARS-CoV-2 phylogeny. The random-effects substitution model captures the C-to-T transition and G-to-T transversion biases (fig. S17 and supplementary text). Using this model, referred to as the unconstrained rooting (fig. S18A), we inferred the ancestral haplotype of the 787 lineage A and B genomes sampled by 14 February 2020.

Our unconstrained rooting strongly favors a lineage B or C/C ancestral haplotype and shows that a lineage A ancestral haplotype is inconsistent with the molecular clock [Bayes factor (BF) = 48.1] (Table 1). Lineage B exhibits more divergence from the root of the tree than would be expected if lineage A were the ancestral virus in humans (figs. S19 and S20). The T/T ancestral haplotype was also disfavored (BF > 10), likely because of the C-to-T transition bias (fig. S17). We acknowledge that the timing of the earliest sampled lineage B genomes associated with the Huanan market could bias rooting inference toward lineage B haplotypes; however, lineage A was still disfavored after excluding all market-associated genomes (BF = 11.0).

Even though sequence similarity to closely related sarbecoviruses alone is insufficient to determine the SARS-CoV-2 ancestral haplo-

type, this similarity can inform phylodynamic inference. Rather than rely on outgroup rooting (fig. S18B) (18), we developed a rooting method that assigns the recCA as the progenitor of the inferred SARS-CoV-2 MRCA (fig. S18C). As opposed to the unconstrained rooting, the recCA root favored a lineage A haplotype over lineage B, although support for C/C was unchanged (Table 1). Our results were insensitive to the method of breakpoint identification in the recCA (supplementary text).

The A.1 and A+C29095T proposed ancestral haplotypes were strongly rejected by all the phylodynamic analyses, even when rooting with recCA or bat sarbecovirus outgroups, which include both C18060T and C29095T (Table 1 and data S3). Hence, WA1-like and 20SF012-like haplotypes cannot plausibly represent the MRCA of SARS-CoV-2 as previously suggested (19–21); the similarity of these genomes to the recCA is due to C-to-T reversions. Haplotypes not reported in Table 1 were similarly rejected (data S3).

We inferred the time of MRCA (tMRCA) for SARS-CoV-2 to be 11 December 2019 [95% highest posterior density (HPD) interval, 25 November to 12 December] by using unconstrained rooting. It has been suggested that a phylogenetic root in lineage A would produce an older tMRCA than would a lineage B rooting (21). Therefore, we developed an approach to assign a haplotype as the SARS-CoV-2 MRCA (A, B, C/C, A.1, or A+C29095T) and inferred the tMRCA (fig. S18D). The tMRCA was consistent with the recCA-rooted and fixed ancestral haplotype analyses (table S2 and supplementary text).

We infer only three plausible ancestral haplotypes: lineage A, lineage B, and C/C. However, the inability to reconcile the molecular clock at the outset of the COVID-19 pandemic with a lineage A ancestor without information from related sarbecoviruses (such as the recCA) requires us to question the assumption that both lineages A and B resulted from a single introduction.

Separate introductions of lineages A and B

We next sought to determine whether a single introduction from one of the plausible ancestral haplotypes (lineage A, lineage B, or C/C) is consistent with the SARS-CoV-2 phylogeny. We simulated SARS-CoV-2–like epidemics (22, 23) with a doubling time of 3.47 days [95% highest density interval (HDI) across simulations, 1.35 to 5.44] (24–26) to account for the rapid spread of SARS-CoV-2 before it was identified as the etiological agent of COVID-19 (figs. S21 and S22, tables S3 and S4, and supplementary text). We then simulated coalescent processes and viral genome evolution across these epidemics to determine how frequently we recapitulated the observed SARS-CoV-2 phylogeny.

Lineages A and B comprise 35.2 and 64.8% of the early SARS-CoV-2 genomes, respectively, and each lineage is characterized by a large polytomy (many sampled lineages descending from a single node on the phylogenetic tree), with the base of lineages A and B being the two largest polytomies observed in the early pandemic (Fig. 1). Furthermore, large polytomies are characteristic of SARS-CoV-2 introductions into geographical regions at the start of the pandemic (for example, fig. S23) (11, 27–29) and would similarly be expected to occur after a successful introduction of SARS-CoV-2 into humans. Congruently, the most common topology in our simulations is a large basal polytomy (with ≥100 descendent lineages), which is present in 47.5% of simulated epidemics (Fig. 2A).

By contrast, a topology corresponding to a single introduction of an ancestral C/C haplotype—characterized by two clades, each comprising ≥30% of the taxa, possessing a large polytomy at the base, and separated from the MRCA by one mutation (Fig. 2B)—was only observed in 0.0% of our simulations. Further, a topology corresponding to a single introduction of an ancestral lineage A or lineage B haplotype—characterized by a large basal polytomy and a large clade, comprising between 30 and 70% of taxa, two mutations from the root with no intermediate genomes—was observed in only 0.5% of our simulations (Fig. 2C and supplementary text).

Our epidemic simulations do not support a single introduction of SARS-CoV-2 giving rise to the observed phylogeny. We therefore quantified the relative support for two
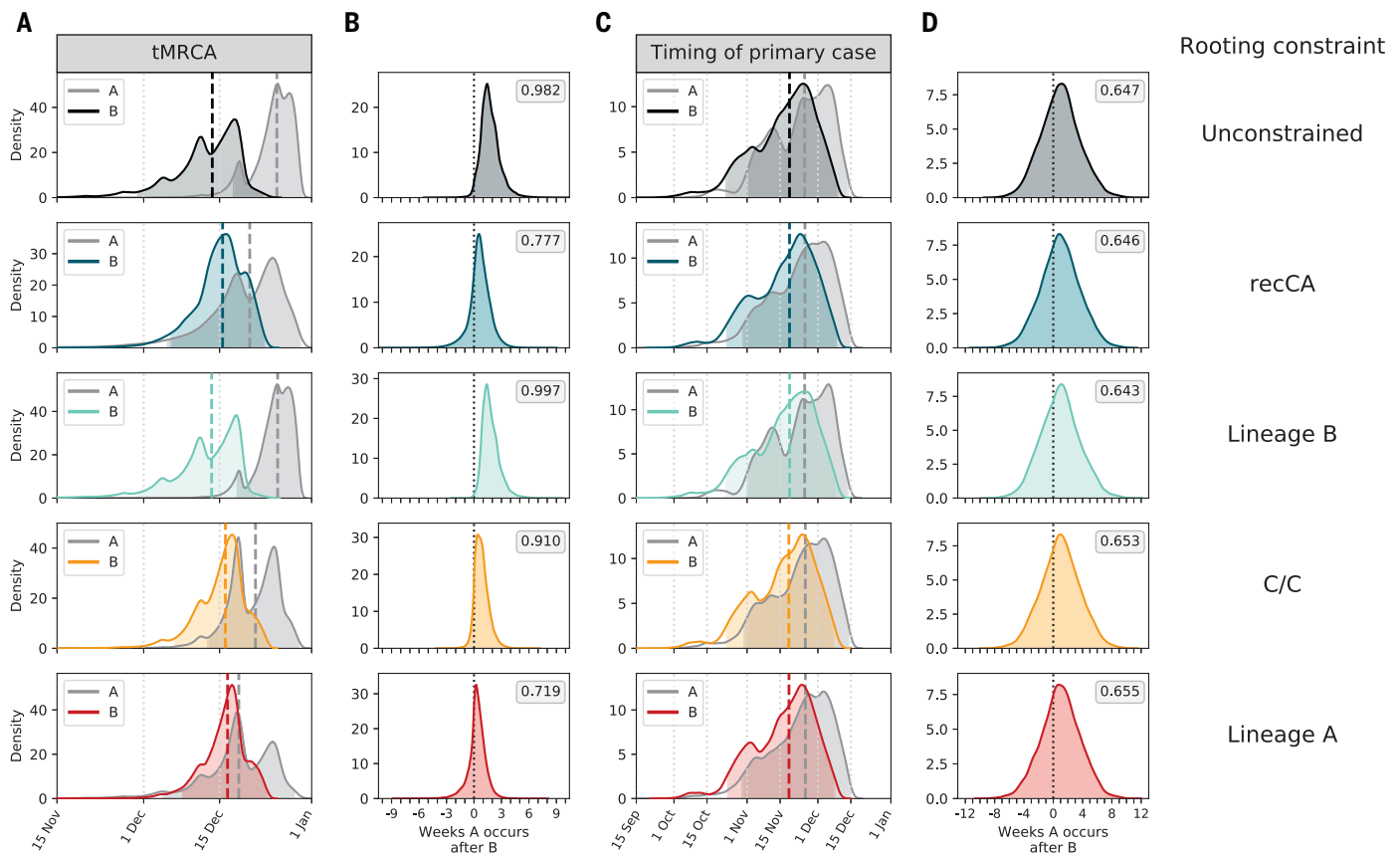
Fig. 3. Comparison of the tMRCA and primary case dates for lineage A and lineage B in late 2019 across rooting strategies. Each row represents a different rooting constraint in phylodynamic analysis, with lineage B, C/C, and lineage A representing a fixed ancestral haplotype. (**A**) The tMRCA for lineages A and B. (**B**) The number of weeks the tMRCA of lineage A occurs after the tMRCA of lineage B. (**C**) The timing of the primary case for lineages A and B. (**D**) The number of weeks the time of the primary case of lineage A occurs after the time of the primary case of lineage B. Long dashed lines indicate the median, and shading indicates the 95% HPD for each distribution. Short dashed lines indicate 0 weeks difference between lineages A and B. Posterior probability that lineage A originated after lineage B is reported in the gray box in each graph in (B) and (D).

introductions resulting in the empirical topology. By synthesizing posterior probabilities of inferred ancestral haplotypes, frequencies of topologies in epidemic simulations, and the expected relationships between these haplotypes and topologies, we inferred strong support favoring separate introductions of lineages A and B (BF = 61.6 and BF = 60.0 by using the recCA and unconstrained rooting, respectively) [supplementary materials (SM), materials and methods]. This support is robust across shorter and longer doubling times, varying ascertainment rates, and minimum polytomy size (tables S4 and S5).

If lineages A and B arose from separate introductions, then the MRCA of SARS-CoV-2 was not in humans, and it is the tMRCAs of lineages A and B that are germane to the origins of SARS-CoV-2 (not the timing of their shared ancestor). Rooting with the recCA, we inferred the median tMRCA of lineage B to be 15 December (95% HPD, 5 December to 23 December) and the median tMRCA of lineage A to be 20 December (95% HPD, 5 December

to 29 December) (Fig. 3A). The tMRCA of lineage B consistently predates the tMRCA of lineage A (Fig. 3B). These results are robust to using unconstrained rooting, fixing the ancestral haplotype, and excluding market-associated genomes (Fig. 3, A and B; table S2; and supplementary text).

Timing the introductions of lineages A and B

The primary case, the first human infected with a virus in an outbreak, could precede the tMRCA if basal lineages went extinct during cryptic transmission (23, 30, 31). The index case, the first identified case, is rarely also the primary case (32, 33). We next used an extension of our previously published framework that combines epidemic simulations and phylodynamic tMRCA inference (SM materials and methods) (23, 30, 31) to infer the timing of the lineage B and lineage A primary cases, accounting for both the index case symptom onset date and earliest documented COVID-19 hospitalization date.

The earliest unambiguous case of COVID-19, with symptom onset on 10 December and

hospitalization on 16 December, was a seafood vendor at the Huanan market. Unfortunately, no published genome is available for this case (8). Nonetheless, we can reasonably assume that this individual had a lineage B virus (supplementary text) because an environmental sample (EPI_ISL_408512) from the stall this vendor operated was lineage B. The earliest lineage A genome (IME-WH01) is from a familial cluster for which the earliest symptom onset is 15 December and earliest hospitalization is 25 December (34). Accounting for these dates and using the recCA rooting, we inferred the infection date of the lineage B primary case to be 18 November (95% HPD, 23 October to 8 December) and the infection date of the primary case of lineage A to be 25 November (95% HPD, 29 October to 14 December). The lineage B primary case predated that of lineage A in 64.6% of the posterior sample, by a median of 7 days (Fig. 3D and table S6).

Our lineage A and B primary case inference is robust to rooting strategy and fixing the plausible ancestral haplotype to lineage A,
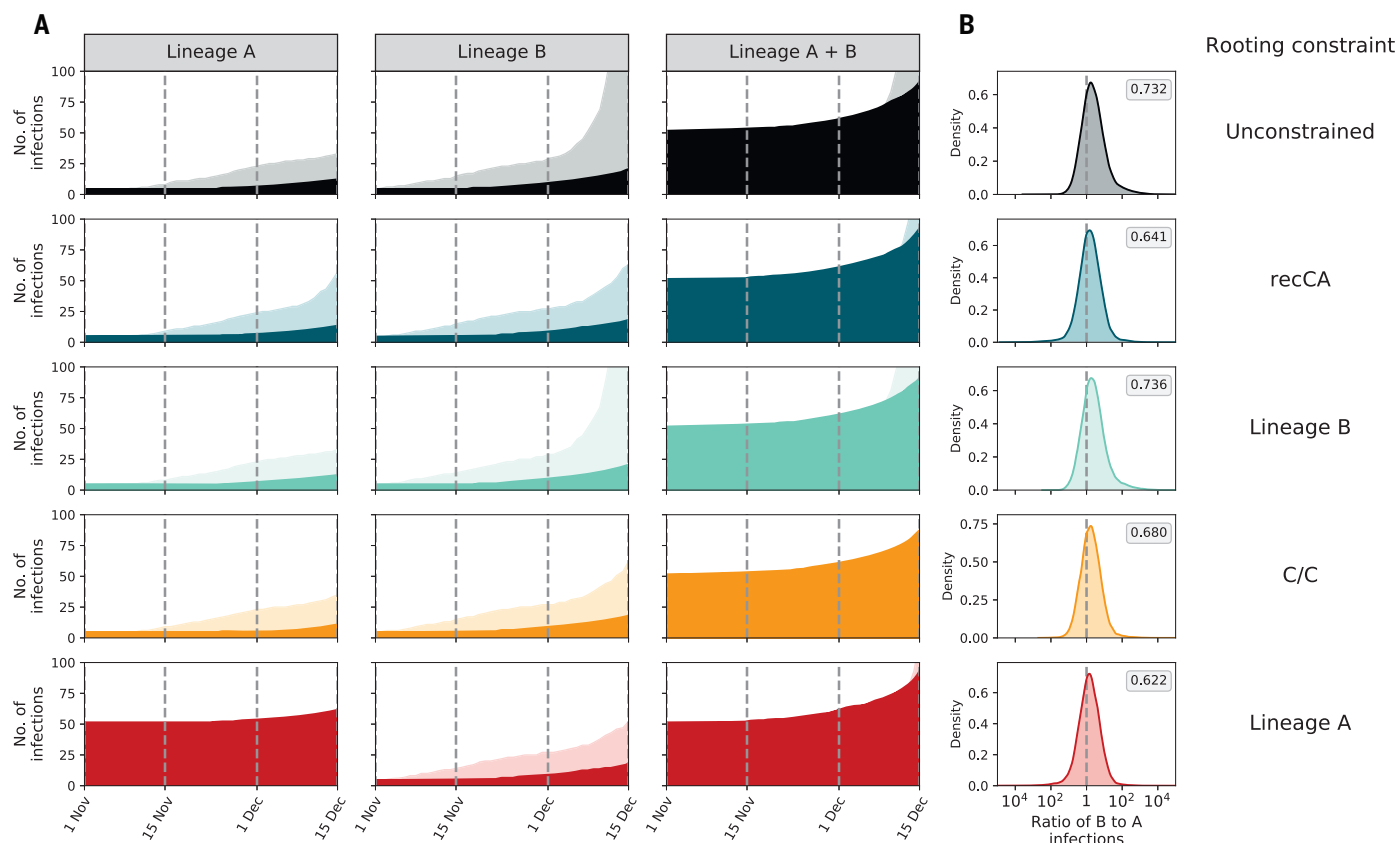
Fig. 4. Dynamics of simulated SARS-CoV-2 epidemics resulting from separate introductions of lineages A and B in late 2019. Each row represents a different rooting constraint in phylodynamic analysis, with lineage B, C/C, and lineage A representing a fixed ancestral haplotype. (**A**) Estimated number of infections. The header of each column indicates whether the number of infections is caused by lineage A, lineage B, or the two lineages combined. Darker and lighter shading indicates the 50 and 95% HPD, respectively. (**B**) The log ratio of lineage B to lineage A infections on 15 December 2019. Posterior probability of having more lineage B infections than lineage A reported in the gray box in each graph.

lineage B, or C/C, as well as different index case dates, accounting for only hospitalization dates and varying growth rates and ascertainment rates (tables S7 to S10 and supplementary text). Therefore, our results indicate that lineage B was introduced into humans no earlier than late October and likely in mid-November 2019, and the introduction of lineage A occurred within days to weeks of this event.

We then inferred the number of ascertained infections and hospitalizations arising from these separate introductions. We found that an earlier introduction of lineage B led to a faster rise in lineage B–associated infections, dominating the simulated epidemics (Fig. 4) and recapitulating the predominance of lineage B observed in China in early 2020 (*35*). Similarly, simulated lineage B hospitalizations are more common than those from lineage A through January 2020 (fig. S24). We observed these patterns regardless of rooting strategy (unconstrained or recCA), ancestral haplotype (B, A, or C/C) (Fig. 4 and tables S11 and S12), and doubling time (figs. S25 to S28).

Minimal cryptic circulation of SARS-CoV-2
We do not see evidence for substantial cryptic circulation before December 2019 (Fig. 4), even if we assume a single introduction (fig. S29 and supplementary text). Our simulated epidemics have a median of three (95% HPD, 1 to 18) cumulative infections at the tMRCA, with 99% of simulated epidemics resulting in at most 33 infections (table S13 and supplementary text). Further, it is unlikely that there were any COVID-19–related hospitalizations before December (*36*) because the simulated epidemics show a median of zero (95% HPD, 0 to 2) hospitalizations by 1 December 2019. These results are in accordance with the lack of a single SARS-CoV-2–positive sample among tens of thousands of serology samples from healthy blood donors from September to December 2019 (*37*) and thousands of specimens obtained from influenza-like illness patients at Wuhan hospitals from October to December 2019 (*34*). Therefore, there was likely extremely low prevalence of SARS-CoV-2 in Wuhan before December 2019. Even when we simulated epidemics with a longer doubling time, resulting in an earlier timing of the

primary cases (tables S8 and S10), there were still few infections before December 2019 (table S13).

Additional introductions
The extinction rate of our simulated epidemics (simulations that did not produce self-sustaining transmission chains) indicate that there were likely multiple failed introductions of SARS-CoV-2. Similar to our previous findings (*23*), 77.8% of simulated epidemics went extinct. These failed introductions produced a mean of 2.06 infections and 0.10 hospitalizations; hence, failed introductions could easily go unnoticed. If we treat each SARS-CoV-2 introduction, failed or successful, as a Bernoulli trial and simulate introductions until we see two successful introductions, we estimate that eight (95% HPD, 2 to 23) introductions led to the establishment of both lineage A and B in humans.

Limitations
Our analysis of the putative intermediate haplotypes suggests that there remain lineage assignment errors between lineages A and B,

particularly of genomes sampled in January and February of 2020, which could influence the precision of the phylogenetic topology and tMRCA inference. We lack direct evidence of a virus closely related to SARS-CoV-2 in nonhuman mammals at the Huanan market or its supply chain. The genome sequence of a virus directly ancestral to SARS-CoV-2 would provide more precision regarding the timing of the introductions of SARS-CoV-2 into humans and the epidemiological dynamics before its discovery. Although we simulated epidemics across a range of plausible epidemiological dynamics, our models represent a time frame before the ascertainment of COVID-19 cases and sequencing of SARS-CoV-2 genomes and thus before when these models could be empirically validated.

Discussion

The genomic diversity of SARS-CoV-2 during the early pandemic presents a paradox. Lineage A viruses are at least two mutations closer to bat coronaviruses, indicating that the ancestor of SARS-CoV-2 arose from this lineage. However, lineage B viruses predominated early in the pandemic, particularly at the Huanan market, indicating that this lineage began spreading earlier in humans. Further complicating this matter is the molecular clock of SARS-CoV-2 in humans, which rejects a single-introduction origin of the pandemic from a lineage A virus. We resolved this paradox by showing that early SARS-CoV-2 genomic diversity and epidemiology are best explained by at least two separate zoonotic transmissions, in which lineage A and B progenitor viruses were both circulating in nonhuman mammals before their introduction into humans (figs. S30 and S31).

The most probable explanation for the introduction of SARS-CoV-2 into humans involves zoonotic jumps from as-yet-undetermined, intermediate host animals at the Huanan market (*34, 38, 39*). Through late 2019, the Huanan market sold animals that are known to be susceptible to SARS-CoV-2 infection and capable of intraspecies transmission (*40–42*). The presence of potential animal reservoirs, coupled with the timing of the lineage B primary case and the geographic clustering of early cases around the Huanan market (*39*), support the hypothesis that SARS-CoV-2 lineage B jumped into humans at the Huanan market in mid-November 2019.

In a related study (*39*), we show that the two earliest lineage A cases are more closely positioned geographically to the Huanan market than expected compared with other COVID-19 cases in Wuhan in early 2020, despite having no known association with the market. This geographic proximity is consistent with a separate and subsequent origin of lineage A at the Huanan market in late November 2019. The presence of lineage A virus at the Huanan market was confirmed by Gao *et al.* (*43*) from a sample taken from discarded gloves.

The high extinction rate of SARS-CoV-2 transmission chains, observed in both our simulations and real-world data (*44*), indicates that the two zoonotic events that established lineages A and B may have been accompanied by additional, cryptic introductions. However, such introductions could easily be missed, particularly if their subsequent transmission chains quickly went extinct or the introduced viruses had a lineage A or B haplotype. Failed introductions of intermediate haplotypes are also possible. Critically, we have no evidence of subsequent zoonotic introductions in late December leading up to the closure of the Huanan market on 1 January 2020. By then, the susceptible host animals that had been documented at the market during the previous months were no longer found in the Huanan market (*34*).

Other coronavirus epidemics and outbreaks in humans—including SARS-CoV-1, Middle East respiratory syndrome coronavirus (MERS-CoV), and most recently, porcine deltacoronavirus in Haiti—have been the result of repeated introductions from animal hosts (*45–47*). These repeated introductions were easily identifiable because human viruses in these outbreaks were more closely related to viruses sampled in the animal reservoirs than to other human viruses. However, the genomic diversity within the putative SARS-CoV-2 animal reservoir at the Huanan market was likely shallower than that seen in SARS-CoV-1 and MERS-CoV reservoirs (*45, 46, 48*). Hence, even though lineages A and B had nearly identical haplotypes, their MRCA likely existed in an animal reservoir. The ability to disentangle repeated introductions of SARS-CoV-2 from a shallow genetic reservoir has previously been shown in the early SARS-CoV-2 epidemic in Washington state, where two viruses, separated by two mutations, were independently introduced from, and shared an MRCA in, China (figs. S23 and S30 and supplementary text) (*11*).

Successful transmission of both lineage A and B viruses after independent zoonotic events indicates that evolutionary adaptation within humans was not needed for SARS-CoV-2 to spread (*49*). We now know that SARS-CoV-2 can readily spread after reverse-zoonosis to Syrian hamsters (*Mesocricetus auratus*), American mink (*Neovison vison*), and white-tailed deer (*Odocoileus virginianus*), indicating its host generalist capacity (*50–55*). Furthermore, once an animal virus acquires the capacity for human infection and transmission, the only remaining barrier to spillover is contact between humans and the pathogen. Thereafter, a single zoonotic transmission event indicates that the conditions necessary for spillovers have been met, which portends additional jumps. For example, there were at least two zoonotic jumps of SARS-CoV-2 into humans from pet hamsters in Hong Kong (*55*) and dozens from minks to humans on Dutch fur farms (*52, 53*).

We show that it is highly unlikely that SARS-CoV-2 circulated widely in humans earlier than November 2019 and that there was limited cryptic spread, with at most dozens of SARS-CoV-2 infections in the weeks leading up to the inferred tMRCA, but likely far fewer. By late December, when SARS-CoV-2 was identified as the etiological agent of COVID-19 (*8*), the virus had likely been introduced into humans multiple times as a result of persistent contact with a viral reservoir.

Materials and methods summary

Materials and methods described in full detail can be found in the supplementary materials.

Sequence data

We queried the GISAID database (*56*), GenBank, and National Genomics Data Center of the China National Center for Bioinformatics (CNCB) for complete high-coverage SARS-CoV-2 genomes collected by 14 February 2020, resulting in a dataset of 787 taxa belonging to lineages A and B and 20 taxa with C/C or T/T haplotypes. Genomes were aligned by using MAFFT v7.453 (*57*) to the SARS-CoV-2 reference genome (Wuhan/Hu-1/2019), and 388 sites were masked at the 5′ and 3′ ends and at sites based on De Maio *et al.* (*58*). All genome accessions are available in data S1 and S2.

Progenitor genome reconstruction and reversion analysis

We reconstructed the progenitor of SARS-CoV-2, the the recCA. We (i) inferred a maximum likelihood tree of 31 sarbecovirus genomes (SARS-CoV-2 and 30 closely related sarbecoviruses sampled from bats and pangolins) across 15 predefined nonrecombinant regions (*13*) with IQ-TREE v2.0.7 (*59*), (ii) inferred the sequence of the ancestor of SARS-CoV-2 in each tree with TreeTime v0.8.1 (*60*), and (iii) concatenated the resulting sequences. We next inferred a maximum likelihood tree of the 787 SARS-CoV-2 taxa with IQ-TREE and performed ancestral state reconstruction with TreeTime to identify substitutions that were reversions from Wuhan-Hu-1 to the recCA across the SARS-CoV-2 phylogeny.

Phylodynamic inference and epidemic simulations

We performed phylodynamic inference using BEAST v1.10.5 (*61*) with the 787-taxon dataset to infer the ancestral haplotype and the tMRCA of SARS-CoV-2 (and the tMRCAs of lineages A and B), using a nonreversible random-effects substitution model and exploring unconstrained rooting, recCA-rooting, fixing the ancestral haplotype as a root, and outgroup rooting. SARS-CoV-2–like epidemics were simulated with FAVITES-COVID-Lite v0.0.1

(22, 62) using a scale-free network of 5 million individuals and a customized extension of the SAPHIRE model (63), producing coalescent trees on which we simulated mutations. We calculated the BF comparing the support of two introductions of SARS-CoV-2 with one introduction by considering the posterior probabilities of the four most likely ancestral haplotypes from the phylodynamic inference (lineage A, lineage B, C/C, and T/T), the frequencies of the phylogenetic structures associated with introductions of these haplotypes in the epidemic simulations, and equal prior probabilities for each ancestral haplotype and the number of introductions.

We connected the phylodynamic inference and epidemic simulations by means of a rejection sampling–based approach (23), accounting for the tMRCAs of lineages A and B and the earliest documented COVID-19 illness onset and hospitalization dates. We then inferred the timing of the introductions of lineages A and B and the infections and hospitalizations for each lineage. The proportion of epidemic simulations that went extinct (no onward transmission by the end of the simulation) was used to approximate the number of SARS-CoV-2 introductions needed to result in two introductions with sustained onward transmission.

REFERENCES AND NOTES

1. E. Dong, H. Du, L. Gardner, *Lancet Infect. Dis.* **20**, 533–534 (2020).
2. L.-L. Ren et al., *Chin. Med. J.* **133**, 1015–1024 (2020).
3. H. Ritchie et al., *Our World in Data* (2022); https://ourworldindata.org/covid-deaths.
4. A. Rambaut et al., *Nat. Microbiol.* **5**, 1403–1407 (2020).
5. F. Wu et al., *Nature* **579**, 265–269 (2020).
6. R. Lu et al., *Lancet* **395**, 565–574 (2020).
7. S. Lytras et al., *Genome Biol. Evol.* **14**, evac018 (2022).
8. M. Worobey, *Science* **374**, 1202–1204 (2021).
9. R. F. Garry, *Virological* (2021); https://virological.org/t/early-appearance-of-two-distinct-genomic-lineages-of-sars-cov-2-in-different-wuhan-wildlife-markets-suggests-sars-cov-2-has-a-natural-origin/691.
10. N. De Maio et al., *Virological* (2020); https://virological.org/t/issues-with-sars-cov-2-sequencing-data/473.
11. M. Worobey et al., *Science* **370**, 564–570 (2020).
12. J. O. Wertheim, M. Steel, M. J. Sanderson, *Syst. Biol.* **71**, 426–438 (2022).
13. S. Temmam et al., *Nature* **604**, 330–336 (2022).
14. J. B. Pease, M. W. Hahn, *Evolution* **67**, 2376–2384 (2013).
15. J. Ratcliff, P. Simmonds, *Virology* **556**, 62–72 (2021).
16. P. Simmonds, *MSphere* **5**, e00408-20 (2020).
17. P. Simmonds, M. A. Ansari, *PLOS Pathog.* **17**, e1009596 (2021).
18. P. Forster, L. Forster, C. Renfrew, M. Forster, *Proc. Natl. Acad. Sci. U.S.A.* **117**, 9241–9243 (2020).
19. J. D. Bloom, *Mol. Biol. Evol.* **38**, 5211–5224 (2021).
20. M. A. Caraballo-Ortiz et al., *Bioinformatics* **38**, 2719–2726 (2022).
21. S. Kumar et al., *Mol. Biol. Evol.* **38**, 3046–3059 (2021).
22. N. Moshiri, M. Ragonnet-Cronin, J. O. Wertheim, S. Mirarab, *Bioinformatics* **35**, 1852–1861 (2019).
23. J. Pekar, M. Worobey, N. Moshiri, K. Scheffler, J. O. Wertheim, *Science* **372**, 412–417 (2021).
24. S. Hsiang et al., *Nature* **584**, 262–267 (2020).
25. A. L. Bertozzi, E. Franco, G. Mohler, M. B. Short, D. Sledge, *Proc. Natl. Acad. Sci. U.S.A.* **117**, 16732–16738 (2020).
26. S. Sanche et al., *Emerg. Infect. Dis.* **26**, 1470–1477 (2020).
27. T. Bedford et al., *Science* **370**, 571–575 (2020).
28. M. Zeller et al., *Cell* **184**, 4939–4952.e15 (2021).
29. C. Alteri et al., *Nat. Commun.* **12**, 434 (2021).
30. L. du Plessis, O. Pybus, *Virological* (2020); https://virological.org/t/further-musings-on-the-tmrca/340.
31. J. Giesecke, *Lancet* **384**, 2024 (2014).
32. Centers for Disease Control and Prevention (CDC), *MMWR Morb. Mortal. Wkly. Rep.* **52**, 986–987 (2003).
33. A. Marí Sáez et al., *EMBO Mol. Med.* **7**, 17–23 (2015).
34. WHO Headquarters, WHO-convened global study of origins of SARS-CoV-2: China Part (2021); https://www.who.int/publications/i/item/who-convened-global-study-of-origins-of-sars-cov-2-china-part.
35. X. Zhang et al., *Nature* **583**, 437–440 (2020).
36. E. O. Nsoesie, B. Rader, Y. L. Barnoon, L. Goodwin, J. Brownstein, *Dig. Acc. Scholar. Harv.* **2**, 019 (2020).
37. L. Chang et al., *Protein Cell* 10.1093/procel/pwac013 (2022).
38. E. C. Holmes et al., *Cell* **184**, 4848–4856 (2021).
39. M. Worobey et al., *Science* **377**, 951–959 (2022).
40. X. Xiao, C. Newman, C. D. Buesching, D. W. Macdonald, Z.-M. Zhou, *Sci. Rep.* **11**, 11898 (2021).
41. C. M. Freuling et al., *Emerg. Infect. Dis.* **26**, 2982–2985 (2020).
42. S. M. Porter, A. E. Hartwig, H. Bielefeldt-Ohmann, A. M. Bosco-Lauth, J. Root, bioRxiv 478082 [Preprint] (2022); https://doi.org/10.1101/2022.01.27.478082.
43. G. Gao et al., *Research Square* [Preprint] (2022); https://doi.org/10.21203/rs.3.rs-1370392/v1.
44. L. du Plessis et al., *Science* **371**, 708–712 (2021).
45. Chinese SARS Molecular Epidemiology Consortium, *Science* **303**, 1666–1669 (2004).
46. G. Dudas, L. M. Carvalho, A. Rambaut, T. Bedford, *eLife* **7**, e31257 (2018).
47. J. A. Lednicky et al., *Nature* **600**, 133–137 (2021).
48. B. Kan et al., *J. Virol.* **79**, 11892–11900 (2005).
49. K. G. Andersen, A. Rambaut, W. I. Lipkin, E. C. Holmes, R. F. Garry, *Nat. Med.* **26**, 450–452 (2020).
50. V. L. Hale et al., *Nature* **602**, 481–486 (2022).
51. J. C. Chandler et al., *Proc. Natl. Acad. Sci. U.S.A.* **118**, e2114828118 (2021).
52. L. Lu et al., *Nat. Commun.* **12**, 6802 (2021).
53. B. B. Oude Munnink et al., *Science* **371**, 172–177 (2021).
54. S. V. Kuchipudi et al., *Proc. Natl. Acad. Sci. U.S.A.* **119**, e2121644119 (2022).
55. H.-L. Yen et al., *Lancet* **399**, 1070–1078 (2022).
56. Y. Shu, J. McCauley, *Euro Surveill.* **22**, 30494 (2017).
57. K. Katoh, D. M. Standley, *Mol. Biol. Evol.* **30**, 772–780 (2013).
58. N. De Maio et al., *Virological* (2020); https://virological.org/t/masking-strategies-for-sars-cov-2-alignments/480.
59. B. Q. Minh et al., *Mol. Biol. Evol.* **37**, 1530–1534 (2020).
60. P. Sagulenko, V. Puller, R. A. Neher, *Virus Evol.* **4**, vex042 (2018).
61. M. A. Suchard et al., *Virus Evol.* **4**, vey016 (2018).
62. N. Moshiri, FAVITES-COVID-Lite: A simplified (and much faster) simulation pipeline specifically for COVID-19 contact + transmission + phylogeny + sequence simulation. Github (2022); https://github.com/niemasd/FAVITES-COVID-Lite.
63. X. Hao et al., *Nature* **584**, 420–424 (2020).
64. J. E. Pekar et al., Code for: The molecular epidemiology of multiple zoonotic origins of SARS-CoV-2. Zenodo (2022); doi: 10.5281/zenodo.6585475.
65. J. E. Pekar et al., Data for: The molecular epidemiology of multiple zoonotic origins of SARS-CoV-2. Zenodo (2022); doi: 10.5281/zenodo.6887186.

SYNTHETIC BIOLOGY

A sustainable mouse karyotype created by programmed chromosome fusion

Li-Bin Wang[1,2,3]†, Zhi-Kun Li[1,2,3]†, Le-Yun Wang[1,2,3]†, Kai Xu[1,2,3]†, Tian-Tian Ji[1,4]†, Yi-Huan Mao[1,2,3], Si-Nan Ma[1,5], Tao Liu[6], Cheng-Fang Tu[6], Qian Zhao[6], Xu-Ning Fan[6], Chao Liu[1,2,3], Li-Ying Wang[1], You-Jia Shu[1,4], Ning Yang[1,4], Qi Zhou[1,2,3]*, Wei Li[1,2,3]*

Chromosome engineering has been attempted successfully in yeast but remains challenging in higher eukaryotes, including mammals. Here, we report programmed chromosome ligation in mice that resulted in the creation of new karyotypes in the lab. Using haploid embryonic stem cells and gene editing, we fused the two largest mouse chromosomes, chromosomes 1 and 2, and two medium-size chromosomes, chromosomes 4 and 5. Chromatin conformation and stem cell differentiation were minimally affected. However, karyotypes carrying fused chromosomes 1 and 2 resulted in arrested mitosis, polyploidization, and embryonic lethality, whereas a smaller fused chromosome composed of chromosomes 4 and 5 was able to be passed on to homozygous offspring. Our results suggest the feasibility of chromosome-level engineering in mammals.

The laboratory house mouse (*Mus musculus*) has maintained a standard 40-chromosome karyotype after more than 100 years of artificial breeding (*1*). Over longer time scales, however, karyotype changes caused by chromosome rearrangements are common: Rodents have 3.2 to 3.5 chromosome rearrangements per million years, whereas primates have 1.6 chromosome rearrangements per million years (*2*). In humans (2n = 46, where n is a single set of chromosomes), the metacentric chromosome 2 was formed by the Robertsonian (Rb) fusion of two acrocentric chromosomes that remain separate in *Gorilla gorilla* (2n = 48) (*3*). A reciprocal translocation between ancestor human chromosomes 5 and 17 produced chromosomes 4 and 19 in the gorilla (*4*). Rb fusion or reciprocal translocation can also cause aneuploidy, uniparental disomy, or childhood leukemia (*5–7*).

Using embryonic stem cells (ESCs) and the Cre-loxP system, researchers have attempted to derive mouse models with programmed chromosomal rearrangements, but only subchromosomal rearrangements have been achieved (*8*). Recent advances in genome editing have greatly facilitated chromosome engineering in haploid yeast (*9–11*). In mammals, yeast-like haploid ESCs (haESCs) were derived first from unfertilized mouse embryos and then from rat, monkey, and human counterparts (*12–16*).

However, genomic imprinting is frequently lost in haESCs, limiting their pluripotency and potential for genetic engineering (*17–19*).

We recently discovered that by deleting three imprinted regions, we could establish a stable sperm-like imprinting pattern in haESCs (*20*). Because they have yeast-like haploidy and passage-persistent pluripotency, we used these cells in this study to test the feasibility of chromosome engineering in mammals. To ligate the entire arms of two nonhomologous mouse chromosomes into one, we designed a strategy that combined Rb fusion and reciprocal translocation. We wished to address whether we could ligate chromosomes in mammalian cells. We also examined how it would affect stem cell differentiation and chromatin organization and to what extent it would affect mouse phenotypes.

Results

Chromosome ligation in mouse haESCs

We chose to ligate two medium-size mouse chromosomes (chromosomes 4 and 5) head to tail (Chr4+5; Fig. 1A) and the two largest mouse chromosomes (chromosomes 1 and 2) in opposite orientations (Chr1+2 and Chr2+1; Fig. 1A). Telomere and centromere neighboring single-guide RNAs (sgRNAs) with cleavage efficiencies greater than 0.17 were used to generate double-strand breaks (DSBs) in these chromosomes (tables S1 and S2). New haESC lines were established and used before passage 15. After cotransfecting sgRNA- and Cas9-expressing plasmids into haESCs, we used polymerase chain reaction (PCR) to genotype the cells for the desired editing results (table S3). Positive outcomes were identified in 0.69 to 1.4% of transfected cells (fig. S1, A to C). Sanger sequencing analysis revealed bivalent endpoint sequences of targeted chromosomes in which nucleotide deletions and insertions were observed (fig. S1, D to F), indicating interchro-

mosomal DNA repair by nonhomologous end joining after CRISPR-Cas9–mediated cleavages.

Fluorescence in situ hybridization (FISH) was also used to confirm Chr4+5 and Chr2+1 ligation in haESCs (Chr4+5 haESCs and Chr2+1 haESCs; Fig. 1B). However, Chr1+2 in haESCs (Chr1+2 haESCs) had been split into two. The first part was a segment of chromosome 1 fused with chromosome 2 (Fig. 1B), and the second part was the remaining chromosome 1 fused with an arm of chromosome 17 (fig. S1G), as indicated by standard G-banding karyotype analyses (Fig. 1C). We found ligated chromosomes in karyotype results of replicated experiments as well (fig. S1, H to K). All ligated chromosomes exhibited complete centromere and telomere signals (fig. S2A). We also found microsegments excised from targeted chromosomes that lacked either telomere or centromere signals, except in one Chr4+5 line where a microchromosome that possessed complete centromere and telomere signals was found, indicating a ligation of two microsegments (fig. S2A). All microsegments and microchromosomes disappeared after passage 20.

Continuous sorting has been shown to be required to maintain haploidy and avoid spontaneous diploidization in mammalian haESCs (*12–16*). After sorting, two Chr4+5 haESC lines, one Chr1+2 haESC line, and two Chr2+1 haESC lines were established. Note that the established Chr1+2 haESC line was one with a split Chr1+2, which indicated that, in comparison to a complete Chr1+2, the split Chr1+2 might be advantageous for the maintenance of haploidy in chromosome-engineered haESCs. Although the appearance and marker-gene expression of engineered haESCs were normal (fig. S2, B and C), DNA content analyses revealed significantly reduced percentages of 1n cells in Chr2+1 haESCs (fig. S2, D and E). Confocal microscopy analysis further revealed the existence of lagging chromosomes that could overlap with one another in dividing Chr2+1 haESCs that maintained haploidy or spontaneously diploidized (fig. S2, F to I). We sorted the cells exhibiting 4n DNA content in each line for ploidy analysis, and those derived from Chr2+1 haESCs showed the highest proportion of authentic polyploidy (24.5%) (fig. S2J).
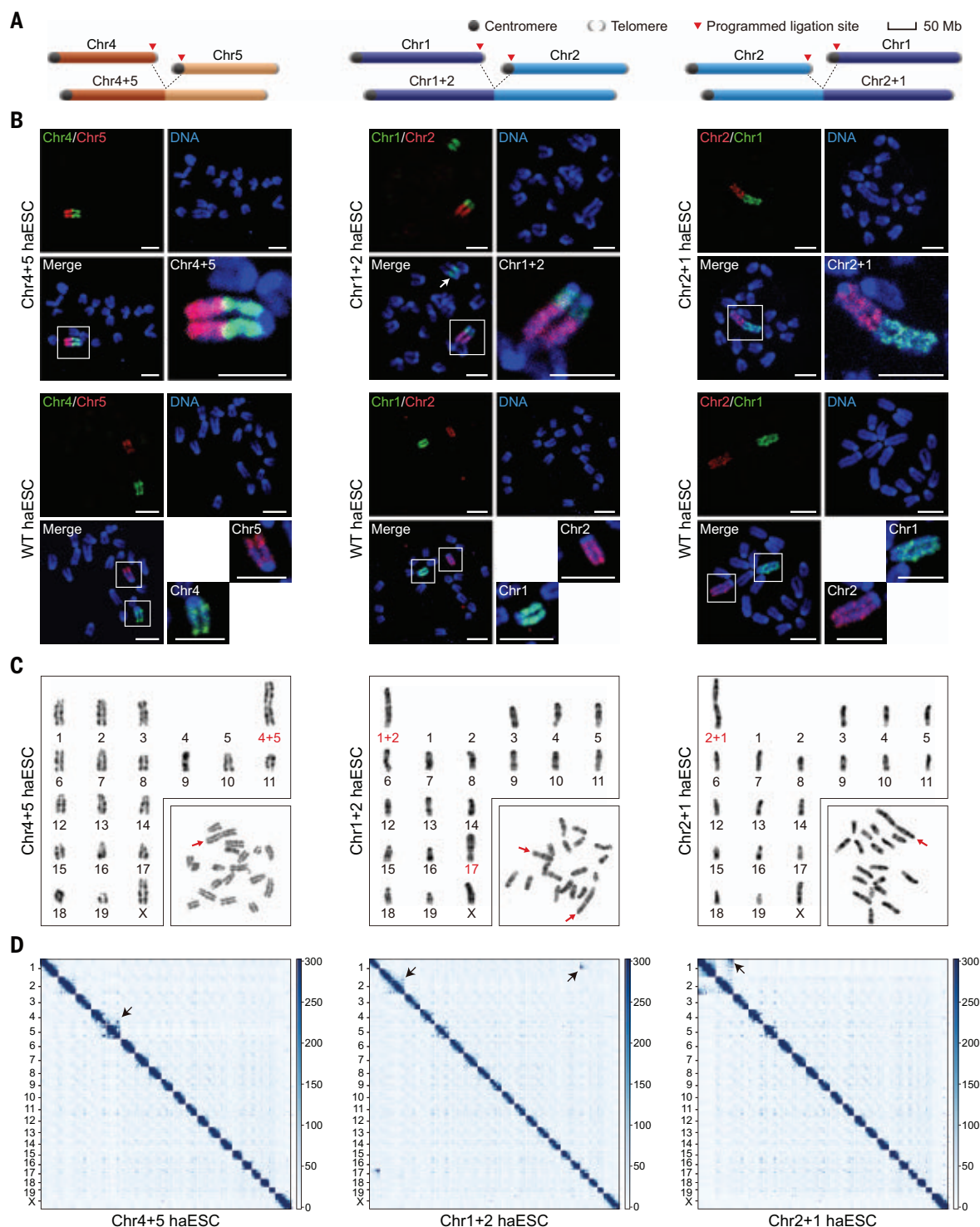
Hi-C analyses revealed strengthened contacts between ligated chromosomes in engineered haESCs (Fig. 1D and fig. S3, A to C). We also found increased contacts between the split Chr1+2 and chromosome 17 in Chr1+2 haESCs (Fig. 1D). Using this feature, we located the splitting site of Chr1+2 at about 114.3 Mb in chromosome 1, whose proximal arm was fused with chromosome 17 (Chr1+17), thus exhibiting strengthened interchromosomal contacts (fig. S3D). Although the biological function of interchromosomal contacts in animal cells remains unknown (*21*), these data indicate that they could be strengthened by chromosome

Fig. 1. Engineered chromosome ligation in mouse haESCs. (**A**) Diagrams for ligation of chromosomes 4 and 5 (Ch4+5), chromosomes 1 and 2 (Chr1+2), and chromosomes 2 and 1 (Chr2+1). (**B**) FISH detection for ligated chromosomes in Chr4+5 (*n* = 10), Chr1+2 (*n* = 6), and Chr2+1 (*n* = 7) haESCs. The chromosome indicated by an arrow is further illustrated in fig. S1G. WT haESCs (*n* = 14) were used as controls.

Scale bars are 5 μm. (**C**) Standard G-banding karyotyping results for Chr4+5, Chr1+2, and Chr2+1 haESCs. Ligated chromosomes are indicated by red arrows and text. (**D**) Contact maps of Chr4+5 (*n* = 2), Chr1+2 (*n* = 2), and Chr2+1 (*n* = 2) haESCs. Arrows indicate increased interchromosomal contacts. Numbers on the left indicate the chromosome; numbers on the right represent contact values.

ligation. Ligated chromosomes exhibited a limited compartment switch, except chromosome 1 in Chr1+2 haESCs (fig. S3E), on which two opposite compartment switch modes divided by the 114.3-Mb splitting site were identified (fig. S3F). All chromosome-ligated haESCs exhibited transcriptomes similar to those of wild-type (WT) counterparts (fig. S3G).

PacBio sequencing analyses were then used to identify ligations and structural variants (SVs) in each engineered haESC line (fig. S4, A to C). Derived from parallel subclones, Chr1+2

Fig. 2. Ligation-induced polyploidization in diploid NSCs. (**A**) Hoechst staining shows overlapped lagging chromosomes in engineered NSCs (white arrows). Scale bars are 5 μm. (**B**) Percentage of cells containing overlapped lagging chromosomes in Chr4+5, Chr1+2, and Chr2+1 NSC lines. (**C**) Ploidy of NSCs carrying ligated chromosomes (n = 3). The sorting of cells with DNA content equal to 2n or >4n is shown in the middle. Ploidy analyses for 2n cells on day 20 are shown on the left. All cells were synchronized with colchicine for 30 hours before the analysis.

Percentages of polyploid cells are indicated. Karyotyping results of >4n cells on day 0 are shown on the right. Arrows indicate ligated chromosomes. Scale bars are 5 μm. (**D**) Chromosome numbers of unsorted WT (n = 32), Chr4+5 (n = 22), Chr1+2 (n = 24), and Chr2+1 (n = 29) NSCs. The arrow indicates a fraction of polyploid Chr2+1 NSCs. Chromosome numbers >4n in Chr2+1 NSCs or >2n in other NSC groups represent overlapped karyotypes. For all graphs, data are means ± SEM. **p < 0.01; ****p < 0.0001; ns, not significant.
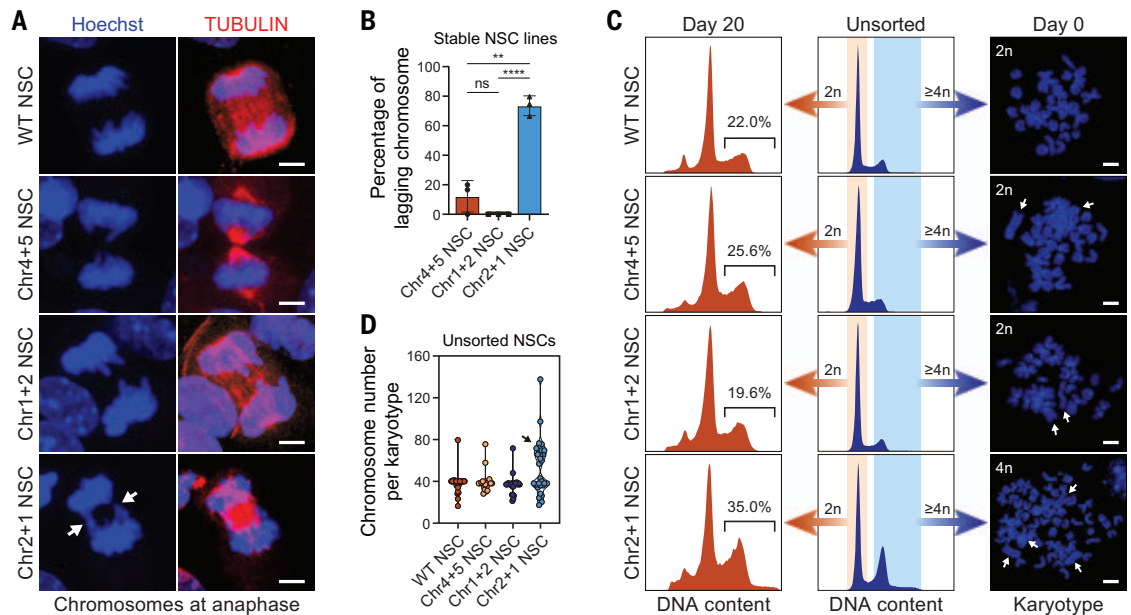
haESCs and Chr1+2 haESCs (sc-2; sc, subclone) exhibited identical ligation and distinct SVs (table S4), implying a random occurrence of the latter. Discontinuous reads mapping to 114.3 Mb of chromosome 1 were found in Chr1+2 haESCs and Chr1+2 haESCs (sc-2) and shared a 14–base pair (bp) AT-rich endpoint sequence that indicated the precise splitting site (fig. S4D). Because the 14-bp nucleotides or their neighboring sequences did not match the sequences of sgRNAs, the split likely resulted from random microhomology-mediated end joining, which usually leaves 5- to 25-bp AT-rich endpoint sequences (22). Average SV sizes were 366, 166, and 558 bp in Chr4+5, Chr1+2, and Chr2+1 haESCs, respectively (fig. S4E). No sgRNA targeting site was found near any identified SVs (table S4). Moreover, no correlation between SVs and neighboring gene expression was found in any chromosome-engineered haESC line (fig. S4, F and G).

Mitotic nuclear division arrested by large chromosome ligation

Based on a combination of Hi-C and PacBio sequencing, the arm length was 308.3 Mb for Chr4+5 (156.5 Mb of chromosome 4 plus 151.8 Mb of chromosome 5; fig. S3A), 377.6 Mb for Chr2+1 (182.1 Mb of chromosome 2 plus 195.5 Mb of chromosome 1; fig. S3B), 263.3 Mb for Chr1+2 (81.2 Mb of distal chromosome 1 plus 182.1 Mb of chromosome 2; fig. S3C), and 209.6 Mb for Chr1+17 (114.3 Mb of proximal chromosome 1 plus 95.3 Mb of chromosome 17; fig. S3D). Chr2+1 haESCs exhibited overlapping

lagging chromosomes and a high tendency toward polyploidization. However, the credibility of these observations was compromised by the spontaneous diploidization tendency of haESCs. Following a three-step differentiation procedure (fig. S5A), we tried to obtain diploid neural stem cells (NSCs) from engineered haESCs. Embryoid bodies and NSCs were successively derived and possessed normal appearances (fig. S5B). NSCs also exhibited normal marker-gene expressions, maintained ligated chromosomes, and had a diploid karyotype (fig. S5, B to D). Hi-C results revealed strengthened contacts between ligated chromosomes (fig. S6, A to E). Anaphase lagging chromosomes were found in 12.2, 0, and 73.9% of NSCs carrying Chr4+5, Chr1+2, and Chr2+1, respectively (Fig. 2, A and B). Chr2+1 NSCs exhibited a high tendency toward polyploidization (Fig. 2C). For sorted cells (DNA content ≥4n), only those from Chr2+1 NSCs showed authentic tetraploidy (Fig. 2C). For unsorted cells, Chr2+1 NSCs exhibited a marked polyploidized fraction not found in other groups (Fig. 2D).

Next, we designed a programmed translocation between Chr1+2 and Chr1+17 in Chr1+2 haESCs, aiming to recover full length Chr1+2 (recovered Chr1+2; Fig. 3A). In parallel, we tried to shorten Chr2+1 to the size of Chr1+2 using a programmed translocation with chromosome 17 (truncated Chr2+1 and Chr2+17; Fig. 3A). sgRNAs were designed according to the splitting site (fig. S4D and table S1). As a result, 0.10 to 0.42% of clones were PCR-positive (n = 4; table S3). Sanger sequencing and karyotype

analysis confirmed the formation of recovered Chr1+2 (recovered Chr1+2 haESCs) and truncated Chr2+1 and Chr2+17 (truncated Chr2+1 haESCs; fig. S7, A to D).

Spontaneously diploidized ESCs in each haESC line were sorted and labeled with a genome-integrating H2B-RFP-PiggyBac plasmid to show chromosome behavior. Normal nuclear division was observed in 82 WT, 131 Chr4+5, and 56 Chr1+2 ESCs. By contrast, 9 of 112 Chr2+1 ESCs polyploidized during the imaged cycle. We found a continuous existence of overlapped lagging chromosomes in all Chr2+1 ESCs that eventually polyploidized, accompanied by arrested anaphase and refusion of daughter nuclei (Fig. 3B). Although lagging chromosomes were also observed in Chr1+2 and Chr4+5 ESCs at certain time points, they detached from one another with spindle elongation (Fig. 3B). In ESCs that carried recovered Chr1+2, a continuous existence of overlapped lagging chromosomes and refusion of daughter nuclei were found in 8 of 67 observed cells (Fig. 3B). None of 87 ESCs that carried truncated Chr2+1 polyploidized during the imaged cycle (Fig. 3B). These results show that the arm of ligated chromosome Chr2+1 or recovered Chr1+2 (both 377.6 Mb in size) was spatially incompatible for diploid mouse cells, leading to arrested nuclear division and cell polyploidization; shortening the arm size by 114.3 Mb could eliminate this effect.

Refusion of daughter nuclei was slower than normal nuclear division (Fig. 3B). Consistent with this observation, we found a lower proliferation

Fig. 3. Cell division is restricted by mouse chromosome engineering. (**A**) Engineered chromosomes in haESCs: (I) Chr4+5 and chromosome 17 in Chr4+5 haESCs, (II) Chr1+2 and chromosome 17 in designed Chr1+2 haESCs, (III) Chr1+2 shortened in accidental translocation with chromosome 17 and Chr1+17 formed in the meantime in Chr1+2 haESCs, (IV) recovered Chr1+2 and Chr1+17 in translocated haESCs, (V) Chr2+1 and chromosome 17 in Chr2+1 haESCs, and (VI) truncated Chr2+1 and Chr2+17 forms in the meantime in another translocated haESC. (**B**) Continuous nuclear imaging of diploid ESCs: (WT) diploid ESCs with a wild-type karyotype, (I) diploidized ESCs sorted from Chr4+5 haESCs, (III) diploidized ESCs sorted from Chr1+2 haESCs, (IV) diploidized ESCs sorted from recovered Chr1+2 haESCs, (V) diploidized ESCs sorted from Chr2+1 haESCs, and (VI) diploidized ESCs sorted from truncated Chr2+1 haESCs. The time point when all chromosomes are arranged in the equatorial plate (metaphase) is set as 0 min.

White arrows indicate overlapped lagging chromosomes; yellow arrows indicate lagging chromosomes detached by spindle elongation. Scale bars are 5 μm.
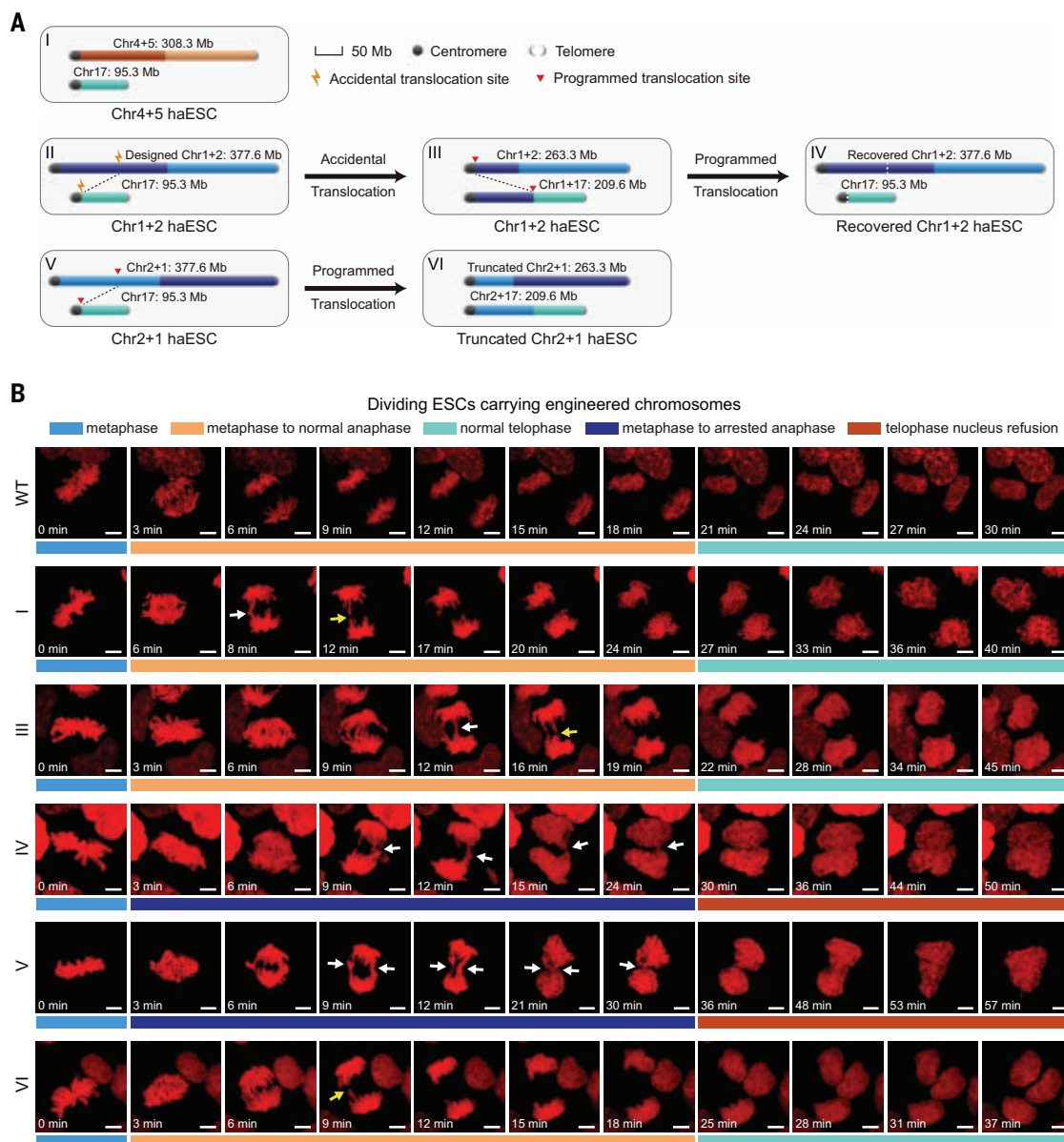
rate in Chr2+1 haESCs (fig. S7E). In truncated Chr2+1 haESCs with normal nuclear division (Fig. 3B), the proliferation rate was recovered (fig. S7E). Sub-G_1 phase proportion analysis indicated that the cell death ratio did not change after the ligations (fig. S7F). Fitted Gaussian curves showed an extended S/G_1 phase in Chr2+1 haESCs (fig. S7G).

Production of viable pups that carry ligated chromosomes

To establish a proper imprinting pattern (20), we deleted three imprinted regions (H19, IG, and Rasgrf1) in engineered haESCs (table S3). Through oocyte injection of derived haESCs, we generated 113 Chr4+5 embryos, 355 Chr1+2 embryos, and 365 Chr2+1 embryos, which were

transferred into surrogate wombs (Fig. 4A). No full-term pup was derived from Chr2+1 embryos, which were abnormal and died before embryonic day 12.5 (E12.5; Fig. 4B and table S5). By contrast, haESC-injected embryos with a WT karyotype achieved full term efficiently (fig. S8A and table S5). Chr2+1 embryos showed a significantly increased percentage of polyploid cells (fig. S8, B to D).

Fourteen and 37 full-term pups were derived from Chr4+5 and Chr1+2 embryos (Chr4+5 and Chr1+2 pups), respectively (Fig. 4B and table S5). Chromosome ligations in these pups were confirmed (Fig. 4C and fig. S8A). Body weights of Chr4+5 (1.37 ± 0.09 g, n = 13) and Chr1+2 pups (1.35 ± 0.15 g, n = 12) were normal (Fig. 4D) and so were their placenta weights (fig. S8E).

By transferring 68 embryos created by oocyte injection of truncated Chr2+1 haESCs, two full-term living pups were also derived (fig. S8F and table S5).

Ligation-triggered polyploidization was confirmed in haESCs that were diploidized in vitro (Fig. 2) but not in bona fide 2n ESCs derived from mouse embryos. We therefore obtained ESCs from E3.5 Chr4+5, Chr1+2, and Chr2+1 embryos. Four out of 60 ESCs that were derived from Chr2+1 embryos exhibited continuously overlapping chromosomes during the imaged cell cycle, followed by arrested anaphase and nuclear refusion (fig. S8G). All ESCs that were derived from Chr4+5 (n = 92), Chr1+2 (n = 89), and truncated Chr2+1 (n = 87) embryos exhibited normal nuclear divisions (fig. S8G).
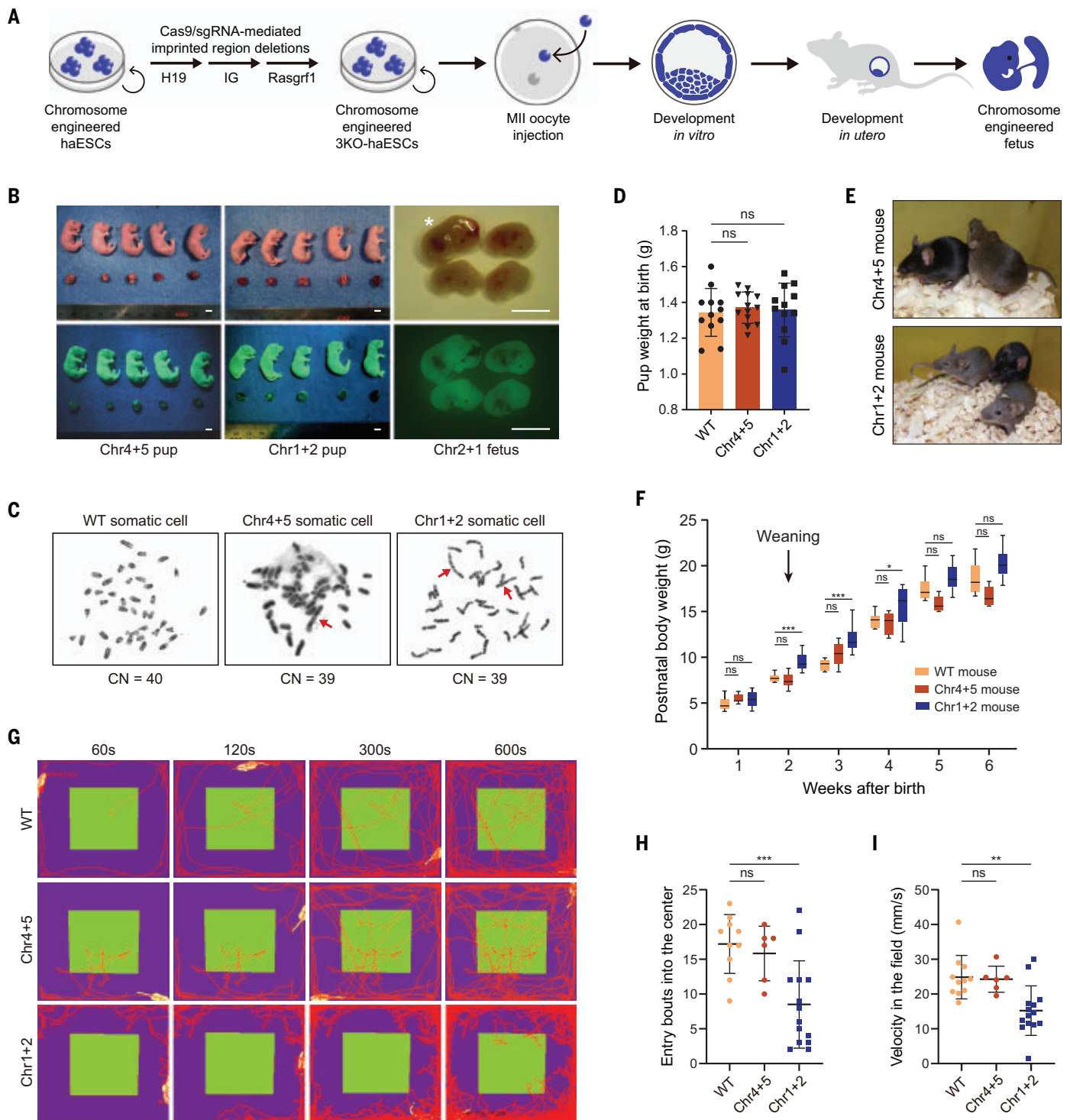
Fig. 4. Production of mice that carry ligated chromosomes. (**A**) Strategy for generating mouse embryos that carry ligated chromosomes. 3KO, deletions of three imprinted regions; MII, metaphase II. (**B**) Full-term Chr4+5 and Chr1+2 pups and arrested E12.5 Chr2+1 embryos. Photographs are shown in the top row, and images for green fluorescent protein–positive signals are shown in the bottom row. The embryo with a heartbeat is labeled with an asterisk. Scale bars are 5 mm. (**C**) Standard G-banding karyotype results. Red arrows indicate ligated chromosomes. CN, chromosome number. (**D**) Body weights of WT ($n = 12$), Chr4+5 ($n = 13$), and Chr1+2 ($n = 12$) full-term pups. (**E**) Adult Chr1+2 (bottom) and Chr4+5 (top) mice. The black mouse is the WT control. (**F**) Growth curves of WT ($n = 11$), Chr4+5 ($n = 7$), and Chr1+2 ($n = 9$) mice. (**G**) Activity traces of 8-week-old WT, Chr4+5, and Chr1+2 mice in the open-field test. The time periods along the top indicate 60, 120, 300, and 600 s after the start of test. (**H**) Entries of WT, Chr4+5, and Chr1+2 mice into the anxiety-provoking central area in the open-field test. (**I**) Velocities of WT, Chr4+5, and Chr1+2 mice in the open-field test. For all graphs, data are means ± SEM. *$p < 0.05$; **$p < 0.01$; ***$p < 0.001$; ns, not significant.
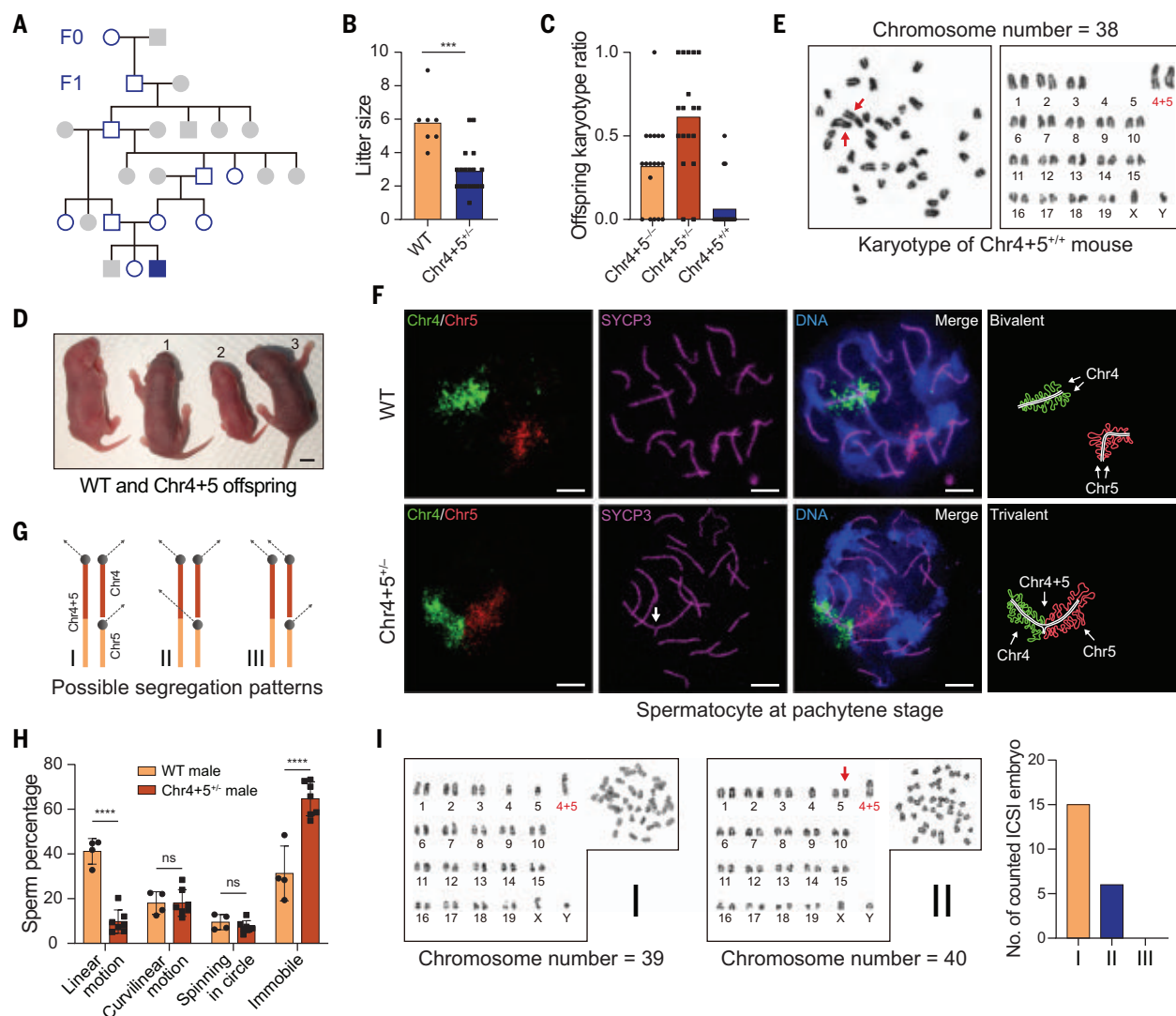
Fig. 5. Deriving homozygous offspring that carry ligated chromosomes.
(**A**) Deriving a homozygous Chr4+5 offspring in five generations. Square, male; circle, female; open, heterozygous Chr4+5 mice; solid, homozygous Chr4+5 mice; gray, WT mice. (**B**) Comparison of the litter sizes of Chr4+5$^{+/-}$ mice ($n = 18$) and WT mice ($n = 7$). (**C**) Ratios of Chr4+5$^{-/-}$, Chr4+5$^{+/-}$, and Chr4+5$^{+/+}$ offspring by mating Chr4+5$^{+/-}$ mice ($n = 18$). (**D**) Female Chr4+5$^{+/-}$ (1), male Chr4+5$^{+/+}$ (2), and male Chr4+5$^{+/-}$ (3) pups. The WT pup is on the left. Scale bar is 5 mm. (**E**) G-banding karyotyping result of a homozygous Chr4+5 mouse. A pair of Chr4+5 is indicated with red arrows and text. (**F**) Shown from left to right are FISH detection for chromosomes 4 and 5, chromosome axes indicated by SYCP3 staining (the Chr4+5-containing axis is indicated by the arrow), merged images with Hoechst-stained DNA, and schemes for trivalent Chr4+5-Chr4-Chr5 and bivalent WT counterparts. Scale bars are 5 μm. (**G**) Three hypothetical segregation patterns of trivalent Chr4+5-Chr4-Chr5 in Chr4+5$^{+/-}$ spermatocytes. (**H**) Comparing sperm mobilities in WT ($n = 4$) and Chr4+5$^{+/-}$ ($n = 7$) mice. (**I**) Karyotype results for ICSI embryos. Example G-banding karyotypes of ICSI embryos that fit hypothetical segregation patterns I and II are shown on the left and middle. Karyotype distributions of 21 counted ICSI embryos are shown on the right. The red arrow indicates a redundant chromosome 5. For all graphs, data are means ± SEM. ***$p < 0.001$; ****$p < 0.0001$; ns, not significant.

Chr4+5 and Chr1+2 pups grew to adulthood (Chr4+5 and Chr1+2 mice; Fig. 4E). Chr4+5 mice had normal growth curves, but Chr1+2 mice exhibited overgrowth at weaning (Fig. 4F). In the open-field test for anxiety, Chr4+5 mice entered the center zone at a normal rate, but Chr1+2 mice tended to avoid entering the center zone (Fig. 4, G and H), indicating a high level of anxiety (23). The moving distance and velocity of Chr4+5 mice were normal, whereas Chr1+2 mice moved significantly less and slower (Fig. 4, H and I, and fig. S8, H and I).

Phenotype-associated gene dysregulation in chromosome-ligated mice

We then compared the transcriptomes of the brain, lung, heart, liver, spleen, kidney, and muscle in Chr1+2 mice with those of the WT mice ($n = 2$) and identified 2137 organ-specific and 50 shared differentially expressed genes (DEGs), 26.4% of which were located on chromosomes 1, 2, and 17 (fig. S9, A and B). Chromosome 17, accounting for 3.5% of the genome, had 7.7% organ-specific DEGs and 20% shared DEGs, suggesting a possible correlation between its rearrangement and gene dysregulation. We

analyzed the gene *Capn11*, which encodes a calcium-dependent protease and is located on chromosome 17. It was down-regulated in all organs (fig. S9C). *Capn11* was also down-regulated in *Shank3*-overexpressing mice, a well-characterized model for autism and schizophrenia (24). We therefore tested whether *Capn11* was related to the abnormal behavior of Chr1+2 mice. We deleted *Capn11* in WT C57 mice (Capn11^{KO} C57 mice; fig. S10, A to C). The mice avoided the center zone in the open-field test and exhibited increased body weight at weaning (fig. S10, D to F). These data
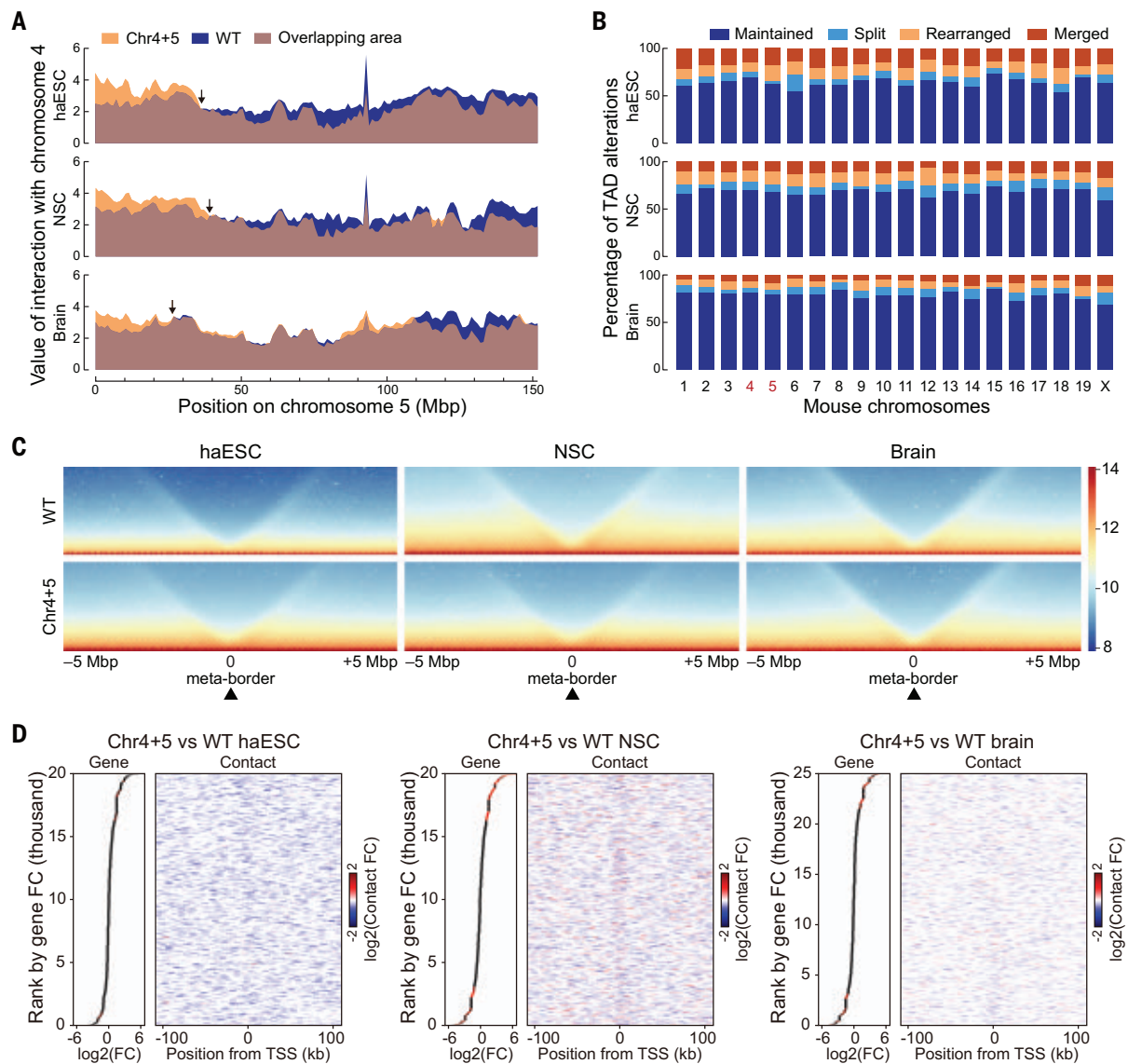
Fig. 6. Chromatin structure disturbances are weakened by differentiation.
(**A**) Interaction values from chromosome 5 to chromosome 4 in Chr4+5 haESCs, NSCs, and brain. Results for WT haESCs, NSCs, and brain were used as controls. Arrows indicate boundaries for increased interactions. (**B**) Frequency of TAD alterations between WT and Chr4+5 haESCs, NSCs, and brain. (**C**) Metaplots for TAD boundaries in Chr4+5 haESCs [mean insulation score (IS) = 2266.48], NSCs (mean IS = 2255.09), and brain (mean IS = 2254.16). Results for WT haESCs (mean IS = 2061.29), NSCs (mean IS = 2345.57), and brain (mean IS = 2224.56) were used as controls. (**D**) Combined analyses illustrating altered gene expression and changed chromatin contacts in WT and Chr4+5 haESCs, NSCs, and brain. Genes with an expression fold change (FC) >2 are in red. TSS, transcription start site.

suggested that *Capn11* dysregulation contributed to the behavior phenotype of Chr1+2 mice.

Reduced *Capn11* levels were also found in Chr1+2 haESCs and NSCs (fig. S11A). However, Hi-C analysis revealed no contact change at the *Capn11* locus in these cells (fig. S11B). PacBio sequencing results revealed an intact *Capn11* locus in Chr1+2 haESCs (fig. S11C). ATAC sequencing (assay for transposase-accessible chromatin using sequencing) results also showed no peak pattern change in Chr1+2 haESCs and NSCs (fig. S11D), and virtual 4C analyses revealed no contact pattern change at this locus (fig. S11E). Inferred three-dimensional structure results showed that the normal fold-ing pattern of chromosome 17 was maintained in Chr1+2 haESCs and NSCs (fig. S11F). A long terminal repeat (LTR) is located within the *Capn11* locus (*25*), which lacked contact with other genome regions (fig. S11B). Deleting this LTR did not rescue the *Capn11* levels (fig. S11, G and H, and table S3). *Capn11* levels were also down-regulated in truncated Chr2+1 haESCs but were restored in Chr2+1 haESCs and even in recovered Chr1+2 haESCs (fig. S11H). Because chromosome 17 was fused with distinct segments in Chr1+2 and truncated Chr2+1 haESCs, these data suggested the existence of a sequence-independent ligation-related effect on *Capn11* dysregulation (*26*).

Deriving homozygous chromosome-ligated mouse offspring

No pup was derived from mating more than 30 Chr1+2 mice. By contrast, Chr4+5 mice (F_0) produced full-term mice (F_1) after mating with WT mice (Fig. 5A). After multiplying the number of viable embryos (those devoid of H19 and IG deletions) in each litter by four, following the Mendelian ratio, the corrected litter size of F_0 was 2.3 ± 3.1 (n = 7), which was significantly lower than that of WT counterparts (5.9 ± 1.6, n = 7; fig. S12A). Of these derived F_1 mice, those carrying ligated chromosomes were identified and confirmed by PCR genotyping, Sanger sequencing, and karyotype analyses

(fig. S12, B to E). Both female and male F_1 mice could transmit Chr4+5 by mating with the WT mice (fig. S12, F and G). We mated female and male heterozygous F_1 mice devoid of all imprinting deletions (Chr4+5$^{+/-}$ mice), which also exhibited a reduced litter size (2.9 ± 1.8, n = 18; Fig. 5, A and B). Three homozygous mice that carried Chr4+5 (Chr4+5$^{+/+}$ mice) were derived. They had 19 chromosome pairs (Fig. 5, C to E).

We also derived ESCs from E3.5 Chr4+5$^{+/+}$ mouse embryos (Chr4+5$^{+/+}$ ESCs). FISH detection showed that chromosomes 4 and 5 were merged in Chr4+5$^{+/+}$ ESCs (fig. S13A). By analyzing the organs of Chr4+5$^{+/+}$ mice, we found merged chromosomes 4 and 5 in all samples by Southern blotting (fig. S13B). Hi-C sequencing results for Chr4+5$^{+/+}$ mouse brains (Chr4+5 brains) revealed an increase in interchromosomal contacts between chromosomes 4 and 5 (fig. S13C), the levels of which were similar to those of intrachromosomal contacts within native chromosomes (fig. S13D). Together, these data indicated that Chr4+5 was homogeneously retained in the cells and organs of Chr4+5$^{+/+}$ mice.

A total of 3 Chr4+5$^{+/+}$ pups, 33 Chr4+5$^{+/-}$ pups, and 17 WT pups were obtained from 18 litters of Chr4+5$^{+/-}$ offspring (Fig. 5C). The percentage of Chr4+5$^{+/+}$ pups (5.7%) was much lower than that of Chr4+5$^{-/-}$ pups (32.1%) or one half of Chr4+5$^{+/-}$ pups (62.2%), which did not fit Mendel's law for mating heterozygous parents (+/+:+/−:−/− = 1:2:1). Because Chr4+5 shared homologous sequences with both chromosomes 4 and 5, potential explanations for the mating results could involve errors in pairing or segregation of chromosomes in Chr4+5$^{+/-}$ germ cells. Using SYCP3 staining to show chromosome axes and FISH detection to indicate chromosomes 4 and 5, we identified separated bivalents of chromosomes 4 and 5 in WT pachytene spermatocytes (n = 18) and trivalents that exhibited both signals of chromosomes 4 and 5 in Chr4+5$^{+/-}$ pachytene spermatocytes (n = 30; Fig. 5F), indicating that Chr4+5 can correctly synapse with chromosomes 4 and 5. We therefore propose three hypothetical segregation patterns for paired Chr4+5, Chr4, and Chr5 (Fig. 5G). To dissect the actual segregation outcome, we derived mature sperm from Chr4+5$^{+/-}$ mice (Chr4+5$^{+/-}$ sperm; movie S1). The percentage of Chr4+5$^{+/-}$ sperm that exhibited high mobility (linear motion) was 9.7 ± 5.2% (n = 7), which was lower than that of the WT counterpart (41.1 ± 5.8%, n = 4; Fig. 5H). To avoid bias for highly motile sperm, we used intracytoplasmic sperm injection (ICSI) to generate embryos (ICSI embryos) whose karyotypes could be used to deduce the chromosomal content of the injected sperm. We found embryos with karyotypes consistent with hypothetical segregation pattern I or II but not with segregation pattern III (Fig. 5I).

Chromatin structure changes after engineered chromosome ligation

We found an increased number of contacts between ligated chromosomes in Chr4+5 haESCs, NSCs, and brain (fig. S3A, S6B, and S13D). In Chr4+5 haESCs, increased contacts of chromosome 5 to chromosome 4 were clustered on proximal chromosome 5 (0 to 40 Mb; Fig. 6A), and increased contacts of chromosome 4 to chromosome 5 were clustered on distal chromosome 4 (140 to 160 Mb; fig. S14A). A similar but minor contact change was found in Chr4+5 NSCs, whereas the minimal change was found in Chr4+5 brain (Fig. 6A and fig. S14A). These findings were confirmed by biological replicates that exhibited correlation values ranging from 0.961 to 0.979 (fig. S15A). Topological associated domain (TAD) scores indicated enhanced TAD compactness in Chr4+5 NSCs and brain (fig. S15B). The percentages of changed TADs were 35.8, 31.3, and 21.0% in Chr4+5 haESCs, NSCs, and brain, respectively, exhibiting no prominent distribution on chromosomes 4 and 5 (Fig. 6B and fig. S15C). For those on chromosome 4, changed TADs were randomly scattered across the entire arm (fig. S15D). Meta-TAD borders were strengthened in Chr4+5 haESCs, weakened in Chr4+5 NSCs, and maintained in Chr4+5 brain (Fig. 6C). We identified 58, 1595, and 418 DEGs in Chr4+5 haESCs, NSCs, and brain, respectively, which were not clustered on chromosomes 4 and 5 (fig. S16, A and B). Changed contacts were not clustered at the transcriptional start sites of DEGs (Fig. 6D and fig. S16C). By analyzing genes that were paired by the same changed contacts, we found no correlation between their expression fold changes (fig. S16D). DEGs within changed contacts were enriched in pathways for exocytosis in haESCs, urogenital system development in NSCs, and axonogenesis in brain (fig. S16E).

Discussion

In this study, we created laboratory mouse models that carried chromosome level fusions by engineering. Some engineered mice showed abnormal behavior and postnatal overgrowth, whereas others exhibited decreased fecundity, suggesting that although the change of genetic information was limited, fusion of animal chromosomes could have profound phenotypic effects. *Capn11*, which is located on a rearranged chromosome, might have contributed to the phenotypes. *Capn11* dysregulation could have arisen by means of a sequence-independent effect associated with the rearrangements (*26*). Changes in TADs and interchromosomal contacts in chromosome-ligated mice were similar to findings with natural Rb mice (*27*), suggesting that our work could help our understanding of evolutionarily derived chromosome fusions. Ligating the two largest mouse chromosome arms led to

refusion of daughter nuclei, consequently to cell polyploidization, and finally to embryonic lethality, but all of these effects were eliminated when the ligated arms were truncated by two independent translocations. This evidence suggests that the physical space of the mitotic nucleus is a potential constraining factor in mammalian karyotype evolution (*28, 29*).

Reproductive isolation and formation of new species may arise through accumulating chromosomal rearrangements that reduce fertility in heterozygous hybrids (*30, 31*). Chr1+2 mice (carrying two rearrangements) did not produce offspring, but Chr4+5 mice (carrying one rearrangement) did, although with limited fecundity. By analyzing the spermatocytes of Chr4+5 mice, we pinpointed the reproduction barrier to a segregation error of ligated chromosomes, which could attribute the reduced fecundity to impaired mobility of aneuploid sperm or the developmental failure of aneuploid embryos. With a lower birth rate, homozygous Chr4+5 mice were derived by mating heterozygous parents, suggesting that one fusion was insufficient for reproductive isolation in mice. Using an imprint-fixed haESC platform and gene editing, we achieved germline-transmittable chromosome ligation in a widely used animal model, the house mouse, which highlights a potential route for large-scale engineering of endogenous or exotic DNA in mammals (*32*).

REFERENCES AND NOTES

1. H. J. Hedrich, *The Laboratory Mouse* (Elsevier, ed. 2, 2012).
2. A. Coghlan, E. E. Eichler, S. G. Oliver, A. H. Paterson, L. Stein, *Trends Genet.* **21**, 673–682 (2005).
3. Y. Fan, E. Linardopoulou, C. Friedman, E. Williams, B. J. Trask, *Genome Res.* **12**, 1651–1662 (2002).
4. P. Stankiewicz, S. S. Park, K. Inoue, J. R. Lupski, *Genome Res.* **11**, 1205–1210 (2001).
5. A. Pujol *et al.*, *Reproduction* **131**, 1025–1035 (2006).
6. M. F. Greaves, J. Wiemels, *Nat. Rev. Cancer* **3**, 639–649 (2003).
7. P. N. Scriven, F. A. Flinter, P. R. Braude, C. M. Ogilvie, *Hum. Reprod.* **16**, 2267–2273 (2001).
8. Y. Yu, A. Bradley, *Nat. Rev. Genet.* **2**, 780–790 (2001).
9. Y. Shao *et al.*, *Nature* **560**, 331–335 (2018).
10. J. Luo, X. Sun, B. P. Cormack, J. D. Boeke, *Nature* **560**, 392–396 (2018).
11. A. Fleiss *et al.*, *PLOS Genet.* **15**, e1008332 (2019).
12. M. Leeb, A. Wutz, *Nature* **479**, 131–134 (2011).
13. U. Elling *et al.*, *Cell Stem Cell* **9**, 563–574 (2011).
14. I. Sagi *et al.*, *Nature* **532**, 107–111 (2016).
15. W. Li *et al.*, *Cell Stem Cell* **14**, 404–414 (2014).
16. H. Yang *et al.*, *Cell Res.* **23**, 1187–1200 (2013).
17. H. Yang *et al.*, *Cell* **149**, 605–617 (2012).
18. W. Li *et al.*, *Nature* **490**, 407–411 (2012).
19. H. Wan *et al.*, *Cell Res.* **23**, 1330–1333 (2013).
20. Z. K. Li *et al.*, *Cell Stem Cell* **23**, 665–676.e4 (2018).
21. P. G. Maass, A. R. Barutcu, C. L. Weiner, J. L. Rinn, *Mol. Cell* **69**, 1039–1045.e3 (2018).
22. M. McVey, S. E. Lee, *Trends Genet.* **24**, 529–538 (2008).
23. D. Lipkind *et al.*, *J. Appl. Physiol.* **97**, 347–359 (2004).
24. C. Jin *et al.*, *Front. Mol. Neurosci.* **11**, 250 (2018).
25. A. Sharifi-Zarchi *et al.*, *BMC Genomics* **18**, 964 (2017).
26. M. Barbieri *et al.*, *Proc. Natl. Acad. Sci. U.S.A.* **109**, 16173–16178 (2012).
27. C. Vara *et al.*, *Nat. Commun.* **12**, 2981 (2021).
28. W. Rens, L. Torosantucci, F. Degrassi, M. A. Ferguson-Smith, *Chromosoma* **115**, 481–490 (2006).
29. M. A. Ferguson-Smith, V. Trifonov, *Nat. Rev. Genet.* **8**, 950–962 (2007).
30. L. H. Rieseberg, *Trends Ecol. Evol.* **16**, 351–358 (2001).

31. J. L. Patton, S. W. Sherwood, *Annu. Rev. Ecol. Syst.* **14**, 139–158 (1983).
32. R. Chari, G. M. Church, *Nat. Rev. Genet.* **18**, 749–760 (2017).

MATERIALS SCIENCE

Growth rules for irregular architected materials with programmable properties

Ke Liu[1,2], Rachel Sun[1]†, Chiara Daraio[1]*

Biomaterials display microstructures that are geometrically irregular and functionally efficient. Understanding the role of irregularity in determining material properties offers a new path to engineer materials with superior functionalities, such as imperfection insensitivity, enhanced impact absorption, and stress redirection. We uncover fundamental, probabilistic structure–property relationships using a growth-inspired program that evokes the formation of stochastic architectures in natural systems. This virtual growth program imposes a set of local rules on a limited number of basic elements. It generates materials that exhibit a large variation in functional properties starting from very limited initial resources, which echoes the diversity of biological systems. We identify basic rules to control mechanical properties by independently varying the microstructure's topology and geometry in a general, graph-based representation of irregular materials.

The properties of materials depend both on their chemical composition and on the geometry of their microstructures. Empowered by carefully engineered sub-scale microstructures, architected materials (*1–5*) have been suggested for applications in optics (*6*), electromagnetics (*7, 8*), acoustics (*9*), and robotics (*10–12*). In mechanics (*13*), architected materials have been designed to exhibit negative thermal expansion (*14*), negative Poisson's ratio (*15*), ultrahigh strength-to-weight ratio (*16, 17*), tunable failure load (*18*), vanishing shear modulus (*19*), and shear-normal coupling (*20*). To reduce the complexity of designing structures in a nearly infinite space, human-made architected materials are mostly designed by periodic tessellations of selected geometric motifs. These motifs are either derived empirically from a limited number of known geometries, such as biomaterials, crystalline solids, and art (*15, 16, 21*), or computationally generated within bounding boxes discretized into pixels or voxels (*22–25*).

Materials with periodic microstructures are special cases in the realm of architected materials. Natural materials are usually characterized by irregular and heterogeneous microstructures, such as wood (*26*), nacre (*27*), insect nests (*28*) (Fig. 1A), or human bones (*29*). They present distinctive properties, such as the exceptionally white scales of some beetles (*30*) or the functional stability to perturbations of proteins (*31*). The geometric irregularity of biomaterials is a natural outcome of self-organized growth, which unfolds through a distributed, stochastic building process that follows simple local rules without a centralized plan (*28*).

Understanding the independent role of geometry and topology in irregular microstructures provides opportunities for the design and fabrication of advanced engineering materials. However, current descriptions of geometry used for periodic systems lead to ambiguity in distinguishing the contribution of specific structural features, or their repetition, on given functionalities. This underlines the importance of developing tools to define spatial characteristics in irregular materials.

Recently, computational methods have been developed to design and characterize irregular microstructures (*32–36*). For instance, the design of random, auxetic truss lattices revealed important connections between Poisson's ratio and lattice connectivity (*33, 34*). However, these tools do not provide a general framework to describe the geometry of architected materials, for example, because they do not include periodic designs in their descriptors.

A virtual growth program for microstructure generation

To better understand the structure–property relationships in irregular architected materials, we created a tool that evokes the distributed stochastic building process of natural growth, which we call the virtual growth program. The program is a graph-based method that builds on the combinatorial space of basic building blocks (Fig. 1B). These building blocks are local structural elements that can be identified in arbitrarily complex microstructures at a scale that is smaller than the typical unit cells in periodic designs. In the virtual growth process, the building blocks are connected stochastically on an underlying network, in which each pair of neighbors abides prescribed adjacency rules (Fig. 1, C and D). In this framework, a material's microstructure can be both periodic and nonperiodic. The framework also decouples topology (the connectivity of the underlying network) from the geometry (the shape of the building blocks) and allows investigating their independent influence on global material properties.

In this work, we use the virtual growth process to unravel structure–property relationships in irregular architected materials. We show that by starting from a very limited number of local structures (i.e., the building blocks), it is possible to generate a rich set of material microstructures with a wide range of functional properties. Specific properties can be targeted, by selecting adjacency rules and building blocks availability

[1]Department of Mechanical and Civil Engineering, California Institute of Technology, Pasadena, CA 91125, USA.
[2]Department of Advanced Manufacturing and Robotics, Peking University, Beijing 100871, China.
*Corresponding author. Email: daraio@caltech.edu.
†Present address: Department of Mechanical Engineering, Massachusetts Institute of Technology, Cambridge, MA 02139, USA.
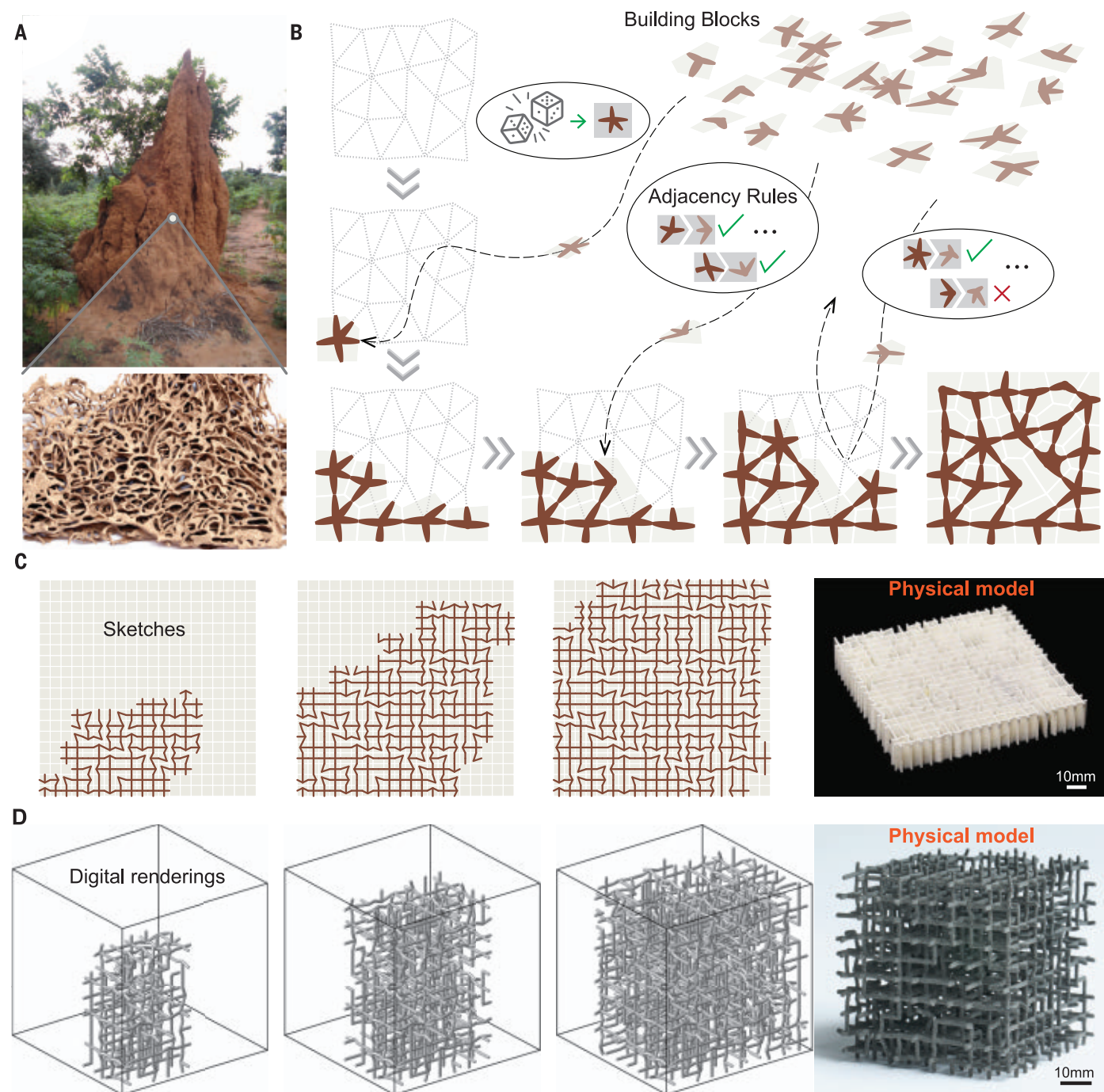
Fig. 1. Schematic of the virtual growth process of irregular architected materials. (**A**) Termite nests have irregular internal structures that are optimized for structural stability and ventilation (*28*). (**B**) Abstraction of the "growth" process, which assigns building blocks on an underlying graph. (**C** and **D**) Illustration of the virtual growth process (C) in 2D (movie S1) and (D) in 3D (movie S2). The physical models in (C) and (D) are 3D printed.

during "growth." These findings provide insight into how to program material properties in stochastic, self-assembly processes, and may influence future manufacturing of engineering materials.

The virtual growth program relies on four major inputs, which serve as the genome for the generation of architected materials: (i) the topology of the underlying network, (ii) the geometry of building blocks, (iii) the adjacency

rules between building blocks, and (iv) the availability of (or frequency hint for) building blocks. The program can create materials with different microstructures (Fig. 2). For example, the same square network (Fig. 2A) can be used to accommodate different building blocks (Fig. 2, B to D), including their reflections and rotations (fig. S1A). The adjacency rules define whether and how the basic building blocks can pair with each other (fig. S1B) by enforcing

geometrical compatibility at the interface and avoiding unwanted geometric features. For example, in the case of Fig. 2B, we forbid two "L"-shaped building blocks from connecting to avoid forming disconnected loops. The availability of building blocks resembles natural resource limits and influences how many times each building block appears in the final design (fig. S1C). Infinite availability of building blocks leads to constant frequency hints throughout
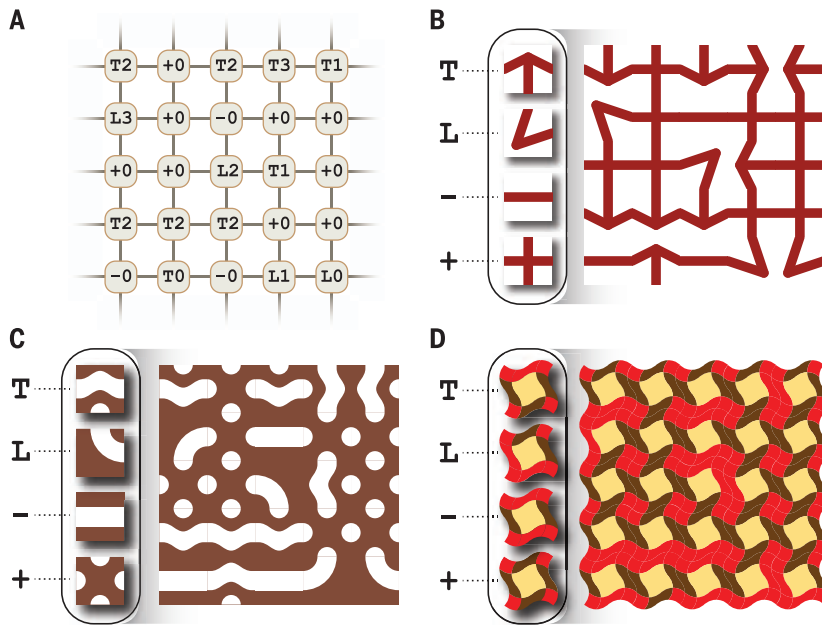
Fig. 2. Irregular materials generated by the virtual growth program. (**A**) Typical output of the virtual growth program, which is a symbolic graph. The letters and numbers are indexes that refer to the basic building blocks and their orientations. (**B**) Lattice-like design, which is the focus of this article. The "—," "T," "L," and "+" symbols represent the building blocks in the box. (**C**) Spinodal pattern–like design. (**D**) Multimaterial composite. We note that the building blocks are not limited to square shapes as long as the interfaces between building blocks are compatible.
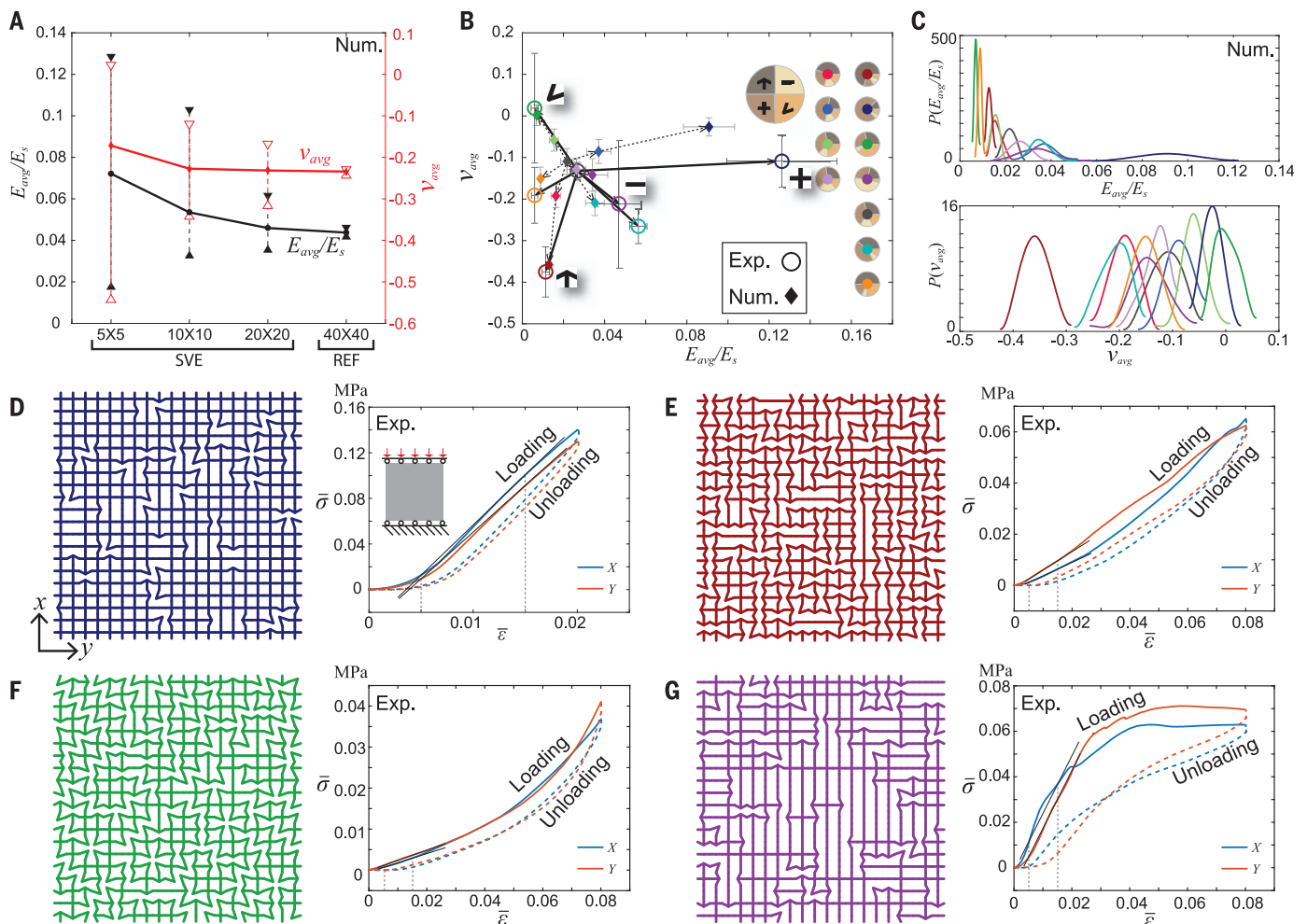
Fig. 3. Mechanical properties of the 2D irregular architected materials. (**A**) Numerically evaluated Young's modulus (E_{avg}/E_S) and average Poisson's

ratio (v_{avg}) values for different sizes of materials samples as a function of the dimension of the underlying networks. The first three groups are evaluated by

homogenization (SVE), and each point with error bars contains 100 samples. The (last) reference group contains 10 samples and is evaluated by a direct simulation, with boundary condition as shown in the inset of (D). The error bars extend minimal and maximal values. Num, numerical; Ref, reference. (**B**) Plot of E_{avg}/E_S vs. v_{avg} for 11 sample groups generated by using different frequency hints, each containing numerical 100 samples. The insets use pie plots to show the resultant probabilities of appearance of the basic building blocks. Experiments are performed for seven groups, each with five samples. The error bars extend to one standard deviation. The arrows indicate trends of property changes. Exp, experimental. (**C**) Smoothed distributions of v_{avg} and E_{avg}/E_S, based on the numerical samples. The color code follows (B). P, probability density function. (**D** to **G**) Representative designs and their experimental stress ($-\sigma$)-strain ($-\varepsilon$) curves under compression along both x and y directions (movie S3). The stresses ($-\sigma$) are calculated as effective stress for the bulk volume, in units of megapascals. The stress and strains are effective values with respect to the bulk dimension of architected materials. The colors of the designs refer to the different sample groups. The inset shows the boundary conditions. The thin black lines show our definition of Young's modulus as a secant modulus between 0.005 and 0.015 strain.

the "growth" process. Defects are likely to happen when the availability of a certain building block is very low (fig. S1, D and E). To avoid defects, in the rest of this study, we assume that there is an infinite amount of building blocks available for each "growth" process.

The virtual growth process (movie S1) implements a *WaveFunctionCollapse* algorithm (*37*). In each step, the algorithm assigns a random building block to the node on a predefined network with minimal nodal entropy. Here, nodal entropy is related to the number of building blocks that can be assigned to a given node. For example, if only one building block can be assigned to a given node to satisfy adjacency

rules, then its nodal entropy is zero. If a node can be filled with any building block, its nodal entropy is maximal. When the algorithm cannot assign any building block to a node, a defect forms. This process continues until all nodes are assigned, and the nodal entropies are updated after each step.

Clustering and convergence of material properties

We constrain the underlying network to be a squared grid, without loss of generality, and use the building blocks in Fig. 2B and fig. S1. The nondeterministic assignment of building blocks leads to a diversity of architected materials. Even given the same building blocks,

adjacency rules, and frequency hints, the program generates different material microstructures every time. After generating the microstructures, we evaluate their linear elastic properties, Young's modulus, and Poisson's ratio in the x and y directions. To obtain these properties, we perform numerical homogenization (*38*) using the statistical volume element (SVE) approach (*39*). The convergence of linear elastic properties is tested on three different sample sizes for the SVE and compared to the results of direct simulations on larger patches (40 by 40 squared grid) of materials. As observed in Fig. 3A, when the SVEs are of grid size 20 by 20, their properties are close enough to
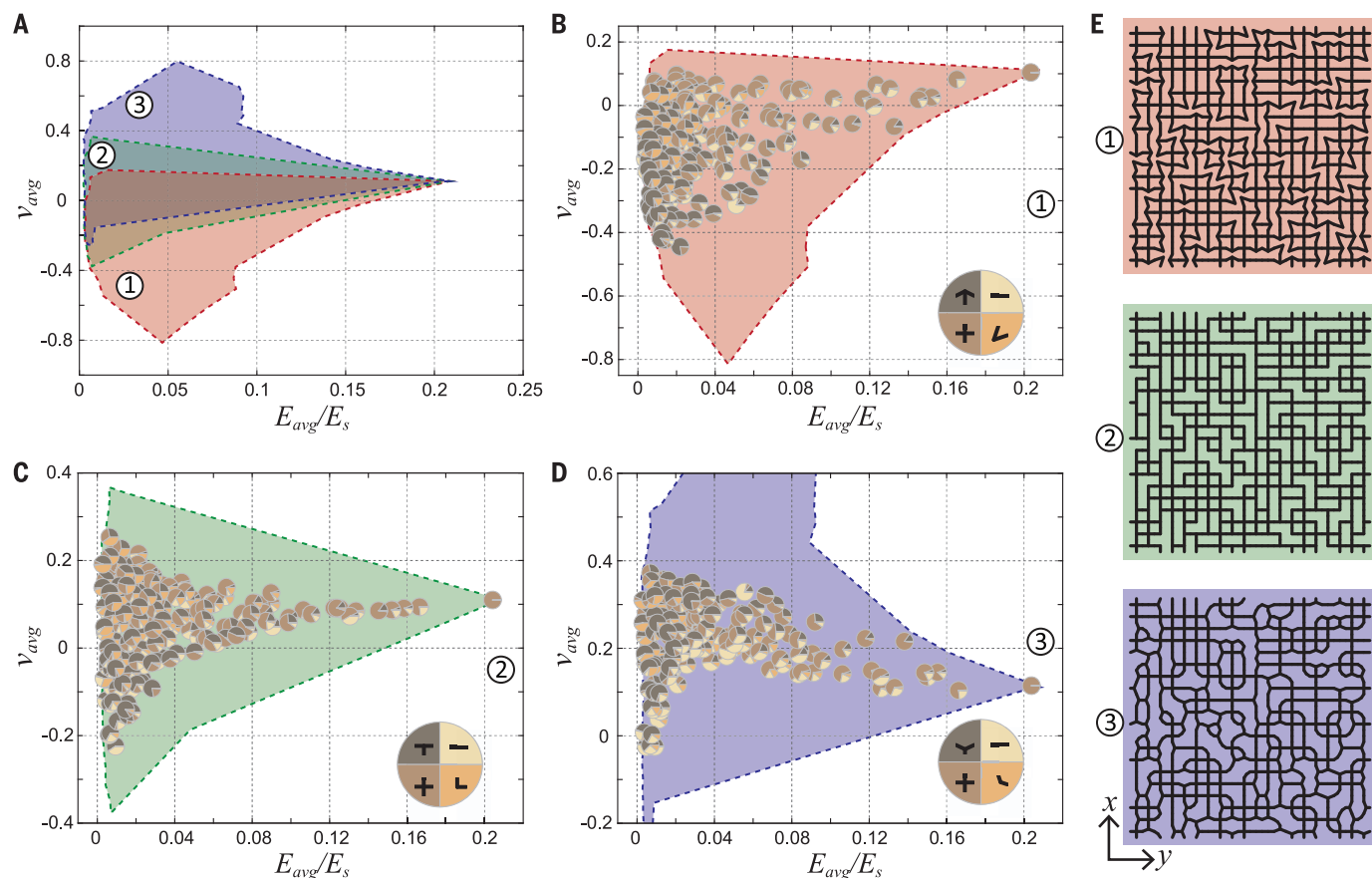
Fig. 4. Decoupled effect of topology and geometry on material properties. (**A**) Ranges of properties covered by three different databases of samples, each obtained with different variants of building blocks. The dashed boundary of each cloud reaches to the extremal values of individual samples. (**B** to **D**) Zoom-in distribution of samples in each database. The pie plots are located at the mean value of a group of 100 samples, with fractions of the pie showing probabilities of appearance of the corresponding building blocks. The insets show the geometries of the basic building blocks and their reference colors in the pie plots. (**E**) Typical designs from each of the three databases are shown, with the background colors matching the colors of the corresponding database.
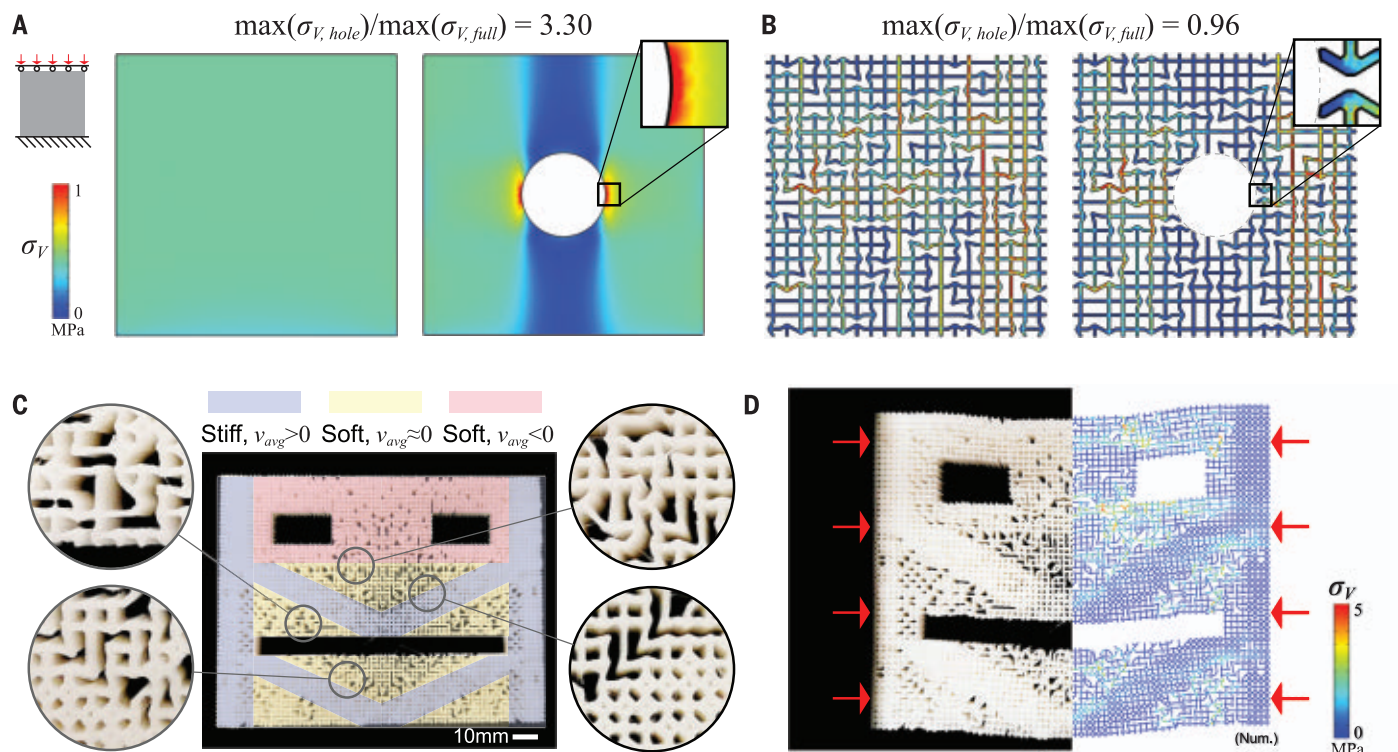
Fig. 5. Redirection of stresses and deformations. (**A** and **B**) Stress distribution in a piece of material compressed by a prescribed displacement, with and without the presence of a hole. (A) Piece of continuum material that has the same elastic properties as the homogenized properties of the irregular sample in (B). (B) Piece of irregular architected material. For all four cases in (A) and (B), the boundary condition and the color scale of Von Mises stress (σ_V) are shown on the left. Insets show a zoom-in view of stress near the hole. (**C** and **D**) Face that "smiles" under lateral compression, owing to its heterogeneous microstructures. (C) 3D printed structure before compression. The false color shades refer to regions generated by different frequency hints that lead to different mechanical properties. The zoomed-in views show the smooth transition between different regions of the microstructure. (D) Structure during compression. The right half shows the stress distribution from numerical simulation. The arrows show the direction of loading.

that of the large 40 by 40 samples. Therefore, for each particular set of inputs to the virtual growth program, we generate 100 material samples on a grid with 20 by 20 nodes and obtain the distribution of mechanical properties by evaluating these 100 samples.

We evaluate 11 groups of architected materials generated by different frequency hints, but with the same basic building blocks and adjacency rules (Fig. 3B). The experimental samples are manufactured by three-dimensional (3D) printing that uses a stiff rubbery material [Semiflex, NinjaTek (38)]. In the examples shown in Fig. 3B, the generated materials exhibit nearly tetragonal symmetry (not isotropic) with similar effective Young's moduli and Poisson's ratio when loaded along the x and y directions (38). Hence, we use their average values, i.e., E_{avg} (average effective Young's modulus) and v_{avg} (average Poisson's ratio), to compare performance of different architected materials' groups. To obtain a dimensionless measurement, E_{avg} is normalized by the Young's modulus of the constituent material (E_S). From the numerical samples (fig. S2), irregular architected materials of the same group tend to cluster together, in different patterns. The marginal distributions of E_{avg} and v_{avg} are shown in Fig. 3C. The experimental samples also follow similar trends in properties' distribution, in agreement with numerical simulations.

To study the structure–property relation determined by the presence of different building blocks, we focus on analyzing the mean values of the clusters (Fig. 3B). We observe that the probabilities of appearance of different building blocks have a distinctive impact on the mechanical properties. For example, a higher probability of the "T"-shaped building block yields a decreasing Poisson's ratio toward negative values but has minimal influence on the material's average Young's modulus. A higher probability of "+"-shaped building block yields a larger Young's modulus, but it has negligible effects on the Poisson's ratio. In addition, a higher probability of both "T"- and "+"-shaped building blocks leads to materials with a relatively high Young's modulus and relatively large negative Poisson's ratio, displaying an additive influence of building block probabilities on mechanical properties. Such trends are robust and remain consistent in both numerical and experimental results. We note that the resultant probabilities of appearance of the building blocks in the generated material samples are slightly different from the input frequency hints. This is due to the constraints imposed by the adjacency rules, as compatibility requirements override the frequency hints (fig. S3).

We observe some hysteresis effects from the experimental stress-strain curves (Fig. 3, D to G). This is likely due to the constituent material's viscoelasticity and large deformation-induced contacts and frictions between nearby elements (fig. S4). Nevertheless, we only focus on the linear regime of the experimental loading curves and extract the value of the Young's modulus in a particular direction, as the secant modulus between 0.005 and 0.015 strain. We use a digital image correlation system to track the deformations and obtain the values of Poisson's ratio (38). The discrepancies between the numerical and experimental results (Fig. 3B) are possibly caused by imperfect boundary conditions (e.g., friction), manufacturing error, and local nonlinear effects. In particular, the group of samples with a high probability of the "—" building block (Fig. 3G) experiences strong nonlinear effects, as the long beams buckle immediately after being loaded. In fact, our experiments show that not only the linear elastic properties but also the nonlinear responses of the samples from the same group tend to behave similarly (fig. S3).
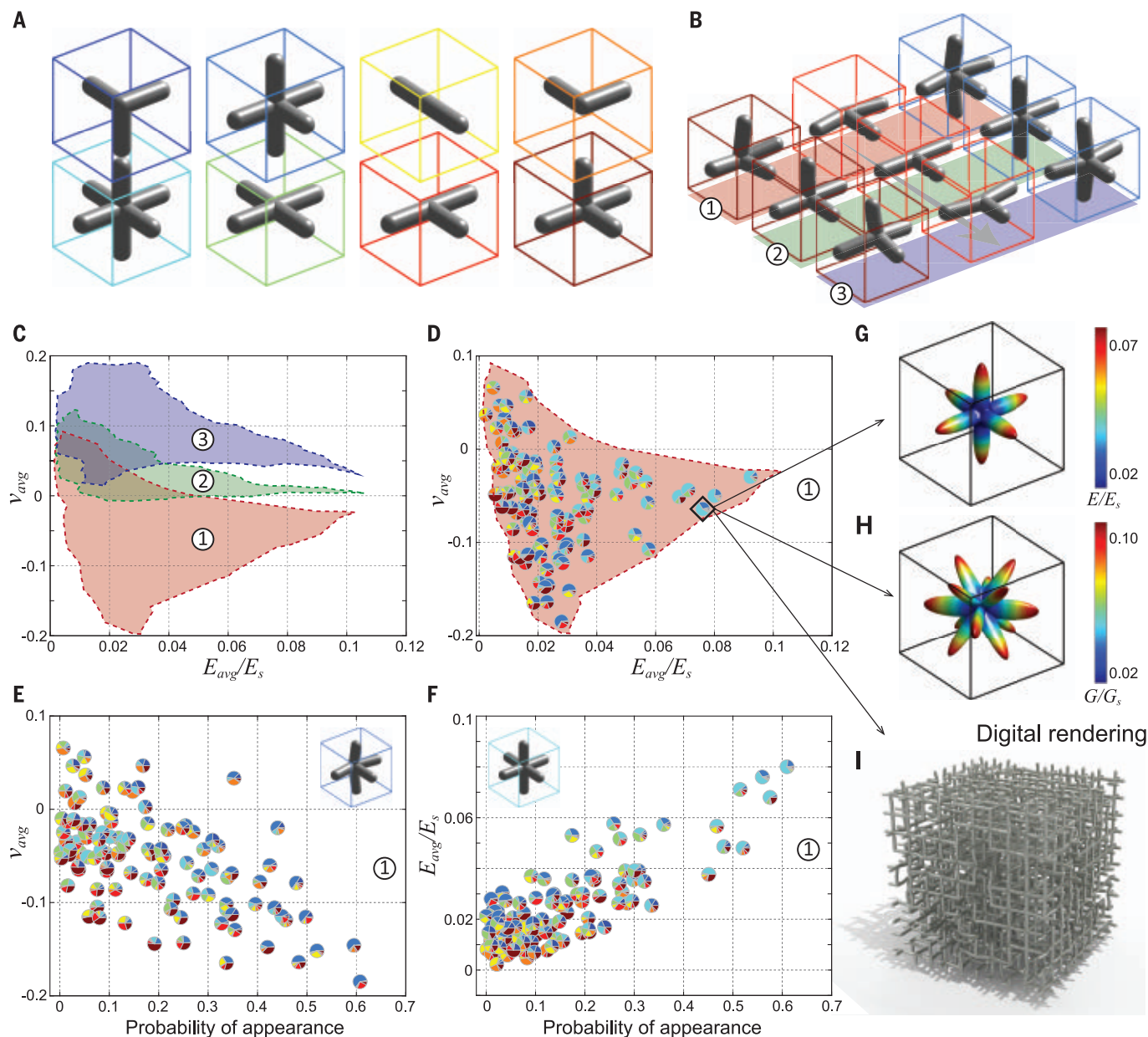
Fig. 6. Extension to 3D irregular microstructures. (**A**) Basic building blocks. (**B**) Three geometric variants of selected building blocks. (**C**) Ranges of properties covered by the generated architected materials. Each cloud corresponds to the database that was generated by using different variants of building blocks in (B). (**D**) Zoom-in distribution of samples in the first database. The pie plots are located at the mean value of a group of 100 samples, with fractions of the pie showing probabilities of appearance of the building blocks within the bounding box of the corresponding color in (A). (**E** and **F**) Influence of the probability of appearance of certain basic building blocks (insets) on different mechanical properties. (**G** and **H**) Directional Young's modulus (E, normalized by E_S, the Young's modulus of the constituent material) and shear modulus (G, normalized by G_s, the shear modulus of the constituent material) of the group of samples marked a diamond box in (D). (**I**) Digital rendering of a material sample in the marked group in (D).

Construction of material databases

The virtual growth program efficiently generates materials that cover a wide range of linear elastic properties (Fig. 3). Hence, it can be used as a tool to explore the design and property space of architected materials by varying inputs. We demonstrate how changing both the topology and geometry of material microstructures (Fig. 4) results in three databases that contain 54,000 samples of architected materials.

The three clouds in different colors refer to the material samples that were generated by using three geometric variants of the building blocks. Each cloud consists of 180 groups of samples generated by 180 different combinations of frequency hints (*38*). The angles of the "T"-shaped and "L"-shaped building blocks are changed from an acute angle to a right angle and to an obtuse angle (Fig. 4, B to D). The red shaded cloud is occupied by the material samples that were generated by using the first set of variants. Because these materials are rich in the "T"-shaped building blocks with a re-entrant acute angle, they mostly appear to be auxetic. As we change the geometries of the building blocks (Fig. 4, C and D), the range of the average Young's modulus remains almost the same, but the Poisson's ratio of the entire cloud shifts toward the positive range (Fig. 4A). An obvious negative correlation is observed between the average Poisson's ratio and the probability of the appearance of the

"T"-shaped building block (fig. S5). In general, the growth rules and mechanical properties present nontrivial yet clear correlations (fig. S5). Typical materials from each of the three clouds of samples are shown in Fig. 4E. Despite the different geometries, these three samples share the same topology because they have the same underlying network, only filled with different building blocks, similar to the examples in Fig. 2.

With the virtual growth program, we can obtain a wide range of irregular, yet programmable, architected materials. The programmable properties result from the nontrivial probability distribution of the stochastic topologies and geometries. The property space can be further expanded. For example, we can introduce directional preferences of the building blocks, which drives the current nearly tetragonal elasticity to orthotropic. Moreover, by adding new building blocks, we can substantially improve the overall shear modulus of the generated materials [see (38) and fig. S6 for elaboration].

One advantage offered by irregular materials is that they offer redundant load paths: When one part of the material is damaged, the stress within the irregular architecture is redistributed through the complex microstructural network. This redistribution ensures that the maximum stress anywhere within material remains almost the same, before and after damage, which prevents a cascading failure. We compare the stress distribution in a continuum and in an irregular architected material, before and after punching a hole in the sample (Fig. 5, A and B). Results of compression tests show that, although the uniform sample shows classical stress concentration near the hole, the irregular material shows no such stress concentration. Rather, the stress in the sample with a hole is redistributed throughout the entire sample without drastic variations in peak stress, compared with peak stress values of the sample without a hole.

Irregular microstructures can be designed to present heterogeneous distributions of local elastic properties (40). For nonperiodic architected materials that are designed from a database of unit cells (24), tessellating different structures and constituent materials while ensuring connectedness and compatibility is challenging (25, 40, 41). By using the virtual growth program, designing materials with inhomogeneous properties is possible with a single, continuous process by assigning different frequency hints to different regions of the sample. With this approach, connectedness and compatibility are automatically guaranteed by the adjacency rules. For instance, we show how it is possible to design an inhomogeneous microstructure that can concentrate deformations in selected areas of a sample. We highlight this ability by designing a "face" that "smiles" when being compressed

from the sides (Fig. 5, C and D). To change the deformation characteristics, we assigned different frequency hints to the different regions on the "face" (Fig. 5C). These sets of frequency hints are extracted from our databases (Fig. 4 and fig. S6).

By defining 3D building blocks (Fig. 6A) and adjacency rules, the virtual growth program can be extended to produce 3D irregular architected materials. Similar to the 2D case, we constructed a database of 33,000 material samples that were based on three different geometric variations on selected building blocks (Fig. 6B) and 110 different frequency hints (Fig. 6, C and D). Each material sample is generated on a 10 by 10 by 10 cubic grid. Each building block is enclosed in a cube of size 5 mm by 5 mm by 5 mm, and the lattice (beam) members are assumed to be circular, with a radius of 1 mm. We observe interesting correlations between the probabilities of appearance of building blocks and the mechanical properties (Fig. 6, E and F, and figs. S7 to S9). The anisotropy of the generated materials can be seen from the directional Young's modulus and shear modulus (Fig. 6, G and H) as a result of our particular selection of basic building blocks. A rendered image of a typical sample highlights the 3D irregular architecture (Fig. 6I).

Discussion and outlook

We describe fundamental, probabilistic rules that control the overall mechanical response of irregular materials. Our approach establishes a general, graph-based representation of material microstructures, which we use to create architected materials with functionally graded properties and to demonstrate robustness against damage. In the future, the approach could be further extended to design materials with prespecified properties by incorporating optimization approaches in the selection of building blocks and/or in the adjacency rules for growth. The basic building blocks could also be selected to have more geometries (e.g., learned from data), different constitutive materials, and dimensional scales (e.g., to realize hierarchical materials). The underlying graph, which in this work is represented as squared or cubic grids, can be extended to have more complex connectivity. Because the virtual growth program is independent from any particular material properties, it is readily applicable to discover nonlinear and multiphysical properties of materials.

REFERENCES AND NOTES

1. K. Bertoldi, V. Vitelli, J. Christensen, M. van Hecke, *Nat. Rev. Mater.* **2**, 17066 (2017).
2. H. Nassar et al., *Nat. Rev. Mater.* **5**, 667–685 (2020).
3. L. Wu et al., *Mater. Today* **44**, 168–193 (2021).
4. N. A. Fleck, V. S. Deshpande, M. F. Ashby, *Proc. R. Soc. A Math. Phys. Eng. Sci.* **466**, 2495–2516 (2010).
5. L. A. Shaw et al., *Nat. Commun.* **10**, 291 (2019).
6. Z. Vértesy et al., *J. Microsc.* **224**, 108–110 (2006).
7. D. Schurig et al., *Science* **314**, 977–980 (2006).
8. W. Man et al., *Proc. Natl. Acad. Sci. U.S.A.* **110**, 15886–15891 (2013).
9. M. I. Hussein, M. J. Leamy, M. Ruzzene, *Appl. Mech. Rev.* **66**, 040802 (2014).
10. J. I. Lipton et al., *Science* **360**, 632–635 (2018).
11. C. Luo et al., *Mater. Horiz.* **7**, 229–235 (2020).
12. M. Skouras, B. Thomaszewski, S. Coros, B. Bickel, M. Gross, *ACM Trans. Graph.* **32**, 1–10 (2013).
13. G. W. Milton, A. V. Cherkaev, *J. Eng. Mater. Technol.* **117**, 483–493 (1995).
14. Q. Wang et al., *Phys. Rev. Lett.* **117**, 175901 (2016).
15. P. P. Pratapa, K. Liu, G. H. Paulino, *Phys. Rev. Lett.* **122**, 155501 (2019).
16. L. R. Meza, S. Das, J. R. Greer, *Science* **345**, 1322–1326 (2014).
17. X. Zhang, A. Vyatskikh, H. Gao, J. R. Greer, X. Li, *Proc. Natl. Acad. Sci. U.S.A.* **116**, 6665–6672 (2019).
18. S. S. Injeti, C. Daraio, K. Bhattacharya, *Proc. Natl. Acad. Sci. U.S.A.* **116**, 23960–23965 (2019).
19. M. Kadic, T. Bückmann, N. Stenger, M. Thiel, M. Wegener, *Appl. Phys. Lett.* **100**, 191901 (2012).
20. T. Frenzel, M. Kadic, M. Wegener, *Science* **358**, 1072–1074 (2017).
21. D. Yang et al., *Extreme Mech. Lett.* **6**, 1–9 (2016).
22. Y. Mao, Q. He, X. Zhao, *Sci. Adv.* **6**, eaaz4169 (2020).
23. D. Chen, M. Skouras, B. Zhu, W. Matusik, *Sci. Adv.* **4**, eaao7005 (2018).
24. C. Schumacher et al., *ACM Trans. Graph.* **34**, 1–13 (2015).
25. E. D. Sanders, A. Pereira, G. H. Paulino, *Sci. Adv.* **7**, eabf4838 (2021).
26. J. Song et al., *Nature* **554**, 224–228 (2018).
27. H. Gao, B. Ji, I. L. Jäger, E. Arzt, P. Fratzl, *Proc. Natl. Acad. Sci. U.S.A.* **100**, 5597–5600 (2003).
28. A. Heyde, L. Guo, C. Jost, G. Theraulaz, L. Mahadevan, *Proc. Natl. Acad. Sci. U.S.A.* **118**, e2006985118 (2021).
29. A. M. Torres et al., *Proc. Natl. Acad. Sci. U.S.A.* **116**, 24457–24462 (2019).
30. D. S. Wiersma, *Nat. Photonics* **7**, 188–196 (2013).
31. Z. Liu, Y. Huang, *Protein Sci.* **23**, 539–550 (2014).
32. S. Kumar, S. Tan, L. Zheng, D. M. Kochmann, *npj Comput Mater.* **6**, 73 (2020).
33. D. R. Reid et al., *Proc. Natl. Acad. Sci. U.S.A.* **115**, E1384–E1390 (2018).
34. M. J. Mirzaali, H. Pahlavani, A. A. Zadpoor, *Appl. Phys. Lett.* **115**, 021901 (2019).
35. Y. Zhang, M.-T. Hsieh, L. Valdevit, *Compos. Struct.* **263**, 113693 (2021).
36. F. V. Senhora, E. D. Sanders, G. H. Paulino, *Adv. Mater.* **34**, e2109304 (2022).
37. M. Gumin, *WaveFunctionCollapse* (2021); https://github.com/mxgmn/WaveFunctionCollapse.
38. Materials and methods are available as Supplementary Materials.
39. X. Yin, W. Chen, A. To, C. McVeigh, W. K. Liu, *Comput. Methods Appl. Mech. Eng.* **197**, 3516–3529 (2008).
40. C. Coulais, E. Teomy, K. de Reus, Y. Shokef, M. van Hecke, *Nature* **535**, 529–532 (2016).
41. L. Wang et al., *Proc. Natl. Acad. Sci. U.S.A.* **119**, e2122185119 (2022).

HUMAN GENETICS

Ancient DNA from Mesopotamia suggests distinct Pre-Pottery and Pottery Neolithic migrations into Anatolia

Iosif Lazaridis[1,2]*†, Songül Alpaslan-Roodenberg[2,3]*†, Ayşe Acar[4], Ayşen Açıkkol[5], Anagnostis Agelarakis[6], Levon Aghikyan[7], Uğur Akyüz[8], Desislava Andreeva[9], Gojko Andrijašević[10], Dragana Antonović[11], Ian Armit[12], Alper Atmaca[13], Pavel Avetisyan[7], Ahmet İhsan Aytek[14], Krum Bacvarov[15], Ruben Badalyan[7], Stefan Bakardzhiev[16], Jacqueline Balen[17], Lorenc Bejko[18], Rebecca Bernardos[2], Andreas Bertsatos[19], Hanifi Biber[20], Ahmet Bilir[21], Mario Bodružić[22], Michelle Bonogofsky[23], Clive Bonsall[24], Dušan Borić[25], Nikola Borovinić[26], Guillermo Bravo Morante[3], Katharina Buttinger[3], Kim Callan[2,27], Francesca Candilio[28], Mario Carić[29], Olivia Cheronet[3], Stefan Chohadzhiev[30], Maria-Eleni Chovalopoulou[19], Stella Chryssoulaki[31], Ion Ciobanu[32,33], Natalija Čondić[34], Mihai Constantinescu[35], Emanuela Cristiani[36], Brendan J. Culleton[37], Elizabeth Curtis[2,27], Jack Davis[38], Tatiana I. Demcenco[39], Valentin Dergachev[40], Zafer Derin[41], Sylvia Deskaj[42], Seda Devejyan[7], Vojislav Djordjević[43], Kellie Sara Duffett Carlson[3], Laurie R. Eccles[44], Nedko Elenski[45], Atilla Engin[46], Nihat Erdoğan[47], Sabiha Erir-Pazarcı[48], Daniel M. Fernandes[3,49], Matthew Ferry[2,27], Suzanne Freilich[3], Alin Frînculeasa[50], Michael L. Galaty[42], Beatriz Gamarra[51,52,53], Boris Gasparyan[7], Bisserka Gaydarska[54], Elif Genç[55], Timur Gültekin[56], Serkan Gündüz[57], Tamás Hajdu[58], Volker Heyd[59], Suren Hobosyan[7], Nelli Hovhannisyan[60], Iliya Iliev[16], Lora Iliev[1,27], Stanislav Iliev[61], İlkay İvgin[62], Ivor Janković[29], Lence Jovanova[63], Panagiotis Karkanas[64], Berna Kavaz-Kındığılı[65], Esra Hilal Kaya[66], Denise Keating[3], Douglas J. Kennett[37,67], Seda Deniz Kesici[68], Anahit Khudaverdyan[7], Krisztián Kiss[58,69], Sinan Kılıç[20], Paul Klostermann[70], Sinem Kostak Boca Negra Valdes[68], Saša Kovačević[71], Marta Krenz-Niedbała[72], Maja Krznarić Škrivanko[73], Rovena Kurti[74], Pasko Kuzman[75], Ann Marie Lawson[2,27], Catalin Lazar[76], Krassimir Leshtakov[77], Thomas E. Levy[78], Ioannis Liritzis[79,80], Kirsi O. Lorentz[81], Sylwia Łukasik[72], Matthew Mah[2,27,82], Swapan Mallick[2,27], Kirsten Mandl[3], Kristine Martirosyan-Olshansky[83], Roger Matthews[84], Wendy Matthews[84], Kathleen McSweeney[24], Varduhi Melikyan[7], Adam Micco[2], Megan Michel[1,2,27], Lidija Milašinović[85], Alissa Mittnik[1,2,86], Janet M. Monge[87], Georgi Nekhrizov[15], Rebecca Nicholls[88], Alexey G. Nikitin[89], Vassil Nikolov[15], Mario Novak[29], Iñigo Olalde[2,90], Jonas Oppenheimer[2,27], Anna Osterholtz[91], Celal Özdemir[13], Kadir Toykan Özdoğan[3], Nurettin Öztürk[65], Nikos Papadimitriou[92], Niki Papakonstantinou[93], Anastasia Papathanasiou[94], Lujana Paraman[95], Evgeny G. Paskary[96], Nick Patterson[1,82], Ilian Petrakiev[45], Levon Petrosyan[7], Vanya Petrova[77], Anna Philippa-Touchais[97], Ashot Piliposyan[98], Nada Pocuca Kuzman[75], Hrvoje Potrebica[99], Bianca Preda-Bălănică[59], Zrinka Premužić[100], T. Douglas Price[101], Lijun Qiu[2,27], Siniša Radović[102], Kamal Raeuf Aziz[103], Petra Rajić Šikanjić[29], Kamal Rasheed Raheem[103], Sergei Razumov[104], Amy Richardson[84], Jacob Roodenberg[105], Rudenc Ruka[74], Victoria Russeva[106], Mustafa Şahin[57], Ayşegül Şarbak[107], Emre Savaş[68], Constanze Schattke[3], Lynne Schepartz[108], Tayfun Selçuk[68], Ayla Sevim-Erol[109], Michel Shamoon-Pour[110], Henry M. Shephard[111], Athanasios Sideris[112], Angela Simalcsik[32,113], Hakob Simonyan[114], Vitalij Sinika[104], Kendra Sirak[2], Ghenadie Sirbu[115], Mario Šlaus[116], Andrei Soficaru[35], Bilal Söğüt[117], Arkadiusz Sołtysiak[118], Çilem Sönmez-Sözer[109], Maria Stathi[119], Martin Steskal[120], Kristin Stewardson[2,27], Sharon Stocker[38], Fadime Suata-Alpaslan[121], Alexander Suvorov[59], Anna Szécsényi-Nagy[122], Tamás Szeniczey[58], Nikolai Telnov[104], Strahil Temov[123], Nadezhda Todorova[77], Ulsi Tota[74,124], Gilles Touchais[125], Sevi Triantaphyllou[93], Atila Türker[126], Marina Ugarković[71], Todor Valchev[16], Fanica Veljanovska[123], Zlatko Videvski[123], Cristian Virag[127], Anna Wagner[3], Sam Walsh[128], Piotr Włodarczak[129], J. Noah Workman[2], Aram Yardumian[130,131], Evgenii Yarovoy[132], Alper Yener Yavuz[133], Hakan Yılmaz[20], Fatma Zalzala[2,27], Anna Zettl[3], Zhao Zhang[2], Rafet Çavuşoğlu[20], Nadin Rohland[2], Ron Pinhasi[3,134]*, David Reich[1,2,27,82]*

We present the first ancient DNA data from the Pre-Pottery Neolithic of Mesopotamia (Southeastern Turkey and Northern Iraq), Cyprus, and the Northwestern Zagros, along with the first data from Neolithic Armenia. We show that these and neighboring populations were formed through admixture of pre-Neolithic sources related to Anatolian, Caucasus, and Levantine hunter-gatherers, forming a Neolithic continuum of ancestry mirroring the geography of West Asia. By analyzing Pre-Pottery and Pottery Neolithic populations of Anatolia, we show that the former were derived from admixture between Mesopotamian-related and local Epipaleolithic-related sources, but the latter experienced additional Levantine-related gene flow, thus documenting at least two pulses of migration from the Fertile Crescent heartland to the early farmers of Anatolia.

Previous work has documented the existence of highly differentiated Neolithic populations in ancient West Asia (1–9) and some of their pre-Neolithic antecessors in the Caucasus (10), Iran (1, 11), Anatolia (6), and the Levant (1). To anchor our integrative genomic history of the Southern Arc, a region we define as including Anatolia and its neighbors in Southeastern Europe and West Asia (12), we sought to understand how the earliest Neolithic populations were formed, with a particular focus on the Pre-Pottery period of Northern (or Upper) Mesopotamia, the area between the Tigris and Euphrates rivers of Southeastern Turkey, Northwestern Iraq, and Northeastern Syria, within the Pre-Pottery Neolithic interaction sphere (13). Despite the centrality of Mesopotamia in the archaeolog-

ical record of the origin of farming (14), no genome-wide ancient DNA data from early Mesopotamian farmers has been published. We used in-solution enrichment for ~1.2 million single nucleotide polymorphisms (SNPs) to study Pre-Pottery Neolithic farmers from the Tigris side of Northern Mesopotamia: one from Boncuklu Tarla near Mardin in Southeastern Turkey and two from Nemrik 9 in Northern Iraq. We also report the first Pre-Pottery Neolithic data from Cyprus, an island to the south of the Anatolian peninsula and west of the Levant, which witnessed the earliest maritime expansion of Pre-Pottery farmers from the Eastern Mediterranean; our data come from three individuals whose fragmentary remains were found in a Neolithic disused and filled-in water well at Kissonerga-Mylouthkia

(15). Furthermore, we report the first ancient DNA data from the Neolithic of Armenia, from two individuals buried at the sites of Masis Blur and Aknashen in the sixth millennium BCE. These individuals represent an inland Pottery Neolithic population, which we could compare to the Pre-Pottery one from Northern Mesopotamia to its south, the Pottery Neolithic one of Azerbaijan to its east (7), and later Chalcolithic individuals from Armenia (1). Finally, we sampled three Pre-Pottery Neolithic farmers from the Northern Zagros at Bestansur and the Zawi Chemi component of Shanidar cave in Iraq, who fill a gap between the more western and northern individuals and published data from the Central Zagros in Iran (1).

Details of the newly sampled individuals can be found in (12), and their geographical and

temporal distributions can be seen in Fig. 1. To improve the statistical power of our analyses, we also increased data quality for a number of individuals with previously reported data, making and sequencing additional ancient DNA libraries from four Epipaleolithic Natufians from Israel, six Pre-Pottery Neolithic individuals from Jordan (1), and nine Neolithic individuals from the Eastern Marmara region (Northwest Anatolia, sites of Barcın and Menteşe) (2). From Eastern Marmara, we also

sampled an individual from Barcın and two from the previously unsampled site of Ilıpınar. Individuals from the three sites were genetically similar, and we analyze them, together with later Chalcolithic individuals from the same site, in a study of later periods of Anatolia (12).

We carried out principal components analysis (PCA) (16) (Fig. 2A), projecting the ancient individuals onto the variation of present-day West Eurasians (17). Two main clusters emerge: an "Eastern Mediterranean" Anatolian/Levantine

cluster that also includes the geographically intermediate individuals from Cyprus, and an "inland" Zagros-Caucasus-Mesopotamia-Armenia-Azerbaijan cluster. There is structure within these groupings. Anatolian individuals group with each other and with those from Cyprus, whereas Levantine individuals are distinct. Within the inland cluster, individuals that are more geographically distant from the Mediterranean, such as those from the South Caucasus [Caucasus hunter-gatherers

[1]Department of Human Evolutionary Biology, Harvard University, Cambridge, MA 02138, USA. [2]Department of Genetics, Harvard Medical School, Boston, MA 02115, USA. [3]Department of Evolutionary Anthropology, University of Vienna, 1030 Vienna, Austria. [4]Department of Anthropology, Faculty of Letters, Mardin Artuklu University, 47510 Artuklu, Mardin, Turkey. [5]Department of Anthropology, Faculty of Letters, Sivas Cumhuriyet University, 58140 Sivas, Turkey. [6]Department of History, Adelphi University, Garden City, NY 11530, USA. [7]Institute of Archaeology and Ethnography, NAS RA, 0025 Yerevan, Armenia. [8]Samsun Museum of Archeology and Ethnography, Kale Mahallesi, Merkez, İlkadım, 55030 Samsun, Turkey. [9]Iskra Museum of History, 6100 Kazanlak, Bulgaria. [10]Historical Musem in Kotor, 85330 Kotor, Montenegro. [11]Institute of Archaeology, 11000 Belgrade, Serbia. [12]Department of Archaeology, University of York, York YO1 7EP, UK. [13]Amasya Archaeology Museum, Mustafa Kemal Paşa Caddesi, 05000 Amasya, Turkey. [14]Department of Anthropology, Faculty of Arts and Science, Burdur Mehmet Akif University, 15100 Burdur, Turkey. [15]National Institute of Archaeology and Museum, Bulgarian Academy of Sciences, 1000 Sofia, Bulgaria. [16]Yambol Regional Historical Museum, 8600 Yambol, Bulgaria. [17]Archaeological Museum in Zagreb, 10000 Zagreb, Croatia. [18]Department of Archaeology and Heritage Studies, University of Tirana, 1010 Tirana, Albania. [19]Department of Animal and Human Physiology, Faculty of Biology, School of Sciences, National and Kapodistrian University of Athens, 10679 Athens, Greece. [20]Department of Archaeology, Faculty of Humanities, Van Yüzüncü Yıl University, 65090 Tuşba, Van, Turkey. [21]Department of Archaeology, Faculty of Science and Letters, Düzce University, 81620 Düzce, Turkey. [22]Stratum Ltd., 21218 Seget Donji, Croatia. [23]Independent Researcher, Berkeley, CA 94720, USA. [24]School of History, Classics and Archaeology, University of Edinburgh, Edinburgh EH8 9AG, UK. [25]The Italian Academy for Advanced Studies in America, Columbia University, New York, NY 10027, USA. [26]Center for Conservation and Archaeology of Montenegro, 81250 Cetinje, Montenegro. [27]Howard Hughes Medical Institute, Harvard Medical School, Boston, MA 02115, USA. [28]Servizio di Bioarcheologia, Museo delle Civiltà, 00144 Rome, Italy. [29]Centre for Applied Bioanthropology, Institute for Anthropological Research, 10000 Zagreb, Croatia. [30]Department of Archaeology, University of Veliko Tarnovo "St. Cyril and St. Methodius," 5003 Veliko Tarnovo, Bulgaria. [31]Hellenic Ministry of Culture and Sports, Ephorate of Antiquities of Piraeus and the Islands, 10682 Piraeus, Greece. [32]"Orheiul Vechi" Cultural-Natural Reserve, Institute of Bioarchaeological and Ethnocultural Research, 3552 Butuceni, Moldova. [33]National Archaeological Agency, 2012 Chişinău, Moldova. [34]Archaeological Museum in Zadar, 23000 Zadar, Croatia. [35]"Francisc I. Rainer" Institute of Anthropology, 050711 Bucharest, Romania. [36]Department of Oral and Maxillo-Facial Sciences, Sapienza University of Rome, 00161 Rome, Italy. [37]Institutes of Energy and the Environment, The Pennsylvania State University, University Park, PA 16802, USA. [38]Department of Classics, University of Cincinnati, Cincinnati, OH 45221, USA. [39]Independent Researcher, Aberystwyth SY23 4UH, UK. [40]Center of Archaeology, Institute of Cultural Heritage, Academy of Science of Moldova, 2001 Chişinău, Moldova. [41]Department of Archaeology, Faculty of Letters, Ege University, 35100 Bornova-Izmir, Turkey. [42]Museum of Anthropological Archaeology, University of Michigan, Ann Arbor, MI 48109, USA. [43]Narodni muzej Panččevo, 26101 Pančevo, Serbia. [44]Human Paleoecology and Isotope Geochemistry Lab, Department of Anthropology, The Pennsylvania State University, University Park, PA 16802, USA. [45]Regional Museum of History – Veliko Tarnovo, 5000 Veliko Tarnovo, Bulgaria. [46]Department of Archaeology, Faculty of Science and Letters, Gaziantep University, 27310 Gaziantep, Turkey. [47]Mardin Archaeological Museum, Şar, Cumhuriyet Meydanı üstü, 47100 Artuklu, Mardin, Turkey. [48]Muğla İl Kültür ve Turizm Müdürlüğü, 48000 Muğla, Turkey. [49]Research Centre for Anthropology and Health (CIAS), Department of Life Sciences, University of Coimbra, 3000-456 Coimbra, Portugal. [50]Prahova County Museum of History and Archaeology, 100042 Ploieşti, Romania. [51]Institut Català de Paleoecologia Humana i Evolució Social, 43007 Tarragona, Spain. [52]Departament d'Història i Història de l'Art, Universitat Rovira i Virgili, 43002 Tarragona, Spain. [53]School of Archaeology and Earth Institute, University College Dublin, Belfield, Dublin 4, Ireland. [54]Department of Archaeology, Durham University, Durham DH1 3LE, UK. [55]Department of Archaeology, Faculty of Science and Letters, Çukurova University, 01330 Balçalı-Sarıçam-Adana, Turkey. [56]Department of Anthropology, Faculty of Humanities, Ankara University, 06100 Sıhhiye, Ankara, Turkey. [57]Department of Archaeology, Faculty of Science and Letters, Bursa Uludağ University, 16059 Görükle, Bursa, Turkey. [58]Department of Biological Anthropology, Institute of Biology, Eötvös Loránd University, 1053 Budapest, Hungary. [59]Department of Cultures, University of Helsinki, 00100 Helsinki, Finland. [60]Department of Ecology and Nature Protection, Yerevan State University, 0025 Yerevan, Armenia. [61]Regional Museum of History, 6300 Haskovo, Bulgaria. [62]Ministry of Culture and Tourism, İsmet İnönü Bulvarı, 06100 Emek, Ankara, Turkey. [63]Museum of the City of Skopje, 1000 Skopje, North Macedonia. [64]Malcolm H. Wiener Laboratory, American School of Classical Studies at Athens, 10676 Athens, Greece. [65]Department of Archaeology, Faculty of Letters, Atatürk University, 25100 Erzurum, Turkey. [66]Muğla Archaeological Museum and Yatağan Thermal Power Generation Company, Rescue Excavations, 48000 Muğla, Turkey. [67]Department of Anthropology, University of California, Santa Barbara, Santa Barbara, CA 93106, USA. [68]Bodrum Museum of Underwater Archeology, Çarşı Neighbourhood, 48400 Bodrum, Muğla, Turkey. [69]Department of Anthropology, Hungarian Natural History Museum, 1117 Budapest, Hungary. [70]Department of Anthropology, Natural History Museum Vienna, 1010 Vienna, Austria. [71]Institute of Archaeology, 10000 Zagreb, Croatia. [72]Faculty of Biology, Adam Mickiewicz University in Poznań, 61-614 Poznań, Poland. [73]Municipal Museum Vinkovci, 32100 Vinkovci, Croatia. [74]Prehistory Department, Albanian Institute of Archaeology, Academy of Albanian Studies, 1000 Tirana, Albania. [75]National Museum in Ohrid, 6000 Ohrid, North Macedonia. [76]ArchaeoSciences Division, Research Institute of the University of Bucharest, University of Bucharest, 050663 Bucharest, Romania. [77]Department of Archaeology, St. Kliment Ohridski University of Sofia, 1504 Sofia, Bulgaria. [78]Department of Anthropology, University of California, San Diego, La Jolla, CA 92093, USA. [79]Key Research Institute of Yellow River Civilization and Sustainable Development and the Collaborative Innovation Center on Yellow River Civilization of Henan Province, Laboratory of Yellow River Cultural Heritage, Henan University, 475001 Kaifeng, China. [80]European Academy of Sciences and Arts, 5020 Salzburg, Austria. [81]Science and Technology in Archaeology and Culture Research Center, The Cyprus Institute, 2121 Aglantzia, Nicosia, Cyprus. [82]Broad Institute of Harvard and MIT, Cambridge, MA 02142, USA. [83]Cotsen Institute of Archaeology, University of California, Los Angeles, Los Angeles, CA 90095, USA. [84]Department of Archaeology, University of Reading, Reading RG6 6AB, UK. [85]National Museum of Kikinda, 23300 Kikinda, Serbia. [86]Department of Archaeogenetics, Max Planck Institute for Evolutionary Anthropology, 04103 Leipzig, Germany. [87]University of Pennsylvania Museum of Archaeology and Anthropology, Philadelphia, PA 19104, USA. [88]School of Archaeological and Forensic Sciences, Faculty of Life Sciences, University of Bradford, Bradford BD7 1DP, UK. [89]Department of Biology, Grand Valley State University, Allendale, MI 49401, USA. [90]BIOMICs Research Group, University of the Basque Country UPV/EHU, 01006 Vitoria-Gasteiz, Spain. [91]Department of Anthropology and Middle Eastern Cultures, Mississippi State University, Mississippi State, MS 39762, USA. [92]Paul and Alexandra Canellopoulos Museum, 105-55 Athens, Greece. [93]Faculty of Philosophy, School of History and Archaeology, Aristotle University of Thessaloniki, 54124 Thessaloniki, Greece. [94]Ephorate of Paleoanthropology and Speleology, Greek Ministry of Culture, 11636 Athens, Greece. [95]Trogir Town Museum, 21220 Trogir, Croatia. [96]Moldovan Historic - Geographical Society, 2044 Chişinău, Moldova. [97]French School of Archaeology at Athens, 10680 Athens, Greece. [98]Armenian State Pedagogical University After Khachatur Abovyan, 0010 Yerevan, Armenia. [99]Department of Archaeology, Faculty of Humanities and Social Sciences, University of Zagreb, 10000 Zagreb, Croatia. [100]Independent Researcher, 10000 Zagreb, Croatia. [101]Laboratory for Archaeological Chemistry, University of Wisconsin–Madison, Madison, WI 53706, USA. [102]Institute for Quaternary Paleontology and Geology, Croatian Academy of Sciences and Arts, 10000 Zagreb, Croatia. [103]Sulaymaniyah Directorate of Antiquities and Heritage, Sulaimaniyah, Iraq. [104]Pridnestrovian University named after Taras Shevchenko, 3300 Tiraspol, Moldova. [105]The Netherlands Institute for the Near East, 2311 Leiden, Netherlands. [106]Institute of Experimental Morphology, Pathology and Archeology with Museum, Bulgarian Academy of Science, 1113 Sofia, Bulgaria. [107]Department of Anthropology, Faculty of Science and Letters, Hitit University, 19040 Çorum, Turkey. [108]School of Anatomical Sciences, The University of the Witwatersrand, 2193 Johannesburg, South Africa. [109]Department of Anthropology, Faculty of Language and History - Geography, Ankara University, 06100 Sıhhiye, Ankara, Turkey [110]Department of Anthropology, Binghamton University, Binghamton, NY 13902, USA. [111]Archaeological Institute of America, Boston, MA 02108, USA. [112]Institute of Classical Archaeology, Charles University, 11636 Prague, Czechia. [113]"Olga Necrasov" Centre of Anthropological Research, Romanian Academy Iaşi Branch, 2012 Iaşi Romania. [114]Scientific Research Center of the Historical and Cultural Heritage, 0010 Yerevan, Armenia. [115]Thracology Scientific Research Laboratory of the State University of Moldova, Department of Academic Management, Academy of Science of Moldova, 2009 Chişinău, Moldova. [116]Anthropological Center of the Croatian Academy of Sciences and Arts, 10000 Zagreb, Croatia. [117]Department of Archaeology, Faculty of Science and Arts, Pamukkale University, 20070 Denizli, Turkey. [118]Faculty of Archaeology, University of Warsaw, 00-927 Warszawa, Poland. [119]Ephorate of Antiquities of East Attica, Ministry of Culture and Sports, 10682 Athens, Greece. [120]Austrian Archaeological Institute at the Austrian Academy of Sciences, 1190 Vienna, Austria. [121]Department of Anthropology, Faculty of Letters, Istanbul University, 34134 Istanbul, Turkey. [122]Institute of Archaeogenomics, Research Centre for the Humanities, Eötvös Loránd Research Network, 1097 Budapest, Hungary. [123]Archaeology Museum of North Macedonia, 1000 Skopje, North Macedonia. [124]Culture and Patrimony Department, University of Avignon, 84029 Avignon, France. [125]Department of the History of Art and Archaeology, Université Paris 1 Panthéon-Sorbonne, 75006 Paris, France. [126]Department of Archaeology, Faculty of Science and Letters, Ondokuz Mayıs University, 55139 Atakum-Samsun, Turkey. [127]Satu Mare County Museum, 440031 Satu Mare, Romania. [128]School of Natural Sciences, University of Central Lancashire, Preston PR1 2HE, UK. [129]Institute of Archaeology and Ethnology, Polish Academy of Sciences, 31-016 Kraków, Poland. [130]Department of History and Social Sciences, Bryn Athyn College, Bryn Athyn, PA 19009, USA. [131]Penn Museum, University of Pennsylvania, Philadelphia, PA 19104, USA. [132]History of the Ancient World and Middle Ages Department, Moscow Region State University, Moscow Region, 141014 Mytishi, Russia. [133]Department of Anthropology, Burdur Mehmet Akif Ersoy University, Istiklal Campus, 15100 Burdur, Turkey. [134]Human Evolution and Archaeological Sciences, University of Vienna, 1030 Vienna, Austria.
*Corresponding author. Email: lazaridis@genetics.med.harvard.edu (I.La.); msglalpaslan@gmail.com (S.A.-R.); ron.pinhasi@univie.ac.at (R.P.); reich@genetics.med.harvard.edu (D.R.)
†These authors contributed equally to this work.

Fig. 1. Studied individuals. (**A**) Time frame of Pre-Neolithic, Pre-Pottery Neolithic, and Pottery Neolithic populations in West Asia. (**B**) Geographical location of populations from (A) shown on the map of West Asia.

from Georgia (10) and Ganj Dareh from Central Zagros], are also genetically more distant as compared with the geographically and genetically intermediate individuals from Mesopotamia and Armenia/Azerbaijan. The Eastern Mediterranean and inland clusters are separated by a gap in Fig. 2A, which may correspond to geographically intermediate areas between sampling locations, for example, the Euphrates region of North Mesopotamia. The totality of Neolithic West Asia is enclosed within the range of variation of the quadrangle formed by Caucasus hunter-gatherers, Ganj Dareh, Levantine Natufians (1) from Israel, and Epipaleolithic Pınarbaşı (6) from Central Anatolia.

In a linked study, we developed a mathematical framework for estimating the ancestry proportions of individuals of the entire Southern Arc across space and time with a common metric (12), and here we discuss the results of applying this model to the Neolithic period (Fig. 2B). This model includes Caucasus hunter-gatherers (10), Eastern European hunter-gatherers (2, 18), Levantine Pre-Pottery Neolithic (1), Balkan hunter-gatherers from the Iron Gates in Serbia (19), and Anatolian Neolithic [from Barcın in the Marmara region of Northwest (NW) Anatolia (2)] as surrogates for five ancestry sources. Within this framework, the highest proportion of Anatolian Neolithic-related ancestry is observed in Neolithic Anatolian populations as well as the early farmers of Cyprus. The Balkan hunter-gatherer-related affinity in the Pre-Pottery population at Boncuklu and the Epipaleolithic one from Pınarbaşı—both of which predate the Pottery Neolithic from Barcın by thousands of years—does not indicate that these older individuals were admixed with European hunter-gatherers. Rather, it reflects the fact that in comparison to the Barcın population, both Pınarbaşı and Boncuklu were "less Levantine" (Fig. 2A), a finding that is consistent with the Levantine influx into the Pottery Neolithic populations that is revealed by the analysis that follows. A con-

trasting case is that of the Natufians, who are inferred to be "more Levantine" (along the Anatolian/Levantine cline) and are unsurprisingly inferred to derive all of their ancestry from the Levant Pre-Pottery Neolithic source; this of course does not mean that the earlier Natufians are descended from the Pre-Pottery Neolithic farmers that followed them but rather that both share ancestry (in reality, from the Natufians to the Pre-Pottery Neolithic farmers), which is modeled in this way within the limitations of the five-way model. Similarly, the Ganj Dareh population (most extreme) of the inland group derives all its ancestry from the Caucasus hunter-gatherer source used in the five-way model, and Caucasus hunter-gatherer–related ancestry levels are high in all inland populations, that is, of the Northern Zagros, Armenia, and Azerbaijan, as well as those of North Mesopotamia.

The high Anatolian-related ancestry in Cyprus revealed by this model (Fig. 2) and subsequent analyses (Fig. 3) sheds light on debates about the origins of the people who spread Pre-Pottery Neolithic culture to Cyprus. Parallels in subsistence, technology, settlement organization, and ideological indicators (15) suggest close contacts between Pre-Pottery Neolithic B people in Cyprus and on the mainland (13), but the geographic source of the Cypriot Pre-Pottery Neolithic populations has been unclear, with many possible points of origin (20). An inland Middle Euphrates source has been suggested on the basis of architectural and artifactual similarities (14, 21). However, the faunal record at Cypriot Pre-Pottery Neolithic B sites and the use of Anatolian obsidian as raw material suggest linkages with Central and Southern Anatolia (15), and the genetic data increase the weight of evidence in favor of this scenario of a primary source in Anatolia.

The two individuals from Armenia, from the sites of Aknashen (~5900 BCE) and Masis Blur (~5600 BCE) differ in being more Caucasus- and Anatolia/Levant-like, respectively, despite

being buried just ~200 km and a few centuries apart; thus, Neolithic people of Armenia were not homogeneous but instead exhibited variation that also encompassed two ~5700 to 5400 BCE individuals buried in neighboring Azerbaijan (7), who are intermediate between the two from Armenia in both PCA and the five-way model. But in comparison to the individuals from Mesopotamia to the south, the individuals from Armenia and Azerbaijan had more Anatolian Neolithic admixture (visible in both PCA and the five-way model). Conversely, some Neolithic Anatolian populations from Central Anatolia had Caucasus hunter-gatherer–related admixture, more than Pınarbaşı and the NW Anatolian source population, where such ancestry is not evident, but less than the proportion inferred for the individual from Mardin from Southeast Anatolia, which belonged (together with its neighbors at Nemrik 9 in Northern Iraq) to the inland group characterized by high Caucasus hunter-gatherer–related ancestry. These observations form a consistent picture of a Neolithic continuum characterized by the Anatolian/Levantine cline on one end and inland influence related to the Zagros-Caucasus set of populations, with the geographically intermediate individuals from Mesopotamia, Armenia, and Azerbaijan occupying genetically intermediate positions.

To avoid publication-order bias, that is, the tendency to update published models to accommodate new data rather than always inferring models taking all samples equally into account, we coanalyzed new data from the Neolithic together with previously published data to arrive at a model of Neolithic origins that can account for patterns of genetic variation in Neolithic West Asia as a whole (22). The Neolithic continuum emerges from this analysis too, as all Neolithic populations under study can be modeled as mixtures of three pre-Neolithic sources representing Anatolian (Pınarbaşı), Levantine (Natufian), and inland sources (either Caucasus hunter-gatherer, as in Fig. 3A, or Ganj Dareh, as in Fig. 3B); the two inland sources are not independent but to a first degree of approximation represent the same source of ancestry (Fig. 3C). When we attempt to model Neolithic populations using either Caucasus hunter-gatherers or Ganj Dareh as a source population and the other as an outgroup, we obtain good model fits for most populations (further suggesting that neither population is a better source than the other), except (i) for the high Caucasus hunter-gatherer ancestry individual from Aknashen, where the Caucasus hunter-gatherer model is not rejected ($P = 0.46$) while the Ganj Dareh one is ($P < 0.001$); (ii) the Azerbaijan and Mesopotamian Neolithic for which both models are rejected ($P < 0.01$); and (iii) the Barcın Neolithic for which the Ganj Dareh model is narrowly not rejected at the $P = 0.01$ level ($P = 0.0142$), while

Fig. 2. Overview of Neolithic variation. (**A**) Principal components analysis of ancient individuals projected onto West Eurasian variation. (**B**) Application of the five-way model from (12) to Neolithic populations with Caucasus hunter-gatherer (CHG), Eastern European hunter-gatherer (EHG), Levant Pre-Pottery Neolithic (PPN), Serbian (SRB) Iron Gates hunter-gatherer, and NW Anatolian Neolithic from Barcın sources.
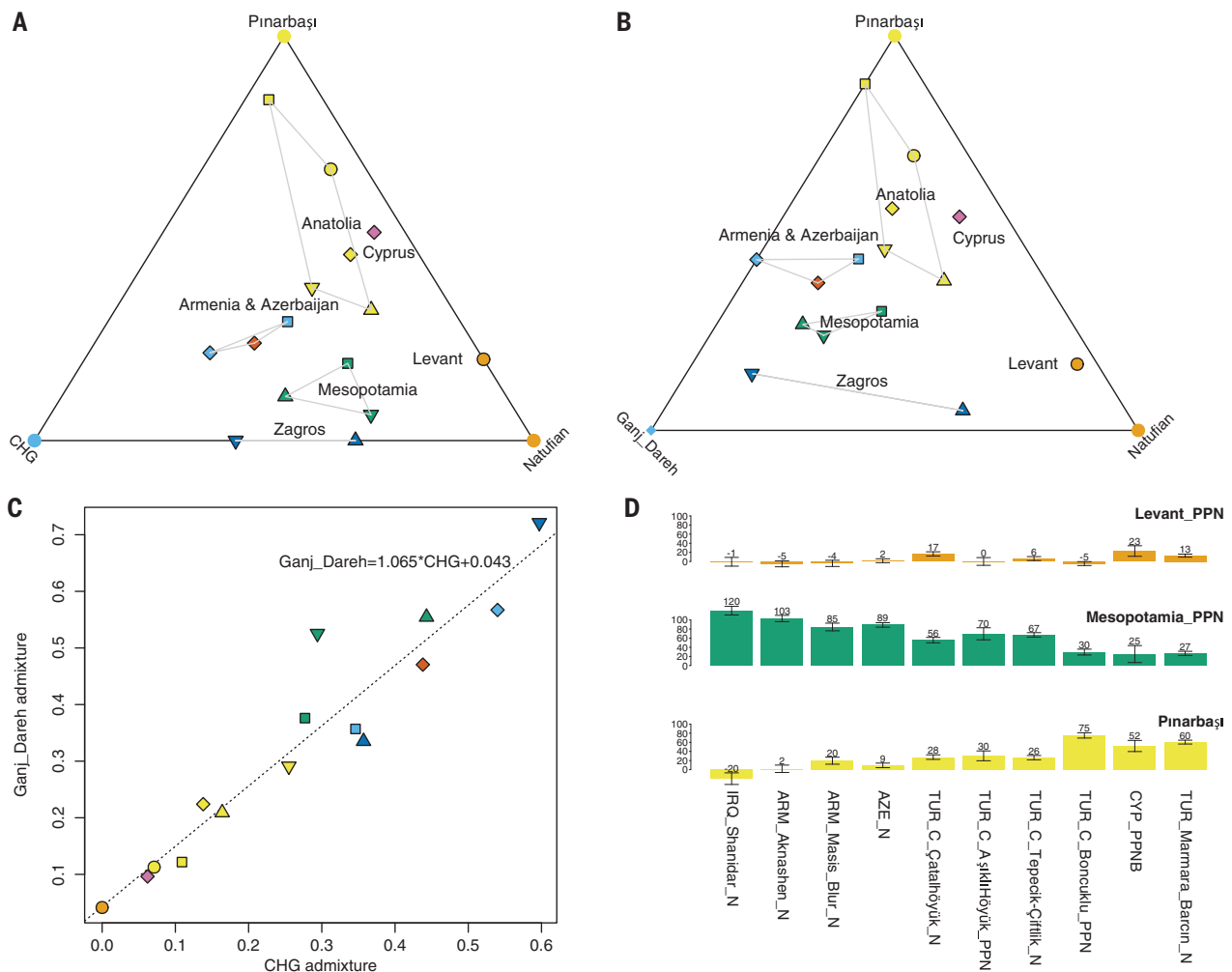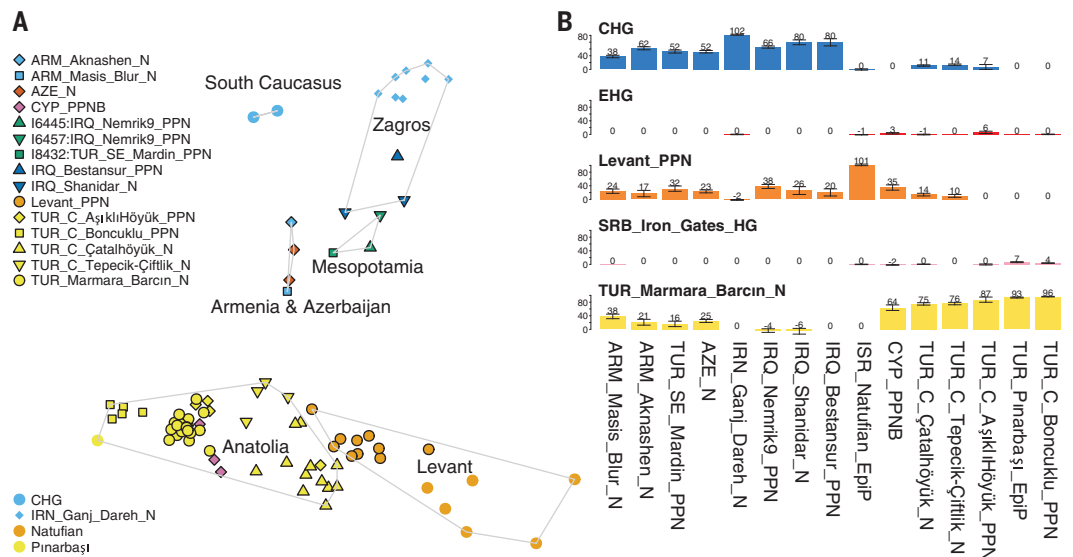
Fig. 3. The Neolithic continuum. (**A**) Three-way model of Neolithic admixture with Caucasus hunter-gatherer (CHG) (10) as a source. (**B**) Three-way model of Neolithic admixture with Ganj Dareh (1) as a source. (**C**) Caucasus hunter-gatherer and Ganj Dareh admixture proportions from (A) and (B) are strongly correlated [coefficient of determination (R^2) = 0.91; $P < 1 \times 10^{-7}$]. (**D**) We also modeled Neolithic populations with local, Anatolian [Pınarbaşı (6)] and Eastern, Mesopotamian Pre-Pottery Neolithic

(PPN), proximal sources. Both Pre-Pottery Neolithic populations from Anatolia [from Boncuklu (6) and Aşıklı Höyük (8)] have no significant evidence for extra Levantine ancestry. However, all three Pottery Neolithic ones [from Barcın in NW Anatolia and Tepecik-Çiftlik (5) and Çatalhöyük (8) in Central Anatolia] have significant additional Levantine ancestry. (Ancestry proportions for some groups are nonsignificantly negative, reflecting statistical uncertainty in the estimates.)
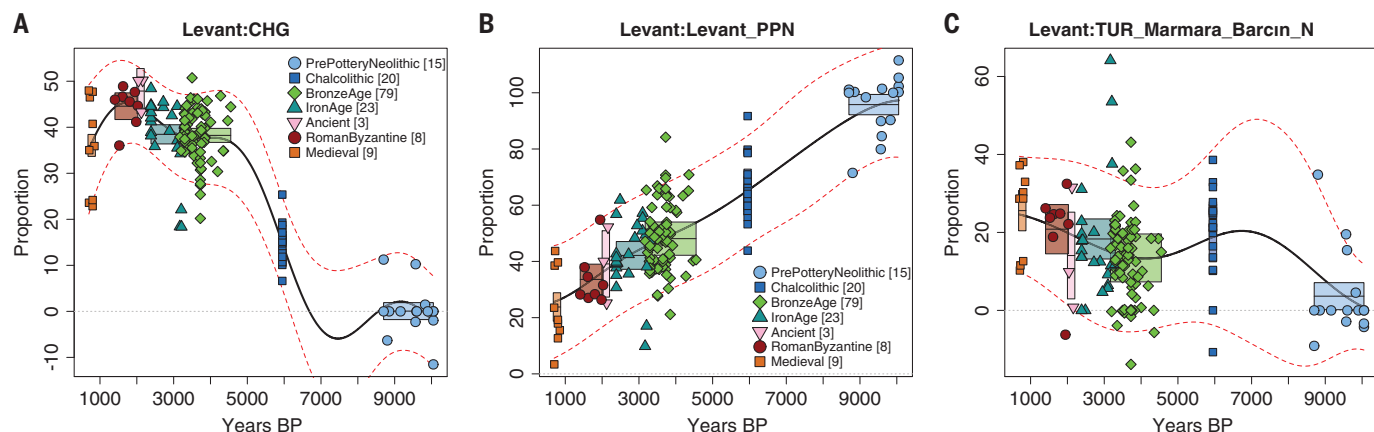
Fig. 4. The dilution of Neolithic ancestry in the Levant. The trajectory of West Asian components of ancestry in the Levant. (**A**) Caucasus hunter-gatherer ancestry increased over time, beginning in the Chalcolithic period and continuing into the Bronze Age, while the local Levantine ancestry (**B**) was diluted during the past 10,000 years. (**C**) Anatolian ancestry, like Caucasus hunter-gatherer ancestry, also increased by the Chalcolithic period (26), undergoing fluctuations thereafter.

the Caucasus hunter-gatherer one is rejected (P = 0.001). These results tentatively suggest that Caucasus hunter-gatherer and Ganj Dareh Neolithic are interchangeable for the purposes of quantifying the amount of inland admixture, although some populations may have a clearer connection with one or the other (e.g., the Neolithic of Armenia with the hunter-gatherers of the South Caucasus rather than Iran, and the geographically intermediate Azerbaijan and Mesopotamia with both).

The fact that regardless of the chosen sources, none of the Neolithic populations of West Asia were simple descendants of their pre-Neolithic antecedents when we had the data to test this (in which case some of them would occupy the corner positions of Fig. 3, A and B) suggests that some history of admixture may have led to their appearance; the details of this process could be elucidated by examining even older populations from across West Asia. When pre-Neolithic antecedents are not available, as is the case for North Mesopotamia, it remains an open question whether the local hunter-gatherers were genetically continuous with the first farmers of the region, or if there was a history of admixture across the Neolithic transition there as well. Notably, this highlights that intermediate populations of the ternary plots of Fig. 3 need not have come about by admixture from the corner populations used to model them; alternatively, they could be drawn toward the middle by unsampled pre-Neolithic populations of West Asia, for example, hunter-gatherers of the Tigris and Euphrates regions predating the Pre-Pottery Neolithic farmers studied here.

When we attempted to model Neolithic populations as mixtures of each other, we observed that at least in Anatolia (Fig. 3D), where most of the data are from and from which both Pre-Pottery and Pottery Neolithic populations have been published, an interesting distinction be-

came clear. Pre-Pottery Neolithic populations from Central Anatolia can be modeled as mixtures of a group related to the local Pınarbaşı Epipaleolithic with variable (~30 to 70%) Mesopotamian admixture, suggesting that Pre-Pottery cultures of Anatolia may have been formed with the contribution of both local hunter-gatherers and migrants from the east, where agriculture first appeared. But we cannot model the Pottery Neolithic Anatolians with just these two sources and instead require an extra ~6 to 23% Levantine Neolithic admixture. The source of this admixture is unclear; it need not have come from the Southern Levant (Jordan) from which the Levantine Neolithic individuals were sampled and may instead represent a geographically closer source for which there is no available genome-wide data, for example, from Syria, where early Pottery Neolithic cultures such as the Halafian flourished and for which the available polymerase chain reaction–based mitochondrial DNA data cannot distinguish alternative scenarios (23).

We caution that while our results point to migration from, and admixture with, Mesopotamian and Levantine populations, when we use the term "migration," we are not claiming that we have detected a "migratory movement," that is, a planned translocation of a large number of people over a long distance within the space of years [for discussion of nuances in the use of the term migration, see (24)]. Migration in the sense that we use it may either be intentional or not; it may involve few or many individuals; and it may either be rapid or continue across many generations. Some such migration and admixture must have taken place, as indicated by the genetic data, but its causes, routes, and fine-grained temporality remain to be clarified.

A further caveat is that the Levantine influence detected in Anatolian Pottery Neolithic

populations need not have been the result of unidirectional migration into Anatolia but may also have come about if Anatolia and the Levant became part of a mating network spanning both regions. Data from Pottery Neolithic cultures of the Levant are needed to test this hypothesis and to determine whether there was movement of mating partners in both directions.

Levantine ancestry may have flourished during the Neolithic, and yet its later trajectory in the Levant itself (including individuals from Jordan, Israel, Syria, and Lebanon) exhibits a decrease of ~8% per millennium from the Pre-Pottery Neolithic down to the Medieval period, largely replaced by Caucasus- and Anatolian-related ancestry from the north and west (Fig. 4). This persistent and sustained trend after the formation of the Neolithic West Asian populations studied here reminds us that large-scale admixture continued in ensuing millennia. Despite the major decline in the contribution of Levantine Neolithic farmers to peoples in the region where they originated, this key ancestry source made a vital contribution to peoples of later periods, continuing until the present and weaving, through migrations and mixtures within and beyond the Southern Arc (12, 25), the tapestry of ancestry of all those that followed them.

REFERENCES AND NOTES

1. I. Lazaridis *et al.*, *Nature* **536**, 419–424 (2016).
2. I. Mathieson *et al.*, *Nature* **528**, 499–503 (2015).
3. F. Broushaki *et al.*, *Science* **353**, 499–503 (2016).
4. Z. Hofmanová *et al.*, *Proc. Natl. Acad. Sci. U.S.A.* **113**, 6886–6891 (2016).
5. G. M. Kılınç *et al.*, *Curr. Biol.* **26**, 2659–2666 (2016).
6. M. Feldman *et al.*, *Nat. Commun.* **10**, 1218 (2019).
7. E. Skourtanioti *et al.*, *Cell* **181**, 1158–1175.e28 (2020).
8. R. Yaka *et al.*, *Curr. Biol.* **31**, 2455–2468.e18 (2021).
9. M. Gallego-Llorente *et al.*, *Sci. Rep.* **6**, 31326 (2016).
10. E. R. Jones *et al.*, *Nat. Commun.* **6**, 8912 (2015).
11. V. M. Narasimhan *et al.*, *Science* **365**, eaat7487 (2019).
12. I. Lazaridis *et al.*, *Science* **377**, eabm4247 (2022).
13. E. Asouti, *J. World Prehist.* **20**, 87–126 (2006).

14. J. Cauvin, *Naissance des divinités, naissance de l'agriculture: la révolution des symboles au néolithique* (Empreintes de l'homme, CNRS Éditions, 1997).
15. E. Peltenburg, Ed., *The Colonisation and Settlement of Cyprus:Investigations at Kissonerga-Mylouthkia, 1976-1996* (Paul Åströms Förlag, 2003).
16. N. Patterson, A. L. Price, D. Reich, *PLOS Genet.* **2**, e190 (2006).
17. I. Lazaridis *et al.*, *Nature* **513**, 409–413 (2014).
18. W. Haak *et al.*, *Nature* **522**, 207–211 (2015).
19. I. Mathieson *et al.*, *Nature* **555**, 197–203 (2018).
20. A. H. Simmons, R. D. Mandel, *Science* **317**, 1679–1679 (2007).
21. D. Stordeur, in *Bulletin de Correspondance Hellenique* (Ecole française d'Athènes, 2003), pp. 353–371.
22. Detailed information is provided in the supplementary materials.
23. E. Fernández *et al.*, *PLOS Genet.* **10**, e1004401 (2014).
24. N. Patterson *et al.*, *Nature* **601**, 588–594 (2022).
25. I. Lazaridis *et al.*, *Science* **377**, 940–951 (2022).
26. É. Harney *et al.*, *Nat. Commun.* **9**, 3336 (2018).
27. S. Alpaslan-Roodenberg *et al.*, *Nature* **599**, 41–46 (2021).

NANOPHYSICS

Tunable light-induced dipole-dipole interaction between optically levitated nanoparticles

Jakob Rieser[1], Mario A. Ciampini[1], Henning Rudolph[2], Nikolai Kiesel[1], Klaus Hornberger[2], Benjamin A. Stickler[2]*, Markus Aspelmeyer[1,3], Uroš Delić[1]*

Arrays of optically trapped nanoparticles have emerged as a platform for the study of complex nonequilibrium phenomena. Analogous to atomic many-body systems, one of the crucial ingredients is the ability to precisely control the interactions between particles. However, the optical interactions studied thus far only provide conservative optical binding forces of limited tunability. In this work, we exploit the phase coherence between the optical fields that drive the light-induced dipole-dipole interaction to couple two nanoparticles. In addition, we effectively switch off the optical interaction and observe electrostatic coupling between charged particles. Our results provide a route to developing fully programmable many-body systems of interacting nanoparticles with tunable nonreciprocal interactions, which are instrumental for exploring entanglement and topological phases in arrays of levitated nanoparticles.

W hen a dielectric subwavelength particle is illuminated by laser light, the particle is polarized in phase with the incoming electromagnetic wave. The induced dipole makes the particle a high-field seeker, which enables optical trapping in the intensity maximum of focused lasers (*1*). Additionally, the dipole radiation field acquires the optical phase of the trapping field. This process, called coherent scattering, has been used in combination with an optical cavity to cool the motion of atoms and polarizable nanoparticles in far-detuned traps (*2–5*). More recently, it has been applied to achieve motional ground-state cooling of single silica nanoparticles in an optical cavity (*6*) and with real-time feedback (*7, 8*).

Simultaneous trapping of more than one particle in a single optical potential allows for the creation of a self-organized structure of particles that interact through the scattered light (*9*). The particles assume steady-state positions at locations where the constructive interference of scattered fields is maximized, thereby minimizing the total energy. This optical interaction is fundamentally conser- vative and reciprocal, giving rise to a spring-type interaction called optical binding (*9, 10*). Optical binding between dielectric objects has been realized for microparticles (where the radius is comparable to or larger than the wavelength) in many experiments (*10–18*). In this regime, the effect is well described by Mie scattering theory (*9*), in which the light scattered from one of these particles is not spatially coherent over the extension of a neighboring particle. For the case of nano- scale objects, optical binding has been demonstrated with metal particles in liquid, where plasmon resonances enhance the interaction (*19–21*). However, making full use of the op- portunities provided by optically trapped nanoparticle arrays for investigating complex nonequilibrium phenomena requires controlla- ble interactions beyond the current framework of optical binding (*22–24*). The tools presented in this article pave the way to using the tech- nology of atomic physics (*25, 26*) for the gen- eration and observation of quantum correlations and topological phases in a fully programmable mechanical array (*27, 28*).

In contrast with previous experiments, our work shows fully tunable and nonrecip- rocal optical interactions between two silica nanoparticles—with radius ($r = 105 \pm 3$ nm) appreciably smaller than the wavelength ($\lambda = 1064$ nm)—that are levitated in two distinct, phase-coherent optical traps at a variable trap separation d_0. Each particle behaves as an induced dipole driven by the total optical

[1]Faculty of Physics, University of Vienna, Vienna Center for Quantum Science and Technology (VCQ), A-1090 Vienna, Austria. [2]Faculty of Physics, University of Duisburg-Essen, 47048 Duisburg, Germany. [3]Institute for Quantum Optics and Quantum Information (IQOQI), Vienna Austrian Academy of Sciences, A-1090 Vienna, Austria.
*Corresponding author. Email: benjamin.stickler@uni-due.de (B.A.S.); uros.delic@univie.ac.at (U.D.)
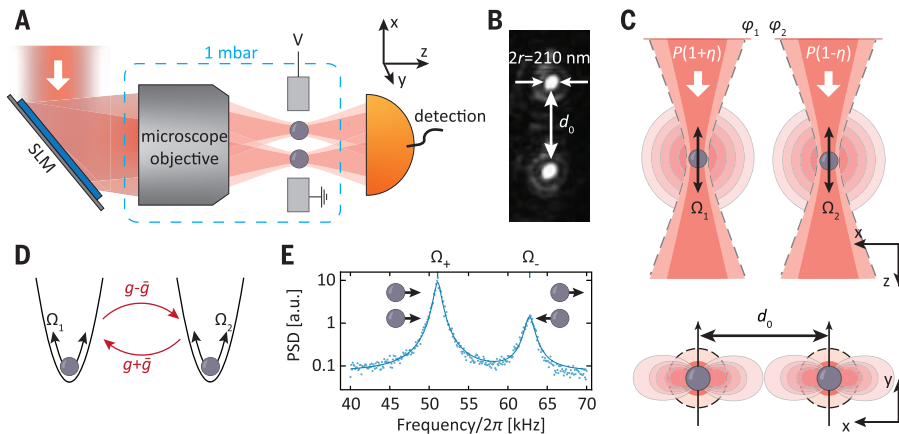
Fig. 1. Experimental setup. (**A**) Two laser beams are diffracted by the SLM and focused with the microscope objective to create two distinct optical tweezers. The optical traps are in the vacuum chamber at a pressure of ~1 mbar. The light is collected after the focus and used for detection of mechanical modes. We drive the electrodes with a voltage V to calibrate the number of charges. (**B**) Camera image of two nanoparticles (radius $r = 105$ nm) trapped in two optical traps at a distance $d_0 \sim 10$ μm. (**C**) Side view (above) and top view (below) of the trap foci. Two parallel laser beams are used to trap two nanoparticles at a distance d_0. Intrinsic mechanical frequencies along the z axis $\Omega_1 \propto \sqrt{P(1+\eta)}$ and $\Omega_2 \propto \sqrt{P(1-\eta)}$ are controlled by a single parameter η. Polarization is set along the y axis to maximize dipole radiation along the x axis. We set the optical phases ϕ_1 and ϕ_2 with the SLM. (**D**) Our system can be simplified to two harmonic oscillators with frequencies $\Omega_{1,2}$ that are coupled through dipole-dipole interaction with nonreciprocal coupling rates $g \pm \bar{g}$. (**E**) In case of reciprocal coupling ($\bar{g} \equiv 0$), the normal modes of the system, the COM mode z_+ and the breathing mode z_-, are nondegenerate with frequencies $\Omega_+ = \Omega$ and $\Omega_- = \Omega + 2g$, respectively. We observe the normal modes at frequencies $\Omega_+/2\pi \approx 51$ kHz and $\Omega_-/2\pi \approx 63$ kHz in the power spectral density (PSD) of the detector signal, which we fit to determine the mechanical frequencies. a.u., arbitrary units.

field, which is a sum of the trapping field, and the coherently scattered light from the other particle. The interference between these two fields gives rise to the interaction between the particles and affects their motion in all three dimensions. The total light-induced interaction is a combination of a conservative gradient force and a nonconservative radiation pressure force, in analogy to the forces acting on a single nanoparticle in an optical trap (*1*). The relevant contributions to the optical interparticle forces oscillate periodically and decay with the interparticle distance d as (*29*)
$$\mathbf{F}_{1,2} \propto \sin(kd \mp \Delta\phi)[\pm k\mathbf{n} + (k - 1/z_R)\mathbf{e}_z]/kd$$
in the far field ($kd \gg 1$, $k = 2\pi/\lambda$). Here, $\Delta\phi$ denotes the optical phase difference between the trapping lasers at the particle position, **n** is the unit vector pointing from particle 1 to particle 2, and z_R is the Rayleigh length. The interaction between two equally sized particles is thus fundamentally nonreciprocal ($\mathbf{F}_1 \neq -\mathbf{F}_2$), which has not been explored in previous theoretical and experimental optical binding studies (*9, 14, 16*).

We obtain the linear coupling between the particles from expanding the optical forces in terms of the relative motion along the trap axes (x, y, and z). The particle motion along the x direction modifies the distance to $d = d_0 + x_1 - x_2$, where the primary contribution to the coupling follows from the spatial dependence kd of the interference between the

local trapping and scattered fields. The coupling rate thus depends on the distance as $\propto (kd_0)^{-1}$, which has been confirmed in several studies of the lateral optical binding with microparticles (*10, 13, 16, 21, 29*). On the other hand and in contrast with previous optical binding studies, the dominant contribution to the coupling along the z direction stems from the phase dependence of the interference as the motions are encoded in the optical phase $\Delta\phi = \Delta\phi_0 + (k - 1/z_R)(z_1 - z_2)$ (*4*), where $\Delta\phi_0$ is the optical phase difference between the trapping lasers in the focal plane. This previously unexplored coupling mechanism results in a long-range coupling rate that depends on the distance as $\propto (kd_0)^{-1}$ as well. The ratio of the coupling rates along the z and x directions depends on the inverse ratio of the mechanical frequencies (~4), thus making it compelling to explore interactions along the z direction. Altogether, attaining precise control over the optical phase difference $\Delta\phi$ allows us to realize nonreciprocal and ultrastrong light-induced dipole-dipole interaction between nanoscale dielectric objects for the first time.

In the experiment, the phase-coherent trapping lasers are generated in the first-order diffraction of a spatial light modulator (SLM). The lasers are focused by a microscope objective into two independent traps (Fig. 1, A and B). The total trapping power of $2P \sim 800$ mW is split between the two traps as $P_{1,2} = P(1 \pm \eta)$,

with the control variable η, which allows us to modify the mechanical frequencies along the z axis as $\Omega_{1,2} \propto \sqrt{P(1 \pm \eta)}$ (Fig. 1C). We control η, the optical phases $\phi_{1,2}$ at each trapping site, and the trap separation d_0 (distance between the trap foci along the x axis) with the SLM. We set the laser polarization along the y axis to maximize the dipole radiation along the x axis and hence the interaction strength. Each particle is randomly charged; therefore, we calibrate their absolute charges by applying an AC voltage to two electrodes placed along the x axis and select particles based on the desired charge (*29*). We monitor the particle motion with homodyne detection of the light transmitted from the optical traps.

The linearized dynamics with particle center-of-mass (COM) positions $z_{1,2}$ follow as (*29*)

$$m\ddot{z}_1 + m\gamma\dot{z}_1 = -(m\Omega_1^2 + k_1 + k_2)z_1 + (k_1 + k_2)z_2$$
$$m\ddot{z}_2 + m\gamma\dot{z}_2 = -(m\Omega_2^2 + k_1 - k_2)z_2 + (k_1 - k_2)z_1$$
(1)

where m is the mass of each particle, and the displacement resulting from the homogeneous part of the forces has been absorbed in $z_{1,2}$. The spring constant $k_1 = G\cos(kd_0)\cos(\Delta\phi_0)/kd_0$ describes the conservative part of the optical forces (tunable optical binding), whereas $k_2 = G\sin(kd_0)\sin(\Delta\phi_0)/kd_0$ describes a nonconservative interaction, as indicated by a change of sign between the equations. The non-reciprocity of the interaction is maximized by $\Delta\phi_0 = \pi/2 + n\pi$, where $n \in \mathbb{Z}$. The constant $G \propto \alpha^2 \sqrt{P_1 P_2}$ is a positive function of the trap powers $P_{1,2}$ and the particle polarizability α. The scaling of G with α^2 reflects the nature of the dipole-dipole interaction. At the pressures in our experiment, mechanical damping γ is dominated by the collisions with the surrounding gas. For weak coupling between the particles $(k_1, k_2 \ll m\Omega_{1,2}^2)$, Eq. 1 yields the eigenfrequencies of the coupled system $\Omega_\pm(\eta_m) \approx \Omega + g \mp \sqrt{g^2 - \bar{g}^2}$, where we define the conservative and nonconservative coupling rates as $g = k_1/2m\Omega$ and $\bar{g} = k_2/2m\Omega$, respectively. The control parameter $\eta_m = -k_2/m\Omega^2$ defines the value at which the frequency splitting $\Omega_+ - \Omega_-$ is minimal and Ω is the intrinsic mechanical frequency in the absence of interactions at $\eta = 0$. Therefore, at the avoided crossing, our system is described as two harmonic oscillators with frequencies $\Omega_{1,2}$ mutually coupled with non-reciprocal coupling rates $g \pm \bar{g}$ (Fig. 1D), which can be fully controlled by the distance d_0 and the optical phase difference $\Delta\phi_0$. In the case of purely conservative interaction ($\bar{g} \equiv 0$) and for equal mechanical frequencies, the normal modes of the system become the COM mode $z_+ = z_1 + z_2$ and the breathing mode $z_- = z_1 - z_2$. Only the breathing mode is affected by the interaction, such that its eigenfrequency shifts to $\Omega_- \approx \Omega + 2g$, whereas the COM mode
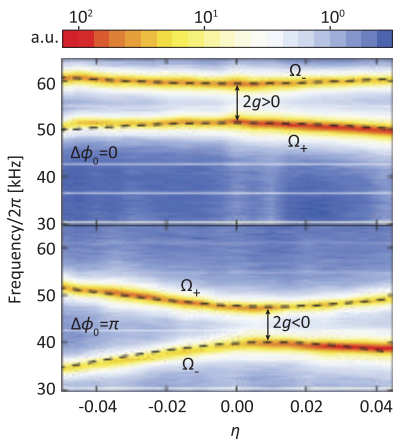
Fig. 2. Avoided crossing between the breathing and the COM mode. We plot a spectrogram of the relevant frequency region as a function of the control parameter η. Attractive ($g > 0$) and repulsive ($g < 0$) conservative dipole-dipole interactions are observed at the trap separation of $d_0 \approx 3.15$ μm and for the optical phase differences $\Delta\phi_0 = 0$ (above) and $\Delta\phi_0 = \pi$ (below), respectively. The COM mode is always at the frequency $\Omega_+/2\pi \approx 50$ kHz, whereas the breathing mode Ω_- has a higher or lower frequency by $2g/2\pi \approx 8$ kHz for $\Delta\phi_0 = 0$ or $\Delta\phi_0 = \pi$, respectively. Black dashed lines are fits to experimental data. The avoided crossing is shifted from η = 0 for $\Delta\phi_0 = \pi$ because of the interference of the trapping lasers in the focal plane. The amplitude of the detected motion is not constant owing to variations in detection sensitivity during the measurement.

eigenfrequency remains unchanged at $\Omega_+ = \Omega$ (normal mode splitting). In Fig. 1E, we show the normal modes at $\Omega_+/2\pi \approx 51$ kHz and $\Omega_-/2\pi \approx 63$ kHz in the power spectral density of the detector signal, where the mechanical frequency is $\Omega/2\pi \approx 51$ kHz when the interaction is switched off.

To obtain the coupling rate g, we measure the eigenfrequencies as a function of η (Fig. 2). We set the trap separation to $d_0 \sim 3.15$ μm and the optical phase difference to either $\Delta\phi_0 = 0$ (above) or $\Delta\phi_0 = \pi$ (below), such that the interaction is purely conservative but of either positive (attractive) or negative (repulsive) nature. The spectrogram exhibits an avoided crossing between the normal modes, which typically occurs for equal intrinsic mechanical frequencies ($\eta \equiv 0$), but only if $|g| > \gamma/2$. All measurements are conducted at pressures of ~1.5 mbar, thus the avoided crossing is observable for coupling rates larger than $\gamma/2\pi \approx 1.5$ kHz. From here on, the coupling rate is expressed in units of the modified mechanical frequency $\Omega' \approx \Omega + g$ as the ratio g/Ω' is independent of the optical power. We observe a frequency splitting of ~±8 kHz, which corresponds to a coupling of $g/\Omega' = \pm(0.09 \pm 0.01)$. Other coupling mechanisms can be neglected

in our investigations of the light-induced dipole-dipole interaction. First, we select particles with few charges, such that the additional coupling as a result of the electrostatic interaction was smaller than $|g_C|/\Omega' = (1.4 \pm 0.6) \times 10^{-3}$ (29). Furthermore, interparticle coupling resulting from the ambient gas or liquid (aero- or hydrodynamic coupling) can be dominant for large objects and small distances; however, in our experiment it is negligible because the ratio of the particle radius to the trap separation is small ($r/2d_0 < 0.05$) (16, 18).

In our experiment, we achieve full control over the conservative and nonconservative coupling rates. Because the interaction arises from the interference between the trapping and scattered fields, we expect the coupling rate to oscillate with particle distance with a period of λ and decay as d_0^{-1} owing to the far-field nature of the dipole radiation at distances $d_0 \gg \lambda$. We measure the normal mode splitting for trap separations d_0 in the range of 2.2 to 3.7 μm and for phase differences $\Delta\phi_0 = 0$ (blue points) or $\Delta\phi_0 = \pi$ (orange points) to maximize the conservative interaction (Fig. 3A). Good agreement is observed with our theoretical model and the measured coupling rates in both cases (29). At a distance of $d_0 \approx 2.2$ μm and for $\Delta\phi_0 = 0$, we observe the maximum coupling of $g/\Omega' = 0.186 \pm 0.017$. The effect of the dominant nonconservative interaction is apparent for the trap separation of $d_0 \approx 2.2$ μm and the phase difference of $\Delta\phi_0 = 0.8\pi$ (Fig. 3B). The constant pumping of energy into the system as a result of the nonconservative forces increases the particle motional amplitude by an order of magnitude. The eigenfrequencies are degenerate for $\eta \in [0, 0.07]$, from which we estimate the couplings of $g/\Omega \approx 0$ and $\bar{g}/\Omega \approx -0.017$. To demonstrate its dependence on the optical phase difference $\Delta\phi_0$, we measure the normal mode splitting at a fixed separation of $d_0 \approx 3.2$ μm (Fig. 3C). Our theoretical model of linear interactions (blue line) fails to fully predict the observed behavior because of several effects. For example, the actual interparticle distance is different from the trap separation owing to the radiation pressure force of the dipole radiation, which provides a constant displacement force. Moreover, in the absence of an additional cooling mechanism, the particles are able to explore nonlinear terms in the interaction Hamiltonian, which affects the eigenfrequencies and modifies the normal mode splitting. We observe a zero crossing because of the absence of the conservative forces at the phase of $\Delta\phi_0 \approx 0.8\pi$, in agreement with our measurement in Fig. 3B. In future work, feedback cooling can be used to constrain the particle motion within linear dynamics.

Rotating the trapping laser polarization by an angle Θ from the y axis provides for another
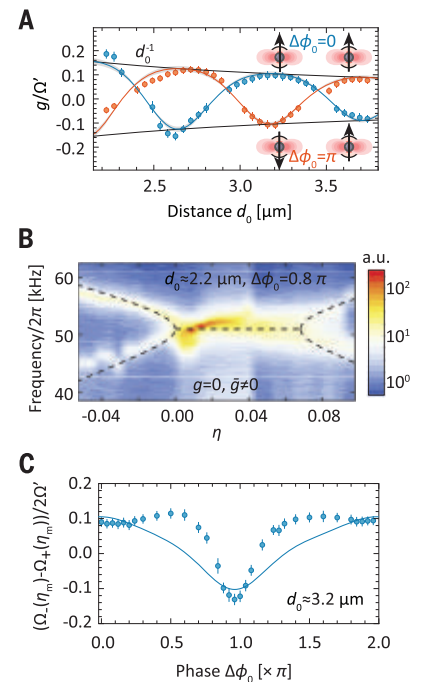
Fig. 3. Controllable dipole-dipole coupling.
(**A**) Trap separation d is changed while keeping the optical phase difference fixed at $\Delta\phi_0 = 0$ (blue circles) or $\Delta\phi_0 = \pi$ (orange circles). We observe a change of the coupling rate g with periodicity of ~λ and an envelope that drops off as d_0^{-1}. Amplitudes of blue and orange lines are calculated from the system parameters with the grayed region given by the standard deviation of the particle size. (**B**) At the trap separation $d_0 \approx 2.2$ μm, the particles experience a combination of the conservative and nonconservative forces. For the optical phase difference of $\Delta\phi_0 = 0.8\pi$, only the nonconservative interaction is present ($g = 0$), and the eigenmodes are degenerate for η between 0 and 0.07. The motion is strongly amplified in this region. The dashed lines are theory based on the estimated conservative and nonconservative coupling rates. (**C**) We set the trap separation at $d_0 \approx 3.2$ μm and tune the optical phase difference $\Delta\phi_0$ from 0 to 2π and measure the mode splitting $\Omega_- - \Omega_+$. Interaction is mostly conservative at $\Delta\phi_0 = n\pi (n \in \mathbb{Z})$ and can be explained by the linearized model (blue line). The nonconservative force contributes to the total force for all other values of $\Delta\phi_0$ and is able to amplify the particle motion, thus modifying the normal mode splitting.

way to control the dipole-dipole interaction (Fig. 4A). The magnitude of the dipole radiation along the x axis is smaller by a factor of cosΘ owing to the characteristic spatial profile of the dipole radiation in the far field. The interference of the dipole radiation with the trapping field is suppressed by a factor of cosΘ as a result of the scalar product of the two field components. Altogether, this yields a decrease of the coupling rate by $\cos^2\Theta$ in the
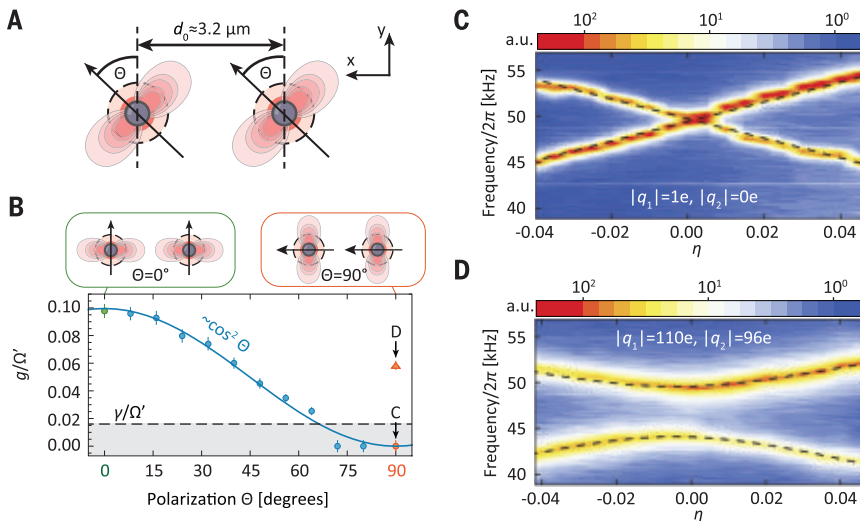
Fig. 4. Turning off dipole-dipole interaction to detect electrostatic interaction. (**A**) For arbitrary polarization angle Θ, the interference of electric fields is suppressed by $\cos^2\Theta$. Two special cases of $\Theta = 0°$ and $\Theta = 90°$ are presented in green and orange rectangles, respectively. In the case of $\Theta = 90°$, there is no interference of the trapping and the scattered fields. (**B**) We measure the coupling rate resulting from the dipole-dipole interaction as a function of the polarization angle Θ between particles with an absolute number of 1 ± 1 and 0 ± 1 charges (circles). The interaction is maximal for the angle $\Theta = 0°$ (green circle). The avoided crossing is unresolved for coupling rates smaller than the mechanical linewidth γ (gray region). At the angle $\Theta = 90°$, the dipole-dipole interaction is suppressed (orange circle). We measure coupling resulting from the electrostatic interaction between particles with 96 ± 21 and 110 ± 24 charges (orange triangle). (**C**) The avoided crossing is absent for horizontally polarized tweezers ($\Theta = 90°$) because the far-field dipole-dipole interaction is strongly suppressed. (**D**) In the absence of optical interactions, we observe the avoided crossing for highly charged particles owing to strong electrostatic interaction.

far-field approximation, which is confirmed in the measurement in Fig. 4B (circles and blue line). For the angle $\Theta = 90°$, the residual dipole-dipole interaction scales with $(kd_0)^{-3}$ because of the radial near-field component of the radiated field. We estimate the coupling of $g/\Omega' \approx 6 \times 10^{-4}$ at $d_0 \sim 3\lambda$, which we are unable to detect in the current experiment as $g/\gamma < 10^{-2}$ (Fig. 4C) (*29*). Suppression of the dipole-dipole interaction allows us to explore electrostatic interaction between strongly charged particles. We trap particles with absolute charges $|q_1|/e = 96 \pm 21$ and $|q_2|/e = 110 \pm 24$ and equal signs ($q_1 q_2 = |q_1 q_2|$) and observe an avoided crossing as a result of electrostatic coupling (Fig. 4D). The ordering of normal mode frequencies $\Omega_- < \Omega_+$ reflects the repulsive interaction between the particles. The measured coupling $g_C/\Omega' = -0.058 \pm 0.003$ fits well to the expected $g_C/\Omega' = -0.047 \pm 0.015$. Because the electrostatic coupling rate scales as $\propto d_0^{-3}$, we infer that electrostatic interaction between particles—each carrying a single charge—can be resolved at a distance of $d_0 \sim 2$ μm and at pressures below 10^{-3} mbar. Altogether, our platform allows for exploring hybrid schemes with both dipole-dipole and electrostatic interactions.

We have demonstrated the controllable (attractive and repulsive) light-induced dipole-dipole interaction between two silica nano-

particles levitated in distinct optical traps with coupling rates up to 20% of the mechanical frequency. These results expand the toolbox of optical binding by trapping in a phase-coherent optical tweezers array, which will enable further studies of optical interactions between Rayleigh particles (*9*) or atoms (*30*) at subwavelength distances. Furthermore, we control the nonreciprocal interactions between the particles by tuning conservative and nonconservative interactions. By effectively switching off the optical interaction, we observe electrostatic interaction between two charged particles. The demonstrated strength and level of control of optical and electrostatic interactions in arrays of levitated solid-state objects, in combination with the previously realized quantum state preparation, provides a platform that may open up many research avenues in quantum physics. We foresee that this platform—with a possible addition of an optical cavity—can be used for quantum simulation with mechanical degrees of freedom (*31–33*), enhanced quantum sensing (*34*), collective effects (*35*), and phonon transport and thermalization (*24*).

REFERENCES AND NOTES

1. A. Ashkin, J. M. Dziedzic, J. E. Bjorkholm, S. Chu, *Opt. Lett.* **11**, 288 (1986).
2. D. R. Leibrandt, J. Labaziewicz, V. Vuletić, I. L. Chuang, *Phys. Rev. Lett.* **103**, 103001 (2009).
3. M. Hosseini, Y. Duan, K. M. Beck, Y.-T. Chen, V. Vuletić, *Phys. Rev. Lett.* **118**, 183601 (2017).
4. U. Delić *et al.*, *Phys. Rev. Lett.* **122**, 123602 (2019).
5. D. Windey *et al.*, *Phys. Rev. Lett.* **122**, 123601 (2019).
6. U. Delić *et al.*, *Science* **367**, 892–895 (2020).
7. L. Magrini *et al.*, *Nature* **595**, 373–377 (2021).
8. F. Tebbenjohanns, M. L. Mattana, M. Rossi, M. Frimmer, L. Novotny, *Nature* **595**, 378–382 (2021).
9. K. Dholakia, P. Zemánek, *Rev. Mod. Phys.* **82**, 1767–1791 (2010).
10. M. M. Burns, J.-M. Fournier, J. A. Golovchenko, *Phys. Rev. Lett.* **63**, 1233–1236 (1989).
11. W. Singer, M. Frick, S. Bernet, M. Ritsch-Marte, *J. Opt. Soc. Am. B* **20**, 1568 (2003).
12. S. A. Tatarkova, A. E. Carruthers, K. Dholakia, *Phys. Rev. Lett.* **89**, 283901 (2002).
13. S. Mohanty, J. Andrews, P. Gupta, *Opt. Express* **12**, 2746–2753 (2004).
14. M.-T. Wei, J. Ng, C. T. Chan, H. D. Ou-Yang, *Sci. Rep.* **6**, 38883 (2016).
15. D. S. Bykov *et al.*, *Light Sci. Appl.* **7**, 22 (2018).
16. Y. Arita, E. M. Wright, K. Dholakia, *Optica* **5**, 910 (2018).
17. J. Damková *et al.*, *Light Sci. Appl.* **7**, 17135 (2018).
18. V. Svak *et al.*, *Optica* **8**, 220 (2021).
19. Y. Zhang, C. Gu, A. M. Schwartzberg, S. Chen, J. Z. Zhang, *Phys. Rev. B* **73**, 165405 (2006).
20. F. Svedberg, Z. Li, H. Xu, M. Käll, *Nano Lett.* **6**, 2639–2641 (2006).
21. V. Demergis, E.-L. Florin, *Nano Lett.* **12**, 5756–5760 (2012).
22. W. Lechner, S. J. M. Habraken, N. Kiesel, M. Aspelmeyer, P. Zoller, *Phys. Rev. Lett.* **110**, 143604 (2013).
23. D. Holzmann, M. Sonnleitner, H. Ritsch, *Eur. Phys. J. D* **68**, 352 (2014).
24. S. Liu, Z. Yin, T. Li, *Adv. Quantum Technol.* **3**, 1900099 (2020).
25. S. Ebadi *et al.*, *Nature* **595**, 227–232 (2021).
26. P. Scholl *et al.*, *Nature* **595**, 233–238 (2021).
27. V. Peano, C. Brendel, M. Schmidt, F. Marquardt, *Phys. Rev. X* **5**, 031011 (2015).
28. N. Goldman, J. C. Budich, P. Zoller, *Nat. Phys.* **12**, 639–645 (2016).
29. See the supplementary materials.
30. J. K. Asbóth, P. Domokos, H. Ritsch, *Phys. Rev. A* **70**, 013414 (2004).
31. M. Ludwig, F. Marquardt, *Phys. Rev. Lett.* **111**, 073603 (2013).
32. G. Heinrich, M. Ludwig, J. Qian, B. Kubala, F. Marquardt, *Phys. Rev. Lett.* **107**, 043603 (2011).
33. D. Holzmann, M. Sonnleitner, H. Ritsch, *Photonics* **8**, 228 (2021).
34. A. McDonald, A. A. Clerk, *Nat. Commun.* **11**, 5382 (2020).
35. P. Domokos, H. Ritsch, *Phys. Rev. Lett.* **89**, 253003 (2002).

METASURFACES

Resonant metasurfaces for generating complex quantum states

Tomás Santiago-Cruz[1,2], Sylvain D. Gennaro[3,4], Oleg Mitrofanov[3,5], Sadhvikas Addamane[3,4], John Reno[3,4], Igal Brener[3,4]*, Maria V. Chekhova[1,2]*

Quantum state engineering, the cornerstone of quantum photonic technologies, mainly relies on spontaneous parametric downconversion and four-wave mixing, where one or two pump photons spontaneously decay into a photon pair. Both of these nonlinear effects require momentum conservation for the participating photons, which strongly limits the versatility of the resulting quantum states. Nonlinear metasurfaces have subwavelength thickness and allow the relaxation of this constraint; when combined with resonances, they greatly expand the possibilities of quantum state engineering. Here, we generated entangled photons via spontaneous parametric downconversion in semiconductor metasurfaces with high–quality factor, quasi-bound state in the continuum resonances. By enhancing the quantum vacuum field, our metasurfaces boost the emission of nondegenerate entangled photons within multiple narrow resonance bands and over a wide spectral range. A single resonance or several resonances in the same sample, pumped at multiple wavelengths, can generate multifrequency quantum states, including cluster states. These features reveal metasurfaces as versatile sources of complex states for quantum information.

Optical quantum state engineering mainly relies on nonlinear optical effects such as spontaneous parametric downconversion (SPDC) or spontaneous four-wave mixing (SFWM). These effects have been used to create a vast variety of photonic quantum states, including single (1) and entangled (2) photons, squeezed states (3), and cluster states (4–6). However, both SPDC and SFWM in conventional nonlinear crystals and waveguides require strict momentum conservation for the involved photons, which strongly limits the versatility of the states they produce. The emergent concept of quantum optical metasurfaces (QOMs) helps to overcome this constraint. Metasurfaces (i.e., arrays of nanoresonators) feature unique abilities to manipulate and control the amplitude, phase, and polarization of light in the nonlinear (7–9) and quantum (10, 11) regimes using a single ultrathin device. In particular, all-dielectric metasurfaces made of materials with high second-order nonlinearities offer a potential route for on-chip quantum state generation (12–14). As a result of the subwavelength thickness of metasurfaces, the momentum conservation (or phase-matching) requirement is relaxed (15), enabling multiple nonlinear processes to occur with comparable efficiencies (16). In addition, optical resonances in metasurfaces and nanoresonators enhance the vacuum field fluctuations through enhanced density of states at certain wavelengths, boosting the spontaneous emission of photons (17).

Vacuum fluctuation enhancement scales with the quality (Q) factor of the resonance. In metasurfaces, Q-factors are especially high for bound states in the continuum (BIC) resonances (18, 19), which are discrete-energy modes whose energy levels overlap with a continuous spectrum of radiating modes (20). In symmetry-protected BIC metasurfaces, the outcoupling of radiation in the normal direction is forbidden by symmetry (19). Hence, Q-factors of these modes may be infinite; in theory, they could infinitely enhance the spontaneous emission of photons and photon pairs. In practice, symmetry breaking (quasi-BICs) leads to finite enhancement (19), which can still be as high as 10^2 to 10^4.

Here, we report on the experimental generation of tunable photon pairs via SPDC driven by high-Q quasi-BIC resonances in gallium arsenide (GaAs) QOMs. Our QOMs emit frequency-degenerate and nondegenerate narrowband photon pairs tunable over more than 100 nm by changing either the optical pump or the spectral location of the resonances without appreciable loss of efficiency. Moreover, by judicious choice of resonance and pump wavelengths, we can simultaneously drive as many SPDC processes as necessary, obtaining frequency-multiplexed entangled photons and enabling multichannel heralding. Our work paves the way for building nanoscale sources of complex tunable entangled states for quantum networks.

In SPDC, a pump photon of a higher frequency ω_p downconverts in a second-order nonlinear material into a pair of signal and idler photons of lower frequencies, ω_s and ω_i, following energy conservation (Fig. 1A). Unlike in bulk crystals, SPDC in subwavelength sources does not require longitudinal momentum conservation (15), leading to the

broadband emission of photon pairs over a wide range of angles (21, 22). In optical nanoantennae and metasurfaces, however, the resonances select the range of wavelengths and wave vectors where the photon emission is enhanced (12, 14, 23). Therefore, with judicious choice and design of optical modes and resonances, metasurfaces can be used to generate tunable and unidirectional entangled photons.

To demonstrate SPDC with quasi-BICs, we fabricated various arrays of broken-symmetry resonators arranged in a square lattice of different periodicities and scaling by means of standard electron beam lithography and chlorine-based dry etching. Subsequent fabrication steps included epoxy bonding and curing, substrate lapping and polishing, wet etching, and transferring the metasurface onto a transparent fused silica substrate. We chose GaAs because it possesses one of the highest second-order susceptibilities among traditional materials, $\chi^{(2)}$ = 400 to 500 pm/V, for the range of pump wavelengths involved in this work; these susceptibilities exceed those of ferroelectric nonlinear materials such as lithium niobate by more than an order of magnitude (24). The structure of the metasurfaces is shown in Fig. 1B.

The existence of symmetry-protected BICs can be explained through symmetry breaking and coupling between allowed and forbidden optical Mie modes (25), or using group theory arguments (26). A metasurface consisting of square nanoresonators obeys C_2 and C_4 rotational symmetry; photons at the BIC frequency are trapped inside the resonators because of zero coupling to radiating modes. A small notch in the cube breaks the rotational symmetry (Fig. 1C) and transforms these symmetry-protected BICs into quasi-BICs, which can outcouple to the far field. Spectrally, they appear as narrow transmission peaks in the white-light far-field transmittance (Fig. 1D). The modes, labeled electric dipole (ED)–qBIC and magnetic dipole (MD)–qBIC, reach Q-factors of $Q_{BIC(ED)} \approx 330$ and $Q_{BIC(MD)} \approx 1000$, respectively. The ED-qBIC and MD-qBIC have different coupling efficiencies with respect to the incident beam polarization. For the lowest-order quasi-BICs, simulated electric field profiles resemble those of out-of-plane dipole modes (see Fig. 1D, insets, and fig. S1).

By tuning the period of the array and the proportions of the resonators, the central wavelengths of the quasi-BIC resonances can be tuned over a wide range. For emission normal to the QOM, the Q-factor is the highest because most of the system symmetry is preserved. Off-normal excitation leads to coupling to free-space radiation, reducing the Q-factor of each quasi-BIC resonance and lowering the field enhancement (fig. S2). Thus, we should also expect the emitted SPDC photon pairs to
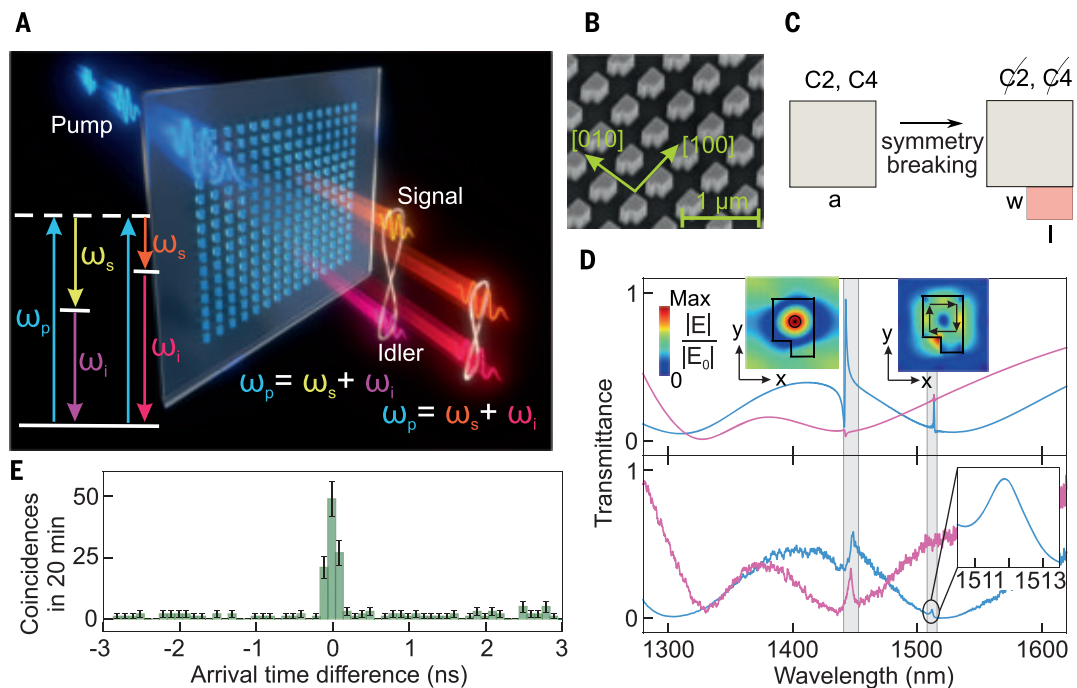
[1]Max Planck Institute for the Science of Light, 91058 Erlangen, Germany. [2]Friedrich-Alexander-Universität Erlangen-Nürnberg, 91058 Erlangen, Germany. [3]Center for Integrated Nanotechnologies, Sandia National Laboratories, Albuquerque, NM 87185, USA. [4]Sandia National Laboratories, Albuquerque, NM 87185, USA. [5]University College London, London WC1E 7JE, UK.
*Corresponding author. Email: ibrener@sandia.gov (I.B.); maria.chekhova@mpl.mpg.de (M.V.C.)

Fig. 1. Spontaneous parametric downconversion (SPDC) using symmetry-protected quasi-BIC resonances in a semiconductor metasurface.
(**A**) Conceptual diagram of multiplexed entangled photon generation in a multiresonance semiconductor metasurface.
(**B**) Scanning electron micrograph of the metasurface at an intermediate step of nanofabrication (see supplementary materials). (**C**) Structure of the broken-symmetry resonators (see table S1 for the various metasurfaces' dimensions). The addition of a small rectangle (pink) breaks the rotational symmetries C_2, C_4 of the metasurface, turning the BIC into a quasi-BIC. (**D**) Simulated (top) and measured (bottom) white-light linear transmission spectra of one QOM, for the incident polarization along the [110] crystal direction (magenta)

and orthogonal to it (blue). Gray areas highlight the locations of the quasi-BIC resonances: ED-qBIC ($\lambda = 1446.9$ nm) and MD-qBIC ($\lambda = 1511.8$ nm). The insets show the normalized distribution and direction (black arrows) of electric field xy calculated at the center of the nanoresonator for both resonances. (**E**) Typical distribution of the photon arrival time difference for two detectors, demonstrating photon pair generation. Error bars denote the statistical uncertainty.

be radiated almost unidirectionally along the metasurface normal, as observed for emission from quantum dots embedded inside a symmetry-protected, quasi-BIC metasurface (*17*).

To demonstrate multiplexed entangled photon generation via SPDC, we investigated three QOMs, labeled QOM-A, QOM-B, and QOM-C, with different resonator sizes and spacings, such that the ED-qBIC and MD-qBIC optical modes were resonant at different wavelengths (Fig. 2, A to C, upper panels; also see table S1 and fig. S3). All metasurfaces were pumped with linearly polarized continuous-wave lasers of different wavelengths, focused into 140-μm spots. Two superconducting nanowire single-photon detectors placed at the two outputs of a fiber beamsplitter (fig. S4) enabled registration of photon pairs as joint detection events. For all QOMs considered, we registered a high number of simultaneous photon detections—coincidences (Fig. 1E)—which indicates the presence of photon pairs. For further details, see the supplementary materials. Figures S5 and S6 also show the results of second-harmonic generation, which is mediated by the same nonlinear tensor as SPDC and was therefore helpful for optimizing the experiment.

We then performed fiber-assisted spectroscopy of photon pairs with 3-nm resolution (see supplementary materials). The three corresponding SPDC spectra are shown in Fig. 2, A to C (bottom panels), each one below its white-light transmission spectrum. Thanks to the relaxed

momentum conservation, the pump wavelength λ_p can be arbitrary, and thus we use different pumps and different QOMs to demonstrate various types of photon pair generation.

For QOM-A, we used $\lambda_p = 723.4$ nm, such that the degenerate wavelength $2\lambda_p$ overlapped with the ED-qBIC resonance wavelength. In this case, both SPDC photons were emitted within a single narrow peak, centered at the resonance wavelength $2\lambda_p = 1446.8$ nm (Fig. 2A). The full width at half maximum (FWHM) of 4.3 nm matched the linewidth of the ED-qBIC resonance. This corroborates previous observations on QOMs (*12*) that the presence of an optical resonance enhances the quantum vacuum field within the resonance's bandwidth.

However, very different spectra were obtained when we pumped QOM-B at 718.2 nm, such that the degenerate wavelength $2\lambda_p$ was off-resonance from the ED-qBIC modes. Now, we found that the SPDC spectrum exhibited two narrow peaks, one centered at the ED-qBIC peak wavelength ($\lambda_s = 1390.9$ nm) and the other at a wavelength $\lambda_i = 1485$ nm (Fig. 2B). Here, the ED-qBIC resonance enhances the vacuum field at the signal wavelength, forcing the QOM to emit a photon at this wavelength simultaneously with its partner at the idler wavelength, as dictated by energy conservation:

$$\lambda_i = \left(\frac{1}{\lambda_p} - \frac{1}{\lambda_s}\right)^{-1} \quad (1)$$

This indicates that narrowband, frequency-nondegenerate photon pairs (ubiquitous in photonic state engineering, i.e., for heralding) have been generated from a nanostructured photonic device such as a metasurface.
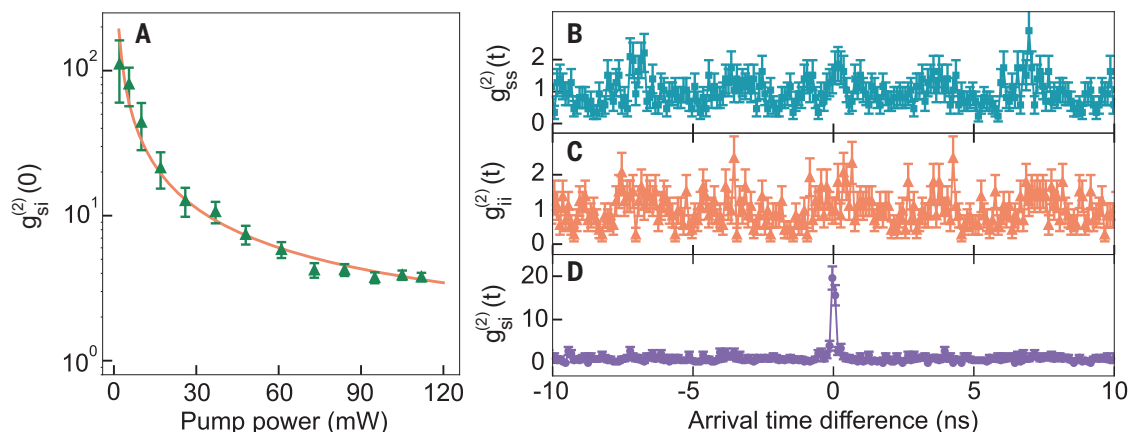
The spectrum of the entangled photons gets richer when both ED-qBIC and MD-qBIC resonances are active in SPDC (Fig. 2C). We achieved this by pumping our third metasurface QOM-C at 725.4 nm, with the pump radiation polarized at 175°, so that the MD-qBIC resonance was activated. We now observed four peaks, two of them corresponding to signal photons emitted at the ED-qBIC (1359.4 nm) and MD-qBIC (1429.4 nm) resonances, and the other two to their idler partners. We found that because the MD-qBIC resonance has a higher Q-factor than the ED-qBIC resonance, its emission FWHM is smaller, causing the signal and idler SPDC spectra to also be narrower. It might be possible to obtain higher rates (i.e., larger peak heights), but we note that the Q-factor of a resonance provides only the upper boundary for SPDC enhancement, which also depends on the vacuum field distribution in the nanoresonators and the nonlinear tensor symmetry and values.

We also found that our QOMs can produce degenerate and nondegenerate photon pairs over a broad spectral range without considerable reduction of efficiency (Fig. 2D). As a consequence of the high-Q resonances, the efficiency is at least three orders of magnitude
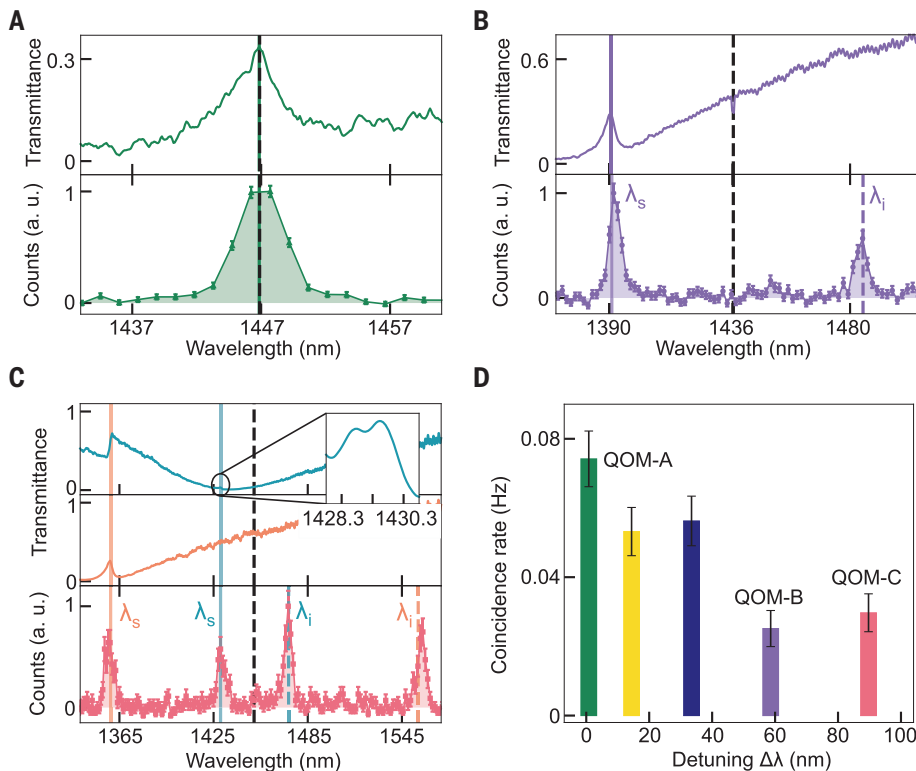
Fig. 2. SPDC spectra for the QOMs considered in this work. (**A** to **C**) Measured white-light transmission spectra (top) and SPDC spectra (bottom) for QOMs A, B, and C, respectively. The SPDC spectra show (A) degenerate photon pairs at wavelength $2\lambda_p = 1446.8$ nm (vertical dashed line), which overlaps with the ED-qBIC resonance of QOM-A; (B) nondegenerate photon pairs, where only the signal photon is emitted at the ED-qBIC mode wavelength $\lambda = 1390.9$ nm (purple vertical solid line) of QOM-B; (C) two types of nondegenerate photon pairs, where signal photons are emitted at wavelengths $\lambda = 1359.4$ nm of the ED-qBIC resonance (orange vertical solid line) and $\lambda = 1429.4$ nm of the MD-qBIC resonance (green vertical solid line) of QOM-C. Both ED- and MD-qBIC modes are active in SPDC because of the choice of pump polarization. Black dashed lines show the degenerate wavelength $2\lambda_p$. The peak heights at signal and idler wavelengths are unequal because of the different detection efficiency of the two IR detectors and the asymmetric splitting ratio of the fiber splitter. (**D**) Coincidence rate, with 9.6 mW pumping at 725.4 nm, versus wavelength detuning $\Delta\lambda = 2\lambda_p - \lambda_{ED\text{-}qBIC}$ between the degenerate wavelength ($2\lambda_p$) and the ED-qBIC resonance, $\lambda_{ED\text{-}qBIC}$, of five different QOMs. Error bars denote the statistical uncertainty.
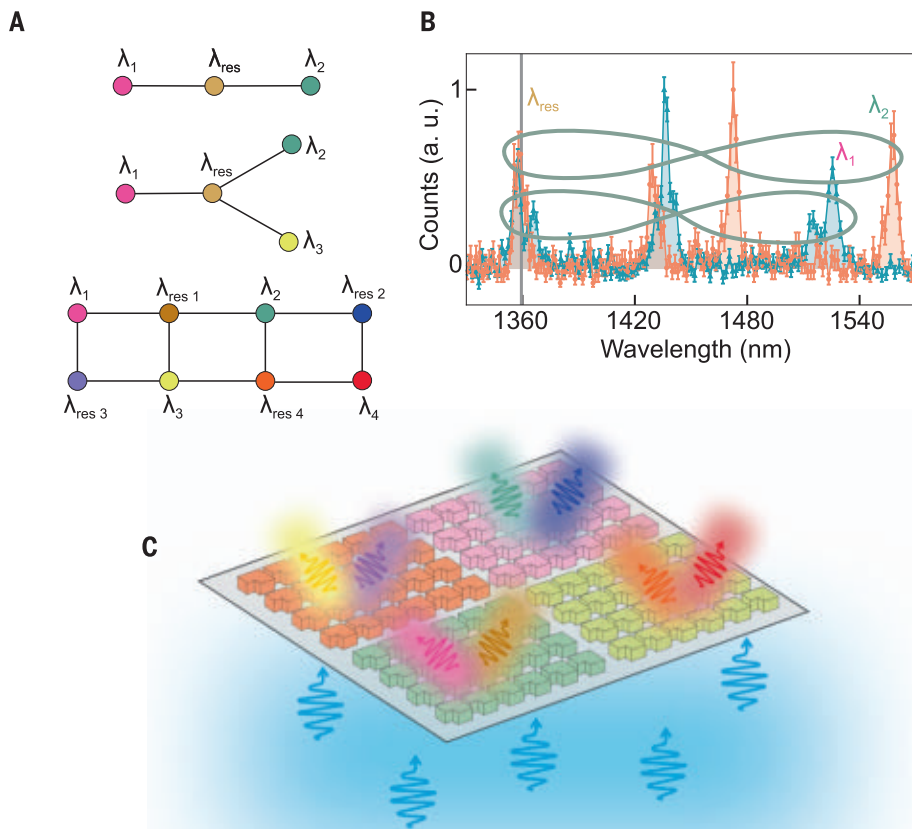
higher than in an unpatterned GaAs film of the same thickness (see supplementary text and fig. S7).

To verify the nonclassicality of our photon pairs, we measured the pump-power dependence of the second-order cross-correlation function (CF) at zero time delay, defined as $g_{si}^{(2)}(0) = \langle \hat{N}_s \hat{N}_i \rangle / \langle \hat{N}_s \rangle \langle \hat{N}_i \rangle$, where $\hat{N}_{s,i}$ are photon-number operators for the signal and idler modes. The cross-CF is measured as $g_{si}^{(2)}(0) = R_c/(R_s R_i T_c)$, where $R_{c,s,i}$ are the rates of the signal-idler coincidences, signal photon detections, and idler photon detections, respectively, and T_c is the coincidence resolution time (27). Because all three numbers $R_{c,s,i}$ scale linearly with the pump power, $g_{si}^{(2)}(0)$ has an inverse dependence on it, as indeed we observed (Fig. 3A). Although this dependence indicates photon pair detection, a formal proof of nonclassicality requires the violation of the Cauchy-Schwarz (CS) inequality (28),

$$\left[g_{si}^{(2)}(0)\right]^2 \leq g_{ss}^{(2)}(0) \cdot g_{ii}^{(2)}(0) \qquad (2)$$

where $g_{ss,ii}^{(2)}(0)$ are second-order auto-CFs for signal and idler modes, respectively. For QOM-B, which generates signal and idler photons at two distinguishable wavelengths (1390.9 nm and 1485 nm), we measured the auto-CFs of modes s and i after 50-nm FWHM bandpass filters centered at 1400 nm (s) and 1475 nm (i), respectively (Fig. 3, B and C). Single-count graphs for each measurement are shown in fig. S9. We obtained $g_{ss}^{(2)}(0) = 1.6\pm0.3$ and $g_{ii}^{(2)}(0) = 1.2\pm0.2$. The cross-CF, measured without bandpass filters (Fig. 3D), was $g_{si}^{(2)}(0) = 10.5\pm1.1$. Hence, the CS inequality is violated by >50 standard deviations, $[g_{si}^{(2)}(0)]^2 = 110\pm2$, $g_{ss}^{(2)}(0) \cdot g_{ii}^{(2)}(0) = 1.9\pm0.3$, revealing the nonclassical character of photon pairs.

Fig. 3. Second-order cross-correlation and autocorrelation functions. (**A**) Pump-power dependence of the second-order cross-correlation function at zero time delay measured for photon pairs emitted by QOM-A (points) and its theoretical fit (line). For raw data, see fig. S8. (**B** and **C**) Second-order auto-correlation functions $g_{ss}^{(2)}$ and $g_{ii}^{(2)}$ measured for QOM-B at the signal (1390.9 nm) and idler (1485 nm) wavelengths, respectively. (**D**) Second-order cross-correlation function $g_{si}^{(2)}$ measured for QOM-B. Error bars are obtained from the statistical uncertainties via the propagation of errors.

Fig. 4. Cluster state generation with QOMs. (**A**) Examples of cluster states: a linear three-qubit state (top), a Greenberger-Horne-Zeilinger state (middle), and a more general graph state (bottom). Links between the vertices are provided by different pumps. (**B**) SPDC spectrum illustrating how a linear three-qubit graph state of photons $|\lambda_{res}\rangle$, $|\lambda_1\rangle$, $|\lambda_2\rangle$ can be generated from QOM-C. (**C**) Spatial multiplexing of four metasurfaces for generating the state of (A), bottom, using a single multifrequency pump beam.

The presence of narrow optical resonances allows one to create, apart from entangled states, more complicated graph quantum states (Fig. 4A). In our setup (fig. S4), the state preparation relies on the fiber beamsplitter sending a photon to each detector; events where both photons arrive at the same detector are ignored. For a nondegenerate photon pair at wavelengths λ_{res} (resonant) and λ_1 (matching via energy conservation), after the beamsplitter, photon $|\lambda_{res}\rangle$ is path-entangled with photon $|\lambda_1\rangle$. For a second nondegenerate pair at wavelengths λ_{res} and λ_2, photon $|\lambda_{res}\rangle$ is also path-entangled with photon $|\lambda_2\rangle$ after the beamsplitter. Note that this photon pair needs another pump for its generation. If photons $|\lambda_{res}\rangle$ from each pair are indistinguishable, which requires two mutually coherent pumps, a linear graph state of three pairwise entangled qubits is created (Fig. 4A, top). This strategy for cluster state generation, called pairwise coupling (6), can be implemented using pump beams

at wavelengths of 725.4 nm and 718.2 nm and an ED-qBIC resonance at $\lambda_{res} = 1359.4$ nm. Figure 4B shows the corresponding spectra with orange and blue colors, respectively, with only two entangled photon pairs ($|\lambda_{res}\rangle$ and $|\lambda_1\rangle$, $|\lambda_{res}\rangle$ and $|\lambda_2\rangle$) marked for simplicity. In our experiment, the pump beams are incoherent, but they still provide the desired spectrum. By adding a third pump, generating photon pairs at wavelengths λ_{res} and λ_3, a more complicated graph state can be created, called a Greenberger-Horne-Zeilinger state (5) (Fig. 4A, middle).

The state becomes increasingly complex by adding multiple coherent pump beams at different wavelengths—that is, using a frequency comb or a filtered supercontinuum as an excitation source. By appropriately matching the wavelength separation of the comb and the optical resonances of the QOMs, photons at multiple wavelengths can be entangled via pairwise couplings. With this approach, one

could implement a scalable cluster state, needed for one-way quantum computation (5), as shown in Fig. 4A (bottom). Such methods of quantum state engineering are enabled by the use of our QOMs with relaxed phase matching and engineered high-Q resonances, and are impossible with bulk crystal or waveguide SPDC sources. Moreover, QOMs provide a unique way to spatially multiplex multiple metasurfaces within the area of a single pump beam (possibly multifrequency) by exciting resonances at different wavelengths and entangling multiple photon pairs across separate wavelengths with a single multifrequency pump beam, as shown in Fig. 4C. But even without links between different pairs, the existence of multifrequency or multispatial channels suggests a new architecture for heralding single photons in many different modes (29).

The use of a highly nonlinear metasurface with narrowband resonances at arbitrary, discrete, and multiple wavelengths enables new opportunities for generating quantum states that have no counterpart when using traditional nonlinear optical crystals or passive (30) or conventional Mie-type metasurfaces (12). First, we have shown enhancement in pair emission rates of at least three orders of magnitude relative to an unpatterned film of the same material and thickness. Second, we have demonstrated nonclassical correlations between downconverted photons at broadly separated wavelengths, opening the possibility of photon heralding. Third, combining single or multiple coherent laser sources with two or more quasi-BIC resonances from a single or multi-patch metasurface, we can create photon pairs at multiple frequencies with comparable efficiencies. Such a multitude of photon pairs can be used to create complex photon quantum states, including cluster states and multichannel single photons, that could facilitate compact quantum information processing (4, 5, 29). Finally, achieving this level of quantum state engineering with a single nanoscale source can potentially lead to future miniaturization of photonic quantum processing, not possible today with other photonic platforms.

REFERENCES AND NOTES

1. B. Lounis, M. Orrit, *Rep. Prog. Phys.* **68**, 1129–1179 (2005).
2. M. Chekhova, *Prog. Optics* **56**, 187–226 (2011).
3. R. Schnabel, *Phys. Rep.* **684**, 1–51 (2017).
4. G. Vallone, E. Pomarico, P. Mataloni, F. De Martini, V. Berardi, *Phys. Rev. Lett.* **98**, 180502 (2007).
5. H. J. Briegel, D. E. Browne, W. Dür, R. Raussendorf, M. van den Nest, *Nat. Phys.* **5**, 19–26 (2009).
6. M. V. Larsen, X. Guo, C. R. Breum, J. S. Neergaard-Nielsen, U. L. Andersen, *Science* **366**, 369–372 (2019).
7. G. Li, S. Zhang, T. Zentgraf, *Nat. Rev. Mater.* **2**, 17010 (2017).
8. A. Krasnok, A. Alù, *ACS Photonics* **9**, 2–24 (2022).
9. M. Shcherbakov, S. Liu, I. Brener, A. Fedyanin, in *Dielectric Metamaterials*, I. Brener, S. Liu, I. Staude, J. Valentine, C. Holloway, Eds. (Elsevier, 2020), pp. 223–248.

10. A. S. Solntsev, G. S. Agarwal, Y. S. Kivshar, *Nat. Photonics* **15**, 327–336 (2021).
11. J. Liu *et al.*, *Opto-Electron. Adv.* **4**, 200092 (2021).
12. T. Santiago-Cruz *et al.*, *Nano Lett.* **21**, 4423–4429 (2021).
13. L. Li *et al.*, *Science* **368**, 1487–1490 (2020).
14. J. Zhang *et al.*, *Sci. Adv.* **8**, eabq4240 (2022).
15. C. Okoth, A. Cavanna, T. Santiago-Cruz, M. V. Chekhova, *Phys. Rev. Lett.* **123**, 263602 (2019).
16. S. Liu *et al.*, *Nat. Commun.* **9**, 2507 (2018).
17. S. Liu *et al.*, *Nano Lett.* **18**, 6906–6914 (2018).
18. P. P. Vabishchevich *et al.*, *ACS Photonics* **5**, 1685–1690 (2018).
19. K. Koshelev, S. Lepeshov, M. Liu, A. Bogdanov, Y. Kivshar, *Phys. Rev. Lett.* **121**, 193903 (2018).
20. C. W. Hsu, B. Zhen, A. D. Stone, J. D. Joannopoulos, M. Soljačić, *Nat. Rev. Mater.* **1**, 16048 (2016).
21. T. Santiago-Cruz, V. Sultanov, H. Zhang, L. A. Krivitsky, M. V. Chekhova, *Opt. Lett.* **46**, 653–656 (2021).
22. C. Okoth *et al.*, *Phys. Rev. A* **101**, 011801 (2020).
23. G. Marino *et al.*, *Optica* **6**, 1416 (2019).
24. S. D. Gennaro *et al.*, *ACS Photonics* **9**, 1026–1032 (2022).
25. S. Campione *et al.*, *ACS Photonics* **3**, 2362–2367 (2016).
26. A. Cerjan *et al.*, *Sci. Adv.* **7**, eabk1117 (2021).
27. L. Mandel, E. Wolf, *Optical Coherence and Quantum Optics* (Cambridge Univ. Press, 1995).
28. D. F. Walls, G. J. Milburn, *Quantum Optics* (Springer, 2008).
29. A. Crespi *et al.*, *Nat. Photonics* **7**, 545–549 (2013).
30. K. Wang *et al.*, *Science* **361**, 1104–1108 (2018).

OPTICS

Massively degenerate coherent perfect absorber for arbitrary wavefronts

Yevgeny Slobodkin[1]†, Gil Weinberg[1]†, Helmut Hörner[2]†, Kevin Pichler[2], Stefan Rotter[2]*, Ori Katz[1]*

One of the key insights of non-Hermitian photonics is that well-established concepts such as the laser can be operated in reverse to realize a coherent perfect absorber (CPA). Although conceptually appealing, such CPAs are limited so far to a single, judiciously shaped wavefront or mode. Here, we demonstrate how this limitation can be overcome by time-reversing a degenerate cavity laser based on a unique cavity that self-images any incident light field onto itself. Placing a weak, critically coupled absorber into this cavity, any incoming wavefront, even a complex and dynamically varying speckle pattern, is absorbed with close to perfect efficiency in a massively parallel interference process. These characteristics open up interesting new possibilities for applications in light harvesting, energy delivery, light control, and imaging.

The absorption of light is a fundamental process in nature, physics, and engineering that is central to many important tasks ranging from photosynthesis to the operation of solar panels and detectors. Whereas light is readily absorbed by thick materials that we perceive as black, thin and weakly absorbing media are inherently far less efficient in capturing incoming radiation and converting it into heat or other forms of energy. A well-known strategy to make even such weakly dissipative substances strongly absorbing is to embed them into a resonant structure (*1*, *2*). At the so-called critical coupling condition, where the coupling strength to such a resonator is exactly balanced with the internal dissipation, the incoming field gets perfectly absorbed with no energy being back-reflected from the resonator (*3*). However, this interferometric enhancement of absorption places severe restrictions on the properties of the incoming field. For example, in the case of a single incoming channel (mode), the optical frequency needs to be precisely tuned to a resonator's critically coupled resonance frequency (*1*). Generalizing the critical coupling condition to multichannel scattering problems leads to the phenomenon of coherent perfect absorption, for which the incoming wavefront in all available scattering channels needs to be adjusted, in addition to the spectral tuning (*4*, *5*). In other words, whether it is two laser beams impinging on an absorbing structure (*6–8*) or a complex microwave field hitting a disordered arrangement of obstacles (*9*), at the critical coupling condition, only a single, suitably adjusted wavefront (or spatial mode) gets coherently perfectly absorbed. Al-

though this required wavefront adjustment opens up the possibility of controlling the absorption process interferometrically (*5*), it also comes with the limitation that, apart from the correctly matched input wavefront, all of the possibly many other modes are only weakly absorbed because of the different interference patterns that they create. To overcome this restriction (*10*), recent works have managed to merge two perfectly absorbed modes at a so-called exceptional point, resulting in chiral absorption (*11–13*).

Here, we demonstrate how to remove the limitation of the number of perfectly absorbed modes in a coherent perfect absorber (CPA) entirely. Our design principle for a corresponding multimode CPA is based on the insight that coherent perfect absorption formally corresponds to the time-reverse of laser emission at the first lasing threshold (*7*, *14*). To create a device that can perfectly absorb arbitrary combinations of incoming modes interferometrically, one is thus required to time-reverse a laser that emits all of these modes in parallel. Such a laser is known as a degenerate cavity laser (*15–17*) and is based on a cavity that self-images the field on either one of the two outer cavity mirrors onto itself after each cavity round trip. This can be realized in a straightforward fashion by placing two lenses in an imaging telescope configuration inside the cavity, ensuring coherent perfect absorption of any combination of modes regardless of their relative phases.

We illustrate the concept of a massively degenerate CPA (MAD-CPA) side by side with a conventional single-mode CPA (Fig. 1). The simplest conventional CPA is engineered to absorb a plane-wave input at normal incidence by placing a critically coupled absorber between two plane mirrors. For such an input, all reflections from the multiple cavity round trips overlap and destructively interfere when the CPA condition is met. The total reflection is reduced to zero and all of the energy is

[1]Applied Physics Department, The Hebrew University of Jerusalem, Jerusalem 9190401, Israel. [2]Institute for Theoretical Physics, Vienna University of Technology (TU Wien), 1040 Vienna, Austria.
*Corresponding author. Email: orik@mail.huji.ac.il (O.K.); stefan.rotter@tuwien.ac.at (S.R.)
†These authors contributed equally to this work.

A   Conventional (single-mode) CPA

B   Massively degenerate (multi-mode) CPA
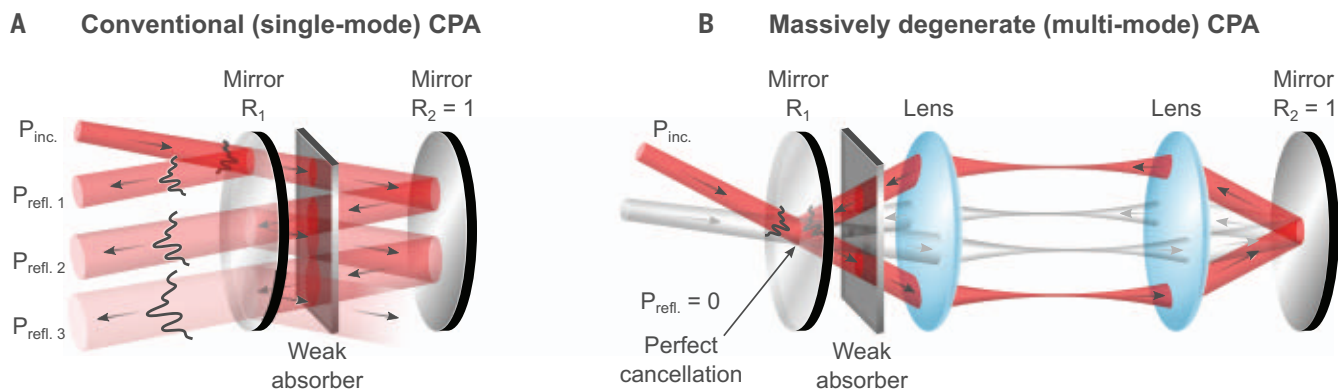
Fig. 1. MAD-CPA for arbitrary wavefronts: concept. (**A**) Conventional (single-mode) CPA composed of a weak absorber placed between two flat mirrors. Although perfect absorption is achieved for a normal-incident plane wave through destructive interference of reflections, any other incoming mode, such as the simple tilted beam shown, results in multiple reflections that cannot destructively interfere. (**B**) By contrast, the proposed massively degenerate multimode CPA can perfectly absorb any complex incident wavefront. This is achieved by placing the weak absorber in a degenerate (self-imaging) cavity, realized here by a cavity with two lenses in a telescopic arrangement. In such a degenerate cavity, all reflections from the multiple cavity round trips show perfect destructive interference with the outer reflection from the front cavity mirror, R_1 (depicted for two incoming beams at different angles).

absorbed. However, for any other input field that is incident at a different angle or in another mode, the reflected fields from the multiple round trips do not have a spatially identical distribution anymore; their destructive interference is out of sync and perfect absorption cannot be achieved (Fig. 1A). To realize a CPA that can universally absorb any arbitrary, complex spatial mode, one must ensure that all of the resonant cavity reflections coincide and destructively interfere with the nonresonant reflection at the front cavity mirror. This condition is naturally fulfilled in a degenerate (self-imaging) cavity design (Fig. 1B), which forms the basis for the degenerate cavity lasers that have been studied extensively for their unique lasing properties (*18–20*). Self-imaging is maintained for any mode supported by the cavity optics, be it a plane wave at any angle or a highly complex field with a complicated wavefront or even spatially incoherent fields.

In our experiment, we used a degenerate linear cavity composed of a lens-based telescope placed inside a cavity having a total length of $4-f$ (Fig. 2A), with f being the focal length of each lens (*21*). This resonant cavity featured a partially reflecting mirror at the front (with a reflectivity of $R_1 = 70\%$) and a nearly perfectly reflecting mirror at the back (with $R_2 = 99.90\%$). A weakly absorbing 0.6-mm-thick color-glass absorber with a single-pass transmission of $T_{abs} = 85.2\%$ was placed next to the front cavity mirror. The CPA conditions were met simultaneously for all input modes (even for the relatively thick absorber; see supplementary text S3.1) when the cavity length was resonant with the laser wavelength. The coherent nature of absorption in the MAD-CPA allowed rapid control, including strong suppression of the absorption to values well below the

absorber's bare absorption value, by simply tuning the cavity length by a fraction of a wavelength. We characterized the degenerate CPA by injecting complex input fields using a spatial light modulator (SLM) illuminated by a wavelength-stabilized helium–neon laser. For each injected complex field, we measured the spatial distribution of the reflected light by imaging the front cavity mirror on an sCMOS camera. The very weak light intensity transmitted through the back cavity mirror was also measured for validation purposes (fig. S4).

With the MAD-CPA being the equivalent of a time-reversed degenerate laser at threshold, the conditions necessary for reaching degenerate CPA are the same as the threshold lasing conditions. First, in lasing, the round-trip power gain, G, should be equal to the round-trip losses, i.e., $R_1G = 1$ (assuming $R_2 = 1$). In a CPA, this condition translates to the critical coupling condition (*3*): $R_1(T_{abs}^2)^{-1} = 1$. Second, the cavity must be aligned for perfect self-imaging after one round-trip propagation. Third, the cavity length must be resonant with the input wavelength. As detailed in supplementary text S3, these conditions were met in our experiments by selecting a front cavity-mirror reflectivity that matched the absorption of the cavity absorber, carefully aligning the cavity optics, and tuning the cavity length to resonant maximal absorption (Fig. 2, C to E).

To illustrate the versatility of our MAD-CPA setup, we injected into it a highly complex input field, in which >1000 modes coherently formed a speckled yin-yang symbol. Figure 2, B to E, presents the corresponding experimental results for the back-reflected light field while tuning the cavity length. As a hallmark of the successful operation of our device, we observed that the reflected power of all the

input modes in the yin-yang input field was simultaneously minimized when the cavity length was tuned to meet the CPA condition (Fig. 2, C and E, and movie S1).

The minimal experimental value reached for the reflectivity was ≈5%, indicating that the weak 15% absorption of the intracavity absorber now featured >94% absorption for all incoming modes simultaneously. Moreover, each spatially localized mode (speckle) of the complex field was nearly perfectly absorbed, reaching a reflected power of ≲2% (Fig. 2, C and D, insets). When the cavity length was tuned by $\lambda/4$ away from perfect absorption condition, absorption was interferometrically suppressed to values well below the incoherent single-pass transmission of the absorber, providing a modulation depth of >50 for each spatially localized mode.

The small experimental deviations from perfect absorption were mainly the result of weak spurious reflections from the cavity lenses' antireflection coatings ($R \approx 0.13\%$ per surface; fig. S3) and by the very small aberrations ($<\lambda/100$) of the self-imaging cavity optics and alignment, which led to slightly different cavity round-trip lengths for the different modes (Fig. 2C, inset, and fig. S1). Our numerical study showed that the small mismatch in the absorption value of the cavity absorber from the critical coupling condition was not a dominant source of deviation from perfect absorption (fig. S2C), such that a commercially available absorber and a suitable front cavity mirror can be used. The influence of such experimental imperfections is discussed and analyzed numerically in supplementary text S2, showing very good agreement with the experimental measurements (Fig. 2D).

To further demonstrate the flexibility inherent in the MAD-CPA design, we illustrated
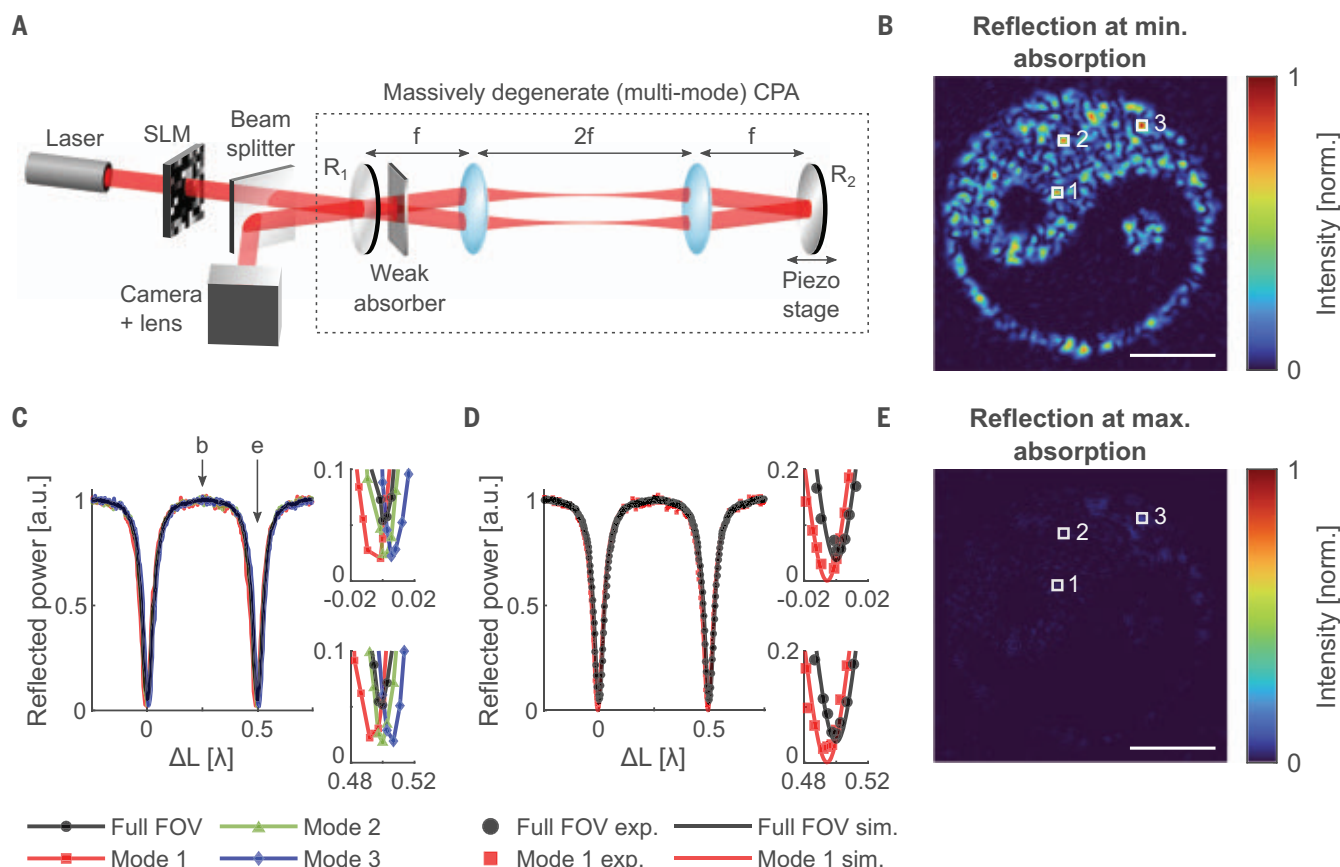
Fig. 2. MAD-CPA setup and experimental results. (**A**) MAD-CPA setup in which complex input fields are injected into a degenerate cavity containing a critically coupled weak absorber using a computer-controlled SLM illuminated by a wavelength-stabilized laser. A camera measures the spatial intensity distribution of the reflected light. Coherent perfect absorption is achieved by tuning the cavity length to be resonant with the laser wavelength. (**B** to **E**) Results for a complex input field in the form of a speckled yin-yang symbol composed of >1000 modes. (B) Measured reflected intensity distribution when the cavity length is tuned for minimal absorption, coherently suppressing absorption [see (C)] and displaying the incident input field. (C) Total back-reflected power as a function of the cavity length (black trace). Red/green/ blue traces are the measured reflected power of the three individual localized modes 1/2/3 (speckle grains), respectively, marked by white squares in (B) and (E). Insets are magnified plots of the two minima in (C). (D) Same experimental measurements as in (C) for the total reflected power (black dots) and for the reflected power of one individual mode (red squares), together with the numerical prediction for the total reflected power for a 100-mode input (black lines) and for a single mode (red line) based on the experimental parameters with no free parameters (*21*). Insets are magnified plots of the two minima in (D). (E) Measured reflected intensity distribution when the cavity length is tuned for maximum absorption, showing near-perfect absorption of all input modes (see movie S1). Scale bars, 1 mm.

its ability to absorb dynamic, rapidly changing complex random light fields that were naturally generated by transmission through flexible multimode fibers (MMFs) and dynamic atmospheric aberrations (Fig. 3). We achieved this by replacing the SLM with a 40-cm-long MMF (*21*). The coherent light propagation through the MMF generated complex speckle fields caused by the dispersion of the fiber modes (Fig. 3C). To generate not only such a spatial complexity but also complex temporal dynamics, we rapidly shook the MMF using an external airflow. Moreover, before injecting the speckle fields into the cavity, we let them propagate through dynamic atmospheric aberrations generated by a hot air stream from a heat gun (Fig. 3A). The results of these experiments are shown in Fig. 3 for different variations dynamics. In all cases, similar near-

perfect absorption values were achieved at CPA conditions (Fig. 3B), even for temporal variations that were faster than the camera exposure time, representing the absorption of spatially incoherent light fields, the time-reversed version of spatially incoherent lasing (*19*). Absorption will remain unchanged as long as the bandwidth of the input fields is narrower than the cavity absorption linewidth. This enables perfect absorption of dynamically varying fields as long as the correlation time, τ_{corr}, of the temporal dynamics is longer than the photon-decay time in the cavity. Figure 3C displays individual camera frames from these dynamic absorption experiments (see also movies S2 to S5).

The number of modes that can be supported by the MAD-CPA is limited by the space-bandwidth product of the self-imaging optics

(*19*). Perfect absorption occurs as long as the incoming wavefronts are within the angular acceptance and the imaged area of the self-imaging cavity optics (*19*) and their spectral bandwidth is within the spectral linewidth of the degenerate cavity (supplementary text S3.2).

It may be interesting to explore whether perfect absorption can also be useful for enhancing the sensitivity in multipass microscopy (*22*, *23*) and if other degenerate cavity designs, such as those making use of a smaller number of optical elements, may offer practical advantages (*15*). The ability of a MAD-CPA to enhance or suppress absorption with high contrast for thousands of modes simultaneously also offers the interesting potential for optical modulation and switching, particularly when the goal is to absorb a large fraction of the incidence power in a weakly absorbing
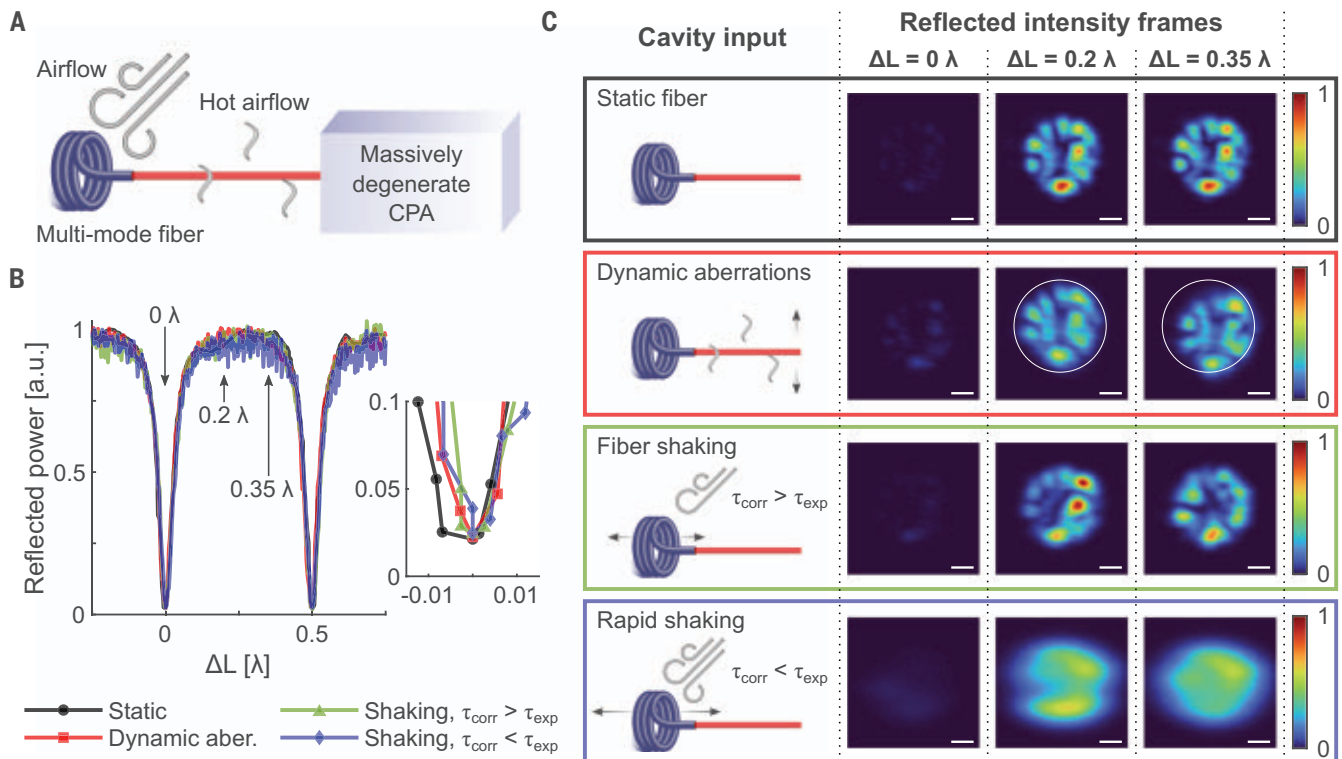
Fig. 3. Coherent perfect absorption of rapidly varying complex fields.
(**A**) Experimental setup in which dynamic complex fields are naturally generated by passing the illuminating laser field through a flexible MMF shaken by strong airflow. The light emanating from the MMF is further subjected to atmospheric aberrations generated by passing it through a hot airflow from a heat gun.
(**B**) Total back-reflected power as a function of cavity length in four different experiments. Black trace, static fiber and no atmospheric turbulence; red trace, static fiber with additional dynamic atmospheric aberrations; green trace, dynamic shaking of the fiber by airflow; blue trace, rapid shaking of the fiber, where the field dynamics are faster than the camera exposure time, effectively demonstrating absorption of spatially-incoherent fields. Inset is a magnification of the left minimum in (B). (**C**) Individual camera frames from the four experiments showing the reflected intensity at maximum absorption ($\Delta L = 0$) and at two different cavity lengths ($\Delta L = 0.2\lambda$ and $\Delta L = 0.35\lambda$), demonstrating interferometric control of absorption. Scale bars, 100 μm.

sample such as a single or a few molecular layers. This flexible enhancement and suppression of absorption is hard to achieve by simple optical focusing on a given absorber.

Other promising extensions of the MAD-CPA concept include its use as a highly multimode reflectionless scattering system (*24*). Placing an SLM inside the laser cavity (*19*) may also allow one to digitally control or compensate for absorption and aberrations.

Although our work has focused on the spatial degrees of freedom of the incoming waves, it would be fascinating to achieve broadband absorption also in the spectral domain (*25*–*27*), a direction in which advances have recently been made using exceptional points and nonlinear media (*11*–*13*, *28*).

REFERENCES AND NOTES

1. K. Kishino *et al.*, *IEEE J. Quantum Electron.* **27**, 2025–2034 (1991).
2. M. Ünlü, K. Kishino, H. Liaw, H. Morkoç, *J. Appl. Phys.* **71**, 4049–4058 (1992).
3. A. Yariv, *IEEE Photonics Technol. Lett.* **14**, 483–485 (2002).
4. Y. D. Chong, L. Ge, H. Cao, A. D. Stone, *Phys. Rev. Lett.* **105**, 053901 (2010).
5. D. G. Baranov, A. Krasnok, T. Shegai, A. Alù, Y. Chong, *Nat. Rev. Mater.* **2**, 17064 (2017).
6. W. Wan *et al.*, *Science* **331**, 889–892 (2011).
7. H. Noh, Y. Chong, A. D. Stone, H. Cao, *Phys. Rev. Lett.* **108**, 186805 (2012).
8. D. G. Baranov, A. Krasnok, A. Alù, *Optica* **4**, 1457 (2017).
9. K. Pichler *et al.*, *Nature* **567**, 351–355 (2019).
10. P. Bai, Y. Wu, Y. Lai, *Europhys. Lett.* **114**, 28003 (2016).
11. W. R. Sweeney, C. W. Hsu, S. Rotter, A. D. Stone, *Phys. Rev. Lett.* **122**, 093901 (2019).
12. C. Wang, W. R. Sweeney, A. D. Stone, L. Yang, *Science* **373**, 1261–1265 (2021).
13. S. Soleymani *et al.*, *Nat. Commun.* **13**, 599 (2022).
14. S. Longhi, *Phys. Rev. A* **82**, 031801 (2010).
15. J. A. Arnaud, *Appl. Opt.* **8**, 189–195 (1969).
16. M. Nixon, E. Ronen, A. A. Friesem, N. Davidson, *Phys. Rev. Lett.* **110**, 184102 (2013).
17. C. Tradonsky *et al.*, *Sci. Adv.* **5**, eaax4530 (2019).
18. M. Nixon *et al.*, *Nat. Photonics* **7**, 919–924 (2013).
19. H. Cao, R. Chriki, S. Bittner, A. A. Friesem, N. Davidson, *Nat. Rev. Phys.* **1**, 156–168 (2019).
20. R. Chriki, S. Mahler, C. Tradonsky, A. A. Friesem, N. Davidson, *Phys. Rev. A* **105**, 033527 (2022).
21. Materials and methods are available as supplementary materials.
22. T. Juffmann, B. B. Klopfer, T. L. I. Frankort, P. Haslinger, M. A. Kasevich, *Nat. Commun.* **7**, 12858 (2016).
23. B. B. Klopfer, M. A. Kasevich, Continuous wave multipass microscopy. arXiv:2107.04707 [physics.optics] (2021).
24. W. R. Sweeney, C. W. Hsu, A. D. Stone, *Phys. Rev. A* **102**, 063511 (2020).
25. H. Wu, M. Xiao, *Phys. Rev. A* **77**, 031801 (2008).
26. O. Kotlicki, J. Scheuer, *Opt. Lett.* **39**, 6624–6627 (2014).
27. T. Y. Kim *et al.*, *Sci. Rep.* **6**, 22941 (2016).
28. S. Suwunnarat *et al.*, *Commun. Phys.* **5**, 5 (2022).

NEUROSCIENCE

A cognitive process occurring during sleep is revealed by rapid eye movements

Yuta Senzai[1,2]* and Massimo Scanziani[1,2]*

Since the discovery of rapid eye movement (REM) sleep, the nature of the eye movements that characterize this sleep phase has remained elusive. Do they reveal gaze shifts in the virtual environment of dreams or simply reflect random brainstem activity? We harnessed the head direction (HD) system of the mouse thalamus, a neuronal population whose activity reports, in awake mice, their actual HD as they explore their environment and, in sleeping mice, their virtual HD. We discovered that the direction and amplitude of rapid eye movements during REM sleep reveal the direction and amplitude of the ongoing changes in virtual HD. Thus, rapid eye movements disclose gaze shifts in the virtual world of REM sleep, thereby providing a window into the cognitive processes of the sleeping brain.

REM sleep is a phase of sleep characterized by rapid eye movements, from which it gets its acronym (1, 2). This phase of sleep is present across many vertebrates (3, 4) and has been associated with dreaming (5, 6). Indeed, when awakened during REM sleep, human subjects are more likely to report vivid dreams as compared to when they are awakened during other phases of sleep (7–10). This observation has led to the proposal that the nature of rapid eye movements during REM sleep may relate to the content of the ongoing dream (7–11). If so, rapid eye movements may represent a readout of some of the cognitive processes that occur in the sleeping brain. The verification of this hypothesis, however, has led to contradictory results. Some initial studies indicated a correlation between the content of dreams reported by the subject and the direction or frequency of rapid eye movements recorded immediately before awakening (7–10). However, other studies did not reproduce these results (12, 13). Furthermore, lifelong blind individuals who do not report visual experiences during dreams do have rapid eye movements during REM sleep (14). Thus, alternative hypotheses suggested that rapid eye movements may be unrelated to the mental processes that occur during REM sleep and simply reflect random brainstem activity (11, 15).

Most of these studies, however, were based on the potentially inaccurate reporting of dreams by human subjects rather than on an objective measure of the cognitive processes that occur in the brain during REM sleep. Thus, we reasoned that by directly monitoring some of the cognitive processes that occur in the brain during REM sleep, we could gain insight into whether rapid eye movements actually occur in coordination with such processes.

We decided to use the head direction (HD) system of the mouse as the objective readout. HD cells are a population of neurons present, among other structures, in the anterodorsal nucleus of the thalamus (ADN). Their ensemble activity reports the direction of the head of the animal along the azimuth as it explores or navigates through its environment (16–18). During REM sleep, the population activity of HD cells is similar to that which occurs during actual navigation (19, 20), thus potentially representing an internal "virtual heading" of the sleeping animal.

In awake, behaving mice exploring their environment, changes in HD are accompanied by fast, saccade-like movements of the eyes in the same direction (21, 22). Does a similar coordination exist in the sleeping mouse? Clearly, a sleeping mouse maintains a fixed heading. However, putative changes in the internal representation of heading of the sleeping mouse may be coordinated with the rapid eye movements that occur during REM sleep. By monitoring rapid eye movements, we may be able to reveal changes in internal heading that are occurring in the virtual world of the sleeping brain.

We recorded from HD cells in the ADN of mice with extracellular linear probes while monitoring the movements of both eyes with head-mounted cameras (Fig. 1A and movies S1 and S2). Mice were free to explore an open-field arena, and their heading was monitored with a top-view camera (Fig. 1B). Mice were allowed to fall asleep, and their sleep phase was identified as REM or non-REM using standard electrophysiological parameters (animals spent 40 to 52% of the session asleep, and 10% of the sleeping period was identified as REM sleep; see table S1 and methods). To determine whether, during REM sleep, rapid eye movements are coordinated with the internal representation of heading, we proceeded through three steps: First, we established, in awake mice, the relationship between saccade-like eye movements and the internal representation of the heading of the animal as decoded from the activity of HD cells (Fig. 1). Second, we determined the properties of rapid eye movements in mice during REM sleep (Fig. 2). Finally, we investigated the nature of the relationship between rapid eye movements in REM sleep and the internal representation of heading (Figs. 3 and 4).

We identified saccade-like eye movements in awake animals based on their fast dynamics (>400° per second). During the exploration of the open-field arena, saccade-like eye movements occurred mainly along the nasotemporal axis (fig. S1, A and B), the vast majority (94.1%) of these eye movements were conjugated—that is, both eyes moved in the same direction, either clockwise (CW) or counterclockwise (CCW)—and the amplitude of these eye movements was correlated across eyes ($R = 0.89$, $P < 10^{-6}$; fig. S1C). Here, we focus on conjugated saccade-like eye movements of at least 2° in amplitude and refer to them simply as saccades. CW and CCW saccades were coupled to head turns in the same direction, that is, with CW and CCW head turns along the azimuth, respectively, consistent with previous reports (21, 22) (fig. S1, E and F). To determine the relationship between the direction of saccades and the internal representation of heading, we analyzed the population activity of HD cells recorded in the ADN while the animal explored the open-field arena (Fig. 1C and fig. S2, A and B). We recorded between 30 and 72 HD cells per animal ($n = 6$ mice; table S1), which were defined as neurons whose activity was modulated by the heading of the animal along the azimuth (Fig. 1D and see methods). Using the heading of the animal and the simultaneously recorded HD cells, we trained an algorithm to report the heading solely based on the firing of HD cells (see methods). When tested on untrained periods of HD cell activity, the algorithm accurately decoded the heading of the mice as they explored their environment (Fig. 1E) with an error of only $10.2° \pm 3.5°$ ($n = 6$ mice; See fig. S2, C and D, and methods). How well does the direction of a saccade match the internal representation of a head turn? We quantified the internal representation of a head turn as the difference between the heading decoded 200 ms before and 200 ms after a saccade (Fig. 1F). The vast majority of saccades ($95.2 \pm 1.3\%$, $n = 6$ mice) occurred in the same direction (CW or CCW) as the ongoing head turns decoded from HD cell activity (Fig. 1, G and H). In awake animals, saccade direction and the internal representation of head turns are thus tightly coupled.

Is this relationship maintained during REM sleep? To monitor rapid eye movements during REM sleep, we took advantage of the fact that

[1]Department of Physiology, University of California, San Francisco, San Francisco, CA, USA. [2]Howard Hughes Medical Institute, University of California, San Francisco, San Francisco, CA, USA.
*Corresponding author. Email: yuta.senzai@gmail.com (Y.S.); massimo@ucsf.edu (M.S.)

Fig. 1. Saccade direction predicts internal representation of head turns. (**A**) Schematic of the experimental configuration illustrating a chronic electrophysiological recording from the ADN while eye and head movements are monitored with cameras. (**B**) Schematic illustration of the open-field arena with a mouse carrying head-mounted eye cameras and silicon probes. The heading of the animal is monitored with a top-view camera. IR LED, infrared light-emitting diode. (**C**) An example frame from the top-view camera is shown at the top left, and a schematic illustration of the frame is shown at the top right. The top and bottom middle panels present example frames showing a CCW turn and a CW turn, respectively. Arrows indicate the heading of the animal in each frame. (**D**) The tuning curves of 11 example HD cells recorded from the ADN of an awake mouse. The arrows on the right indicate the preferred HD of each HD cell. Peak firing rates for HD cells are shown on the right. (**E**) Shown at the top is a raster plot of the firing of the 11 example HD cells shown in (D). Middle traces illustrate the actual heading of the animal (gray) and heading decoded from the population activity of HD cells (green). Triangles mark the timing of example frames for the CCW turn (cyan) and CW turn (magenta) shown in (C). Bottom traces illustrate the horizontal position of the two eyes (red and blue). The vertical dashed lines indicate the onset of saccades. (**F**) Two snapshots of the right eye taken before and after a CCW saccade are shown at the top. The pupil is delineated with a black circle. A dashed circle in the right image labels the pupil's original position (N, nasal commissure; T, temporal commissure). The red trace illustrates the right eye's horizontal position in time. Saccade amplitude was defined as the change in the horizontal eye position upon a saccade. The green trace illustrates the decoded heading. The head-turn amplitude is the change in the decoded heading between 200 ms before and 200 ms after saccade onset. Note the CCW shift in decoded heading concomitant with the CCW saccade. (**G**) Summary scatter plot of the amplitude of conjugated saccades during the
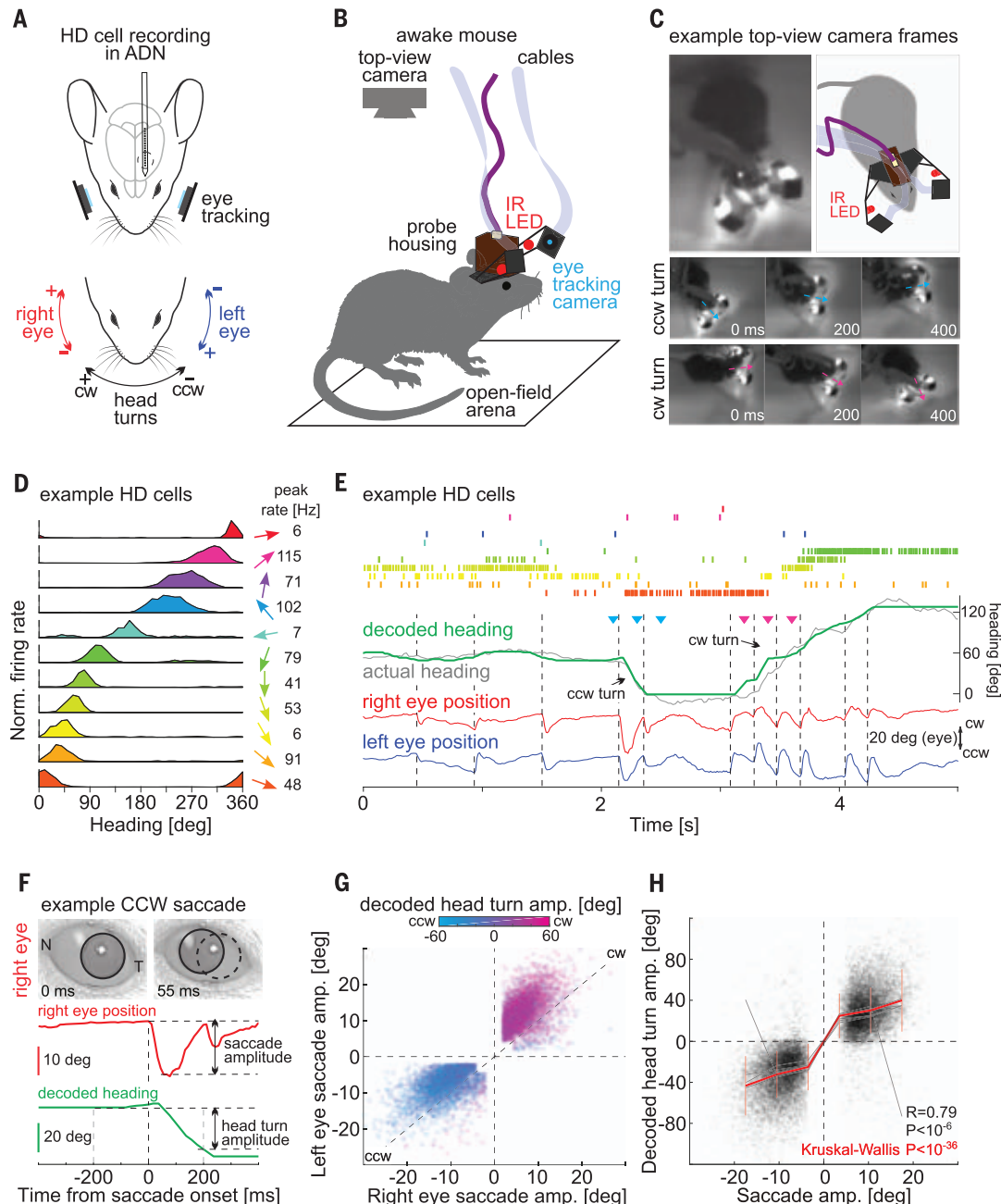

exploration in the open field arena (n = 13,778 from six mice). The amplitude and sign of the decoded head turn during the saccade are color coded. Note that the direction of the saccades matches the direction of the decoded head turn. In this and the rest of the figures, the upper-right and lower-left quadrants of the scatter plots represent CW and CCW movements, respectively. (**H**) Correlation between the amplitude of conjugated saccades (averaged over both eyes) and the decoded head-turn amplitude. Saccade amplitude predicted the amplitude of decoded head turns for each individual mouse (gray lines) as well as for all mice (red line; vertical lines represent standard deviation).

mice do not always close their eyes while asleep (Fig. 2, A and B, and movie S2). We quantified the direction and amplitude of rapid eye movements in the sleeping animal using the head-mounted cameras (23, 24). During REM sleep

(Fig. 2C and see methods), rapid eye movement occurred along the nasotemporal axis (monitored over a total of 68 min of REM sleep in six mice; fig. S3, A and B), and the direction of these movements, CW or CCW, was well correlated

across both eyes (R = 0.58, P < 10⁻⁶; Fig. 2, C to E), thus similar to saccades observed in awake animals (fig. S3C), albeit with smaller amplitudes (average amplitude: 5.1° ± 2.5° for rapid eye movements and 9.7° ± 3.5° for saccades) and
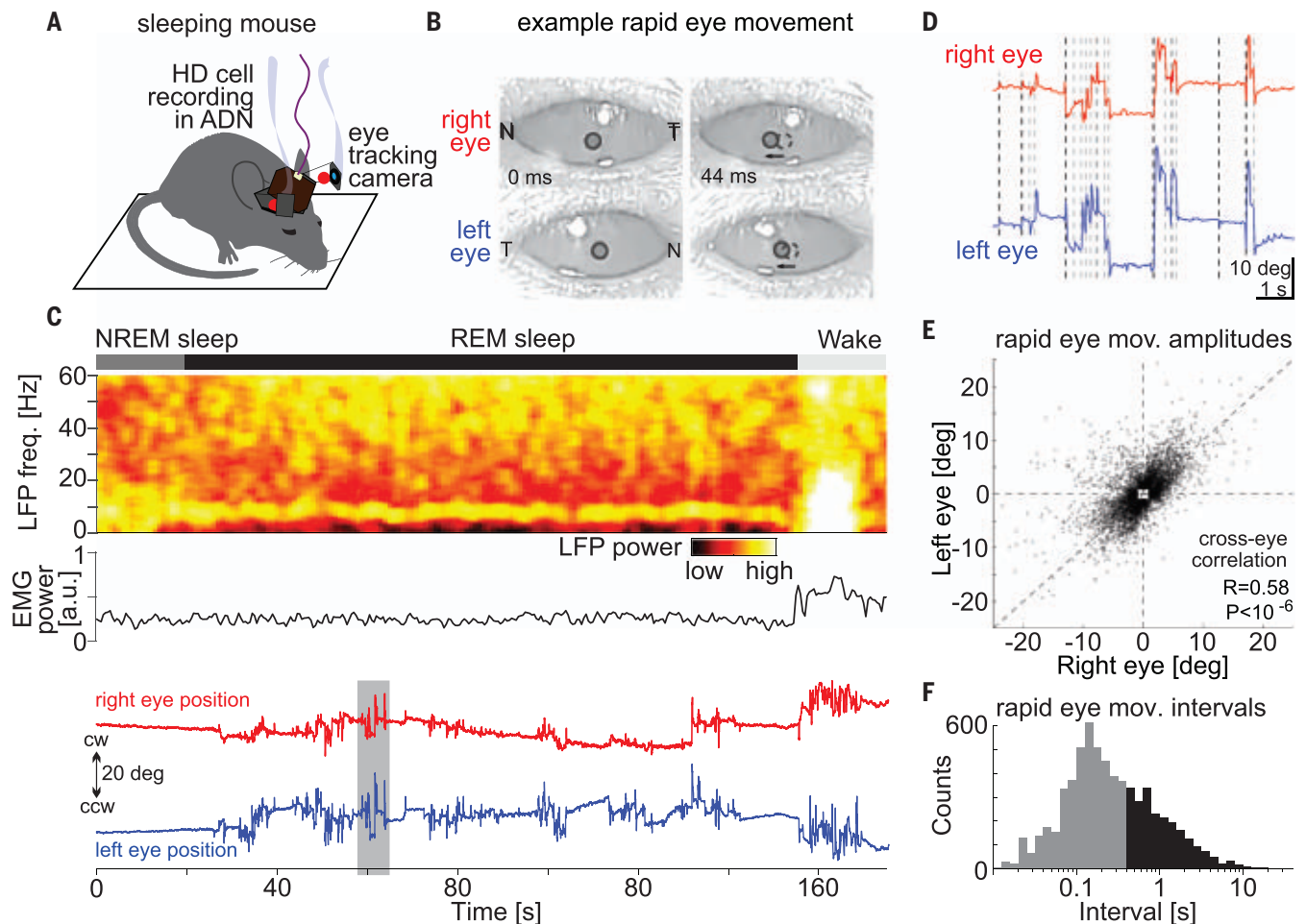
Fig. 2. Rapid eye movements during REM sleep. (**A**) Schematic of the experimental configuration illustrating a chronic electrophysiological recording from the ADN while rapid eye movements are monitored with cameras in a sleeping mouse. (**B**) Snapshots of the right (top) and left (bottom) eye before (left) and after (right) a CCW rapid eye movement. The pupil is delineated with a black circle. A dashed circle in the right image labels the pupil's original position. Note that both eyes move CCW. (**C**) An example spectrogram of the local field potential (LFP) recorded in the ADN during non-REM sleep (NREM), REM sleep, and wakefulness (Wake) is shown at the top. Electromyography (EMG) power is shown in the middle. The horizontal position of the two eyes (red and blue) is shown at the bottom. Note the increase in eye movements at the onset of REM sleep. a.u., arbitrary units. (**D**) The shaded time interval in (C) shown on an expanded time scale. Note that for most rapid eye movements, both eyes moved to the same direction. Dashed black and gray vertical lines indicate the onset of leading (not preceded by a rapid eye movement for at least 400 ms) and follower rapid eye movements. (**E**) Scatter plots of the amplitude of right versus left rapid eye movements during REM sleep for all mice (n = 6689 from six mice). Note that most data points are in the lower-left or upper-right quadrants, indicating CCW and CW movements of both eyes. (**F**) Distribution of intervals between rapid eye movements during REM sleep for all mice (n = 6689 from six mice). Leading eye movements are in black, and followers are in gray.

at higher frequency (median interval: 267 ms for rapid eye movements and 521 ms for saccades; Fig. 2F and fig. S1D).
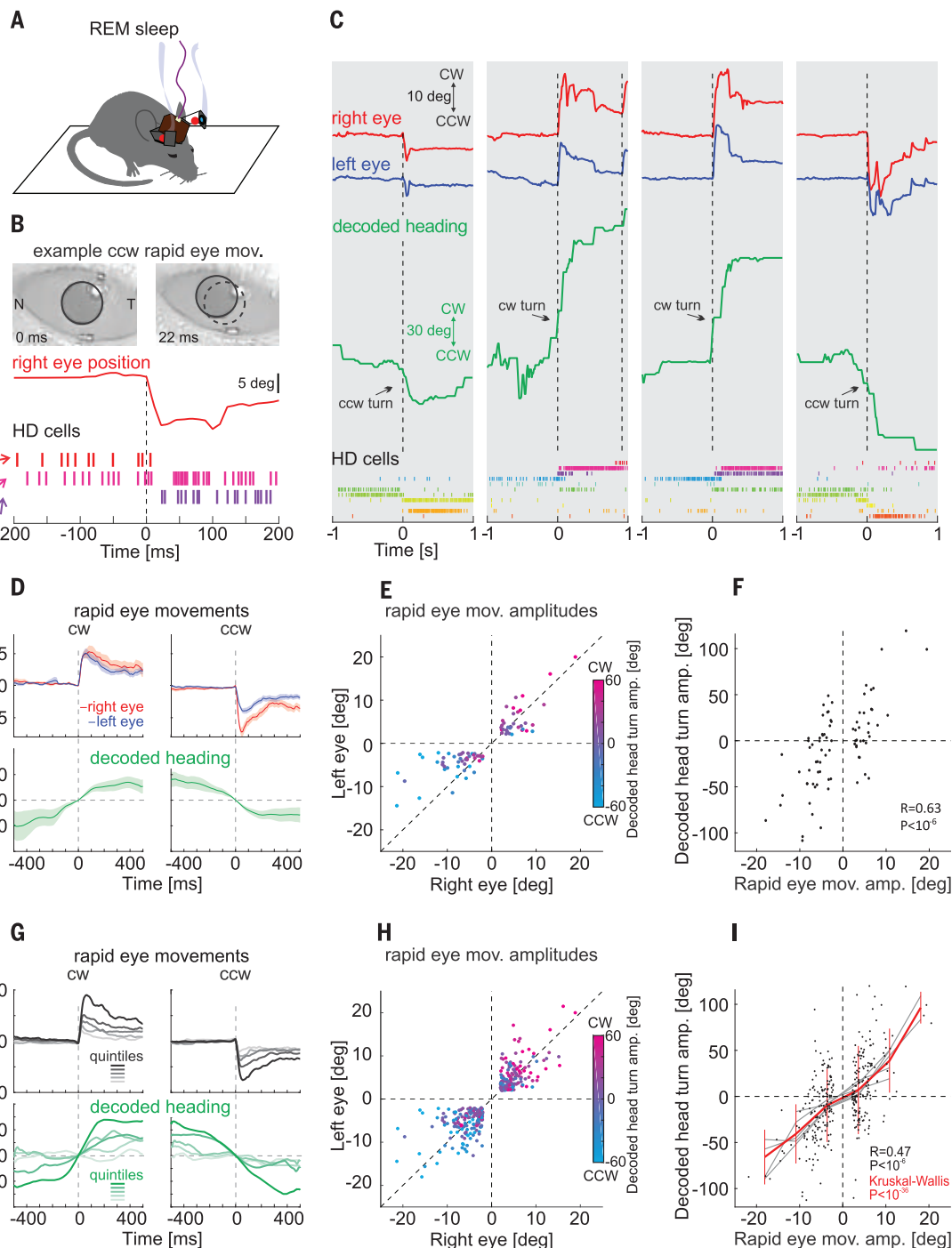
We decoded the internal representation of heading during REM sleep, that is, the virtual heading, by applying the algorithm described above. Virtual heading was decoded from the activity of the same set of HD cells that was used to train the algorithm, this time, however, recorded during REM sleep. Changes in virtual heading, that is, virtual turns, occurred with an angular velocity that was similar to that decoded during actual turns in awake mice exploring the arena (fig. S4, A and B), consistent with previous results (19). Further-

more, during REM sleep, HD cells maintained a similar correlational structure as that observed during wakefulness: HD cells that either fired or did not fire together in wakefulness exhibited the same pattern during REM sleep (fig. S4, C and D). To test the relationship between rapid eye movements and virtual heading, we first focused our analysis on rapid eye movements that were not preceded by any eye movement for at least 400 ms (Fig. 2F) and in which both eyes moved by at least 2° in the same direction (i.e., conjugated rapid eye movements; see methods). This allowed us to have a sufficiently long baseline to detect potential changes in virtual heading that were specif-

ically associated with the selected conjugated rapid eye movements. We refer to these rapid eye movements as "leading" eye movements. The direction of leading rapid eye movements matched the direction of simultaneously recorded virtual turns (Fig. 3, A to C). A CCW leading rapid eye movement, for example, occurred as the ensemble activity of HD cells shifted CCW (Fig. 3B), and vice versa (Fig. 3C). Overall, during REM sleep, the direction of leading rapid eye movements predicted the direction of the changes in virtual heading, both in each individual mouse (Fig. 3, D to F, and fig. S5) as well as in the population (Fig. 3, G and H). Furthermore, not only the direction

Fig. 3. Leading rapid eye movements predict decoded head turns during REM sleep. (**A**) Schematic of the experimental configuration (same as Fig. 2A). (**B**) Two snapshots of the right eye during REM sleep taken before and after a CCW rapid eye movement are shown at the top. The red trace illustrates the right eye's horizontal position in time. A raster plot of the firing of three example HD cells (out of the 11 HD cells illustrated in Fig. 1D, with the same color coding) is shown at the bottom. Note the CCW shift in heading representation concomitant with the CCW rapid eye movement. (**C**) Four example episodes illustrating a concomitant shift in decoded heading and eye position during REM sleep. The top traces illustrate the horizontal position of the two eyes (red and blue) and decoded heading (green). The vertical dashed lines indicate the onset of leading rapid eye movements. Shown at the bottom is a raster plot of the firing of the 11 example HD cells (same as in Fig. 1D). (**D**) The average relative position of the right (red) and left (blue) eyes for CW (left) and CCW (right) leading eye movements is shown at the top. The average decoded heading (green) is shown at the bottom. Shaded areas are standard error of the mean [average of 34 traces for CW and 47 traces for CCW leading eye movements]. (**E**) Scatter plot of the amplitude of

leading right versus left eye movements during REM sleep. The amplitude and sign of the decoded head turns during the eye movements are color coded. Note the good match between the direction of the rapid eye movements and the direction of the decoded head turn. (**F**) Correlation between the amplitude of leading eye movements during REM sleep (averaged over both eyes) and the decoded head-turn amplitude. For (B) to (F), the representative mouse is the same as that in Fig. 1, C to E. (**G**) Mean traces of horizontal eye position averaged across both eyes for CW (left) and CCW (right) leading eye movements (*n* = 6 mice) are shown at the top. The dataset was separated into quintiles based on the amplitude. Mean traces of the decoded heading in each quintile based on the

amplitude of leading rapid eye movements are shown at the bottom. Note that leading rapid eye movements with larger amplitude coincide with larger decoded head turns. (**H**) Summary scatter plot of the amplitude of leading right versus left eye movements during REM sleep (*n* = 330 from six mice). The amplitude and sign of the decoded head turns during the eye movements are color coded. (**I**) Correlation between the amplitude of leading eye movements during REM sleep and the decoded head-turn amplitude (*n* = 330 from six mice). Leading rapid eye movements predicted the direction and amplitude of decoded head turns in each individual mouse (gray lines) as well as for all mice (red line; vertical lines indicate standard deviation).

A

example first followers

B

**correlation between rapid eye movements
and decoded heading**
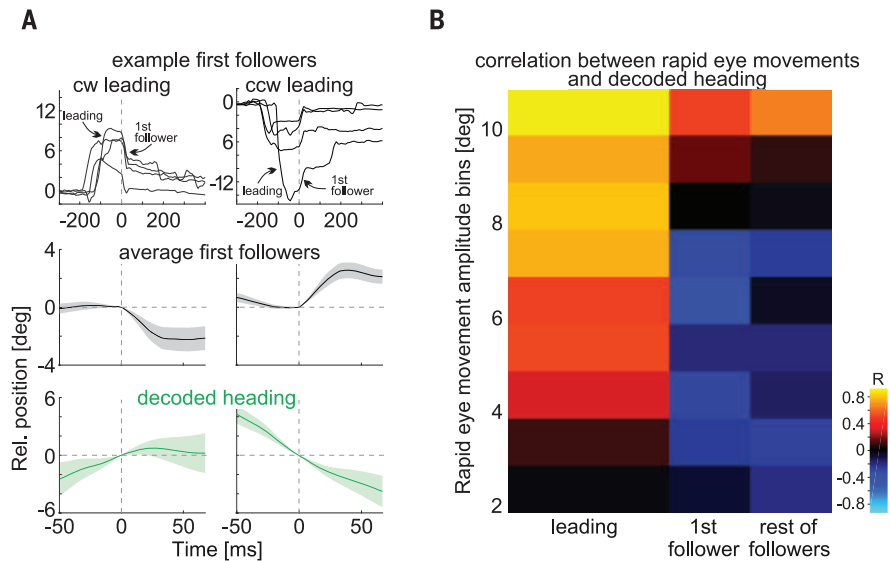
Fig. 4. Small-amplitude follower eye movements represent recentering eye movements. (**A**) Example traces of horizontal eye position (averaged across both eyes) aligned to the onset of first follower rapid eye movement after a CW (left) and CCW (right) leading eye movement are shown at the top. Average relative positions (mean of both eyes) for first follower eye movements after CW (left) and CCW (right) relative movement (average over 132 traces for CW and 107 traces for CCW from six mice) are shown in the middle. Average traces of concomitantly decoded heading are shown at the bottom. Note that, on average, first followers occur in the opposite direction as compared to the preceding leading eye movement and to the decoded head turn. Shaded areas represent standard error of the mean. The time scale of the top panels covers a larger interval to include the preceding leading eye movement. (**B**) Correlation (heatmap) between the decoded head-turn amplitude and amplitude of rapid eye movement (in bins; averaged for both eyes; y axis). The first column from the left shows leading eye movements (n = 330 from six mice), the second column shows first followers (n = 239 from six mice), and the third column shows the rest of the followers (n = 970 from six mice). Note the increased positive correlation with increasing eye movement amplitude.

of the leading eye movements but also their amplitude provided information about the ongoing internal representation of heading: the larger the amplitude of the leading rapid eye movement, the larger the angle of the simultaneously recorded virtual turn (Fig. 3, G to I).

What is the relationship between rapid eye movements that follow leading eye movements and the virtual heading of the animal? We refer to these eye movements as "followers," that is, those that occur less than 400 ms after another rapid eye movement. The above results (top panels of Fig. 3, D and G) show that the average position of the eye following a leading eye movement progressively returns to the original position occupied before the leading movement, as if recentering the eye [400 ms after a leading eye movement, the eye returned to 34.1 ± 3.3% (mean ± SEM) relative to its peak position after the leading eye movement]. By contrast, the simultaneously decoded virtual heading did not (bottom panels of Fig. 3, D and G). If the recentering of the eye is mediated by followers, the direction of these rapid eye movements should be opposite relative to that of leading eye movements and to the ongoing changes in virtual heading. Indeed,

the direction of followers that occur immediately after a leading eye movement (first followers) were, on average, opposite to the direction of the preceding leading eye movement (Fig. 4A and fig. S6A) and thus opposite to the direction of the ongoing head turns (Fig. 4, A and B, and fig. S6, B and C). Overall, the direction of followers was opposite to the direction of changes in virtual heading, but for the small fraction of followers (4.3%) with the largest amplitudes (>10°; Fig. 4B and fig. S6, D and E) that, like leading eye movement, matched the directions of virtual head turns.

Taken together, these data demonstrate a tight relationship between rapid eye movements and the internal representation of the heading of the animal during REM sleep (Fig. 4B). Not only does the direction of leading rapid eye movements predict the direction of change in virtual heading, but their amplitude predicts the magnitude of the change. Conversely, follower eye movements recenter the eye. Thus, our results demonstrate that rapid eye movements provide a readout of the internal representation of heading in the sleeping brain. The coordination between rapid eye movements during REM sleep and the HD system

suggests that shifts in virtual heading are part of a globally orchestrated representation of "virtual navigation" by the sleeping brains rather than the result of some uncorrelated random walk of the HD system (20).

How do eye movements that occur during REM sleep map onto eye movements observed during wakefulness? Leading rapid eye movements may correspond to saccades because both match the direction of the ongoing head turn, virtual or real (21, 22, 25). Follower eye movements, however, appear unlike any eye movement in the awake animal. In the awake mouse, the recentering of the eye after a saccade is mediated by image stabilizing reflexes—the vestibular and optokinetic reflexes—that are engaged by the ongoing head turn (21, 22, 25). In the sleeping, motionless animal, however, the sensory periphery that triggers these reflexes is not engaged. It is conceivable that recentering eye movements during REM sleep may still be triggered by activity in the vestibular nuclei. Such activity, although independent of the sensory periphery, could be part of the globally orchestrated virtual navigation mentioned above.

Whether rapid eye movements in REM sleep reveal the subjects' direction of gaze in the imagery of dreams has been debated since the discovery of this sleep phase and its association with vivid dreams (7–13). Because of the lack of objective measures that assess the content of dreams, initial studies have led to conflicting results, leading to the conclusion that rapid eye movements are likely uncorrelated with the cognitive activity of the sleeping brain (12, 13). More recently, studies performed on human patients or animal models that partially enact their dreams because of reduced muscle atonia during REM sleep have led to a reevaluation of the original hypothesis (26, 27). In these studies, at least some rapid eye movements appeared to be coordinated with the direction of the behavior enacted during REM sleep. However, the extent to which the coordination between eye and body movement is a result of the pathological or experimentally reduced atonia still remains unclear.

By harnessing the HD system of the rodent and the correlation between orienting head and eye movements in awake animals, we have established a clear relationship between changes in virtual heading and rapid eye movements during REM sleep. Thus, our results indicate that rapid eye movements provide an external readout of an internal cognitive process that is occurring during REM sleep, namely the change in virtual heading. Our results further suggest the existence of a globally coordinated activity among distinct systems in the sleeping brain during REM sleep, a coordination that may underlie the realistic and vivid experience of dreams. Understanding the neurophysiological mechanisms of this coordination will give us

insight into the organization of the brain's generative model of the world (28, 29).

REFERENCES AND NOTES

1. E. Aserinsky, N. Kleitman, *Science* **118**, 273–274 (1953).
2. M. Jouvet, *Prog. Brain Res.* **18**, 20–62 (1965).
3. M. S. Blumberg, J. A. Lesku, P.-A. Libourel, M. H. Schmidt, N. C. Rattenborg, *Curr. Biol.* **30**, R38–R49 (2020).
4. J. B. Jaggard, G. X. Wang, P. Mourrain, *Curr. Opin. Neurobiol.* **71**, 44–51 (2021).
5. J. A. Hobson, *Nat. Rev. Neurosci.* **10**, 803–813 (2009).
6. Y. Nir, G. Tononi, *Trends Cogn. Sci.* **14**, 88–100 (2010).
7. W. Dement, N. Kleitman, *J. Exp. Psychol.* **53**, 339–346 (1957).
8. H. P. Roffwarg, W. C. Dement, J. N. Muzio, C. Fisher, *Arch. Gen. Psychiatry* **7**, 235–258 (1962).
9. R. J. Berger, I. Oswald, *Science* **137**, 601 (1962).
10. J. H. Herman *et al.*, *Sleep* **7**, 52–63 (1984).
11. I. Arnulf, *Arch. Ital. Biol.* **149**, 367–382 (2011).
12. E. Moskowitz, R. J. Berger, *Nature* **224**, 613–614 (1969).
13. L. Jacobs, M. Feldman, M. B. Bender, *Psychophysiology* **9**, 393–401 (1972).
14. N. H. Kerr, D. Foulkes, M. Schmidt, *J. Nerv. Ment. Dis.* **170**, 286–294 (1982).
15. G. Vanni-Mercier, G. Debilly, *Neuroscience* **86**, 571–585 (1998).
16. J. B. Ranck, *Soc. Neurosci. Abstr.* **10**, 599 (1984).
17. J. S. Taube, R. U. Muller, J. B. Ranck Jr., *J. Neurosci.* **10**, 436–447 (1990).
18. J. S. Taube, *J. Neurosci.* **15**, 70–86 (1995).
19. A. Peyrache, M. M. Lacroix, P. C. Petersen, G. Buzsáki, *Nat. Neurosci.* **18**, 569–575 (2015).
20. R. Chaudhuri, B. Gerçek, B. Pandey, A. Peyrache, I. Fiete, *Nat. Neurosci.* **22**, 1512–1520 (2019).
21. A. F. Meyer, J. O'Keefe, J. Poort, *Curr. Biol.* **30**, 2116–2130.e6 (2020).
22. A. M. Michaiel, E. T. Abe, C. M. Niell, *eLife* **9**, e57458 (2020).
23. Ö. Yüzgeç, M. Prsa, R. Zimmermann, D. Huber, *Curr. Biol.* **28**, 392–400.e3 (2018).
24. G. Ungurean, D. Martinez-Gonzalez, B. Massot, P. A. Libourel, N. C. Rattenborg, *Curr. Biol.* **31**, 5370–5376.e4 (2021).
25. J. H. Fuller, *Vision Res.* **25**, 1121–1128 (1985).
26. L. Leclair-Visonneau, D. Oudiette, B. Gaymard, S. Leu-Semenescu, I. Arnulf, *Brain* **133**, 1737–1746 (2010).
27. K. Soh, Y. Morita, H. Sei, *Physiol. Behav.* **52**, 553–558 (1992).
28. G. E. Hinton, P. Dayan, B. J. Frey, R. M. Neal, *Science* **268**, 1158–1161 (1995).
29. J. A. Hobson, C. C.-H. Hong, K. J. Friston, *Front. Psychol.* **5**, 1133 (2014).
30. Y. Senzai, M. Scanziani, A cognitive process occurring during sleep is revealed by rapid eye movements. Dryad (2022); https://doi.org/10.7272/Q6P26WDC.

MATERIALS SCIENCE

Structurally integrated 3D carbon tube grid–based high-performance filter capacitor

Fangming Han[1]†, Ou Qian[1,2]†, Guowen Meng[1,2]*, Dou Lin[1,2], Gan Chen[1,2], Shiping Zhang[1,2], Qijun Pan[1,2], Xiang Zhang[1,2], Xiaoguang Zhu[1], Bingqing Wei[3]*

Filter capacitors play a critical role in ensuring the quality and reliability of electrical and electronic equipment. Aluminum electrolytic capacitors are the most commonly used but are the largest filtering components, limiting device miniaturization. The high areal and volumetric capacitance of electric double-layer capacitors should make them ideal miniaturized filter capacitors, but they are hindered by their slow frequency responses. We report the development of interconnected and structurally integrated carbon tube grid–based electric double-layer capacitors with high areal capacitance and rapid frequency response. These capacitors exhibit excellent line filtering of 120-hertz voltage signal and volumetric advantages under low-voltage operations for digital circuits, portable electronics, and electrical appliances. These findings provide a sound technological basis for developing electric double-layer capacitors for miniaturizing filter and power devices.

Filter capacitors play a critical role in ensuring the quality and reliability of electrical and electronic equipment, especially memory devices and computers (1, 2). Circuit filtering has been dominated by aluminum electrolytic capacitors (AECs), which, unfortunately, are always the largest electronic component owing to their low volumetric capacitances (1, 3, 4). Therefore, developing new types of small-sized filter capacitors is vital to meet the current and emerging demands of digital circuits and portable electronics. The high areal and volumetric capacitance of electric double-layer capacitors (EDLCs) should make them an ideal candidate, but this is hindered by their slow frequency response (<1 Hz) (2, 5, 6). Miller *et al.* demonstrated the feasibility of using graphene-based EDLCs for circuit filtering (1). They revealed that the slow response of EDLCs could be modulated to meet the needs of circuit filtering applications by manipulating electrode materials and structures to enhance electrical and ionic conductivities.

EDLCs can be used in filter circuits to convert alternating current (ac) into direct current, however, they are required to have a high-frequency response to smooth the leftover ac ripples (7–12). The electrode materials must have superior electrical conductivity and fast ionic response to achieve rapid frequency performance (13). Additionally, the EDLCs are expected to have a high volumetric (C_V) and areal (C_A) specific capacitance. C_A is a more accurate evaluation index because the electrode thickness would be limited to ensure the rapid distribution of ions onto the inner surfaces to secure the high-frequency response. For a given capacitance, a low C_A will require increasing the active and inactive materials in the EDLC (2, 14), resulting in a low C_V. Currently, EDLCs mainly use nanostructured carbon-based electrodes (15, 16). To achieve a high-frequency response, such EDLCs can only use low loading of active materials, resulting in a subordinate C_A (9, 16, 17). This is because a high loading of active materials, such as graphene or carbon nanotube (CNT) arrays, tends to agglomerate into multilayer forms or bundles, leading to increased resistance to ion distribution and, hence, slow response (18, 19). Although various approaches, such as using vertically structured and macroporous graphene, have been reported, these issues remain unresolved (1, 3, 17). Therefore,

[1]Key Laboratory of Materials Physics and Anhui Key Laboratory of Nanomaterials and Nanotechnology, Institute of Solid State Physics, Hefei Institutes of Physical Science, Chinese Academy of Sciences, Hefei 230031, China. [2]Department of Materials Science and Engineering, University of Science and Technology of China, Hefei 230026, China. [3]Department of Mechanical Engineering, University of Delaware, Newark, DE 19716, USA.
*Corresponding author. Email: gwmeng@issp.ac.cn (G.M.); weib@udel.edu (B.W.)
†These authors contributed equally to this work.
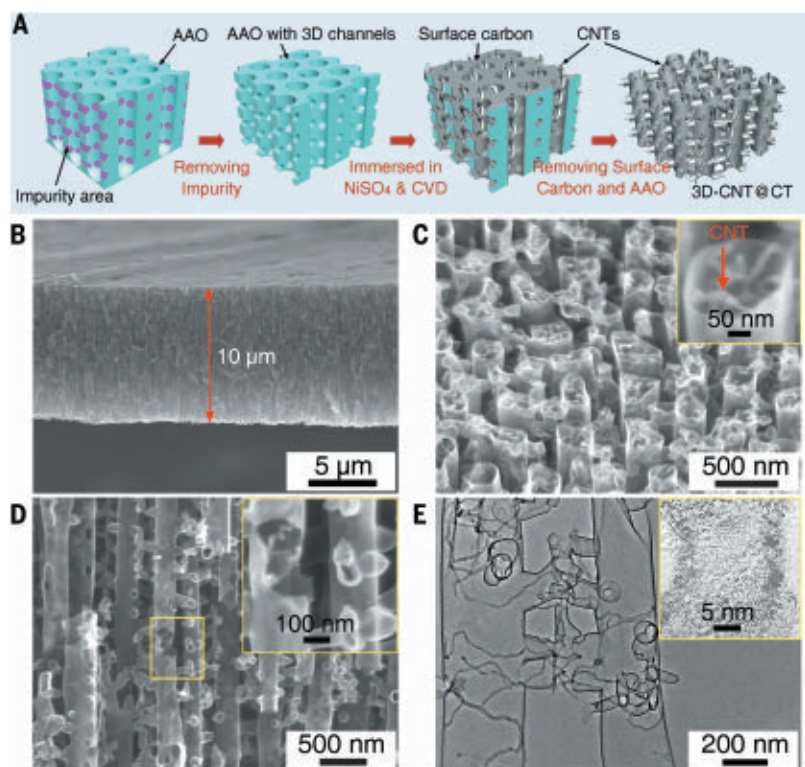
Fig. 1. Synthesis and characteristics of the 3D-CNT@CT grid. (**A**) Schematic illustration of synthetic procedures of the 3D-CNT@CT grid. (**B**) Typical cross-sectional view, (**C**) top view, and (**D**) enlarged cross-sectional view SEM images of 3D-CNT@CT. (Insets) High-magnification SEM images. (**E**) High-resolution TEM image of two adjacent vertical CTs connected by lateral CTs with filling CNTs. (Inset) Magnified TEM image of a CNT.
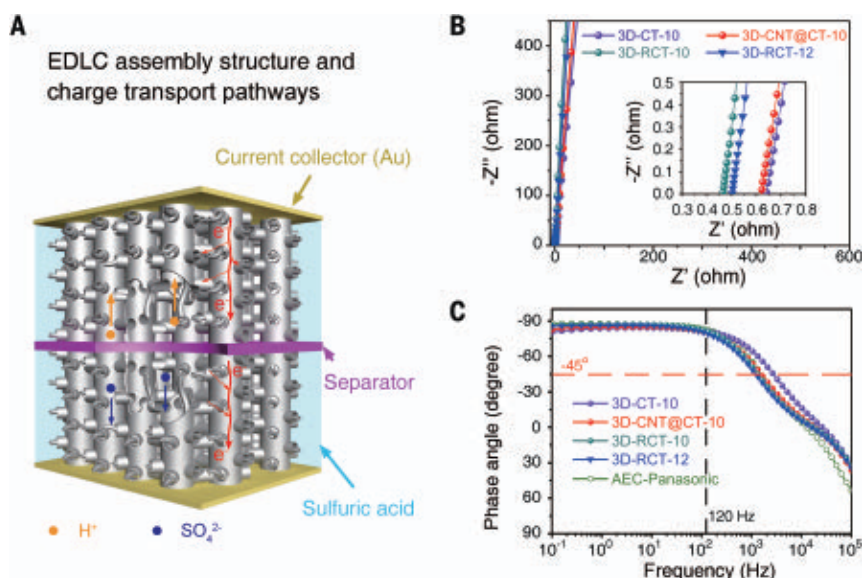
Fig. 2. Assembly structure and electrochemical impedance spectra of the 3D-CTG capacitor. (**A**) Schematic of EDLC assembly structure. (**B**) Complex plane plot of the 3D-CTG–based EDLCs. (**C**) Phase angle versus frequency of 3D-CT-10–, 3D-CNT@CT-10–, 3D-RCT-10–, and 3D-RCT-12–based EDLCs and commercial AEC (Panasonic, Japan, 6.3 V/330 µF).

it is envisaged that a high-performance carbon-based filter EDLC electrode must have superior structural stability to maintain its high volumetric and areal capacitances and fast ion migration under operando conditions.

Here, we demonstrate the fabrication of high-performance line-filtering EDLCs using

a three-dimensional (3D) carbon tube (CT) grid (3D-CTG) as the electrode. This grid, with truly interconnected and structurally integrated vertical and lateral CTs (denoted as 3D-CTs), can provide high structural stability, superior electrical conductivity, and an effective open porous structure and was synthesized by a chemical vapor deposition (CVD) method with the aid of a 3D interconnected nanoporous anodic aluminum oxide (3D-AAO) template (see materials and methods and figs. S1 and S2 in the supplementary materials) (19–21). The 3D-AAO template with lateral pores connecting the adjacent vertical channels was obtained by the anodization of Al foils with Cu impurity to form highly ordered vertically aligned nanochannels with Cu-contained nanoparticles embedded in the channel walls and subsequent selective wet-chemical etching of the nanoparticles (20, 21). The 3D-CTs were constructed after growing CTs inside the 3D-AAO nanoporous template by pyrolyzing acetylene and removing the template. To increase the specific surface area and further enhance C_A, the 3D-CTs can be modified, as exemplified by filling with much-smaller-diameter CNTs within the vertical and lateral CTs (3D-CNT@CT) by means of the Ni catalyst–assisted CVD method (Fig. 1A) (22), or surface-treated with $KMnO_4$ (3D-RCT, i.e., 3D-CT with a rough surface) (fig. S3) (23).

The synthesized 3D-CTG film is flexible, with a diameter of 54 mm and a uniform thickness of 10 µm, and can be controlled using 3D-AAO templates of different sizes and thicknesses (Fig. 1B and fig. S4). Scanning electron microscopy (SEM) images reveal that the 3D-CTG films consist of uniformly distributed vertically aligned CTs, which are interconnected by smaller lateral CTs to form a 3D grid, and for 3D-CNT@CT, much-smaller-diameter CNTs were grown inside the vertical CTs (Fig. 1, C and D, and fig. S5). Transmission electron microscopy (TEM) images show that the vertical and lateral CTs are structurally integrated through chemical means rather than physical attachments (Fig. 1E and fig. S6). Moreover, the rough outer and inner surfaces of the 3D-RCT are also demonstrated (fig. S7).

EDLCs were assembled with two 3D-CTG electrodes of identical thickness [denoted as 3D-CT-10, 3D-CNT@CT-10, 3D-RCT-10, or 3D-RCT-12, where the numbers represent thickness (in micrometers)] separated by a nonwoven membrane with 1 M H_2SO_4 electrolyte (Fig. 2A). The Nyquist plot of the impedance obtained from the EDLCs (Fig. 2B) displays an imaginary response (Z'') almost vertical to the real axis, indicating a near-perfect capacitive characteristic and no porous electrode behavior (1, 24, 25). Also, no features are associated with the series of passive layers, characterized by the high-frequency semicircle (1, 25). The Bode plots (frequency dependence of the phase angle) of

Fig. 3. Frequency-dependent capacitances of 3D-CTG–based EDLCs. (**A** and **B**) C_A and C_V versus frequency of 3D-CT-10–, 3D-CNT@CT-10–, 3D-RCT-10–, and 3D-RCT-12–based EDLCs and commercial AEC. (**C**) Comparison of the C_A at 120 Hz of 3D-CT-10–, 3D-CNT@CT-10–, 3D-RCT-10–, and 3D-RCT-12–based EDLCs and other reported electrochemical capacitors used in the ac filter circuits with the phase angle near or less than −80°. The abbreviations and corresponding phase angles in (C) are as follows: AEC (Panasonic, −83°); VG (vertical graphene, −82°) (*1*); UGN (unzipped graphene nanoribbons, −85°) (*9*); G/CNT (grapheme/CNT, −81.5°) (*15*); ErGO (electrochemical reduction of graphene oxide, −84°) (*7*); POG (perpendicularly oriented graphene, −82°) (*5*); Ti_3C_2/PEDOT:PSS [Ti_3C_2/poly(3,4-ethylenedioxythiophene): poly(styrenesulfonate), −79°] (*13*); CNT (−81°) (*16*); PEDOT:PSS [poly(3,4-ethylenedioxythiophene): poly(styrenesulfonate), −83.6°] (*8*); VOGN (vertically oriented graphene nanosheets, −85°) (*11*); and EOG (edge-oriented graphene, −80.6°) (*27*).
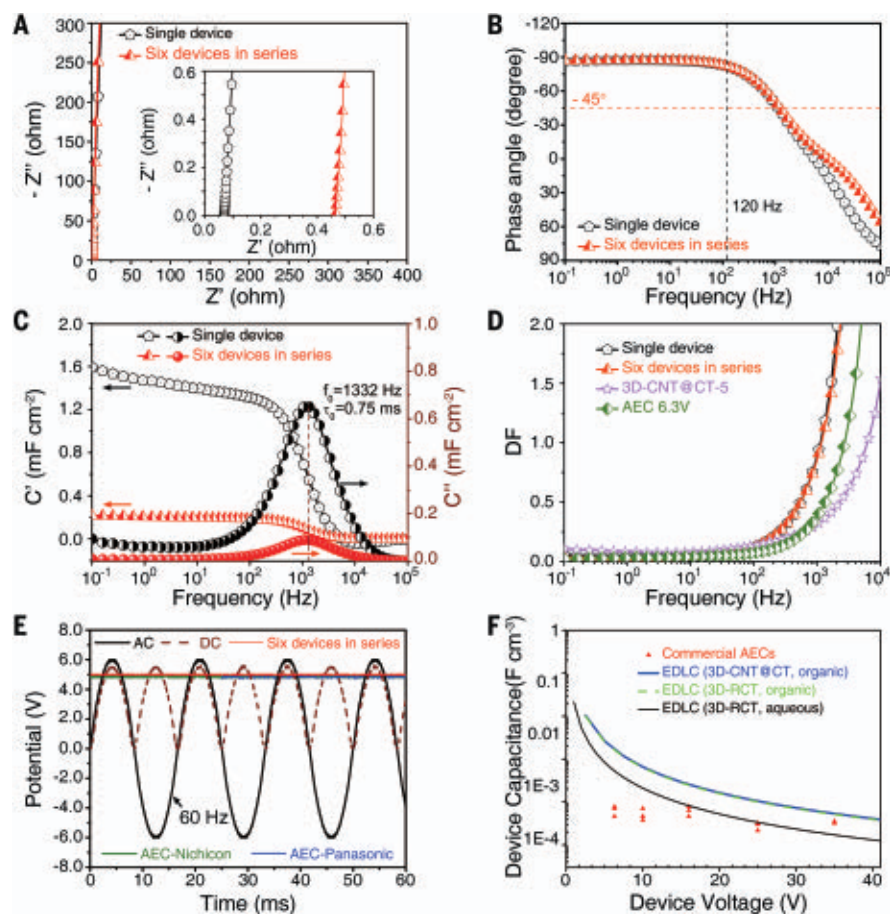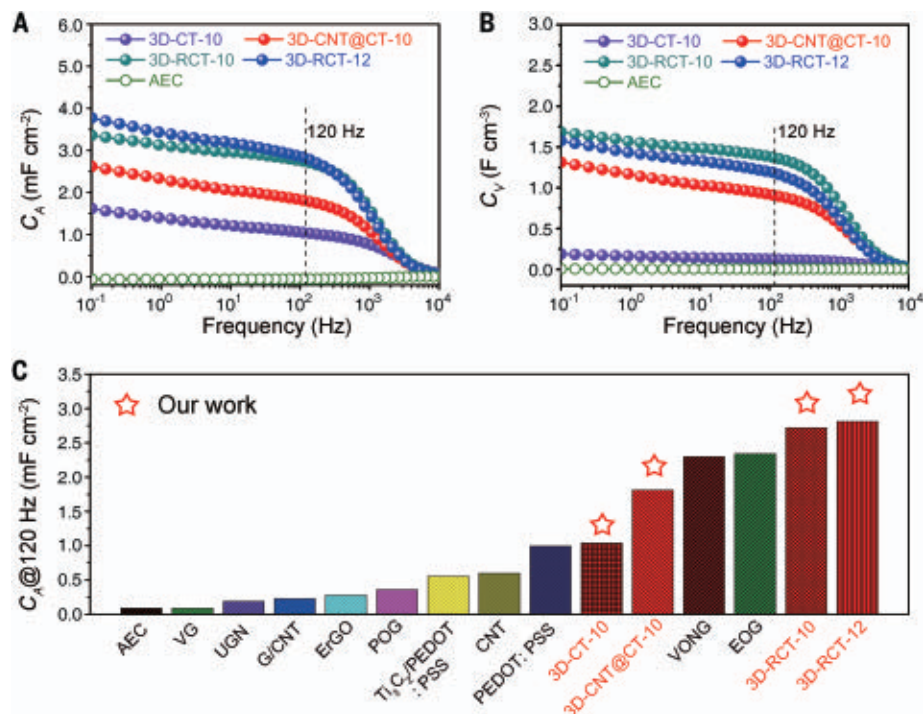
Fig. 4. Performance characteristics of single EDLC and EDLCs in series. (**A**) Nyquist plots. (**B**) Phase angle versus frequency. (**C**) Real and imaginary parts of capacitance versus frequency. (**D**) DF versus frequency. (**E**) Filtering results of the six EDLCs in series in comparison with AECs. (**F**) A volumetric comparison of 3D-CTG–electrode EDLCs with commercial AECs (red triangles; Panasonic, Nichicon, and Nippon, Japan).

the EDLCs and commercial AECs (Fig. 2C and fig. S8) were used to evaluate their frequency responses. An ideal EDLC should have a minimum phase angle of −90° (*1*). The 3D-CTG–based EDLCs and the commercial AEC can achieve phase angles of less than −80° when the frequency is <200 Hz. At a phase angle of −45°, the measured cutoff frequencies ($f_{−45}$; resistance and capacitive reactance are equal, defining the boundary between resistive and capacitive behavior) of 3D-CT-10–, 3D-CNT@ CT-10–, and 3D-RCT-10–based EDLCs and the commercial AEC are 2634, 2360, 1332, and 1502 Hz, respectively. These results demonstrate that the EDLCs built with 3D-CTGs have frequency responses similar to that of the commercial AEC. A low phase angle at 120 Hz is a vital indicator for practical applications of EDLCs as ac line-filtering capacitors. This angle is lower than −81° for the 3D-CTG–based EDLCs, similar to the phase angle of the commercial AEC (−83°, Panasonic Japan, 330 μF, 6.3 V). The excellent and stable ac line-filtering performance is also demonstrated (fig. S9).

The frequency dependences of the areal and volumetric capacitances (Fig. 3, A and B) prove that the 3D-CTG–based EDLCs can deliver much higher capacitances at all frequencies than those of AECs, and only slightly decreased capacitances were observed when the frequency increased from $10^{−1}$ to 10^3 Hz. The C_A of the 3D-RCT-12–based EDLCs can reach 2.81 mF cm$^{−2}$ at 120 Hz, a higher areal-specific capacitance than that of other filtering EDLCs reported to date with a phase angle less than −80° (Fig. 3C and table S1) (*1, 5, 7–9, 11, 13, 16, 26, 27*). The C_V at 120 Hz can

achieve 1.36 F cm^{-3} for 3D-RCT-10 electrodes. These excellent performances—showing the enhancement of structural stability, endorsement of electrical conductivity, and improvement of ion response—illustrate the superiority of the truly interconnected and structurally integrated 3D-CTGs.

To meet the voltage requirements of the ac line filtering, taking the 6.3-V AEC as a benchmark, six EDLCs based on the 1.4-cm-diameter 3D-CT electrodes were assembled in series (fig. S10). The EDLCs in series also show ideal capacitive behavior (fig. S11). To eliminate the influence of the contact resistance, a four-electrode test method was used to evaluate the electrochemical impedance spectroscopy of the EDLCs. Complex plane plots of a single EDLC and the six-EDLC series (Fig. 4A) exhibit close to 90° slopes at a high frequency, which is also characteristic of a pronounced capacitive behavior. Typically, the increase of equivalent series resistance (ESR) caused by capacitors in series would theoretically lead to the degradation of frequency response performance. However, the curves of a single device and the six EDLCs in series showing the frequency dependence of the phase angle in the Bode plots almost exactly overlap below 10^4 Hz (Fig. 4B), and the phase angle at 120 Hz reaches −82°, suggesting that the sixfold increase of ESR does not slow the frequency response. This is mainly because the rise of ESR is accompanied by a corresponding augmentation in capacitive reactance (X_c) (table S2), which would result in high-voltage line-filtering EDLCs.

In the complex model of the capacitance (Fig. 4C), $C'(f)$ represents the accessible capacitance at the corresponding frequency, while $C''(f)$ accounts for energy dissipation due to irreversible processes caused by the diffusion and polarization (28). The 3D CT array structure allows high capacitance to be maintained to frequencies exceeding 120 Hz, and the capacitance of a single EDLC is almost six times that of the six EDLCs in series, which is consistent with the law of capacitors in series. Especially for the single EDLC and six EDLCs in series, $C''(f)$ goes through maximum values at the same frequency, f_0, defining a time constant as $\tau_0 = 1/f_0 = 0.75$ ms, which further confirms that high-performance and high-voltage filtering capacitors can be achieved by connecting EDLCs in series.

In addition, the high-frequency response can also be demonstrated by the variation of C'/C and dissipation factors (DFs) with frequency. The C'/C value approaches 1 below a kilohertz (fig. S11C), indicating the ideal capacitive behavior in this frequency range. The DFs have a very small value at 120 Hz (Fig. 4D), suggesting a slight loss characteristic of the devices. Although there is still a gap with an AEC, a smaller DF can be achieved by adjusting the thickness of the 3D-CTG. More critically, the EDLCs in series also ex-

hibit excellent ac line-filtering performance (Fig. 4E), and the ripple current is ~0.014 A at 120 Hz (calculations given in the supplementary materials).

It is critical to compare the volume of the EDLCs to the comparably rated AECs (Fig. 4F and fig. S12). The calculated capacitance per volume (C_V, in farads per cubic centimeter) for the exemplified 3D-RCT–based EDLC in the aqueous electrolyte is $0.21/V^2$, where V is the voltage rating (all components included). The volumetric capacitances are much higher than a commercial AEC when the operation voltage is below ~10 V. To increase operating voltages, the organic electrolyte (tetraethylammonium tetrafluoroborate in acetonitrile) was used (figs. S13 and S14; calculations given in the supplementary materials). The volumetric capacitance to rated voltage increases to $0.66/V^2$, and then volumetric advantages over an AEC are expanded to voltages below ~25 V, exhibiting considerable advantages in low-voltage operations for digital circuits, portable electronics, and small appliances and meeting the roadmap of low operating voltage in high-performance devices and systems (29). The comparison of CV/v value (the amount of electric charge stored per volume, V is voltage, and v is volume) shows a similar result (fig. S15). It should be noted that given the low operation voltage of an individual EDLC, more EDLCs must be connected in series to reach a higher-rated voltage. Further optimization to achieve volumetric advantages at higher voltages is also possible through applying in-plane interdigitated electrode configuration and using solid or ionic electrolytes (25, 30). The developed 3D-CTG–based EDLCs to replace the bulky AECs would benefit the miniaturization of portable electronics, mobile power supply, electrical appliances, and distributed energy harvesting and power supply on the Internet of Things, greatly promoting the development of high-performance digital circuits and emerging electronic technologies.

In this study, we have successfully synthesized freestanding thin films with 3D truly interconnected, structurally integrated CT grids. The freestanding thin films of 3D-CT, 3D-CNT@CT, and 3D-RCT have been innovatively used to fabricate EDLCs with demonstrated effectiveness to resolve the critical bottleneck issues of slow frequency response of the existing carbon-based EDLCs as ac line-filtering capacitors and the low C_A and C_V faced by commercial AECs. These encouraging results pave the way for the miniaturization of filtering capacitors with high capacitance using carbon-based electrodes, which is essential for current and emerging portable electronics.

REFERENCES AND NOTES

1. J. R. Miller, R. A. Outlaw, B. C. Holloway, *Science* 329, 1637–1639 (2010).
2. Z. Y. Fan, N. Islam, S. B. Bayne, *Nano Energy* 39, 306–320 (2017).
3. F. Y. Chi *et al.*, *Adv. Energy Mater.* 7, 1700591 (2017).
4. K. U. Laszczyk *et al.*, *Adv. Energy Mater.* 5, 1500741 (2015).
5. G. F. Ren, X. Pan, S. Bayne, Z. Y. Fan, *Carbon* 71, 94–101 (2014).
6. M. F. El-Kady, V. Strong, S. Dubin, R. B. Kaner, *Science* 335, 1326–1330 (2012).
7. K. Sheng, Y. Sun, C. Li, W. Yuan, G. Shi, *Sci. Rep.* 2, 247 (2012).
8. M. Zhang *et al.*, *Energy Environ. Sci.* 9, 2005–2010 (2016).
9. J. Lim *et al.*, *Nat. Commun.* 7, 10364 (2016).
10. L. Huang, L. Dai, *Angew. Chem. Int. Ed.* 56, 6381–6383 (2017).
11. D. Premathilake *et al.*, *J. Electrochem. Soc.* 165, A924–A931 (2018).
12. M. Wu *et al.*, *Nat. Commun.* 10, 2855 (2019).
13. G. S. Gund *et al.*, *Joule* 3, 164–176 (2019).
14. N. A. Kyeremateng, T. Brousse, D. Pech, *Nat. Nanotechnol.* 12, 7–15 (2017).
15. J. Lin *et al.*, *Nano Lett.* 13, 72–78 (2013).
16. Y. Rangom, X. S. Tang, L. F. Nazar, *ACS Nano* 9, 7248–7255 (2015).
17. D. Premathilake, R. A. Outlaw, S. G. Parler, S. M. Butler, J. R. Miller, *Carbon* 111, 231–237 (2017).
18. H. Sun *et al.*, *Science* 356, 599–604 (2017).
19. M. Tian *et al.*, *Nano Energy* 11, 500–509 (2015).
20. I. S. Molchan, T. V. Molchan, N. V. Gaponenko, P. Skeldon, G. E. Thompson, *Electrochem. Commun.* 12, 693–696 (2010).
21. J. Vanpaemel, A. M. Abd-Elnaiem, S. De Gendt, P. M. Vereecken, *J. Phys. Chem. C* 119, 2105–2112 (2015).
22. J. Shi, Y. F. Lu, K. F. Tan, X. W. Wang, *J. Appl. Phys.* 99, 024312 (2006).
23. G. Wang *et al.*, *Adv. Mater.* 26, 2676–2682 (2014).
24. Z. S. Wu, Z. Liu, K. Parvez, X. Feng, K. Müllen, *Adv. Mater.* 27, 3669–3675 (2015).
25. J. R. Miller, R. A. Outlaw, *J. Electrochem. Soc.* 162, A5077–A5082 (2015).
26. N. Islam *et al.*, *Nano Energy* 40, 107–114 (2017).
27. W. Y. Li, S. Azam, G. Z. Dai, Z. Y. Fan, *Energy Storage Mater.* 32, 30–36 (2020).
28. C. G. Zhang, H. Z. Du, K. Ma, Z. H. Yuan, *Adv. Energy Mater.* 10, 2002132 (2020).
29. Institute for Electrical and Electronics Engineers (IEEE), "International roadmap for devices and systems (IRDS): Beyond CMOS, 2021 Update" (IEEE, 2021); https://irds.ieee.org/images/files/pdf/2021/2021IRDS_BC.pdf.
30. M. F. El-Kady, R. B. Kaner, *Nat. Commun.* 4, 1475 (2013).

SUPPLEMENTARY MATERIALS

FAUNAL DECLINE

Collapse of terrestrial mammal food webs since the Late Pleistocene

Evan C. Fricke[1,2,3]*, Chia Hsieh[1], Owen Middleton[4], Daniel Gorczynski[1], Caroline D. Cappello[5], Oscar Sanisidro[6], John Rowan[7], Jens-Christian Svenning[8], Lydia Beaudrot[1]

Food webs influence ecosystem diversity and functioning. Contemporary defaunation has reduced food web complexity, but simplification caused by past defaunation is difficult to reconstruct given the sparse paleorecord of predator-prey interactions. We identified changes to terrestrial mammal food webs globally over the past ~130,000 years using extinct and extant mammal traits, geographic ranges, observed predator-prey interactions, and deep learning models. Food webs underwent steep regional declines in complexity through loss of food web links after the arrival and expansion of human populations. We estimate that defaunation has caused a 53% decline in food web links globally. Although extinctions explain much of this effect, range losses for extant species degraded food webs to a similar extent, highlighting the potential for food web restoration via extant species recovery.

Human activities have caused global extinction or local extirpation of many animal species (*1*). Habitat loss, direct exploitation, invasive species, and other global change drivers have contributed to recent defaunation (*2*), which in turn has caused cascading impacts on biodiversity and ecosystem functioning through disruption of food webs (*1*, *3*, *4*). Yet defaunation, and the potential for food web disruption, is not only a contemporary phenomenon. Declines in species diversity since the last interglacial period (~130,000 years ago) are well known for groups such as terrestrial mammals (*5*, *6*). Although there are persistent discussions on the relative roles of humans, climate, and their interactions as drivers of these extinctions, the spatiotemporal pattern of declines strongly suggests a major human role (*5*, *7–9*). The past, and ongoing, selective loss of large-bodied mammals has caused a marked downsizing of mammal assemblages relative to the preceding 30 million years (*7*). The strong ecological effects of human-induced food web disruption observed in recent decades (*10*) raise questions regarding the global magnitude and timing of food web changes that have resulted from extinctions, local extirpation, and species introductions throughout human history and prehistory. However, evidence of species-specific predator-prey interactions has seldom been preserved in the fossil record (*11*), and the scarcity of fossil evidence has prevented direct quantification of past defaunation's effects on food webs.

When direct observations are unavailable, researchers can construct food webs by modeling predator-prey interactions; ecologists commonly use two approaches. First, trait-matching models examine how an ecologically relevant trait of predator or prey species relates to observed interactions. Body mass is recognized as a key trait, and the ratio of predator to prey body mass is a central determinant of food web interactions (*12–14*). By fitting a model using interaction observations and body mass ratios, researchers can estimate interactions given masses of candidate predator and prey species (*15–18*). Second, phylogenetic models rely on closely related species preying on, or being preyed on by, other sets of closely related species. Using observed interactions from the field or literature, researchers may estimate that a predator that is known to prey on one member of a genus would also prey on another member of the genus (*19*, *20*). A third approach, which extends the trait-matching approach to multiple traits and complex relationships among them, uses machine learning algorithms trained on observed interactions to predict interactions among candidate species on the basis of their traits (*21*). For each of the three approaches, researchers use a simplifying assumption that species have similar interaction determinants over space and time. This allows researchers to predict food webs given any scenario of species composition, which can include reconstructing food webs that likely occurred under past species composition, generating current food webs in regions where food webs have not been recorded directly, and forecasting future food webs under altered species composition. Most existing applications have reconstructed food webs over time at regional scales using body mass data (*15*, *17*, *22*).

Here, we provide a global reconstruction of terrestrial mammal food webs by modeling predator-prey interactions through a synthesis of data on observed interactions and species

traits. Although food webs involving only mammals represent just a portion of the food web encompassing all species, a spatiotemporal reconstruction of mammal food webs is possible because of the strong fossil record and data on modern predator-prey interactions available for this group (*23*). We assembled a global database encompassing >17,000 unique predator-prey records for co-occurring pairs of extant mammal species from the scientific literature and existing databases of predator-prey interactions (*24*, *25*). We used a synthesis of trait databases (*26*) covering extant and extinct mammals to characterize each species based on variables related to morphology, life history, and ecology (*27*). To assess the ability to predict predator-prey interactions globally using each of the approaches described above, we built a model using 75% of the records and tested its predictive performance on the 25% of records withheld (table S1). The deep learning model strongly outperformed the commonly applied approaches that are based on body mass ratio or genus-level information; when fitted using the full dataset, it achieved 90% accuracy [area under curve (AUC) = 0.93; kappa = 0.52; true skill statistic (TSS) = 0.69].

To illustrate how the deep learning model can be used to reconstruct food webs, Fig. 1 demonstrates, for several locations, food webs generated under alternate scenarios of mammal species composition. The two scenarios shown here represent extant species' current ranges or ranges of both extant and extinct mammals as they would occur today in the absence of human-linked extinction, local extirpation, or introduction from the Late Pleistocene to the present day (*6*). The range reconstructions leverage historical records and fossil evidence to model ranges while accounting for range shifts due to climatic changes since the Late Pleistocene (*27*). Comparisons among species composition scenarios allow us to assess how defaunation at sites worldwide has led to the simplification of food webs.

Having developed the capacity to generate food webs given alternate scenarios of species composition, we sought to quantify how extinctions have affected food webs over time and to assess food web resilience to extinction. We used estimates of extinction dates from the fossil record (*5*) and focused on species extinction at regional scales because detailed temporal estimates of range changes are unavailable for most species. Figure 2 shows change over time, averaged within each region, in two basic measures of food web complexity: the number of species participating in a food web, and the number of food web links (*28*). To examine whether a reduction in the number of species present led to a decline in food web properties different from that expected by chance, we compared observed changes in food web complexity to a null model in which the same

[1]Department of BioSciences, Rice University, Houston, TX, USA. [2]Department of Biology, University of Maryland, College Park, MD, USA. [3]Department of Civil and Environmental Engineering, Massachusetts Institute of Technology, Cambridge, MA, USA. [4]School of Life Sciences, University of Sussex, Brighton, UK. [5]Department of Biology, University of Washington, Seattle, WA, USA. [6]Departamento Ciencia de la Vida, Universidad de Alcalá, Alcalá de Henares, Spain. [7]Department of Anthropology, University at Albany, Albany, NY, USA. [8]Center for Biodiversity Dynamics in a Changing World (BIOCHANGE), Department of Biology, Aarhus University, Aarhus, Denmark.
*Corresponding author. Email: evancfricke@gmail.com
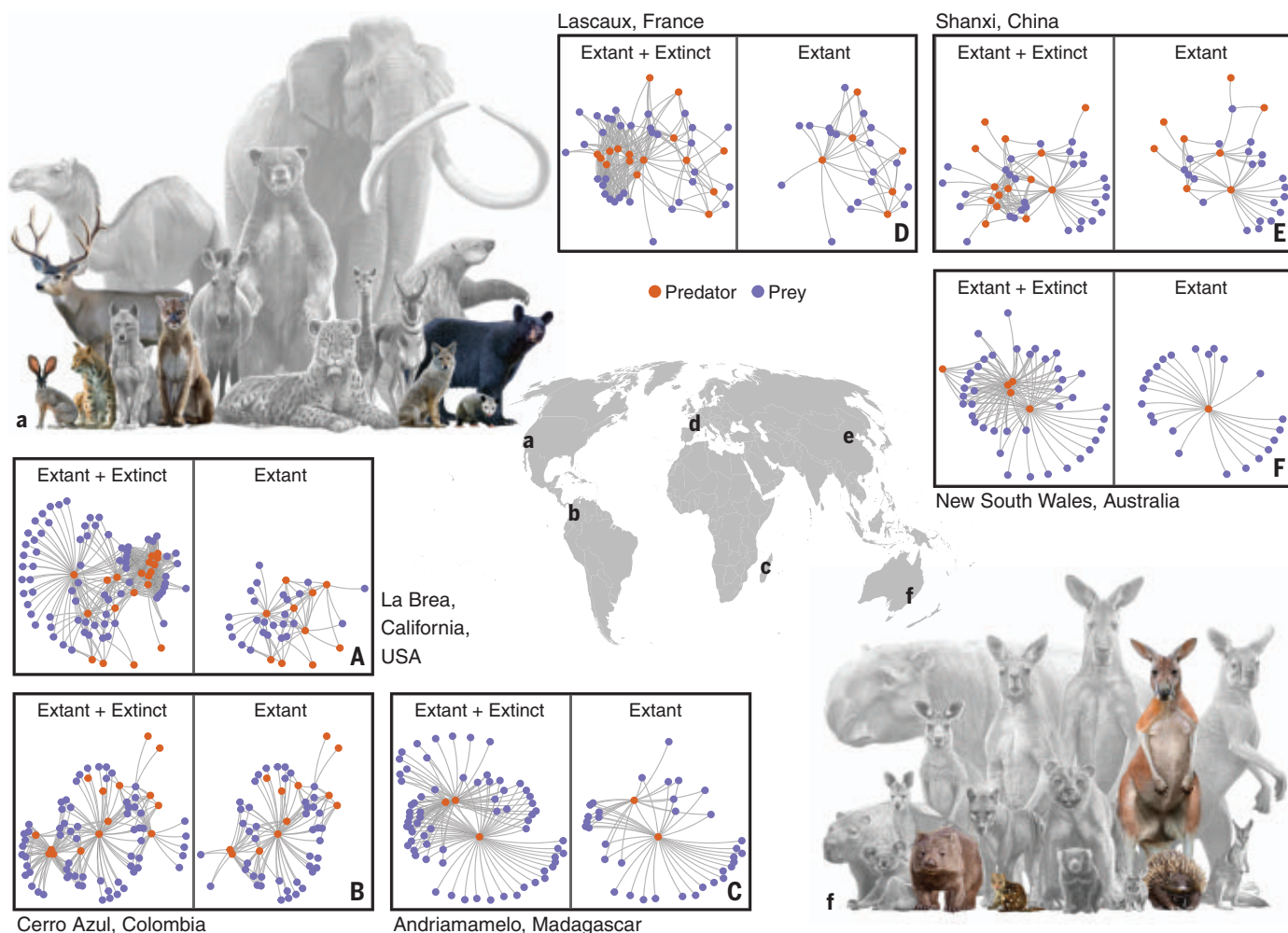
Fig. 1. Comparing terrestrial mammal food webs under current species composition and under species composition unaffected by extinction, local extirpation, and introduction. Lowercase letters correspond to locations on the map and illustrations of species composition, with color showing species that are extant at the site and grayscale indicating species that are extirpated or extinct.

number of extinctions was simulated, but in which the identities of mammal extinctions were randomized. This allowed us to distinguish between two alternatives regarding the resilience of food webs. If food webs have been resilient under extinction pressure either as a result of trophic redundancy (29) or because extinction is less likely for highly interactive species, then food web complexity would decline less than what would be expected by chance under random extinction. Alternatively, disproportionately greater extinction of highly interactive or functionally distinct species (30) would cause greater declines than expected by chance, indicating food web collapse (31). Thus, although food webs would be expected to decline to some extent given reduced species richness, the null model allows us to evaluate quantitatively whether observed food webs exhibit resilience (i.e., declining statistically less than the null model as reflected by nonoverlapping confidence intervals), a proportionate decline (i.e., declining as expected by chance),

or food web collapse (i.e., declining more than expected by chance). Note that the food webs include only species that interact with at least one other mammal species; thus, the number of species participating in a food web may decline faster than the number of species present if a species that is present no longer participates in the mammal food web (e.g., a species no longer co-occurs with its mammalian predator).

We found that in most cases, the observed declines in each region either started to be statistically more severe than the null expectation, or became more severe still, after the arrival of *Homo sapiens* (8) or European colonization (Fig. 2). Notably, the two regions occupied by hominins prior to *Homo sapiens* (Africa and Eurasia) exhibited the smallest-magnitude declines, and these declines differed little from the null expectation until industrialization. One potential explanation for the relative resilience of African and Eurasian food webs compared to other regions may be more gradual coevolution among hominins

and other mammals in these regions (32). Comparing observed extinctions to the null model, we estimate that food webs globally have lost 57% more links and 60% more species than would be expected by chance. Extinct species on average interacted with more species than did extant species (fig. S1A; $F_{1,4001} = 180$, $P \ll 0.0001$), and their loss has contributed to mammal food web collapse.

We next sought to understand how contemporary food webs have been shaped by past extinctions and range changes. We compared food webs constructed under alternate scenarios of species composition to determine the cumulative effects of extinction and range changes. To isolate the effect of extinction, we compared food webs composed of only extant species to food webs composed of both extant and now-extinct mammals. In both cases, we generated food webs as though all species filled their natural ranges (27), with ranges unaffected by range loss or anthropogenic species introductions (6). The largest declines

Fig. 2. Change due to extinction over the past 130,000 years in the number of participating species and links in reconstructed terrestrial mammal food webs. Lines show average percent change, and confidence intervals indicate ±1.96 standard errors, with null model results shown in gray.
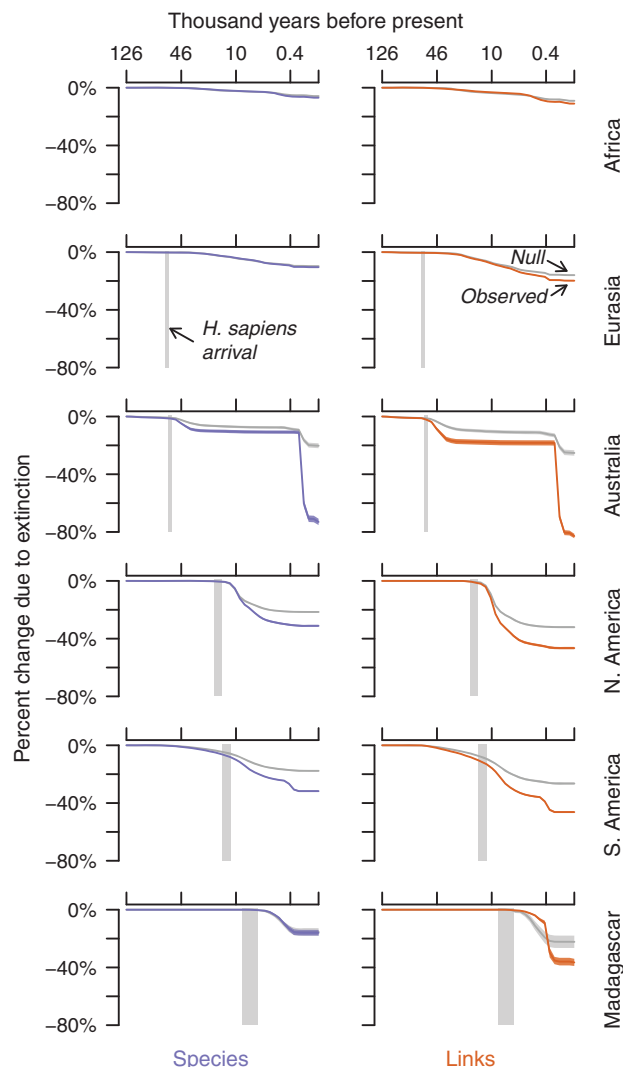
in species and links due to extinction alone were in the Americas, Australia, and Madagascar (Fig. 3, A and B). In these areas, the concomitant decline in links per species indicates that extinct species were disproportionately important for food web complexity (Fig. 3A and fig. S1A). Attempts to fully restore food webs in these areas would require replacements by functionally equivalent species native to other regions (33). At the region scale, extinctions have caused average declines of 7% to 73% in the number of participating species and average declines of 11% to 83% in food web links (Fig. 3B). Globally, we estimate that extinctions alone have caused a 20% decline in the number of species participating in terrestrial mammal food webs and a 29% reduction in food web links.

To assess the net effects of species range changes on food web complexity, we compared food webs consisting of extant species in their current ranges to food webs constructed for extant species as though their ranges were unaffected by local extirpation or anthropo-

genic species introduction (6). We found that further losses were widespread, also greatly affecting areas whose food webs were less affected by extinctions, including Africa and southern Eurasia (Fig. 3). Relative declines due to range changes, considering extant species only, were 7% to 76% across regions in the number of participating species and 13% to 82% in food web links (Fig. 3A), amounting to a further 20% global decline in participating species and 35% in links. Declines in links per species due to range changes indicate that species that experienced distributional contractions were disproportionately interactive within their former ranges (Fig. 3A and fig. S1B; $F_{1,3765} = 114.5$, $P \ll 0.0001$). When cumulative effects of extinctions and range changes were combined at the region scale and compared against the scenario where both extinct and extant species filled their natural ranges, average declines in participating species ranged from 27% to 94% and in links from 45% to 97% (Fig. 3B). At the global scale, we estimate that late-Quaternary defaunation has resulted in mammal food webs

on average consisting of 35% fewer species and 53% fewer links.

Lastly, we considered how the potential future extinction of endangered mammals would affect food webs globally. Relative to current species composition, the largest further losses in the number of participating species and the number of food web links would occur in areas including the Arctic and tropical and subtropical regions of Africa and Asia (Fig. 3A). In most areas where food webs are threatened by species loss, endangered species extinction would decrease the number of links per species (Fig. 3A). In other words, endangered species are central to preserving food web complexity in such areas. Exceptions include equatorial central Africa and parts of southeast Asia, where endangered species extinction would reduce the number of species and food web links but would not substantially alter links per species. Generally, endangered species interact more broadly than extant non-endangered species (fig. S1C; $F_{1,3765} = 19.0$, $P \ll 0.0001$), indicating their greater structural importance within food webs. Across regions, endangered species extinction would cause 10% to 67% further reductions in participating species and 15% to 80% in links beyond that incurred by existing defaunation (Fig. 3A), amounting to a further 14% global reduction in participating species and 21% reduction in food web links.

Our reconstruction of terrestrial mammal food webs allowed us to estimate the global magnitude of mammal food web collapse since the Late Pleistocene. We found that although only ~6% of terrestrial mammal species have gone extinct since the Late Pleistocene (6), more than half of mammal food web links have disappeared. Although much of the global food web simplification has resulted from extinctions that occurred centuries to millennia ago, range contractions in surviving species explain a similar magnitude of simplification. Controlled and natural experiments show that food web complexity supports ecosystem resilience and functioning (10, 34, 35), and ecological network simplification reduces ecosystem functioning (36). We found that the species most affected by defaunation are among the strongest contributors to food web complexity. Recovering food web complexity could be achieved with natural recolonization (37) and reintroduction (38, 39) of native mammals to their historic ranges, or with non-native functional analogs where necessary and appropriate (33, 39). Critical roles played by species affected by range contractions and recognized as endangered further underscore the need for their conservation to sustain food webs, as well as the strong potential for the restoration of food webs in the Anthropocene through recovery of these species to their historic ranges (40).
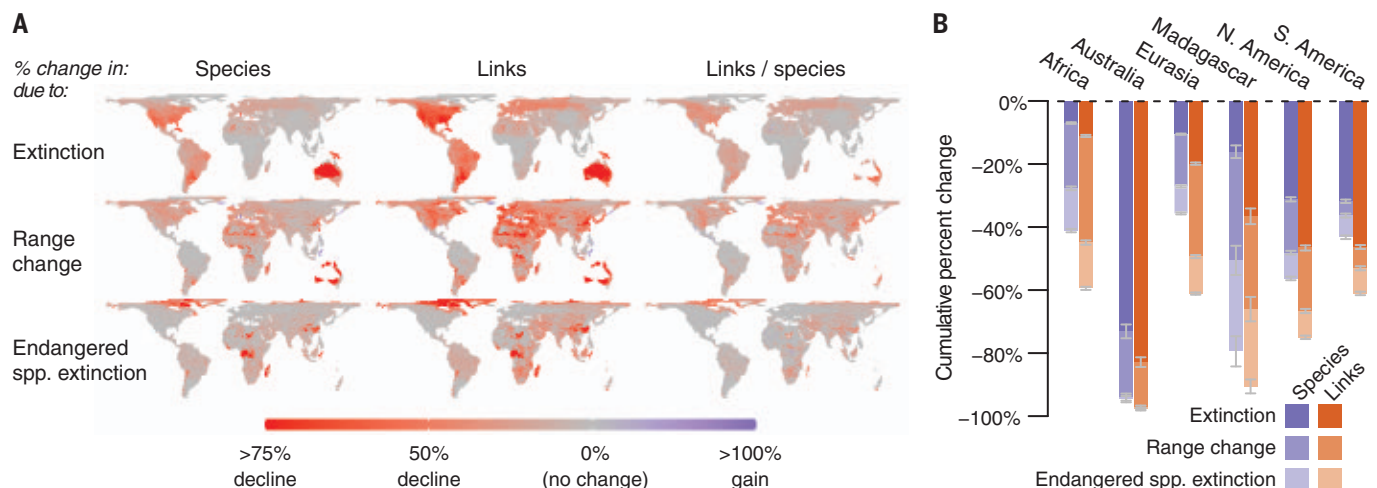
Fig. 3. Attributing change in food webs to extinction and range changes and assessing threats due to species endangerment. (**A**) Color scale indicates relative percent change in the number of participating species, number of links, and links per species due to extinction, the further percent change due to current range losses and species introductions, and the percent change relative to current species composition under potential future extinction of endangered species. Note that relative percent change values can sum to >100%. (**B**) Region-level absolute percent changes, with ±1.96 standard error bars in gray, presented relative to food webs under species composition unaffected by extinction or range changes.

REFERENCES AND NOTES

1. R. Dirzo *et al.*, *Science* **345**, 401–406 (2014).
2. H. S. Young, D. J. McCauley, M. Galetti, R. Dirzo, *Annu. Rev. Ecol. Evol. Syst.* **47**, 333–358 (2016).
3. W. J. Ripple *et al.*, *Sci. Adv.* **1**, e1400103 (2015).
4. S. L. Pimm, J. H. Lawton, J. E. Cohen, *Nature* **350**, 669–674 (1991).
5. T. Andermann, S. Faurby, S. T. Turvey, A. Antonelli, D. Silvestro, *Sci. Adv.* **6**, eabb2313 (2020).
6. S. Faurby *et al.*, *Ecology* **99**, 2626–2626 (2018).
7. F. A. Smith, R. E. Elliott Smith, S. K. Lyons, J. L. Payne, *Science* **360**, 310–313 (2018).
8. L. J. Bartlett *et al.*, *Ecography* **39**, 152–161 (2016).
9. C. Sandom, S. Faurby, B. Sandel, J.-C. Svenning, *Proc. R. Soc. B* **281**, 20133254 (2014).
10. J. A. Estes *et al.*, *Science* **333**, 301–306 (2011).
11. P. Kelley, M. Kowalewski, T. A. Hansen, *Predator-Prey Interactions in the Fossil Record* (Springer, 2003).
12. U. Brose *et al.*, *Nat. Ecol. Evol.* **3**, 919–927 (2019).
13. G. Woodward *et al.*, *Trends Ecol. Evol.* **20**, 402–409 (2005).
14. R. J. Williams, N. D. Martinez, *Nature* **404**, 180–183 (2000).
15. J. D. Yeakel *et al.*, *Proc. Natl. Acad. Sci. U.S.A.* **111**, 14472–14477 (2014).
16. N. Galiana, M. Lurgi, J. M. Montoya, B. C. López, *Oikos* **123**, 721–728 (2014).
17. M. M. Pires *et al.*, *Proc. R. Soc. B* **282**, 20151367 (2015).
18. D. Gravel, T. Poisot, C. Albouy, L. Velez, D. Mouillot, *Methods Ecol. Evol.* **4**, 1083–1090 (2013).
19. G. S. Chiu, A. H. Westveld, *Proc. Natl. Acad. Sci. U.S.A.* **108**, 15881–15886 (2011).
20. S. T. Segar *et al.*, *Trends Ecol. Evol.* **35**, 454–466 (2020).
21. M. Pichler, V. Boreux, A.-M. Klein, M. Schleuning, F. Hartig, *Methods Ecol. Evol.* **11**, 281–293 (2020).
22. M. M. Pires *et al.*, *Quat. Sci. Rev.* **250**, 106696 (2020).
23. P. R. Guimarães Jr., *Annu. Rev. Ecol. Evol. Syst.* **51**, 433–460 (2020).
24. O. Middleton, H. Svensson, J. P. W. Scharlemann, S. Faurby, C. Sandom, *Glob. Ecol. Biogeogr.* **30**, 1175–1182 (2021).
25. J. H. Poelen, J. D. Simons, C. J. Mungall, *Ecol. Inform.* **24**, 148–159 (2014).
26. C. D. Soria, M. Pacifici, M. Di Marco, S. M. Stephen, C. Rondinini, *Ecology* **102**, e03344 (2021).
27. See supplementary materials.
28. J. A. Dunne, R. J. Williams, N. D. Martinez, *Proc. Natl. Acad. Sci. U.S.A.* **99**, 12917–12922 (2002).
29. D. Sanders, E. Thébault, R. Kehoe, F. J. Frank van Veen, *Proc. Natl. Acad. Sci. U.S.A.* **115**, 2419–2424 (2018).
30. D. F. B. Flynn *et al.*, *Ecol. Lett.* **12**, 22–33 (2009).
31. G. S. Cumming, G. D. Peterson, *Trends Ecol. Evol.* **32**, 695–713 (2017).
32. P. S. Martin, R. G. Klein, *Quaternary Extinctions: A Prehistoric Revolution* (Univ. of Arizona Press, 1989).
33. E. J. Lundgren *et al.*, *Proc. Natl. Acad. Sci. U.S.A.* **117**, 7871–7878 (2020).
34. D. L. Finke, R. F. Denno, *Nature* **429**, 407–410 (2004).
35. A. D. Wallach, W. J. Ripple, S. P. Carroll, *Trends Ecol. Evol.* **30**, 146–153 (2015).
36. E. C. Fricke, A. Ordonez, H. S. Rogers, J.-C. Svenning, *Science* **375**, 210–214 (2022).
37. G. Chapron *et al.*, *Science* **346**, 1517–1519 (2014).
38. W. J. Ripple, R. L. Beschta, *Biol. Conserv.* **145**, 205–213 (2012).
39. J.-C. Svenning *et al.*, *Proc. Natl. Acad. Sci. U.S.A.* **113**, 898–906 (2016).
40. C. Vynne *et al.*, *Ecography* **2022**, e06098 (2022).
41. E. Fricke, evancf/AniDiet: First release of data and code, Zenodo (2022); https://doi.org/10.5281/zenodo.6678596.

POSTDOCTORAL POSITION IN HOST-PATHOGEN-VECTOR INTERACTIONS
Department of Internal Medicine and Department of Microbial Pathogenesis

The Laurent-Rolle lab at Yale University, New Haven, CT is now accepting applications for **Postdoctoral associates** in the area of host-pathogen-vector interactions to start as soon as possible.

We are interested in how RNA viruses evade the host immune system and how host-responses to virus infections prevent or enhance infections. There are multiple ongoing projects that are interdisciplinary and highly collaborative including studies on SARS-CoV-2, Zika virus and Eastern Equine Encephalitis virus. Specifically, we are interested in **1)** the mechanisms of actions of interferon stimulated genes in host resistance to viral infections, **2)** dissecting the molecular mechanisms utilized by pathogenic viruses to antagonize host immune responses, **3)** the development of vaccines and novel therapeutics against viral infections, and **4)** identifying biomarkers of viral infections for early diagnosis.

Eligible candidates should have, or be close to completing, a Ph.D. or M.D in immunology, virology, molecular biology, or related fields. Highly motivated individuals with experience in innate immunity, protein biochemistry, and animal experimentation are encouraged to apply.

Interested applicants should send a cover letter explaining why you think this lab would be a good fit for you, a CV, and contact information for three references to Dr. Maudry Laurent-Rolle at **maudry.laurent-rolle@yale.edu**. The subject of the email should be "Postdoctoral Position in Host-Pathogen interaction".

Yale University is an affirmative action, equal opportunity employer. Applications from women and minorities are encouraged.

CENTER FOR MOLECULAR MEDICINE AND GENETICS

WAYNE STATE UNIVERSITY

The Center for Molecular Medicine and Genetics in the Wayne State University School of Medicine (**http://genetics.wayne.edu/**) is expanding its high-impact research unit and is seeking outstanding candidates who are pursuing fundamental and/or translational problems that would complement existing strengths represented in the Center. Particular foci of interest are: **(1)** human genetics and genomics and **(2)** metabolism and inflammation, although we are interested in outstanding candidates in other areas.

This **tenure-track position** can be filled at any level. A competitive start-up package will be provided, commensurate with the candidate's experience and achievement. Candidates will be expected to establish an internationally recognized, extramurally funded research program and to participate in graduate and medical teaching and service. Opportunities for scientific collaboration are available within the Center and externally in multiple areas.

Candidates holding a PhD and/or MD, or equivalent degree(s) with a strong record of research productivity are encouraged to apply. For further information and to submit your application, please visit our online application site at **https://jobs.wayne.edu/ (Posting #046677)**. Candidates should include a cover letter, research description (1-3 pages) and teaching philosophy along with their curriculum vitae.

Our Center has a long history of providing high quality education and pioneering research for medical students, graduate students in our PhD and MS programs, and students in our Genetic Counseling program. A strength of our graduate programs is that, in addition to developing a high level of expertise in a research discipline, our students are required to develop a broad understanding in genetics and genomics technologies and computation.

Wayne State University is a premier, public, urban research university located in the heart of Detroit where students from all backgrounds are offered a rich, high quality education. Our deep-rooted commitment to excellence, collaboration, integrity, diversity and inclusion creates exceptional educational opportunities preparing students for success in a modern global society. Wayne State University encourages applications from women, people of color and others underrepresented in medicine. Wayne State University is an affirmative action/equal opportunity employer. Metropolitan Detroit, with a population of four million, encompasses many outstanding residential areas, fine public and private schools for K-12 education, myriad cultural and recreational opportunities, and proximity to other outstanding institutions of higher education.

IT'S NOT JUST A JOB. IT'S A CALLING.

Find your next job at ScienceCareers.org

Whether you're looking to get ahead, get into, or just plain get advice about careers in science, there's no better or more trusted authority. Get the scoop, stay in the loop with *Science* Careers.

Science Careers
FROM THE JOURNAL SCIENCE AAAS

Massachusetts Institute of Technology

FACULTY POSITIONS
DEPARTMENT OF BIOLOGICAL ENGINEERING

The MIT Department of Biological Engineering in Cambridge, MA invites applications for tenure-track faculty positions at the **assistant professor level**, to begin **July 1, 2023** or on a mutually agreeable date thereafter. MIT Biological Engineering is a unique department that fuses molecular and cellular bioscience with quantitative engineering approaches and includes faculty and students with diverse scientific interests and backgrounds. Areas of high priority for growth include biotechnology beyond medicine, including applications in materials, chemicals, agriculture, sustainability, energy and the environment, as well as innovative new areas for the application of biotechnology. Applicants should hold a Ph.D. in a science or engineering discipline related to Biological Engineering by the beginning of employment and should have demonstrated experience in biological engineering research. A more senior faculty appointment may be considered in special cases. The department culture is vibrant, creative, and collaborative, and we strive to help each member of the community reach their greatest potential. Faculty duties include teaching at the graduate and undergraduate levels, conducting research, as well as supervision, training and mentoring students and junior researchers. Candidates should be capable of instructing in our core biological engineering educational curricula.
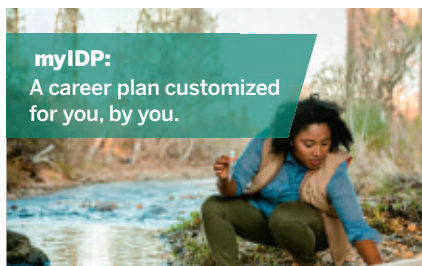
Candidates must register with the BE search website at **http://be-fac-search.mit.edu**, and must submit application materials electronically to this website. Candidate applications should include a description of professional interests and goals in both teaching and research. Each application should include a curriculum vita and the names and addresses of three or more references who will provide recommendation letters. References should submit their letters directly at the **http://be-fac-search.mit.edu** website.

Applications received by **February 28, 2023** will be given priority.

Questions may be directed to: Prof. Angela Belcher, Head, Department of Biological Engineering, MIT: 77 Massachusetts Avenue, 16-343, Cambridge, MA 02139, **bedh@mit.edu**

With MIT's strong commitment to diversity in engineering and science education and research, we especially encourage those who will contribute to our diversity and outreach efforts to apply.

MIT is an equal employment opportunity employer. All qualified applicants will receive consideration for employment and will not be discriminated against on the basis of race, skin color, gender identity, sexual orientation, religion, disability, age, genetic information, veteran status, ancestry, or national or ethnic origin. MIT's full policy on Nondiscrimination can be found at: https://policies.mit.edu/policies-procedures/90-relations-and-responsibilities-within-mit-community/92-nondiscrimination

---

THE UNIVERSITY OF CHICAGO

Instructional Professors in Neuroscience, Biochemistry and Computational Biology

DESCRIPTION
The Neuroscience Institute and the Biological Sciences Collegiate Division at the University of Chicago are accepting applications for **two open rank Instructional Professor positions** pending budgetary approval. These are full-time teaching positions beginning on or after **January 1, 2023**. The appointment will be for an initial term of at least two years with reappointment and progression possible following review.

Responsibilities include teaching undergraduate neuroscience and/or biological science courses. Additional duties include, hiring, training, and supervising teaching assistants. Instructional Professors of all ranks are required to engage in regular professional development.

QUALIFICATIONS
Applicants must have a PhD in a relevant discipline in hand prior to start date and at least one year of teaching university level lectures and/or laboratory courses. We are particularly interested in applicants with expertise in neuroscience, biochemistry, and/or computational biology.

APPLICATION INSTRUCTIONS
Applicants must apply online at the University of Chicago's Interfolio website at **apply.interfolio.com/111651**. The required application materials are: **1)** cover letter; **2)** a curriculum vitae; **3)** a teaching statement; **4)** a sample course syllabus; **5)** course evaluations or evidence of past teaching performance; **6)** the names and contact information for three references

Review of applications will begin on **September 19, 2022** and will continue until the positions are filled or the search is closed.

The positions will be part of the Service Employees International Union.

We seek a diverse pool of applicants who wish to join an academic community that places the highest value on rigorous inquiry and encourages diverse perspectives, experiences, groups of individuals, and ideas to inform and stimulate intellectual challenge, engagement, and exchange. The University's Statements on Diversity are at https://provost.uchicago.edu/statements-diversity.

The University of Chicago is an Affirmative Action/Equal Opportunity/Disabled/Veterans Employer and does not discriminate on the basis of race, color, religion, sex, sexual orientation, gender identity, national or ethnic origin, age, status as an individual with a disability, protected veteran status, genetic information, or other protected classes under the law. For additional information please see the University's Notice of Nondiscrimination.

Job seekers in need of a reasonable accommodation to complete the application process should call 773-834-3988 or email equalopportunity@uchicago.edu with their request.

By **M. Shehryar Khan**

From dropout to Ph.D.

was on a long-haul trucking trip, somewhere between Mississauga and Montreal, but my mind was elsewhere. I was thinking about my personal journey and wondering whether this was my future. I had dropped out of university, and now I was riding with a family friend who owned a trucking company to see whether this might be a viable career option for me. Trucking was more reliable and paid better than what I had been doing, juggling three part-time jobs in retail and customer service to make ends meet. I was helping support my mother and two younger sisters and needed a job I could count on. But I couldn't shake the sense that I would be choosing this route with feelings of failure looming over my head—a path I knew would lead to unhappiness.

When I was younger, I had been a straight-A student with aspirations to attend a top university. But things started to go downhill for me in middle school after the 9/11 attacks perpetrated against the United States, where I was living as a recent immigrant from Pakistan. At school the following day, a teacher publicly insinuated that I was somehow responsible for the attacks. That evening, I was seriously injured during football practice. The next day, our family businesses were vandalized. The racism posed a clear threat to our safety and pushed us to move back to Pakistan.

Then, my parents divorced. Torn between wanting to be with my mother, who moved to Canada alone with no support, or with my beloved aging grandfather in Pakistan, I moved back and forth but became depressed and struggled with my academics. I barely graduated from high school and enrolled at the only university that offered me a spot, feeling that I had already failed.

That mindset triggered a vicious cycle. I was too discouraged to thrive in my studies, and my resulting struggles reinforced my belief that I was failing. I began to suffer from severe depression, and the death of my grandfather was the final straw. With no real hope for the future, I dropped out and returned to my mother and sisters in Mississauga.

That's when I went on the trucking run. During those long hours on the road, my grandfather's last words of advice, in a letter he wrote when I started university, came back to me: "Please be brave (which you are), accept the challenges of life (which is never a bed of roses), work hard and harder, and you will see the blessings of Almighty God and our prayers are with you at all times. It is now or never.

"My path suddenly became clear: I had to finish what I had started and go back to school."

I hope you will never disappoint us." With his words ringing in my ears, I discovered a newfound resolve. My path suddenly became clear: I had to finish what I had started and go back to school.

To get back on track, I needed to redo grade 12. I took a full course load while continuing to work enough part-time hours at Home Depot and Walmart to help pay the bills. After graduating from high school (again!), I began a university engineering co-op program, in which I would work as a paid intern every alternate term, allowing me to keep my student loans in check while continuing to help support my family.

At first, the fear of failure that had doomed my previous university endeavor continued to linger at the back of my mind. But I knew it would hold me back if I didn't do something about it. So, I finally started counseling and therapy, which helped me realize that the outcome didn't matter as much as knowing I tried my best, and over time I learned to keep my fear of failure in check. After completing my bachelor's degree, I went on to a master's and now a Ph.D., winning several research awards along the way—something I scarcely could have imagined just a few years earlier.

Grad school has been full of the challenges and setbacks that every student is well aware of, but my path to this point has made one thing clear: My fear of failure not only limited me, but kept me from achieving my goals. I finally internalized the words my grandfather wrote to me in that letter all those years ago. I hope I have made him proud. ∎

M. Shehryar Khan is a Ph.D. candidate at the University of Waterloo. Send your career story to SciCareerEditor@aaas.org.

ILLUSTRATION: ROBERT NEUBECKER

MICHELSON PHILANTHROPIES & Science | **PRIZE FOR IMMUNOLOGY**

REWARDING HIGH-RISK RESEARCH.
SUPPORTING EARLY-CAREER SCIENTISTS.
HELPING TO FIND CURES FASTER.
APPLY TODAY

Now accepting applications for the Michelson Philanthropies & *Science* Prize for Immunology.

The Michelson Philanthropies and Science Prize for Immunology focuses on transformative research in human immunology, with trans-disease applications to accelerate vaccine and immunotherapeutic discovery. This international prize supports investigators 35 and younger, who apply their expertise to research that has a lasting impact on vaccine development and immunotherapy. It is open to researchers from a wide range of disciplines including computer science, artificial intelligence/machine learning, protein engineering, nanotechnology, genomics, parasitology and tropical medicine, neurodegenerative diseases, and gene editing.

Application deadline: Oct. 1, 2022.

For more information visit:
www.michelsonmedicalresearch.org

#MichelsonPrizes

"The Michelson Philanthropies & Science Prize for Immunology will greatly impact my future work. As I am just starting my scientific career, it will illuminate my work, spark interest and support me to continue my research in this field."

Paul Bastard, MD, PhD,
Laboratory of Human Genetics of Infectious Diseases, Imagine Institute (INSERM, University of Paris), Paris, France; and The Rockefeller University, New York.

Dr. Bastard received the inaugural Grand Prize for his essay: "Why do people die from COVID-19: Autoantibodies neutralizing type I interferons increase with age."
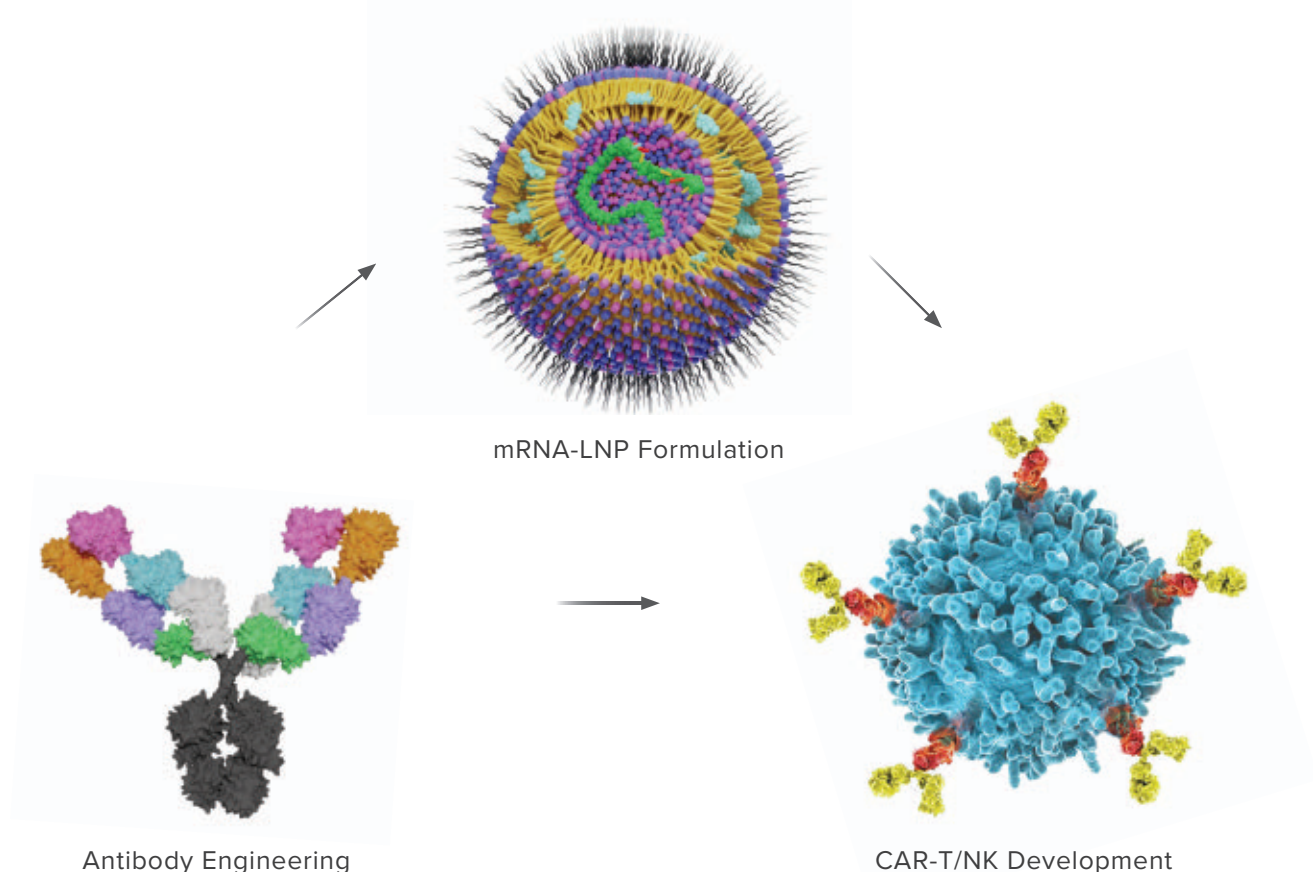
GRAND PRIZE:
$30,000

FINALIST PRIZE:
$10,000

mRNA-LNP Products & Services

For Vaccine and Immunotherapy Development

mRNA-LNP Formulation

Antibody Engineering

CAR-T/NK Development

Antibody Services

- Monoclonal Ab Development
- Hybridoma Sequencing
- Human Antibody Screening
- Antibody Humanization
- Bispecific Antibody Engineering
- Stable Cell Line Generation

mRNA-LNP Services

- mRNA Design and Synthesis (IVT)
- mRNA Capping & Purification
- mRNA-LNP Encapsulation
- mRNA-LNP Scale Up and QC
- mRNA-LNP Validation In Vivo
- Ionizable Lipid Licensing

Immune Cell Services

- Lentivirus Production GMP
- CAR-T/NK Cell Generation
- CAR-T/NK Animal Model
- Immune Cell Engineering
- T/B/NK/Dendritic cell, Macrophages
- TCR knockout by CRISPR

All products are for research use only

Discover more | www.promab.com

ProMab
Biotechnologies, Inc.

⊙ 2600 Hilltop Dr, Building B, Suite C320, Richmond, CA 94806

📞 1.866.339.0871 | ✉ info@promab.com